学位論文

Search for the Lepton Flavor Violating Muon Decay $\mu^+ \to e^+\gamma$ with a Sensitivity below 10^{-12} in the MEG Experiment

訳

(MEG実験による10^{-12}以下の感度でのレプトンフレーバーを破るミューオン崩壊$\mu^+ \to e^+\gamma$の探索)

平成 25 年 12 月 博士（理学）申請

東京大学大学院理学系研究科
物理学専攻

藤井 祐樹

December 2013

Abstract

The Standard Model (SM) of the particle physics has been established by many experimental tests. However, there are still several puzzles which cannot be explained by the SM and it is thought that the SM is an approximation of more fundamental physics theory. The MEG experiment searches for the Lepton Flavor Violating decay: $\mu^+ \to e^+\gamma$ as an evidence of the new physics, since this decay is strictly forbidden in the SM. We perform a $\mu^+ \to e^+\gamma$ search using new data sample and improved analysis methods. Compared with the previous MEG result, the total statistics are doubled by adding the data taken in 2011. In this search, several methods of calibrations and analysis are improved to maximize the experimental sensitivity. In the analysis, 1) new pileup identification method in the gamma reconstruction, 2) the offline noise reduction for the positron reconstruction and 3) new track fitting algorithm are newly implemented and performed. The physics analysis is improved as well. Therefore, the data of 2009–2010 are analyzed again with the new analysis and the new analysis gives a 20% better sensitivity than that with the previous analysis. By analyzing the dataset of 2009–2011, we obtain a branching ratio sensitivity of

$$S = 7.7 \times 10^{-13}.$$

This is the first search for the $\mu^+ \to e^+\gamma$ decay with a sensitivity below 10^{-12}. The result is consistent with background-only hypothesis, therefore we set only the upper limit. The observed 90% C.L. upper limit on the existence on of the $\mu^+ \to e^+\gamma$ decay is calculated to be

$$B(\mu^+ \to e^+\gamma) < 5.7 \times 10^{-13}.$$

This is a four times more stringent upper limit on the existence of the $\mu^+ \to e^+\gamma$ decay than the previous best limit set by MEG.

Contents

1 Physics Motivation **17**
1.1 Muon Decay in the Standard Model . . . 17
1.1.1 Michel Decay . . . 18
1.1.2 The $\mu^+ \to e^+\gamma$ Decay in the Standard Model . . . 18
1.2 The $\mu^+ \to e^+\gamma$ decay and Physics Beyond the Standard Model . . . 19
1.2.1 SUSY GUT SU(5) . . . 19
1.2.2 SUSY Seesaw . . . 21
1.2.3 The $\mu^+ \to e^+\gamma$ Decay and $(g-2)_\mu$ Anomaly . . . 22
1.3 Searches for the CLFV Processes . . . 22
1.3.1 Experimental History of the $\mu^+ \to e^+\gamma$ Decay Searches . . . 22
1.3.2 Background . . . 24
1.3.3 Comparison with Other CLFV Searches . . . 27

2 The MEG Experiment **31**
2.1 Beamline . . . 31
2.1.1 Muon Beamline . . . 33
2.1.2 Beam Transport Solenoid . . . 33
2.1.3 Target . . . 34
2.2 Gamma Detector . . . 34
2.2.1 Liquid Xenon . . . 35
2.2.2 Detector Design . . . 36
2.3 Positron Spectrometer . . . 37
2.3.1 COBRA Magnet . . . 38
2.3.2 Drift Chamber . . . 41
2.3.3 Timing Counter . . . 42
2.4 Front-end Electronics and Data Acquisition System . . . 45
2.4.1 DRS4 . . . 45
2.4.2 Trigger . . . 47
2.4.3 MIDAS . . . 49
2.5 Simulation and Analysis Framework . . . 49
2.5.1 Simulation . . . 49
2.5.2 Analysis . . . 51
2.6 Run Status . . . 51
2.6.1 Run 2009 . . . 51
2.6.2 Run 2010 . . . 52
2.6.3 Run 2011 . . . 52

3 Event Reconstruction **54**
3.1 Gamma Reconstruction . . . 54
3.1.1 Waveform Analysis . . . 54
3.1.2 Position Reconstruction . . . 55
3.1.3 Energy Reconstruction . . . 56
3.1.4 Time Reconstruction . . . 56
3.1.5 Pileup Identification . . . 56
3.1.6 Cosmic-ray Rejection . . . 57
3.2 Positron Reconstruction . . . 57
3.2.1 Hit Reconstruction . . . 60
3.2.2 Cluster Finding . . . 67
3.2.3 Track Finding . . . 67
3.2.4 Track Fitting . . . 68
3.2.5 Time Reconstruction . . . 71
3.2.6 Impact Point in Timing Counter . . . 72

4 Calibrations **74**
4.1 LXe Monitoring and Calibration Methods . . . 74
4.1.1 Charge Exchange Calibration . . . 74
4.1.2 Cockcroft-Walton . . . 75
4.1.3 Neutron Generator . . . 76
4.1.4 Cosmic Ray . . . 76
4.1.5 LED . . . 76
4.1.6 Alpha Source . . . 77
4.1.7 Light Yield History . . . 78
4.2 Drift Chamber Calibrations . . . 78
4.2.1 Hit Z Calibration . . . 78
4.2.2 Hit Time Calibration . . . 78
4.3 Alignment . . . 80
4.3.1 Optical Survey . . . 80
4.3.2 Cosmic Ray Alignment . . . 81
4.3.3 Michel Alignment . . . 81
4.3.4 Relative Alignment . . . 82
4.4 Timing Counter Calibrations . . . 85
4.4.1 Gain Equalization . . . 85
4.4.2 Time Offsets Correction . . . 85
4.4.3 CW-Boron . . . 85
4.5 Relative Time Offset . . . 85

5 Performance **86**
5.1 Performance of the LXe Detector . . . 86
5.1.1 Gamma Selection . . . 86
5.1.2 Gamma Position Resolution . . . 86
5.1.3 Gamma Energy Response . . . 87
5.1.4 Gamma Timing Resolution . . . 87
5.1.5 Gamma Efficiency . . . 89

5.2 Performance of the Positron Spectrometer . . . 89
5.2.1 Positron Selection . . . 89
5.2.2 Single Hit Resolution . . . 90
5.2.3 Positron Energy Response . . . 90
5.2.4 Angular and Vertex Resolutions . . . 91
5.2.5 Positron Timing Resolution . . . 94
5.2.6 Positron Efficiency . . . 94
5.3 Combined Performance . . . 95
5.3.1 Vertex Resolutions . . . 95
5.3.2 Timing Resolution . . . 95
5.3.3 Contributions of Reconstruction Improvements . . . 96
5.4 Performance Summary . . . 104

6 Physics Analysis **105**
6.1 Datasets . . . 105
6.1.1 Pre-Selection . . . 106
6.1.2 Blind Box . . . 106
6.1.3 Analysis Region . . . 106
6.1.4 Sideband Data . . . 107
6.1.5 Time Sidebands . . . 108
6.1.6 Angle Sidebands . . . 109
6.2 Likelihood Analysis . . . 109
6.3 PDF . . . 110
6.3.1 Category PDF . . . 110
6.3.2 Signal PDF . . . 110
6.3.3 Accidental Background PDF . . . 117
6.3.4 RMD PDF . . . 118
6.3.5 Illustration of PDFs . . . 120
6.4 Confidence Region . . . 120
6.4.1 Full-MC study . . . 123
6.5 Normalization . . . 125
6.5.1 Analysis Efficiency . . . 125
6.5.2 Michel Normalization . . . 125
6.5.3 RMD Normalization . . . 127
6.5.4 Combined normalization factors . . . 129

7 Results and Discussions **132**
7.1 Sensitivity . . . 132
7.2 Sideband Results . . . 134
7.2.1 Results with Time Sidebands . . . 134
7.2.2 Results with Angle Sidebands . . . 136
7.3 Result in Analysis Region . . . 136
7.4 Effects of Systematic Uncertainties . . . 142
7.4.1 Uncertainties of Parameters . . . 142
7.4.2 Comparison of Systematic Uncertainties . . . 144
7.5 Further Checks . . . 145

7.5.1 Result from Category PDF 146
7.5.2 Analysis Compatibility 146
7.5.3 Event-by-Event Check and Comparison 147
7.6 Discussions and Prospects 149
7.6.1 Discussions 149
7.6.2 Prospects 151

8 Conclusion **154**

A Geometrical Model of Correlations **156**
A.1 Implementation of Correlations 158

B Radiative Muon Decay **159**

List of Figures

1.1 Feynman diagram for the $\mu^+ \to e^+\gamma$ decay through the neutrino oscillation. 19
1.2 Feynman diagrams for the $\mu^+ \to e^+\gamma$ decay in SU(5) SUSY GUT. 20
1.3 Correlation between $B(\mu \to e\gamma)$ and $B(\tau \to \mu\gamma)$ as a function of m_{N3}, for constraint MSSM assuming universality of the soft-SUSY breaking at the scale of gauge coupling unification, M_X so-called minimal supergravity (mSUGRA) framework from [16]. Different colored regions correspond to $\theta_{13} = 1^\circ, 3^\circ, 5^\circ$ and 10° (red, green, blue and pink, respectively) and recent experiments report the large value of $\theta_{13} \sim 10^\circ$ [17]. Dashed line labeled "MEG2011" is added to the original plot and it represents the 90% C.L. upper limit given by the previous result of MEG [4]. 21
1.4 Simplified Feynman diagram of the $\mu^+ \to e^+\gamma$ decay (left) and the muon magnetic moment (right). 23
1.5 Correlation between $B(\mu^+ \to e^+\gamma)$ and Δa_μ from [20]. Horizontal dashed line labeled "MEG2011" is added to the original plot and it represents the 90% C.L. upper limit given by the previous result of the MEG experiment. Vertical two dashed lines are also added and they represent the 1σ region of the $(g-2)_\mu$ anomaly measured in the E821 experiment [18]. Assumed parameters are as follows;$|\delta^{12}_{LL}| = 10^{-4}$, $|\delta^{23}_{LL}| = 10^{-2}$. Here the relatively small slepton mass and large $\tan\beta$ are assumed. The inner red area satisfy the B-physics constraints. 23
1.6 Left figure shows positron energy spectrum of unpolarized $\mu^+ \to e^+\nu_e\overline{\nu}_\mu$ decay (Michel spectrum). A radiative decay correction [25] is included. Right one shows gamma Energy spectrum of unpolarized $\mu^+ \to e^+\nu_e\overline{\nu}_\mu\gamma$ decay. Positron energy and the angle between a positron and a gamma are integrated. 26

2.1 Top and side view of all the experimental apparatus with coordination. . 32
2.2 3D view of all the experimental apparatus with coordination. 32
2.3 590 MeV proton ring cyclotron at PSI. 33
2.4 Schematic view of the πE5 beam channel including the beam transport system and detectors. 34
2.5 Muon target (a) and installed view inside the COBRA magnet (b). . . . 35
2.6 Schematic views of the LXe detector. 36
2.7 LXe detector before closing a flange of the outer vacuum vessel. 37
2.8 LXe detector inside with PMTs installed on all surfaces. 37

2.9 Concept of the COBRA magnetic field compared with the uniform field. Positrons emitted around 90° are quickly swept away (c) while they stay longer in a uniform field case (a). Positrons which emitted different θ angles have same curvatures in the COBRA magnetic field (d). On the other hand, they have different curvatures in a uniform case (b). 38
2.10 Contour plot of absolute values of the gradient magnetic field generated by the COBRA magnet 39
2.11 Positron hit rate per 1 cm^2 in each drift chamber module with a 3×10^7 Hz muon stopping rate as a function of the radius. Green triangle markers show those with an uniform magnetic field and orange markers show those with the COBRA magnetic field. 40
2.12 Distribution of the magnetic field around the LXe detector. The PMTs of the LXe detector are placed along the trapezoidal box shown in this figure. 40
2.13 Drift chamber modules installed inside the COBRA magnet. 41
2.14 Schematic side views of a drift chamber module. One plane has nine anode wires and all anode and potential wires are supported by a open shape frame as shown in (a). The module is covered by the cathode foil which has 5 cm periodical zig-zag shape called "vernier pattern" as shown in (b). 42
2.15 Configuration of cells inside the chamber module. Two planes are divided with a gap of 3 mm and the position of the sense wires are staggered. Green horizontal lines show the cathode pads. 43
2.16 Field map and drift lines calculated by `GARFIELD` simulation with the nominal operated condition in MEG. 43
2.17 45
2.18 Timing counter bars covered with fibers for z position measurement. . . . 46
2.19 Schematic of DRS principle. 47
2.20 Illustration of the trigger system. 49
2.21 Illustration of the full programming chain for the analysis and the MC simulation in MEG. 50
2.22 Number of stopped muons on the target during physics data taking of 2009–2011. 53

3.1 (a) An example of a PMT raw waveform from the waveform digitizer. (b) An example of a waveform with high-pass filter. 55
3.2 An example event with pileup gamma ray which is identified by using the distribution of the light yield. Magenta circles show the pileup cluster. . 57
3.3 An event with pileup which identified by the peak search. Left plot shows the normal waveform after moving-average and right plot shows the differential one. Magenta stars show the found peaks. 58
3.4 An waveform as same event as shown in Fig. 3.3 before (left) and after (right) applying the pileup elimination. 58
3.5 Two dimensional scatter plot of the charge ratio on the inner/outer faces vs the gamma ray interaction depth. Black points show the data from cosmic ray runs, and green ones shows the signal Monte Carlo events. The two blue lines show the selection criteria for the cosmic ray rejection. . . 59

3.6 Example of waveforms in one cell in an event. Top two waveforms are from both ends of the anode wire, and others are from each side of cathodes. Red horizontal lines show the calculated baseline of each waveform. Red vertical lines at the left edge of each peak show calculated hit timing. . . 61
3.7 Correlation between the vernier circle and z_a. 62
3.8 Relation between distance from anode wire and hit timing calculated by using the `Garfield` simulation. 63
3.9 Example of DCH waveforms in a cell which taken in the 2011 noisy run period. 64
3.10 Example of DCH waveforms taken after hardware investigations. 65
3.11 Power spectrum of accumulated DCH waveforms taken in the 2011 noisy run period. 66
3.12 Raw DCH waveform (black solid line) and after the filtering (red solid line) in noisy run (a). The charge integration is done for the area between 2 blue solid lines. (b) is the power spectrum of waveform (a) before/after filtering (black/red). 67
3.13 A positron trajectory fitted by using the previous track fitting in an event. 70
3.14 Differences of reconstructed hits by using new/old Kalman in X-Y view (left) and X-Z view (right). Red stars show the hits reconstructed by using new Kalman and blue ones show those reconstructed by using old Kalman. Magenta circles in the left plot shows measured hits belonging to the reconstructed track and the radius of each circle shows the measured drift distance. Black points shown in the left plot represent the position of wires. 71

4.1 BGO (NaI) mover(a) and two dimensional plot of gamma ray energies measured by the LXe detector and the BGO detector(b). 75
4.2 Reconstructed positions of 25 α sources inside the LXe detector. In this particular run, the half of the detector was filled with liquid xenon and the other part was filled with gaseous xenon. 77
4.3 Upper plot shows the light yield history measured by using CW-Li peak (black) and background scale (red). To calibrate the light yield history, other possible sources (CEX 55 and 83 MeV gamma, 9 MeV gamma with neutron generator, cosmic-ray, and alpha source peak) are used. Combined history curve is also shown in this plot with a gray curve. Bottom plot shows same history after the correction by using the combined curve so that it becomes flat. 79
4.4 Correlation between z_a and the cathode vernier pad asymmetry (black markers), fitted by a sinusoidal function (red line). 80
4.5 Corner cubes mounted on the downstream side of the drift chambers. . . 81
4.6 3D view of 10 cosmic-ray counter bars (shown in cyan). Green line shows a simulated cosmic-ray, which pass through both drift chambers and the cosmic-ray counter. 82
4.7 Reconstructed positron vertex distribution in Z-Y plane in 2011. 83
4.8 An illustration of the software target alignment with Michel positrons in case of the displacement of the target in horizontal axis. 83

5.1 Reconstructed position distribution projected on the v-axis with a lead collimator in CEX runs. 87
5.2 Fitted energy response of the LXe detector for 55 MeV gamma-ray using CEX data taken in 2011 for $w_\gamma > 2$ cm(a). (b) shows measured resolution map in sigma for $w_\gamma > 2$ cm. 88
5.3 Residual distributions of Z and R in 2011. Red lines are double Gaussian which are used for the fitting. 91
5.4 A E_e distribution from the data taken in 2011 with a fitting result by using Eq. (5.6). Dashed blue line shows a resolution function centered at 52.8 MeV. Dashed black line is the theoretical Michel spectrum. In the bottom plot, the acceptance function is shown. 92
5.5 Differences of ϕ_e(a), θ_e(b), y_e(c) and z_e(d) between two turns from 2011 data fitted by the double Gaussian function. 93
5.6 Relative time distribution from 2011 data. 96
5.7 Residuals of the single hit z-position with/without the noise reduction. . 97
5.8 E_e spectrum in 2011 noisy run period. Red/black lines are with/without the noise reduction. Right figure shows the log scale of the left figure. . . 99
5.9 Distributions of $\Delta x(x = E_e, \phi_e, \theta_e, y_e, z_e)$ from two-turn events in 2011 noisy run period. Red/black lines are with/without the noise reduction. . 100
5.10 E_e spectrum in 2009–2011 combined data. Red/black lines are with/without the noise reduction. Right figure shows the log scale of the left figure. 101
5.11 Distributions of $\Delta x(x = E_e, \phi_e, \theta_e, y_e, z_e)$ from two-turn events in 2009–2011 combined data. Red/black lines are with/without the noise reduction. 101
5.12 Reconstructed energy spectrum of positrons with new track fitting (red) in comparison with that with the previous one (dashed black line). Both spectra are normalized by using the area of each histogram. 102
5.13 Energy spectra of gamma rays in comparison between that by applying new pileup elimination algorithm (red), previous algorithm (blue-dot-dashed) and without the pileup elimination (black-dotted). 103

6.1 Two dimensional event distribution in $t_{e\gamma}$ vs E_γ taken in 2009–2011. The blank box at the center shows the blind box and the inner box with blue lines shows the analysis region. Left and Right boxes with dashed black lines show the sideband data and two boxes with solid magenta lines show the time sidebands which are used for the maximum likelihood fit. A bottom center box shows the energy sideband used to evaluate the expected number of RMD events and the $t_{e\gamma}$ resolution. For the illustration purpose, following loose cuts are applied;$40 \leq E_e \leq 60$ MeV;$40 \leq E_\gamma \leq 60$ MeV;$|\theta_{e\gamma}| \leq 200$ mrad; $|\phi_{e\gamma}| \leq 200$ mrad;$|t_{e\gamma}| \leq 4$ ns. 107
6.2 Two dimensional event distribution in $\theta_{e\gamma}$ vs $\phi_{e\gamma}$ taken in 2009–2011 in time sidebands. The center box with blue lines shows the analysis region in relative angles. Neighboring four boxes with dashed lines show the angle sidebands which we perform the maximum likelihood fitting. For the illustration purpose, following loose cuts are applied;$40 \leq E_e \leq 60$ MeV;$43 \leq E_\gamma \leq 60$ MeV;$|\theta_{e\gamma}| \leq 200$ mrad; $|\phi_{e\gamma}| \leq 200$ mrad;$|t_{e\gamma}| \leq 4$ ns and $|t_{e\gamma}| > 1$ ns. 108

6.3 Calculated covariance matrices, (a) for the accidental background PDF, and (b) the signal PDF for 2009 data set. 112
6.4 (a) $t_{e\gamma}$ PDFs for different categories (2011). (b) Event fractions of the categories. 117
6.5 An example of the spectrum of the accidental background gamma rays used for the PDF in depth is larger than 2 cm in time sideband. Green line is extracted from the MC distribution of RMD and AIF, Blue line show that convolved with resolution and pedestal, namely acceptance. Solid black line is contribution from cosmic-ray background and Red one shows sum of the blue one and black one. 119
6.6 Average PDFs for the 2009–2011 combined dataset. The green, red and magenta lines show the signal, RMD and BG PDFs, respectively. The correlations between the errors of positron observables are corrected except for (f). 121
6.7 Examples of per-event PDF in typical two events observed in the time sideband. (a) shows PDFs in which the positron-track shows good fitting quality. (b) shows ones in the event with worse fitting quality. Green lines show the signal PDFs, Magenta dashed lines show the accidental background PDFs and red lines show the RMD PDFs. Blue lines are sum of those three PDFs and black stars indicate measured variables. 122
6.8 (a) Average distributions of E_e (left), $\theta_{e\gamma}$ (center) and $\phi_{e\gamma}$ (right) of the full-MC (black markers) and the toy-MC (blue solid line). (b) Average correlations of δE_e v.s. $\delta\phi_{e\gamma}$ (left) and $\delta\theta_{e\gamma}$ v.s. $\delta\phi_{e\gamma}$ of the full-MC (black markers) and the toy-MC (blue markers). 124
6.9 (a) Distribution of MC signal events on vertex-angle plane. Missing-turn events make a characteristic pattern on this plane appearing as a band parallel to the red arrow. (b) Scatter plot of the MC events on $t_{e\gamma}$ v.s. a new variable defined by the projection along the red arrow in (a). The missing turn events ranging at the negative $t_{e\gamma}$ are clearly distributed around -28 on the new variable. (c) and (d) show the projected distributions of MC and data (2011), respectively. Fraction of the peak events is estimated by fitting a Gaussian and a quartic function to the distribution and results are shown in (c) and (d). 126
6.10 Distribution of RMD events in 2009–2010 data. Black dots show the measured distribution. Black solid histograms show the expected distribution calculated from the normalization factor from Michel channel and the best estimate value for each parameter, and the gray bands show the uncertainty. Red dashed ones show the distribution with the best-fit values of normalization and systematic parameters. 129
6.11 Distribution of RMD events in 2011 data. Black dots show the measured distribution. Black solid histograms show the expected distribution calculated from the normalization factor from Michel channel and the best estimate value for each parameter, and the gray bands show the uncertainty. Red dashed ones show the distribution with the best-fit values of normalization and systematic parameters. 130

7.1 Distributions of the upper limits of the background-only pseudo experiments. (a) 2009-2010, (b) 2011, (c) 2009-2011. The red arrows show the medians of the distributions. The black arrows show the observed limits. In (a), two arrows are overlapped by chance. 133
7.2 Confidence level curves in time sidebands (a)–(c) before normalization and (d) after normalization. (a) 2009-2010, (b) 2011, (c)(d) 2009-2011. Red lines show the results of the negative time sidebands and blue lines show the results of the positive ones. 135
7.3 Event distributions in E_γ v.s. E_e and $t_{\mathrm{e}\gamma}$ v.s. $\cos\Theta_{\mathrm{e}\gamma}$. Corresponding datasets are 2009-2010 combined (a)(b) and 2011 only (c)(d), respectively. The signal two-dimensional PDFs are superimposed as contours at 1, 1.645, 2 σ as blue dashed, solid, and dotted lines respectively. 138
7.4 Event distributions in the (E_e, E_γ) plane(a) and $(\cos\Theta_{\mathrm{e}\gamma}, t_{\mathrm{e}\gamma})$ plane(b). Corresponding dataset is 2009-2011 combined. Definition of blue contours are same as those in Fig. 7.3. 139
7.5 Likelihood fit result for 2009–2010 combined dataset in the analysis region. Black markers show the data. Red and pink lines show the best fit for RMD and BG, respectively. Green line shows the best fit for the signal (almost invisible because of the small N_sig) and blue one shows total best fit. . . . 140
7.6 Likelihood fit result for 2011 dataset in the analysis region. The definitions of each components are the same as in Fig. 7.5. 140
7.7 Likelihood fit result for 2009–2011 combined dataset in the analysis region. The definitions of each components are the same as in Fig. 7.5. 141
7.8 Profile likelihood curves 141
7.9 Confidence level curves (a)–(c) before normalization and (d) after normalization. (a) 2009-2010, (b) 2011, (c)(d) 2009-2011. 142
7.10 The average signal and background PDFs for the 2011 dataset. The parameters are randomized for each curve according to their uncertainties. Dark green (blue) lines are the signal (BG) PDFs without randomizing parameters and green (cyan) lines are PDFs with randomized parameters. 144
7.11 Difference of reconstructed $t_{\mathrm{e}\gamma}$ (upper left), E_e (upper center), E_γ (upper right), θ_e (bottom left) and ϕ_e (bottom center) in the 2009–2010 data with the old and the new reconstruction algorithms. The definition of Δx is as follows:$\Delta x = x_\mathrm{new} - x_\mathrm{old}$. 147
7.12 Distribution of ΔN_sig upper limits. The black arrow shows the observed difference in the 2009–2010 combined dataset. 148
7.13 3D view of reconstructed events which have the first(a) and second(b) largest R_sig value. 148
7.14 Event-by-event comparison for five high rank events found in new/previous analysis shown by red/black markers. Numbers represent the event of R_sig ordering. The signal two-dimensional PDFs are superimposed as contours at 1, 1.645, 2 σ as blue dashed, solid, and dotted lines respectively. . . . 149
7.15 (a) shows $B(\mu \to \mathrm{e}\gamma)$ v.s. $B(\tau \to \mu\gamma)$ correlation (Fig. 1.3 in Sec. 1.2.2 [16]) with the new upper limit of $B(\mu^+ \to \mathrm{e}^+\gamma)$. (b) shows $B(\mu \to \mathrm{e}\gamma)$ v.s. muon g-2 correlation (Fig. 1.5 in Sec. 1.2.3 [20]) with the new upper limit of $B(\mu^+ \to \mathrm{e}^+\gamma)$. 150

7.16 Sensitivity curve as a function of the accumulated DAQ time. Black solid curve shows the curve of the expected sensitivity and green and yellow regions express the 1 and 2 σ error bands, respectively. Magenta markers are observed 90% C.L. upper limits. Red solid curve shows a 3 σ discovery potential of the experiment for the $\mu^+ \to e^+\gamma$ decay. 152

A.1 Extraction of the $\delta\phi_e$ v.s. δE_e and δy_e v.s. δE_e correlations. The red vertical line shows the target intersection with the transverse plane passing from the muon decay point $V = (X, Y)$. 157
A.2 Extraction of the $\delta\theta_e$ v.s. δz_e correlation. 158

List of Tables

1.1 Decay modes and branching fractions of muon [7]. 18
1.2 All particles and sparticles in the MSSM. 20
1.3 History of the $\mu^+ \to e^+\gamma$ search experiments in the era of meson factories with 90% C.L. upper limits. The resolutions are given as full width at half maximum (FWHM). 24
1.4 Recent the most stringent experimental limits given by the BABAR and Belle experiments. Only four famous decay modes are shown here. 30

2.1 Several characteristics of LXe in comparison with other scintillators. . . . 35
2.2 Characteristics and Parameters of DCH. 44
2.3 Various trigger settings used in the MEG experiment and the prescaling factors in physics run. Approximately $Q_L \sim 30$ MeV,$Q_H \sim 40$ MeV,$T_N \sim 20$ ns and $T_W \sim 40$ ns. DM represents the direction-match algorithm given by the trigger. 48
2.4 List of some important events which are prepared in `MEGMC`. 50

4.1 Several calibration and monitoring methods prepared for the LXe detector. 74

5.1 Single hit resolutions of core/tail in each year. 90
5.2 Performance comparison in 2009. 98
5.3 Performance comparison in 2010. 98
5.4 Performance comparison in 2011 noisy run period. 99
5.5 Performance comparison in 2011 run after hardware investigations. . . . 100
5.6 Performance comparison for 2009-2011 all combined data. 100
5.7 Performance summary. 104

6.1 Parameters for positron energy response. Since errors on all variables are implemented as a covariance matrix in the PDF, they are not shown in this table. 112
6.2 Sigmas of pulls for positron angular and vertex responses. 113
6.3 Parameters for the correlations and their uncertainties. 114
6.4 Breakdown of analysis efficiencies 125
6.5 Michel normalization parameters for 2009 data in comparison with the previous estimation 127
6.6 Michel normalization parameters for 2010 data in comparison with the previous estimation 128
6.7 Michel normalization parameters for 2011 data with old/new Kalman . . 128

6.8 Summary of normalization factors calculated for 2009, 2010 and 2011 dataset. 131

7.1 Results from the previous analysis presented in [4]. 132
7.2 Calculated sensitivities in each dataset. Systematic uncertainties are included. 133
7.3 Time sideband results without including systematic uncertainties. The results in the negative $t_{e\gamma}$ sidebands are labeled as 'negative' and those in opposite sides are labeled as 'positive'. 134
7.4 Angle sideband results with constraining the number of backgrounds. . . 136
7.5 Angle sideband results without constraints on the number of backgrounds (Uncertainties are in 1σ). Parameters in bracket show the expected number of backgrounds and those with a hat show the best fit results. 137
7.6 Expected number of background events and the observed number of events in the analysis region defined in Sec. 6.1.3. 137
7.7 The best fit number of events and the corresponding branching ratios. The uncertainties are MINOS (i.e. profile likelihood ΔNLL method) 1.645σ errors. The numbers with hats show the best fit values. 139
7.8 Confidence intervals (upper limits and lower limits if they are set) on the 2009-2010, 2011 and 2009-2011 datasets calculated from confidence level curves shown in Fig. 7.9(d). The numbers in the first table are written in $N_{\rm sig}$ and those in the second are in $\mathcal{B} \times 10^{13}$. A confidence level at 0 is shown only when $\hat{N}_{\rm sig}$ is positive. The results are including the systematic uncertainties. 143
7.9 Uncertainties associated to the drift chamber alignment and the magnetic field. 143
7.10 Relative contributions of uncertainties to upper limit of $\mathcal{B}$ in RMS of $\Delta\Delta$NLL. 145
7.11 Relative contributions of the uncertainties of the correlations in the positron observables to the upper limit of $\mathcal{B}$ in RMS of $\Delta\Delta$NLL. 146
7.12 Results from category PDF and comparison without systematic uncertainties. 146
7.13 Detector performance which were written in the proposal and those obtained from data taken in 2011. 150

Introduction

Recently, a Higgs boson was discovered by the ATLAS and the CMS collaborations [1] using Large Hadron Collider (LHC) which materialized the collisions of proton-proton with the world highest center of mass energy, up to 8 TeV. Since the Higgs boson was the last missing elementary particle predicted by the Standard Model of the particle physics (SM), this discovery proves the accuracy of the SM in a high precision. Even if the SM well agrees with most of experimental measurements, there are also several issues that cannot be explained by the SM, for example the tiny masses of neutrinos and the existence of dark matter which is the most dominant component and yet unknown matter in our universe. It clearly indicates the existence of new physics beyond the SM (BSM).

In the fermion sector, it is found that there are three generations in quark and lepton sectors as well so-called "Flavor" and the flavor mixing was found in the quark sector which is taken into account by the CKM matrix. In the recent decade, the flavor oscillation in the neutrino sector called "neutrino oscillations" was also confirmed by various experiments, e.g. Super Kamiokande, Daya Bay and T2K. Therefore, the lepton flavor violation in the charged lepton sector (CLFV) has only been undiscovered yet. The $\mu^+ \to e^+\gamma$ decay is one of the simple and famous decay modes of the muon CLFV processes. In the SM framework, CLFV processes are strictly forbidden and even if non-zero neutrino mixing is considered, the branching fraction of the $\mu^+ \to e^+\gamma$ decay is calculated to be $\sim 10^{-50}$. On the other hand, the branching fraction of CLFV processes can be enhanced in many popular BSM models, e.g. SUSY-GUT, and they predict detectable branching ratios of various CLFV processes. For example, the branching fraction of the $\mu^+ \to e^+\gamma$ decay is expected to be in the range of 10^{-11}–10^{-15} order of magnitude depending on the values of parameters in SUSY-GUT. From the experimental point of view, the upper limit on the branching ratio of the $\mu^+ \to e^+\gamma$ decay was given as $B(\mu^+ \to e^+\gamma) < 1.2 \times 10^{-11}$ at 90% C.L. by the MEGA experiment [2] and the value was already close to the region predicted by the new physics. Accordingly, the search for the $\mu^+ \to e^+\gamma$ decay is one of the effective probes to search for the BSM.

Aiming to search for the $\mu^+ \to e^+\gamma$ decay with higher sensitivity, the MEG (Mu to Electron Gamma) experiment was proposed by a group of Japanese and Russian physicists and approved by the research committee of the Paul Scherrer Institut (PSI) in 1999 [3] and then the international collaboration was established. The MEG experiment started the physics data taking in 2008. By using 2009–2010 combined dataset, the MEG experiment has already set the upper limit of 2.4×10^{-12} at 90% C.L. [4]. This means that we set a 5 times tighter upper limit than that of set by the MEGA experiment. If the $\mu^+ \to e^+\gamma$ decay is discovered, it should be an evidence of new physics. Otherwise, the result will set constraint to the region of parameters allowed in the BSM and give an important hint to investigate the unknown mechanism of the BSM. Therefore, it is important to improve

the sensitivity of the $\mu^+ \to e^+\gamma$ search as much as possible.

In order to improve the sensitivity, the MEG experiment continued the physics data taking until the end of August in 2013. In this thesis, we analyze the data taken during 2009–2011. In 2011, we collected data with 1.85×10^{14} stopped muons on the target which is the almost same data statistics as collected in 2009 and 2010. In the new analysis of the $\mu^+ \to e^+\gamma$ decay search, we have four improvements as follows,

- apply offline noise filtering for the drift chamber waveform analysis,
- revise the fitting algorithm for the track reconstruction of positrons,
- improve the gamma ray analysis in order to get higher efficiency and suppress the pileup events,
- take the event-by-event fitting uncertainties on positron observables into account in the physics analysis.

We analyze 2009–2010 data again with these improvements in order to enhance the sensitivity as much as possible. Owing to these efforts, the sensitivity is improved by a factor 2 by analyzing 2009–2011 combined dataset [5] in comparison with the previous result.

In this thesis, the details of the analysis procedure, analysis and calibration improvements, and results by using 2009–2011 combined dataset is described. In Chapter 1, the details of searching for the $\mu^+ \to e^+\gamma$ decay and few related theories are introduced. The apparatus of the MEG experiment and the details of data taking during 2009–2011 are explained in Chapter 2. In Chapter 3, the method of the event reconstruction is described. The calibration tools for the MEG experiment are introduced in Chapter 4 in detail. Chapter 5 summarizes the performance and several improvements due to the new reconstruction algorithms. In Chapter 6, details of the analysis to search for the $\mu^+ \to e^+\gamma$ decay are described. The results of the analysis are written and discussed in Chapter 7. In Chapter 8, we conclude this thesis.

Chapter 1

Physics Motivation

The standard model, which is based on the gauge theory of the strong and electroweak interactions, has withstood many experimental tests since it was established. However, it cannot explain the existence of tiny masses of neutrinos, the origin of dark matter, and the reason of the large discrepancy between electromagnetic scale ($\mathcal{O}(100)$ GeV) and Planck scale ($\mathcal{O}(10^{19})$ GeV) called "hierarchy problem". Hence the SM is thought to be an approximated theory of the more fundamental nature principle. In the present elementary particle physics, the most important subject is to find out the BSM which can explain above issues. Although many experiments have searched for the evidence of the BSM up to now, it has not been discovered yet. In many of the BSMs, new symmetries are introduced and new particles are predicted by those symmetries. Since the achievable energy range of direct searches for new particles such like LHC are limited by present collider technologies, indirect searches are also effective methods because undiscovered heavy particles could exist virtually as a higher order effect. Therefore, searching for the CLFV process is one of the powerful methods to investigate the BSM. In particular, muon CLFV searches are good probes because a large amount of muon can be produced more easily than the case of the tau lepton because of its longer life time (2.2 μs). In addition, the final state of muons are simpler than those of the tau lepton because of the smaller mass of muon ($m_\mu = 105.6$ MeV). The $\mu^+ \to e^+\gamma$ decay is one of the famous muon CLFV processes. In this chapter, several decay modes of the muon in the Standard Model and those in new physics are described. Possible sources of background in searching for $\mu^+ \to e^+\gamma$ decay are also discussed.

1.1 Muon Decay in the Standard Model

The $\mu^+ \to e^+\gamma$ decay has been explored for more than 50 years since the muon was discovered in 1937 [6]. Table 1.1 shows decay modes of muon and its branching fractions or upper limits. As written in this table, $\mu^\pm$ decays into $e^\pm$ and two neutrinos in almost 100% probability. This decay mode is called "*Michel*" decay [13] and the total lepton number is conserved in this process.

Table 1.1: Decay modes and branching fractions of muon [7].

Decay mode	Branching ratio	Reference
$\mu^- \to e^- \nu_\mu \overline{\nu}_e$	$\sim$100%	
$\mu^- \to e^- \nu_\mu \overline{\nu}_e \gamma$	(1.4 ± 0.4)% (for $E_\gamma > 10$ MeV)	[8]
$\mu^- \to e^- \nu_\mu \overline{\nu}_e e^+ e^-$	$(3.4 \pm 0.4) \times 10^{-5}$	[9]
$\mu^- \to e^- \nu_e \overline{\nu}_\mu$	< 1.2 %	[10]
$\mu^+ \to e^+ \gamma$	$< 2.4 \times 10^{-12}$	[4]
$\mu^+ \to e^+ e^+ e^-$	$< 1.0 \times 10^{-12}$	[11]
$\mu^- \to e^- \gamma\gamma$	$< 7.2 \times 10^{-11}$	[12]

1.1.1 Michel Decay

In the SM, muon decay is determined by the $V - A$ interaction. The differential decay rate of Michel decay is given by [14]

$$\begin{aligned} \frac{d^2\Gamma(\mu^+ \to e^+ \nu_e \overline{\nu}_\mu)}{dx d(\cos\theta)} &= \frac{m_\mu}{4\pi^3} {W_{e\mu}}^4 G_F^2 \sqrt{x^2 - x_0^2} \\ &\times (F_{IS}(x) + P_\mu \cos\theta_e F_{AS}(x)) \\ &\times (1 + \vec{P}_e(x, \theta_e \cdot \hat{\xi})), \end{aligned} \tag{1.1}$$

where $W_{e\mu} = (m_\mu^2 + m_e^2)/(2m_e)$, $x = E_e/W_{e\mu}$ and $x_0 = m_e/W_{e\mu}$. Here E_e is the energy of the e^+ and m_e and m_μ are the masses of electron(positron) and muon, respectively. Allowed region of x is from x_0 to 1 by its definition. θ_e is the angle between the muon polarization ($\vec{P}_\mu$) and the positron momentum, and $\hat{\xi}$ is the directional vector of the measurement of the positron spin polarization. $F_{IS}(x)$ and $F_{AS}(x)$ are the isotropic and anisotropic parts of the positron energy spectrum, respectively and they are given by [15]

$$F_{IS}(x) = x(1-x) + \frac{2}{9}\rho(4x^2 - 3x - x_0^2) + \eta x_0 (1-x), \tag{1.2}$$

$$F_{AS}(x) = \frac{1}{3}\xi\sqrt{x^2 - x_0^2}\left(1 - x + \frac{2}{3}\delta[4x - 3 + (\sqrt{1 - x_0^2} - 1)]\right), \tag{1.3}$$

where ρ, η, ξ and δ are called Michel parameters. In the SM, Michel parameters are calculated to be:

$$\rho = \frac{3}{4}, \eta = 0, \xi = 1, \delta = \frac{3}{4}. \tag{1.4}$$

1.1.2 The $\mu^+ \to e^+\gamma$ Decay in the Standard Model

The $\mu^+ \to e^+\gamma$ decay is strictly forbidden in the SM because of the law of lepton flavor conservation. If the neutrino oscillation is considered, the $\mu^+ \to e^+\gamma$ decay can happen through the Feynman diagram shown in Fig. 1.1. However, the calculated branching fraction is approximately 10^{-50} and almost undetectable with any existing experimental technologies. It means that if the $\mu^+ \to e^+\gamma$ decay would be discovered, it should be the evidence of the BSM.

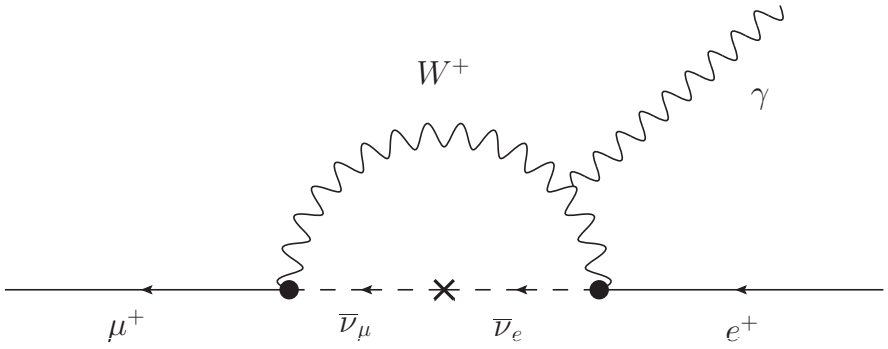

Figure 1.1: Feynman diagram for the $\mu^+ \to e^+\gamma$ decay through the neutrino oscillation.

1.2 The $\mu^+ \to e^+\gamma$ decay and Physics Beyond the Standard Model

Many BSMs predict that the $\mu^+ \to e^+\gamma$ decay can happen in a detectable range of the branching fraction. Here several BSMs that can enhance the branching fraction of the $\mu^+ \to e^+\gamma$ decay are introduced. The effective Lagrangian for the $\mu^+ \to e^+\gamma$ decay is given by [14]

$$\mathcal{L}_{\mu\to e\gamma} = -\frac{4G_F}{\sqrt{2}}[m_\mu A_R \overline{\mu_R}\sigma^{\mu\nu} e_L F_{\mu\nu} + m_\mu A_L \overline{\mu_L}\sigma^{\mu\nu} e_R F_{\mu\nu} + \text{H.c.}]. \tag{1.5}$$

where the term of G_F is the Fermi coupling constant, A_R and A_L are coupling constants that correspond to the left-handed process and right-handed one, respectively. From Eq. (1.5), the differential angular distribution of $\mu^+ \to e^+\gamma$ decay is given by

$$\frac{dB(\mu^+ \to e^+\gamma)}{d(\cos\theta_e)} = 192\pi^2[|A_R|^2(1 - P_\mu \cos\theta_e) + |A_L|^2(1 + \cos\theta_e))], \tag{1.6}$$

where θ_e is the angle between the muon polarization and the e^+ momentum vectors.

The supersymmetric (SUSY) model is one of the candidates of the BSMs, which can answer several issues in the SM. In the SUSY, new gauge symmetry called "supersymmetry" is introduced as an extension of the SM. As a result, all of elementary particles in the SM have their own supersymmetric partners called "sparticles". Table 1.2 shows all particles and sparticles which are contained in the minimal supersymmetric standard model (MSSM). If the supersymmetry is not broken, each sparticle should have the same mass of its own supersymmetric partner. However, such particles have not been discovered yet. Therefore the supersymmetry is thought to be broken. In the MSSM, the different masses between sparticles and their own partners are generated by the soft SUSY-breaking terms. As a result, the branching fractions of CLFV processes are enhanced by the flavor mixing in the slepton sector.

1.2.1 SUSY GUT SU(5)

The SUSY grand unified model (SUSY GUT) is one of attractive models of the SUSY extensions, because three gauge coupling constants of strong, weak, and electromagnetic

Table 1.2: All particles and sparticles in the MSSM.

Names		spin 0	spin 1/2	$SU(3)_C,\ SU(2)_L,\ U(1)_Y$
squarks,	q	$(\tilde{u}_L\ \tilde{d}_L)$	$(u_L\ d_L)$	$(\mathbf{3},\ \mathbf{2},\ 1/6)$
quarks	$\overline{u}$	$\tilde{u}^*_R$	$u^\dagger_R$	$(\overline{\mathbf{3}},\ \mathbf{1},\ -2/3)$
($\times$3 families)	$\overline{d}$	$\tilde{d}^*_R$	$d^\dagger_R$	$(\overline{\mathbf{3}},\ \mathbf{1},\ 1/3)$
sleptons,leptons	l	$(\tilde{\nu}_L\ \tilde{e}_L)$	$(\nu\ e_L)$	$(\mathbf{1},\ \mathbf{2},\ -1/2)$
($\times$3 families)	$\overline{e}$	$\tilde{e}^*_R$	$e^\dagger_R$	$(\mathbf{1},\ \mathbf{1},\ 1)$
Higgs,higgsinos	H_u	$(H^+_u\ H^0_u)$	$(\tilde{H}^+_u\ \tilde{H}^0_u)$	$(\mathbf{1},\ \mathbf{2},\ 1/2)$
	H_d	$(H^0_d\ H^-_d)$	$(\tilde{H}^0_d\ \tilde{H}^-_d)$	$(\mathbf{1},\ \mathbf{2},\ -1/2)$
Names		spin 1/2	spin 1	$SU(3)_C,\ SU(2)_L,\ U(1)_Y$
gluino, gluon		$\tilde{g}$	g	$(\mathbf{8},\ \mathbf{1},\ 0)$
winos, W bosons		$\tilde{W}^\pm\ \tilde{W}^0$	$W^\pm\ W^0$	$(\mathbf{1},\ \mathbf{3},\ 0)$
bino, B boson		$\tilde{B}^0$	B^0	$(\mathbf{1},\ \mathbf{1},\ 0)$

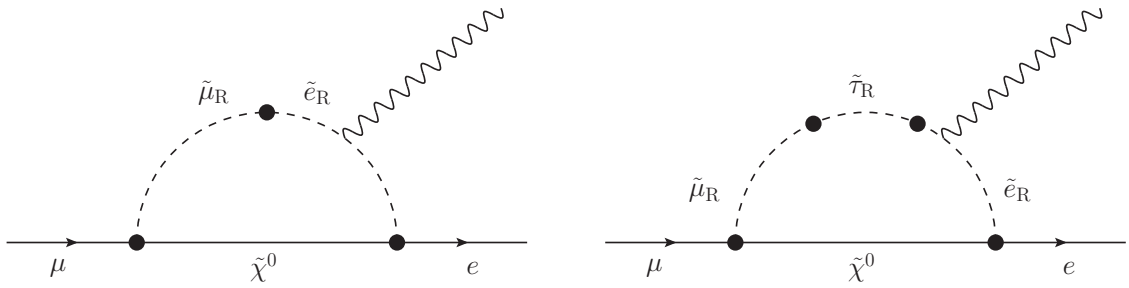

Figure 1.2: Feynman diagrams for the $\mu^+ \to e^+\gamma$ decay in SU(5) SUSY GUT.

interactions are unified to a single $SU(5)$ gauge coupling constant at a scale of the order of 10^{16} GeV (called GUT scale) in the SUSY GUT. The off-diagonal elements of the right-handed slepton mass matrix in the SUSY GUT are given by

$$(m^2_{\tilde{e}_R})_{ij} = -\frac{3}{8\pi^2}(V_R)_{i3}(V_R)^*_{j3}|y_u^{33}|^2 m_0^2(3+|A_0^2|)\ln\left(\frac{M_P}{M_G}\right). \tag{1.7}$$

where V_R is a matrix element to diagonalize the Yukawa coupling constant for leptons, M_P and M_G represent the reduced Planck mass ($\sim 2\times10^{18}$ GeV) and the GUT scale ($\sim 2\times10^{16}$ GeV), respectively. Here m_0 is the universal scalar mass and A_0 is the universal trilinear coupling. As a result, Eq. (1.7) becomes a source of the $\mu^+ \to e^+\gamma$ decay. Figure 1.2 shows possible Feynman diagrams for the $\mu^+ \to e^+\gamma$ decay in SUSY GUT. In the $SU(5)$ SUSY GUT, CLFV processes appear only in the right-handed slepton sector because of moderate values of $\tan\beta$, which is defined by the ratio of two Higgs vacuum expectation values ($\tan\beta \equiv \langle H^0_2\rangle/\langle H^0_1\rangle$). Therefore only $\mu^+ \to e^+_R\gamma$ decay is allowed in this model.

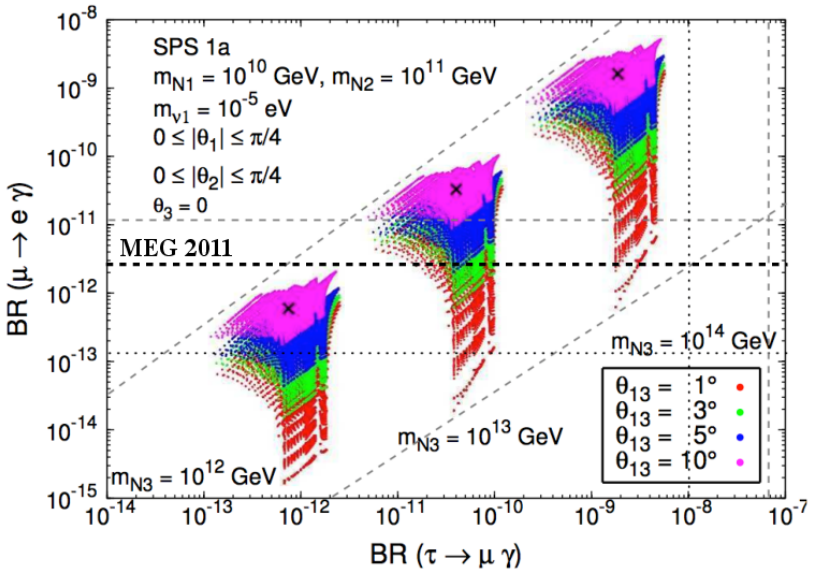

Figure 1.3: Correlation between $B(\mu \to e\gamma)$ and $B(\tau \to \mu\gamma)$ as a function of m_{N3}, for constraint MSSM assuming universality of the soft-SUSY breaking at the scale of gauge coupling unification, M_X so-called minimal supergravity (mSUGRA) framework from [16]. Different colored regions correspond to $\theta_{13} = 1^\circ$, 3°, 5° and 10° (red, green, blue and pink, respectively) and recent experiments report the large value of $\theta_{13} \sim 10^\circ$ [17]. Dashed line labeled "MEG2011" is added to the original plot and it represents the 90% C.L. upper limit given by the previous result of MEG [4].

1.2.2 SUSY Seesaw

In the SUSY seesaw model, right-handed heavy Majorana neutrinos are introduced to explain the tiny masses of neutrinos by the seesaw mechanism. By including the seesaw mechanism in the SUSY standard model, the right-handed neutrino supermultiplets, the Majorana mass matrix and a new Yukawa coupling constant matrix are included in the part of the lepton sector Lagrangian. Because of the presence of the Yukawa coupling constant matrix for the neutrino sector as same as the charged lepton sector, the lepton flavor would no longer be conserved separately for each generation in the SUSY seesaw. Hence the branching fractions of CLFV processes are expected to be enhanced. If we assume that the neutrino mixing mostly originates from the neutrino Yukawa coupling constants, $(y_\nu)_{ij}$, the branching ratios from $\mu^+ \to e^+\gamma$ and $\tau \to \mu\gamma$ decays can be evaluated by using the neutrino mixing parameters. Figure 1.3 shows the scatter plot of the correlation between $B(\mu \to e\gamma)$ and $B(\tau \to \mu\gamma)$ in an example of the SUSY model which including the large mass of right-handed Majorana neutrino. In this model, the $\mu^+ \to e^+\gamma$ decay can happen in somewhere experimentally achievable range.

1.2.3 The $\mu^+ \to e^+\gamma$ Decay and $(g-2)_\mu$ Anomaly

In 2004, the E821 experiment reported about the muon anomalous magnetic moment ($a_\mu = (g-2)_\mu/2$) [18]. From their result, the average of the muon magnetic moment is given as:

$$a_\mu = 11\ 659\ 208(6) \times 10^{-10}\ (0.5\ \text{ppm}), \tag{1.8}$$

while the theoretical calculation with the SM is given as [19]:

$$a_{\text{SM}} = 11\ 659\ 184(6) \times 10^{-10}\ (0.7\ \text{ppm}). \tag{1.9}$$

The discrepancy between a_μ and a_{SM} is calculated to be 2.9σ.

Since both the $\mu^+ \to e^+\gamma$ decay and the muon magnetic moment are generated by dipole operators as shown in Fig. 1.4, the branching ratio of the $\mu^+ \to e^+\gamma$ decay correlates to the value of $\Delta a_\mu = (g_\mu - g_\mu^{\text{SM}})/2$ if Δa_μ is generated by the contribution from the new physics [20]. For example, the $B(l_i \to l_j\gamma)$ can be expressed by using Δa_μ as

$$\frac{B(l_i \to l_j\gamma)}{B(l_i \to l_j\nu_{l_i}\overline{\nu_{l_j}})} = \frac{48\pi^3\alpha}{G_F^2}\left(\frac{\Delta a_\mu}{m_\mu^2}\right)^2 \times \left(\frac{f_{2c}(M_2^2/M_{\tilde{l}}^2, \mu^2/M_{\tilde{l}}^2)}{g_{2c}(M_2^2/M_{\tilde{l}}^2, \mu^2/M_{\tilde{l}}^2)}\right)|\delta_{LL}^{ij}|^2, \tag{1.10}$$

where μ is the supersymmetric-invariant mass term of the Higgs potential, $M_{\tilde{l}}$ is a mass of left-handed slepton, , $f_{2c}(x,y)$ and $g_{2c}(x,y)$ are defined as

$$\begin{aligned} f_{2c}(x,y) &= \frac{-x^2-4x+5+2(2x+1)\ln x}{2(1-x)^4} - \frac{-y^2-4y+5+2(2y+1)\ln y}{2(1-y)^4}, \\ g_{2c}(x,y) &= \frac{(3-4x+x^2+2\log x)}{(x-1)^3} - \frac{(3-4y+y^2+2\log y)}{(y-1)^3}, \end{aligned} \tag{1.11}$$

in the MSSM extension with the seesaw mechanism. Here δ_{LL}^{ij} is the left-handed slepton mass matrices read as

$$\delta_{LL}^{ij} = c_\nu (y_\nu^\dagger y_\nu)_{ij}, \tag{1.12}$$

where c_ν is a numerical coefficient. Figure 1.5 shows correlation between the $B(\mu^+ \to e^+\gamma)$ and Δa_μ including the non-linear effect not shown in Eq. (1.10). Therefore if the reported $(g-2)_\mu$ anomaly is really exist, the branching ratio of the $\mu^+ \to e^+\gamma$ decay might be enhanced. Otherwise, there should be some mechanism which can suppress the lepton flavor violation. Consequently, both the measurement of the muon magnetic moment and the $\mu^+ \to e^+\gamma$ decay search play the important roles to find out the unknown mechanism of new physics.

1.3 Searches for the CLFV Processes

1.3.1 Experimental History of the $\mu^+ \to e^+\gamma$ Decay Searches

Recent results from experimental searches for the $\mu^+ \to e^+\gamma$ decay are shown in Table 1.3. Before starting the MEG experiment, the best upper limit on the $\mu^+ \to e^+\gamma$ decay was set to be 1.2×10^{-11} by the MEGA experiment. The MEG experiment already achieved more stringent upper limit by using 2009–2010 combined dataset in 2011. As already discussed, the $B(\mu^+ \to e^+\gamma)$ is expected to be within 10^{-11}–10^{-15} in several BSMs. According to the upper limit given by the previous result in the MEG experiment, we already achieved the sensitivity which is able to explore the new physics.

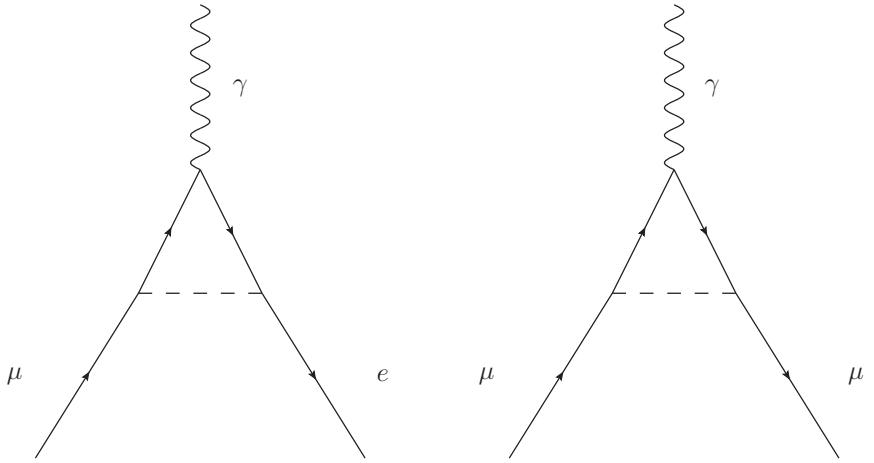

Figure 1.4: Simplified Feynman diagram of the $\mu^+ \to e^+\gamma$ decay (left) and the muon magnetic moment (right).

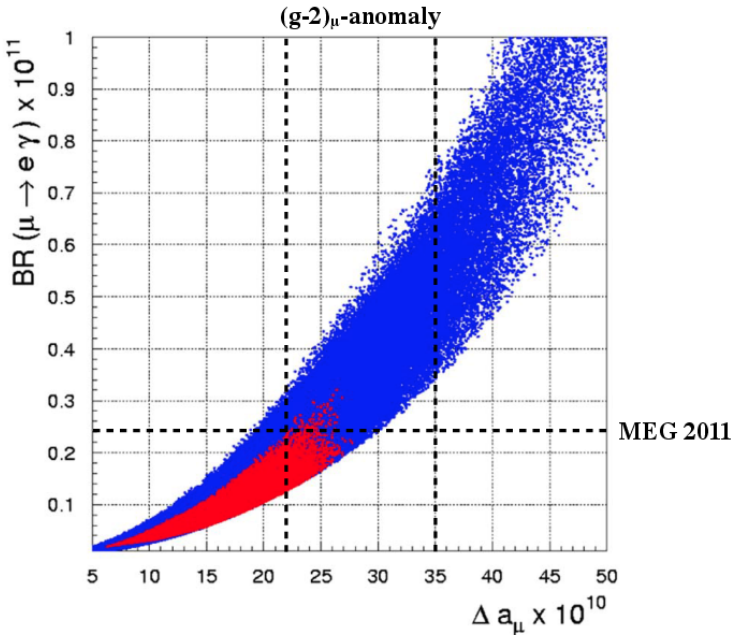

Figure 1.5: Correlation between $B(\mu^+ \to e^+\gamma)$ and Δa_μ from [20]. Horizontal dashed line labeled "MEG2011" is added to the original plot and it represents the 90% C.L. upper limit given by the previous result of the MEG experiment. Vertical two dashed lines are also added and they represent the 1σ region of the $(g-2)_\mu$ anomaly measured in the E821 experiment [18]. Assumed parameters are as follows;$|\delta^{12}_{LL}| = 10^{-4}$, $|\delta^{23}_{LL}| = 10^{-2}$. Here the relatively small slepton mass and large $\tan\beta$ are assumed. The inner red area satisfy the B-physics constraints.

Table 1.3: History of the $\mu^+ \to e^+\gamma$ search experiments in the era of meson factories with 90% C.L. upper limits. The resolutions are given as full width at half maximum (FWHM).

Year	Site	Beam Rate (Hz)	ΔE_e (%)	ΔE_γ (%)	$\Delta t_{e\gamma}$ (ns)	$\Delta\Theta_{e\gamma}$ (mrad)	Upper Limit 90% C.L.	Ref.
1977	SIN	5×10^5 μ^+	10	8.7	6.7		1.0×10^{-9}	[22]
1977	TRIUMF	2×10^5 π^+	8.7	9.3	1.4		3.6×10^{-9}	[23]
1979	LAMPF	2.4×10^6 μ^+	8.8	8	1.9	37	1.7×10^{-10}	[24]
1986	LAMPF	4×10^5 μ^+	8	8	1.8	87	4.9×10^{-11}	[12]
1999	LAMPF	1.3×10^7 μ^+	1.2	4.5	1.6	15	1.2×10^{-11}	[2]
2011	PSI	3×10^7 μ^+	1.6	4.7	0.35	30	2.4×10^{-12}	[4]

1.3.2 Background

Two different types of background sources are considered in the search for the $\mu^+ \to e^+\gamma$ decay. First one is the radiative muon decay (RMD) which is called "prompt background". In RMD, a muon decays into two neutrinos, a positron and a gamma ray. Since there are two invisible particles in the final state, it can be misidentified as a signal event if both a positron and a gamma ray have high energy close to 52.8 MeV. The other is the accidental background (BG) which is the most dominant one in recent $\mu^+ \to e^+\gamma$ search experiments. In the accidental background, a gamma from RMD, annihilation in flight (AIF) of a positron, or bremsstrahlung of a positron accidentally overlaps with a positron from Michel decay. In the MEG experiment, RMD and AIF are main sources of the background gamma ray and the fractions are found to be nearly equivalent from a simulation study. Here the details of each background source are explained and the background situation in the MEG experiment is discussed.

1.3.2.1 Prompt Background

The decay of RMD can be written as $\mu^+ \to e^+\nu_e\overline{\nu}_\mu\gamma$. If two neutrinos carry only a small amount of energy, the opening angle between e^+ and γ ray becomes close to 180°. Moreover, the e^+ and the γ have approximately the same energy as in signal event in this case. The decay width of RMD, $d\Gamma(\mu \to e\nu\nu\gamma)$ is given by

$$\begin{aligned} d\Gamma(\mu \to e\nu\nu\gamma) &= \frac{G_F^2 m_\mu^5 \alpha}{3 \times 2^8 \pi^4} \\ &\times \left[(1-x)^2(1 - P_\mu \cos\theta_e) + \left(4(1-x)(1-y) - \frac{1}{2}z^2\right)(1 + P_\mu \cos\theta_e)\right] \\ &\times dx dy z dz d(\cos\theta_e), \end{aligned} \tag{1.13}$$

where θ_e is the opening angle between the muon spin and the positron direction, $x = 2E_e/m_\mu$, $y = 2E_\gamma/m_\mu$, and z is determined by the opening angle between e^+ and γ ray

$(\Theta_{e\gamma})$ as $z = \pi - \Theta_{e\gamma}$, The differential decay width of RMD is given by

$$\begin{aligned} \mathrm{d}B(\mu \to \mathrm{e}\nu\nu\gamma) &= \frac{1}{\Gamma(\mu \to \mathrm{e}\nu\nu)} \int_{1-\delta x}^{1} \mathrm{d}x \int_{1-\delta y}^{1} \mathrm{d}y \int_{0}^{\min[\delta z, 2\sqrt{(1-x)(1-y)}]} \mathrm{d}z \frac{\mathrm{d}\Gamma(\mu \to \mathrm{e}\nu\nu\gamma)}{\mathrm{d}x\mathrm{d}y\mathrm{d}z}, \\ &= \frac{\alpha}{16\pi}[J_1 \cdot (1 - P_\mu \cos\theta_\mathrm{e}) + J_2 \cdot (1 + P_\mu \cos\theta_\mathrm{e})]\mathrm{d}(\cos\theta_\mathrm{e}), \qquad (1.14) \\ J_1 &= \frac{8}{3}(\delta x)^3(\delta y)\left(\frac{\delta z}{2}\right)^2 - 2(\delta x)^2\left(\frac{\delta z}{2}\right)^4 + \frac{1}{3}\frac{1}{(\delta y)^2}\left(\frac{\delta z}{2}\right)^8, \qquad (1.15) \\ J_2 &= 8(\delta x)^2(\delta y)^2\left(\frac{\delta z}{2}\right)^2 - 8(\delta x)(\delta y)\left(\frac{\delta z}{2}\right)^4 + \frac{8}{3}\left(\frac{\delta z}{2}\right)^6, \qquad (1.16) \end{aligned}$$

where δx, δy and δz are half-widths of the signal region for x, y and z, respectively. Here $\Gamma(\mu \to \mathrm{e}\nu\nu)$ is the total muon decay width and Eq. (1.15) and Eq. (1.16) are determined by assuming $\delta z \leq 2\sqrt{\delta x \delta y}$ and this assumption fits into the situation of the MEG experiment. In case fully depolarized muon, Eq. (1.14) read as

$$\mathrm{d}B(\mu \to \mathrm{e}\nu\nu\gamma) = \frac{\alpha}{8\pi}[J_1 + J_2]. \qquad (1.17)$$

For example, we can calculate the effective branching ratio with Eq. (1.17) in the situation of the MEGA experiment by using numerical numbers written in Table 1.3 by keeping signal efficiency to be 90% as;

$$\delta x = 0.0084, \delta y = 0.032, \delta z = 0.021, \delta t_{\mathrm{e}\gamma} = 1.12 \text{ ns}. \qquad (1.18)$$

By using these numbers, the branching ratio of the prompt background is given as,

$$B(\mu \to \mathrm{e}\nu\nu\gamma) \sim 4.4 \times 10^{-15}. \qquad (1.19)$$

Therefore the prompt background is negligible in recent $\mu^+ \to \mathrm{e}^+\gamma$ search experiments.

1.3.2.2 Accidental Background

The accidental background is the most dominant background to search for the $\mu^+ \to \mathrm{e}^+\gamma$ decay in the recent experiments including MEG. The effective branching fraction (B_{acc}) is given by

$$B_{\mathrm{acc}} = R_\mu \cdot f_\mathrm{e}^0 \cdot f_\gamma^0 \cdot (\frac{\mathrm{d}\omega_{\mathrm{e}\gamma}}{4\pi}) \cdot (2\delta t_{\mathrm{e}\gamma}), \qquad (1.20)$$

where R_μ is the instantaneous muon intensity, the back-to-back resolution ($\mathrm{d}\omega_{\mathrm{e}\gamma}/4\pi$) is given by $(\mathrm{d}\omega_{\mathrm{e}\gamma}/4\pi) = (\mathrm{d}z)^2/4$, f_e^0 and f_γ^0 are integrated spectra of background gamma rays and positrons within the signal region, respectively. Therefore the excellent angular and gamma energy measurements are required to suppress the accidental background. The factor f_e^0 can be approximately estimated to be $\approx 2(\delta x)$ by integrating Michel spectrum over $1 - \delta x \leq x \leq 1$ since it is almost flat at $x \simeq 1$ as shown in Fig. 1.6(a). In order to make a situation simpler, f_γ^0 is assumed to be dominated by the RMD events and muons not to be polarized. In this case, f_γ^0 is given by

$$\begin{aligned} f_\gamma^0 &= \int_{1-\delta y}^{1} \mathrm{d}y \int \mathrm{d}(\cos\theta_\gamma) \frac{\mathrm{d}B(\mu \to \mathrm{e}\nu\nu\gamma)}{\mathrm{d}y\mathrm{d}\cos\theta_\gamma} \\ &\approx \left(\frac{\alpha}{2\pi}\right)(\delta y)^2[\ln(\delta y) + 7.33]. \qquad (1.21) \end{aligned}$$

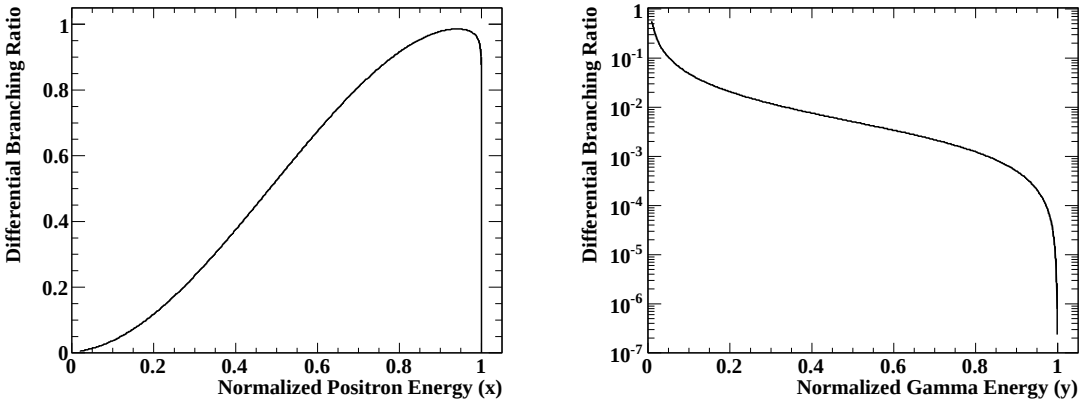

(a) (b)

Figure 1.6: Left figure shows positron energy spectrum of unpolarized $\mu^+ \to e^+\nu_e\overline{\nu}_\mu$ decay (Michel spectrum). A radiative decay correction [25] is included. Right one shows gamma Energy spectrum of unpolarized $\mu^+ \to e^+\nu_e\overline{\nu}_\mu\gamma$ decay. Positron energy and the angle between a positron and a gamma are integrated.

From Eq. (1.20), the branching fraction of the accidental backgrounds is proportional to R_μ.

A gamma ray from annihilation-in-flight (AIF) of a positron is other possible source of the accidental background. The energy spectrum and the production rate of the gamma ray from AIF depends on the materials inside the tracking volume. The rate of the AIF background is also proportional to the instant muon rate (R_μ) since almost all positrons originate from Michel decay of muons.

By way of example, the branching ratio of the accidental background is calculated by using resolution parameters given by the MEGA experiment. In the calculation, it has to be considered that pulsed muon beam was used in the MEGA experiment. The instant beam intensity was 2.6×10^8 in MEGA. The effective branching ratio is given as

$$B_{\rm acc} \sim 2.4 \times 10^{-12}. \tag{1.22}$$

Therefore the accidental background was dominant in their experiment and it could be a serious problem on searching for the $\mu^+ \to e^+\gamma$ decay with higher sensitivity of 10^{-13} level.

1.3.2.3 Experimental Requirement for the $\mu^+ \to e^+\gamma$ Search

As discussed in above sections, it is the most important to reduce the accidental background to achieve the sensitivity below 10^{-12}. Since the background rate is proportional to an instant muon rate, direct-current (DC) muon beam is strongly preferred in order to suppress the accidental background while keeping the total statistics high enough.

Since the incident rate of the AIF background depends on the materials along the positron trajectories, namely the target and the tracking devices, the total amount of materials inside the tracking volume should be as small as possible and they should be

made of materials which have small Z in order to reduce the AIF background. As shown in Fig. 1.6(a), high background rate is expected around the signal region of positrons. Therefore the high rate capability is required for the tracking detector.

Figure 1.6(b) shows the background gamma spectrum from the RMD events. As shown in this figure, background rate is highly suppressed if the gamma energy can be measured very precisely. In MEGA case, they used the pairs of a positron and an electron, which are generated by the gamma ray conversion, in order to measure the energy of the gamma ray. This method helps to achieve the 4.5% precise energy measurement in FWHM, however it causes the trade-off effect of the low detection efficiency which was measured to be 2.4% in MEGA. Consequently, the single event sensitivity was limited in their experiment. In order to achieve the sensitivity less than 10^{-12}, the same level of the energy resolution for gamma rays as MEGA with much higher detection efficiency is required for the gamma ray detector.

1.3.3 Comparison with Other CLFV Searches

Here some of other CLFV processes and related experimental searches are described together with the associated models of new physics for comparisons. The $\mu^+ \to e^+e^+e^-$ decay and the $\mu^- - e^-$ coherent conversion are promising channels to search for the BSM as same as the $\mu \to e\gamma$ decay by using muons. As one can easily imagine, the branching fraction of those two processes are strongly correlated to that of the $\mu^+ \to e^+\gamma$ decay. In case of the $\mu^+ \to e^+\gamma$ decay, contributions for the effective Lagrangian are dominated by photon-penguin diagrams as shown in Fig. 1.2. On the other hand, those of the $\mu^+ \to e^+e^+e^-$ decay and the $\mu^- - e^-$ conversion are enhanced by mediating the direct four-fermion interactions and the contributions from the photonic interactions of these processes are relatively small due to an additional coupling between a gamma line and a fermion line in the Feynman diagrams. Here each of muon CLFV processes are briefly discussed together with the relation to the $\mu^+ \to e^+\gamma$ decay and the experimental aspects.

1.3.3.1 $\mu^+ \to e^+e^+e^-$ decay

If only photon-penguin diagrams contribute to the $\mu^+ \to e^+e^+e^-$ decay, a model-independent branching ratio of $\mu^+ \to e^+e^+e^-$ can be derived by using the branching ratio of $\mu^+ \to e^+\gamma$, as follows [14]:

$$\frac{B(\mu^+ \to e^+e^+e^-)}{B(\mu^+ \to e^+\gamma)} \simeq \frac{\alpha}{3\pi}\left[\ln\frac{m_\mu^2}{m_e^2} - \frac{11}{4}\right] = 0.006. \tag{1.23}$$

The signal event can be well identified by using following two requirements:

- The conservation of momentum ($|\sum_i \vec{p}_i| = 0$) and energy ($\sum_i E_i = m_\mu$),
- Timing coincidence between two positrons and one electron.

For the $\mu^+ \to e^+e^+e^-$ decay search, two main background sources are considered. One is a prompt background; $\mu \to e^+e^+e^-\nu_e\overline{\nu}_\mu$, which is allowed in the SM and can be a fake of the signal event, when two neutrinos have tiny energies. The branching ratio of this decay is $(3.4 \pm 0.4) \times 10^{-5}$ [9]. The other background is an accidental coincidence of an e^+ from normal muon decay with an uncorrelated e^+e^- pair, for example, produced

from Bhabha scattering of e^+. The former one can be suppressed by measuring the total energy of all three charged particles, and latter can be reduced by measuring the relative angles and the timing between three charged particles.

The most stringent upper limit on the $\mu^+ \to e^+e^+e^-$ decay search is given as 1.0×10^{-12} (90% C.L.) by the SINDRUM experiment [11] as shown in Table 1.1 and no experiments are running to search for the $\mu^+ \to e^+e^+e^-$ up to now.

One experiment, aiming to search for the $\mu^+ \to e^+e^+e^-$ decay with 10^4 times higher sensitivity than the present upper limit, was proposed in PSI [26]. They proposed a staged approach in the sensitivity to BR$\sim 10^{-15}$ in phase I and further improvements to BR$\sim 10^{-16}$ at later stages if a new high-intensity muon beam (HiMB), which is a future planned beamline at PSI, is realized. If the photonic contributions are dominant, the current upper limit corresponds to the 10^{-10} order of magnitude of that for the $\mu^+ \to e^+\gamma$ search and the goal sensitivity of proposed new experiment corresponds to 10^{-14} level.

1.3.3.2 $\mu^- - e^-$ Conversion

In the SM, a negative muon, which is captured by an atom and forms muonic atom, can either decay in an orbit ($\mu^- \to e^-\nu_\mu\overline{\nu}_e$) or is captured by a nucleus of mass number A and atomic number Z, namely,

$$\mu^- + (A, Z) \to \nu_\mu + (A, Z-1). \tag{1.24}$$

However, the $\mu^- - e^-$ conversion in a muonic atom, such as

$$\mu^- + (A, Z) \to e^- + (A, Z), \tag{1.25}$$

is expected to occur in the BSM, which violates the conservation of the lepton flavor numbers as same as in the $\mu^+ \to e^+\gamma$ decay. From here, the $\mu^- - e^-$ conversion is expressed as $\mu^-N \to e^-N$. Similar to Eq. (1.23), the ratio of $B(\mu^+ \to e^+\gamma)/B(\mu^-N \to e^-N)$ is given by [14]

$$\frac{B(\mu^-N \to e^-N)}{B(\mu^+ \to e^+\gamma)} = \frac{G_F^2 m_\mu^4}{96\pi^3\alpha} \times 3 \times 10^{12} B(A, Z) \sim \frac{B(A, Z)}{428}, \tag{1.26}$$

where only the photonic contributions are assumed and $B(A, Z)$ represents the factor depending on the mass number (A) and the atomic number (Z) of the target nucleus. For example, for the titanium nucleus, the values of $B(A, Z)$ is calculated to be 1.8–2.2, based on different approximations. Therefore, the ratio of $B(\mu^-N \to e^-N)$ and $B(\mu^+ \to e^+\gamma)$ is calculated to be $B(\mu^-N \to e^-N)/B(\mu^+ \to e^+\gamma) \sim 0.0042$–$0.0051$. In the muonic atom, most muons transit to the ground state before decaying or being captured by the nucleus. Therefore if $\mu^- - e^-$ would happen, the energy of emitted electron should be monochromatic as

$$E_{\mu e} = m_\mu - B_\mu, \tag{1.27}$$

where B_μ is the binding energy of the $1s$ muonic atom. Since the value of B_μ is different for various nuclei, the peak energy of the $\mu^- - e^-$ conversion signal also changes, for example, $E_{\mu e} = 104.3$ MeV for titanium. Event signature is very simple that, only one

electron emitted with about 105 MeV energy. Thus $\mu^- - e^-$ search does not suffered from the accidental combinatrial background, which would be the serious background for searches of the $\mu^+ \to e^+\gamma$ and $\mu^+ \to e^+e^+e^-$ decays. There is one physics background comes from the normal muon decay in orbit (DIO) of the muonic atom. The end-point energy of the DIO corresponds the muon half mass (52.8 MeV) and it is small enough compared with the energy of the signal. Very small fraction of them are given the nuclear recoil energy, but are still negligible for currently planned two experiments which are introduced below. A radiative pion capture ($\pi^- + (A, Z) \to (A, Z-1) + \gamma$) could be one of the background sources. However, they can be suppressed by reducing the amount of pions which reach the muon target by using long enough muon transport solenoid. Other backgrounds could be caused by the decay in flight or interactions of particles (muon, pion, (anti)proton) in a primary proton beam. Since the muonic atoms have lifetimes of the order of 1 μs, the beam origin backgrounds can be suppressed by using high-intensity pulsed beam when the measurements are only done during the beam intervals. In this case, the purity of the pulse, which called "extinction", is essential since the remaining particles between two pulses could make the background.

The current upper limit was set by the SINDRUM-II experiment at 7×10^{-13} (90% C.L.) [21], which used the negative DC muon beam at the πE5 area in PSI.

In near future, two different experiments are being prepared to search for the $\mu^- - e^-$ by using high-intensity pulsed beam at the different places. One is the Mu2e experiment at Fermilab [27] and the other is the COMET experiment at J-PARC [28]. The goal sensitivities of both experiments are similar, at 10^{-16} level. Since the present upper limit and the goal sensitivity are similar to those of $\mu^+ \to e^+e^+e^-$ search, similar calculation can be done for the $\mu^- - e^-$ conversion as well.

For both the $\mu^+ \to e^+e^+e^-$ decay and the $\mu^- - e^-$ conversion searches, the branching fractions could be expected to be enhanced if some other contributions are considered. For example, in the little higgs model with T-parity, the lepton flavor violation can be happen through the additional mirror sector and the lepton flavor is not conserved any more [29]. In this model, the ratios between different three processes become comparable as namely $B(\mu \to e\gamma) \sim B(\mu \to eee) \sim B(\mu - e)$. Accordingly, the more information about the new physics can be obtained by comparing the results of different three CLFV modes.

1.3.3.3 CLFV in τ decay

Here, four CLFV decay modes of tau lepton are briefly described. The experimental searches for CLFV processes of tau lepton channel are done by using those generated by colliders since the tau lepton beam cannot be produced by present technologies because of its extremely shorter lifetime (0.29 ps) compared to that of muon. Current upper bounds are given by BABAR and Belle as shown in Table 1.4. In the near future, Belle-II collaboration aiming to search for the tau LFV with higher intensity electron positron collider. The LHCb experiment will also search for the tau on CLFV processes by using the Large Hadron Collider.

Table 1.4: Recent the most stringent experimental limits given by the BABAR and Belle experiments. Only four famous decay modes are shown here.

Mode	90% upper limit	Experiment
$B(\tau \to \mu\gamma)$	4.4×10^{-8}	BABAR[30]
$B(\tau \to e\gamma)$	3.3×10^{-8}	BABAR[30]
$B(\tau \to \mu\mu\mu)$	2.1×10^{-8}	Belle[31]
$B(\tau \to eee)$	2.7×10^{-8}	Belle[31]

Chapter 2

The MEG Experiment

The MEG (Mu to Electron Gamma) experiment started physics data taking in 2008 at Paul Scherrer Institut (PSI) in Switzerland to search for the $\mu^+ \to e^+\gamma$ decay with a sensitivity goal of 10^{-13}. The experimental proposal was submitted to the science committee of PSI in 1999 and the MEG collaboration was established in collaborating with 50–60 scientists from the institutes in Japan, Switzerland, Italy, Russia and United States. Dedicated detectors were constructed in order to achieve the sensitivity goal for the $\mu^+ \to e^+\gamma$ search [32]. The MEG detector is placed in the πE5 area in which the world most intense Direct-Current (DC) muon beam is provided by the proton ring cyclotron at PSI.

The schematic views of the MEG experiment and the global experimental coordinate is shown in Fig. 2.1 and Fig. 2.2. The center of the coordinate is set a origin at the center of the magnet. Other coordinate expressions as follows are used as well:

$$r = \sqrt{x^2 + y^2},\ \phi = \tan^{-1}(y/x),\ \theta = \tan^{-1}(r/z),\ z = z, \tag{2.1}$$

with a same origin of the (x, y, z) coordinate. For gamma ray measurement, an innovative detector using large volume liquid xenon (900 litters), which works as a total absorption calorimeter, was developed and scintillation photons are read by surrounding 846 Photo Multiplier Tubes (PMTs) to determine the timing, the position and the energy of incident gamma rays. In order to reconstruct the track of positrons, a set of drift chambers built with very low mass materials are used inside a superconducting magnet which has a specially designed gradient magnetic field. At each end of the magnet warm bore outside the drift chambers, 15 plastic scintillating bars are placed to measure the impact time of positrons in several tens ps of precision. For the data taking, we use fast waveform digitizers together with the trigger system consists of Flash Analog-to-Digital Converters (FADC) and a Field Programmable Gate Array (FPGA) system.

This chapter describes the details of the experimental apparatus, the analysis method, and the run conditions in 2009, 2010 and 2011 data taking.

2.1 Beamline

In order to get a high intensity DC muon beam, the proton ring cyclotron located at PSI is a unique choice for the MEG experiment, because it can provide the world most powerful

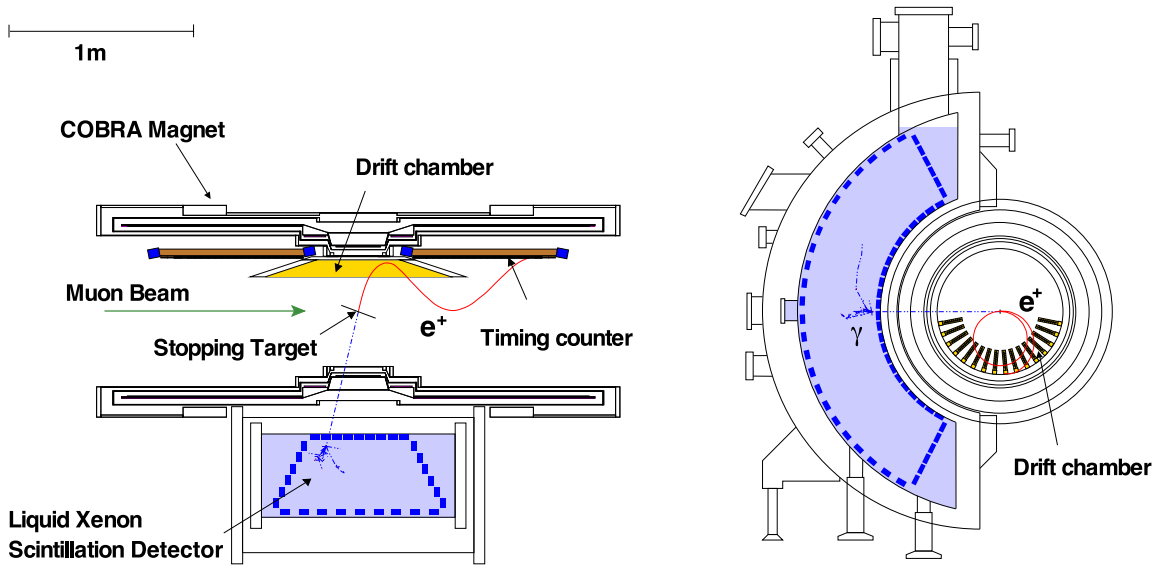

Figure 2.1: Top and side view of all the experimental apparatus with coordination.

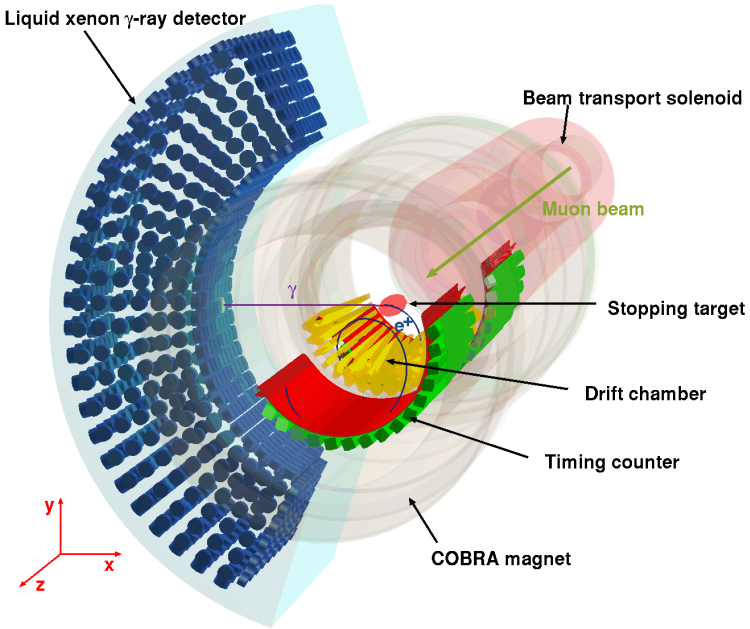

Figure 2.2: 3D view of all the experimental apparatus with coordination.

proton beam up to 2.2 mA (1.3 MW) with a 590 MeV energy [33]. The frequency of the proton beam is 50.6 MHz and the width of the bunch is 0.3 ns.

Figure 2.3: 590 MeV proton ring cyclotron at PSI.

2.1.1 Muon Beamline

In order to avoid muons to form the muonic atoms with materials inside the target, a positive muon (μ^+) is adopted for the experiment. At the πE5 beamline, a positive muon beam is delivered from the main proton ring cyclotron.

In the upstream of the πE5 beamline, muons only from pions decaying at the surface of the pion production target (E-target), are collected (so-called "surface muon") and they are delivered to the MEG detector as shown in Fig. 2.4.

Therefore, almost all muons are fully polarized and have almost same momenta of 28 MeV/c with 5–7% of spread in FWHM (Full Width at Half Maximum). Because of the smaller momentum spread, high purity and high intensity muons are selectable. A large contamination of positrons are separated by using both electric and magnetic fields in a Wien filter with a 8.1σ separation. The low momentum of the surface muon allows to use the thin target to stop muons, which is important to suppress the production of the background gamma rays inside the target. Furthermore, easier modifications of the beam size and the transportation are possible because of its small momentum spread.

Since the frequency of the proton beam is high enough (50.6 MHz) compared with the decay time of pions ($\tau_{\pi^\pm} \approx 26$ ns) and that of muons ($\tau_\mu \approx 2.2$ μs), the muon intensity is almost continuous. At the background reduction point of view, the continuous beam is quite important as already explained in Sec. 1.3.2.2. The stopping rate at the target is tuned to be 3.0×10^7 μ^+/s at a 2.2 mA of proton current.

2.1.2 Beam Transport Solenoid

The superconducting beam transporting solenoid (BTS) is placed to connect between the πE5 beamline and the detector part. Since the BTS is directly couple to the beamline, the inside of the BTS is evacuated. In order to avoid the distortion of the magnetic field,

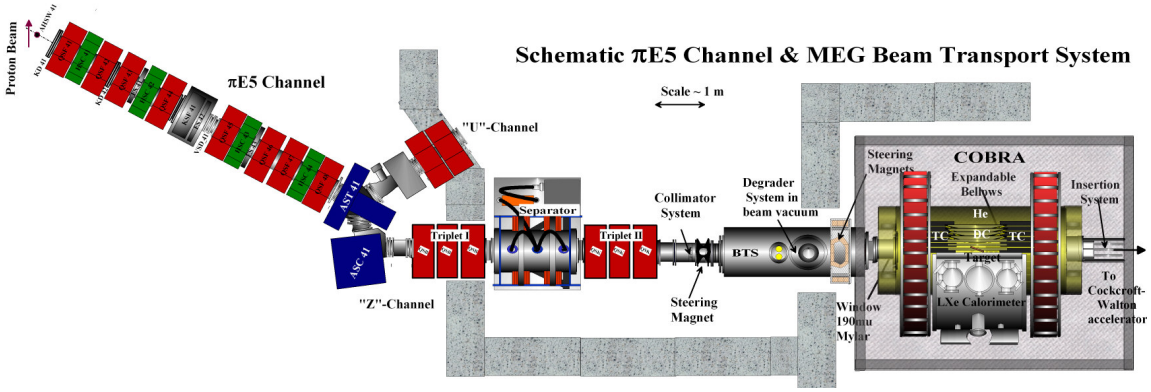

Figure 2.4: Schematic view of the πE5 beam channel including the beam transport system and detectors.

the BTS consists of iron-free cryogenics and magnets. At the central part of the BTS, a 300 μm thick Mylar® degrader is placed to reduce the momentum of muons so that most of them can be stopped in the thin target at the center of the detector magnet with a minimum multiple scattering contribution to the beam. In order to focus the muon beam at the degrader position and inside the detector, a 0.36 T magnetic field is generated by using the double-layered iron-free coil.

2.1.3 Target

In order to get high stopping power of muons and to reduce the materials which can generate the background, the target is implemented as a 205 μm thick sheet of a low-density layered-structure of a polyethylene and polyester with an elliptical shape and placed on the center of the superconducting magnet with a 20° slant angle along the beam axis. The length of semi-major and semi-minor axes are 10 cm and 4 cm respectively. There are six holes on the target in order to perform the software target alignment by analyzing the data as shown in Fig. 2.5(a). The target is placed at the almost center of the COBRA magnet (See Fig. 2.5(b)). At the target, the muon polarization is measured to be $89 \pm 4\%$ by using the angle distribution of Michel positrons and it is confirmed by analyzing RMD events [34].

2.2 Gamma Detector

With a gamma detection part, we need to detect the signal-like high energy gamma rays with a high detection efficiency. On the other hand, the background contamination must be highly suppressed. In order to realize such a kind of detector, following three points,

1. to reconstruct E_γ with an excellent resolution,
2. to measure the first conversion time of gamma rays precisely,
3. to reconstruct the first conversion point with a mm precision,

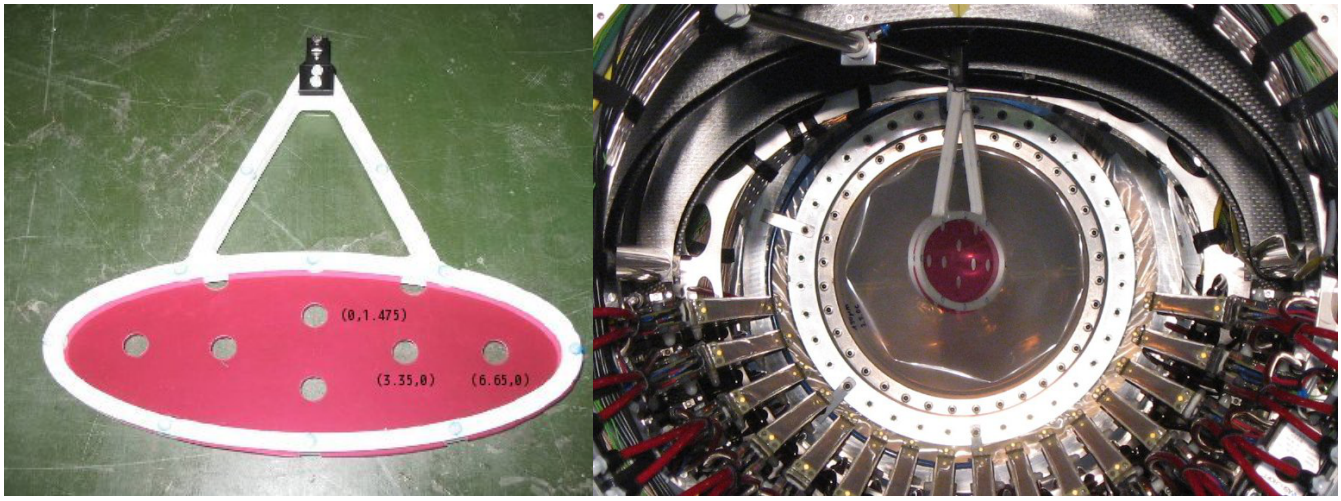

(a) (b)

Figure 2.5: Muon target (a) and installed view inside the COBRA magnet (b).

Table 2.1: Several characteristics of LXe in comparison with other scintillators.

	LXe	LAr	NaI(Tl)	CsI(Tl)	BGO
Density (g/cm^3)	2.98	1.40	3.67	4.51	7.40
Radiation length (cm)	2.77	14	2.59	1.86	1.12
Moliere radius (cm)	4.2	7.2	4.13	3.57	2.23
Decay time (ns)	45	1620	230	1300	300
Wavelength (nm)	178	127	410	560	480
Relative light yield	75	90	100	165	21

are needed to be satisfied for the gamma detector. In the MEG experiment, a Liquid Xenon (LXe) detector is adopted as the gamma detector to fulfill those three requirements. In this section, several properties of the LXe and the principle of the LXe detector are described.

2.2.1 Liquid Xenon

Since the LXe can realize non-segmented volume, the detector response can be more uniform than that of the detector based on segmented crystal. The faster decay time of the LXe helps to reduce the pileup probability effectively and provides good time resolution. Because of its short radiation length and high density, high detection efficiency is achievable. The characteristics of LXe are summarized in Table 2.1. Even though LXe has feasible scintillation properties to measure the energy of the gamma ray, there are mainly three difficulties to overcome as follows:

1. Low and the narrow operational temperature range between 161.4–165.1 K in order to keep the xenon in the liquid phase [7]

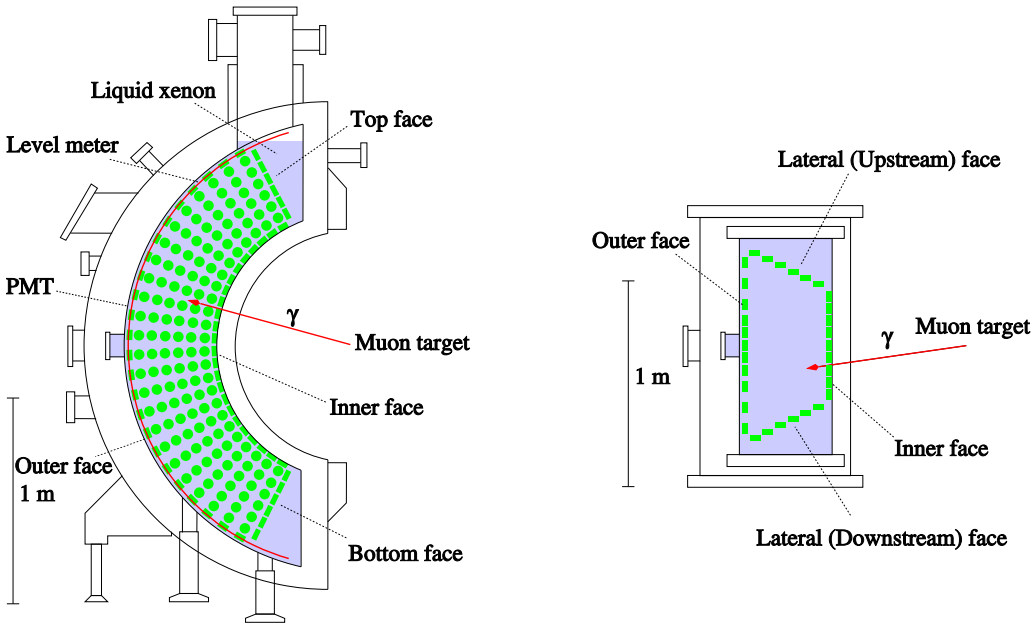

Figure 2.6: Schematic views of the LXe detector.

2. Short wavelength of the scintillation light (178±14 nm, peak±FWHM) [35]

3. High purity of the liquid xenon to avoid absorption of the scintillation light by contamination

In order to develop the LXe detector satisfying these requirements, R&D works, performance check using prototype detectors, design and construction of final detector were done [36].

2.2.2 Detector Design

Figure 2.6 shows schematic views of the LXe detector. The C-shaped structure is suitable for the outer radius of the magnet. The radii of the inner and outer faces of the active volume are 67.85 cm and 106.35 cm respectively. The 38.5 cm depth of the LXe detector is corresponding to 14 X_0. The angular ranges for the the gamma rays from the target are $-60^\circ < \phi < +60^\circ$ and $60^\circ < \theta < 120^\circ$.

A cryostat was constructed with a vacuum layer to keep xenon in liquid phase (See Fig. 2.7). In order to minimize the energy deposition of incident gamma rays before reaching the inner face of the detector, the inner face of the cryostat consists of an aluminum honeycomb panel with inner vessel carbon fiber and the stainless steel part of the window in thickness of only 0.4 mm. The outer vessel of the cryostat is made of 0.7 mm-thick stainless steel. A high pressure tolerance of the cryostat is up to 0.5 MPa while total thickness of the entrance window is only 0.075 X_0.

The inner vessel of the cryostat is filled with 900 litters of LXe. In order to monitor the detector condition, temperature, pressure and liquid level sensors are installed inside the detector. A custom-designed 200 W pulse-tube cryocooler [37] is installed on the top of the detector to maintain the LXe temperature. A circulation liquid purification

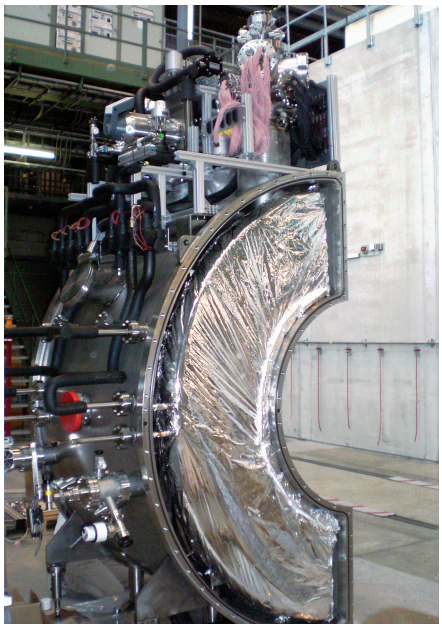

Figure 2.7: LXe detector before closing a flange of the outer vacuum vessel.

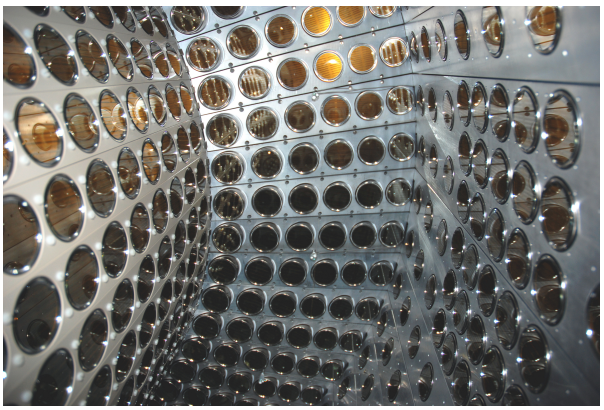

Figure 2.8: LXe detector inside with PMTs installed on all surfaces.

system with the molecular sieves (MS13A) and a cryogenic fluid pump was developed to efficiently remove H_2O from LXe.

All sides of the LXe active volumes are covered by 846 2-inch PMTs as shown in Fig. 2.8. Since the wavelength of LXe is in the region of the Vacuum Ultra Violet (VUV) and shorter than that of standard crystal scintillators, the VUV-sensitive PMT (R9869) was developed for the MEG experiment to obtain the high quantum efficiency (Q.E.) in collaboration with HAMAMATSU Photonics [38]. Each PMT is equipped with a quartz window that transmits VUV photons and a bialkali photo-cathode sensitive to VUV photons. Aluminum strips are added to the surface of the cathode to reduce the sheet resistance at low temperature. The average Q.E. is about 15% and the average gain is about 1.8×10^6 at 850 V.

For a convenience of the analysis, a local coordinate (u, v, w) is defined as:

$$\begin{aligned} u &= z \\ v &= R_{\text{inner}} \times \tan^{-1}(y/x) \\ w &= \sqrt{x^2 + y^2} - R_{\text{inner}} \\ \text{where} \quad & R_{\text{inner}} = 67.85 \text{ cm}, \end{aligned} \tag{2.2}$$

in the LXe detector.

2.3 Positron Spectrometer

For the MEG experiment, there are several requirements for the positron spectrometer as follows;

- operational in high rate environment,
- to contain as small materials as possible,
- to measure momentum, angular, vertex and timing at a very high precision.

In order to satisfy these requirements, the positron spectrometer is constituted by a superconducting magnet with a graded magnetic field, 16 drift chamber modules made of ultra low mass materials to be used for the positron-track reconstruction, and the timing counter for the impact time measurement of positrons. In this section, the details of each part are described.

2.3.1 COBRA Magnet

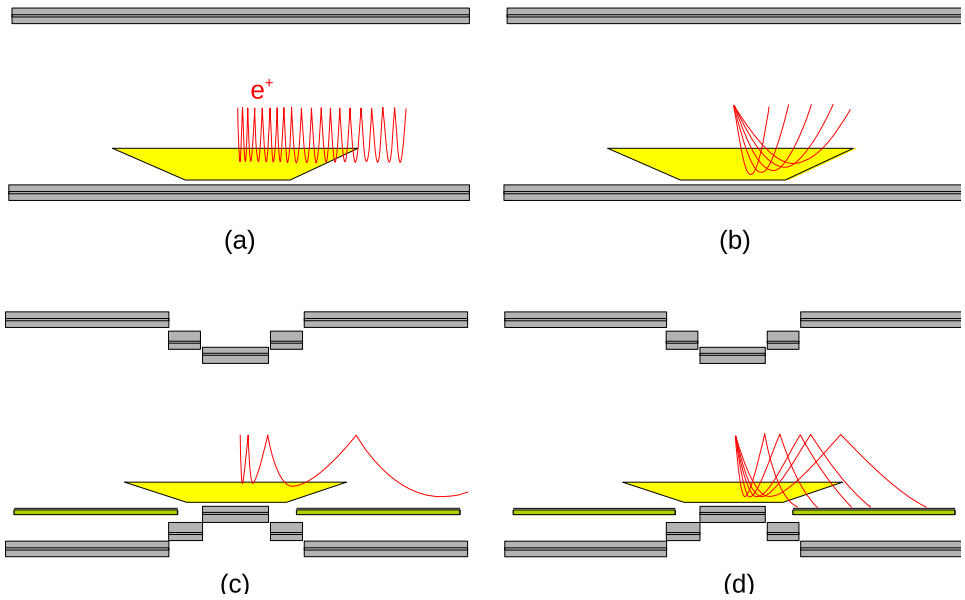

Figure 2.9: Concept of the COBRA magnetic field compared with the uniform field. Positrons emitted around 90° are quickly swept away (c) while they stay longer in a uniform field case (a). Positrons which emitted different θ angles have same curvatures in the COBRA magnetic field (d). On the other hand, they have different curvatures in a uniform case (b).

The COBRA magnet is a superconducting magnet developed for the MEG experiment [39]. The field of the COBRA magnet is graded by five coils with three different radii; one central coil, two gradient coils and two end coils. The central part of the magnet wall is as thin as 0.197 X_0 in order to reduce the energy loss of gamma rays which enter the LXe detector as much as possible.

Owing to the graded field, positrons emitted from the target are swept away quickly and the trajectory of positrons with the same momenta have equal radii independently of their emission angles as shown in Fig. 2.9. This is the reason why the magnet is called

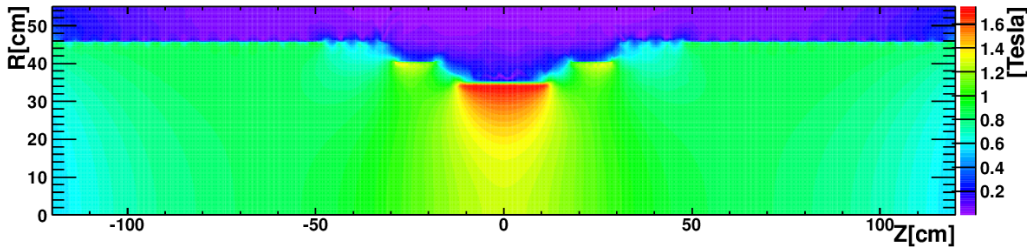

Figure 2.10: Contour plot of absolute values of the gradient magnetic field generated by the COBRA magnet

COBRA (COnstant Bending RAdius). The hit rate of positron inside the drift chambers is significantly reduced because of those two reasons as shown in Fig. 2.11.

Figure 2.10 shows the field strength of the COBRA magnet. Since the response of PMTs inside the LXe detector can be affected by the magnetic field, the normal conductive magnets are installed at the both sides of the superconducting magnet as a compensation coil to keep the field strength inside the LXe detector below 5×10^{-3} T as shown in Fig. 2.12.

Total length of the COBRA magnet is $\sim$2.8 m along the beam axis and the minimum radius at its center is $\sim$30 cm. The warm bore of the COBRA magnet is filled with almost pure helium to reduce the background gamma rays and the multiple scattering of positrons. Small amount of air (5%) is added to the helium gas to avoid the discharging at the front-end part of the drift chambers.

The magnetic field was measured in 2006 with a commercial three-axis Hall probe. The Hall sensors are mounted on a movable stage, which moves along z, r and ϕ. The precision of the sensors themselves are 0.05% and the planar Hall effect is less than 0.2%, the effect from the temperature coefficient of the sensor is estimated to be less than 0.06%. We also calculated the field by assuming an axi-symmetric coil model based on the measured coil dimensions and the alignment with a finite element method. By comparing these two field, it was found that there is larger discrepancy between the measured and calculated field than the precision of the Hall sensors. We evaluated the effect from the misalignment of the Hall probes and then found that the angular displacement of Hall sensors is crucial since the main strongest component B_z can contaminate the other field component, B_r and B_ϕ. Also the offset can cause the systematic effect. Therefore we firstly estimated the global offset by comparing the measured B_z and the calculated one and by minimizing the difference between these two, the offset is found to be $(x_0, y_0, z_0) = (+0.5, -3.0, -0.5)$ mm. After the global offset correction, B_r and B_ϕ were calculated from the measured B_z using the Maxwell equations. Subsequently, we checked the difference between the measured and the calculated fields again, then it was found that the discrepancy became smaller. This reconstructed magnetic field is used for the official simulation and the analysis in MEG.

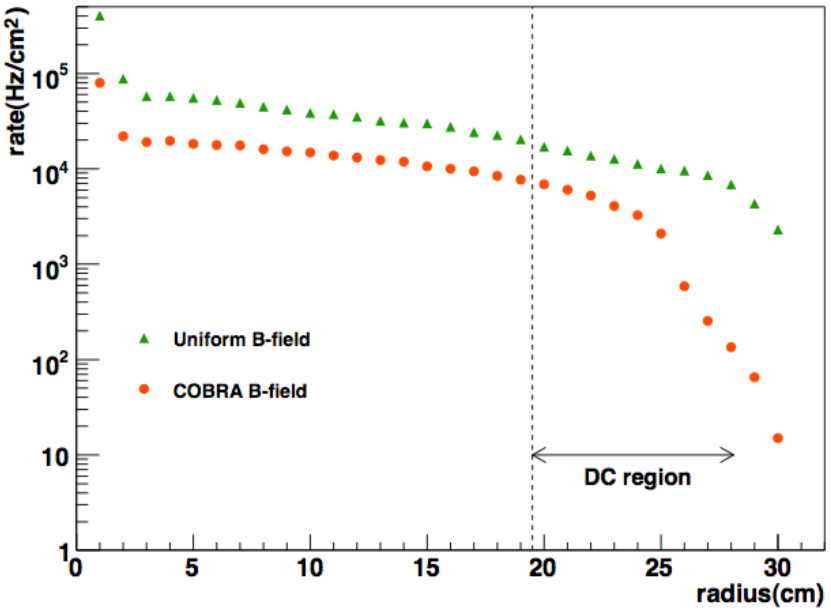

Figure 2.11: Positron hit rate per 1 cm^2 in each drift chamber module with a 3×10^7 Hz muon stopping rate as a function of the radius. Green triangle markers show those with an uniform magnetic field and orange markers show those with the COBRA magnetic field.

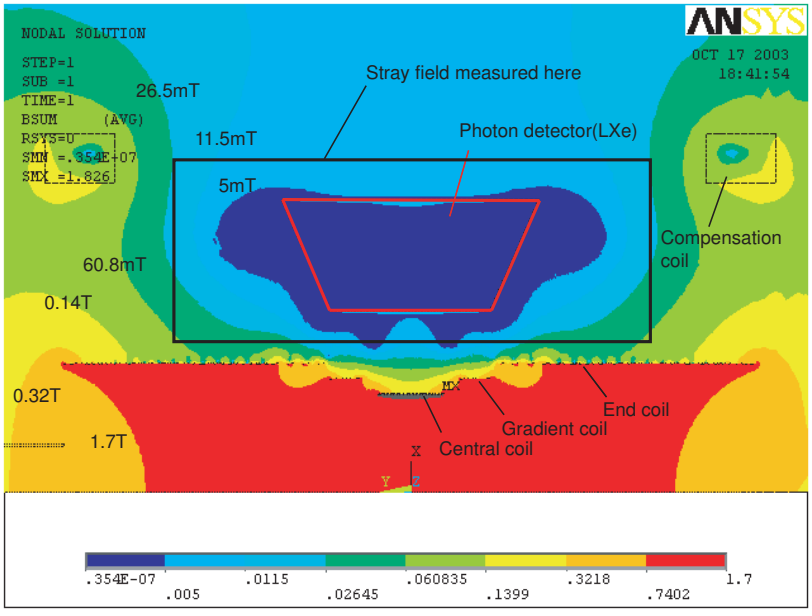

Figure 2.12: Distribution of the magnetic field around the LXe detector. The PMTs of the LXe detector are placed along the trapezoidal box shown in this figure.

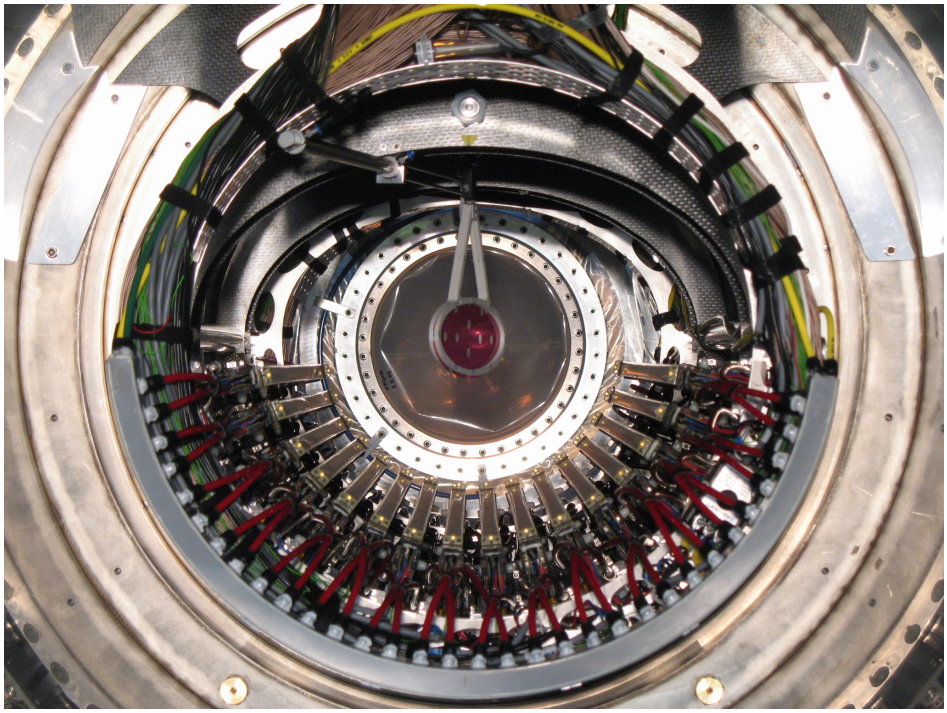

Figure 2.13: Drift chamber modules installed inside the COBRA magnet.

2.3.2 Drift Chamber

In order to minimize the production of the background gamma rays by the interaction of the Michel positrons in the tracking volume, gaseous detector is suitable as a tracking device because it can be constructed from lower Z materials than other devices such as silicon trackers. We therefore developed a Drift CHamber system (DCH) which consists of 16 independent drift chamber modules [40][41]. Drift chamber modules are placed at the bottom center of the COBRA magnet with 10.5° intervals in ϕ direction and aligned radially as shown in Fig. 2.13.

2.3.2.1 Drift Chamber Module

Each module is constructed with ultra low mass materials to reduce the multiple scattering of positrons and the production of background gamma rays inside the tracking volume. Figure 2.14 shows schematic views of each module. As shown in Fig. 2.14 and Fig. 2.15, each module consists of trapezoidal shaped two planes. Two planes are separated by thin cathode foils with 3.0 mm of gap and operated independently and each width is 7.0 mm. Each plane has 9 anode wires and cells are divided to 9.0 mm by potential wires in between each anode wire. Field potential and drift lines of ionized electrons are shown in Fig 2.16. Staggering of 2 layers by half of a cell helps to solve the left-right ambiguities as shown in Fig. 2.15.

Each module is filled with helium-ethane mixed gas in the ratio of 50:50 and the helium based gas mixture helps to suppress the production of background gamma rays from annihilation in flight of positrons and reduce the multiple scattering of positrons

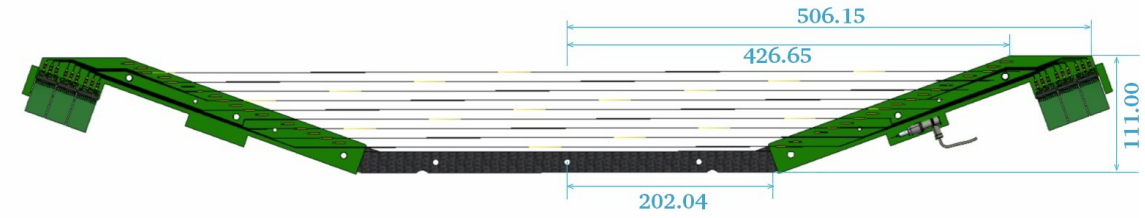

(a)

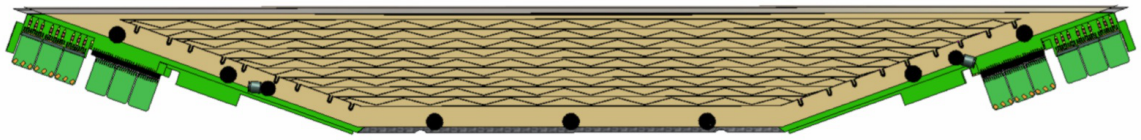

(b)

Figure 2.14: Schematic side views of a drift chamber module. One plane has nine anode wires and all anode and potential wires are supported by a open shape frame as shown in (a). The module is covered by the cathode foil which has 5 cm periodical zig-zag shape called "vernier pattern" as shown in (b).

because of its small Z value. The open shaped support structure of the module is made of carbon fiber in order to keep the tightness with the small Z mass material. Resistive Ni-Cr wires are used for the anodes with a resistance per unit length of 2.2 kΩ/m and a 25 μm diameter. Potential wires are made of Be/Cu with a 2:98 ratio and 50 μm diameter. Cathode foils have 'zig-zag' shaped 5.0 cm periodical pattern called 'Vernier pattern' to improve the z resolution and is constructed by 12.5 μm-thick polyamide foil with an aluminum deposition of 250 nm with a resistance per unit length of 50 Ω/m. The details of the vernier method are described in Chap. 3 and in [42]. The total charge of ionized electrons are amplified by the pre-amplifier boards, which are mounted at each end of the support structure, with a total gain of $\sim$50.

In total, the mean of the radiation length for signal positrons inside the tracking region is $2 \times 10^{-3} X_0$, which is small enough to reduce the multiple scattering of positrons for the better tracking resolution and reduce the gamma ray background generated inside DCH. Table 2.2 shows the summary of the characteristics and design parameters of DCH.

2.3.3 Timing Counter

As shown in Fig. 2.1, Timing Counters (TC) are placed at each end of the COBRA warm bore outside the drift chambers in z-axis to measure the impact time of positrons. Each barrel-shaped sector consists of a longitudinal part (called TICP) and a transversed part (called TICZ) and covers the region from $-150°$ to $10°$ in ϕ and from 28 cm to 109 cm in $|z|$. The longitudinal part is composed of 15 scintillating bars (Saint-Gobain BC404) to measure the timing with 10.5° gaps in the ϕ direction. Since the TC has to be operated inside the COBRA magnet, scintillation photons are collected by 2-inch fine-mesh

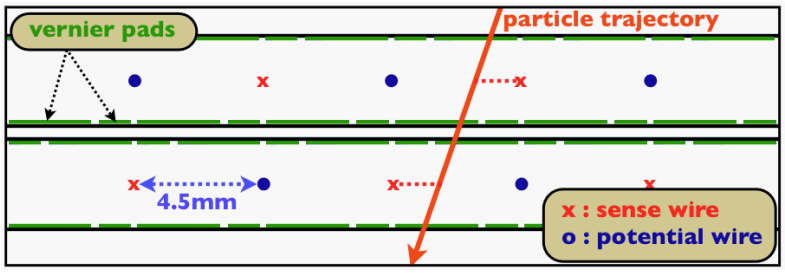

Figure 2.15: Configuration of cells inside the chamber module. Two planes are divided with a gap of 3 mm and the position of the sense wires are staggered. Green horizontal lines show the cathode pads.

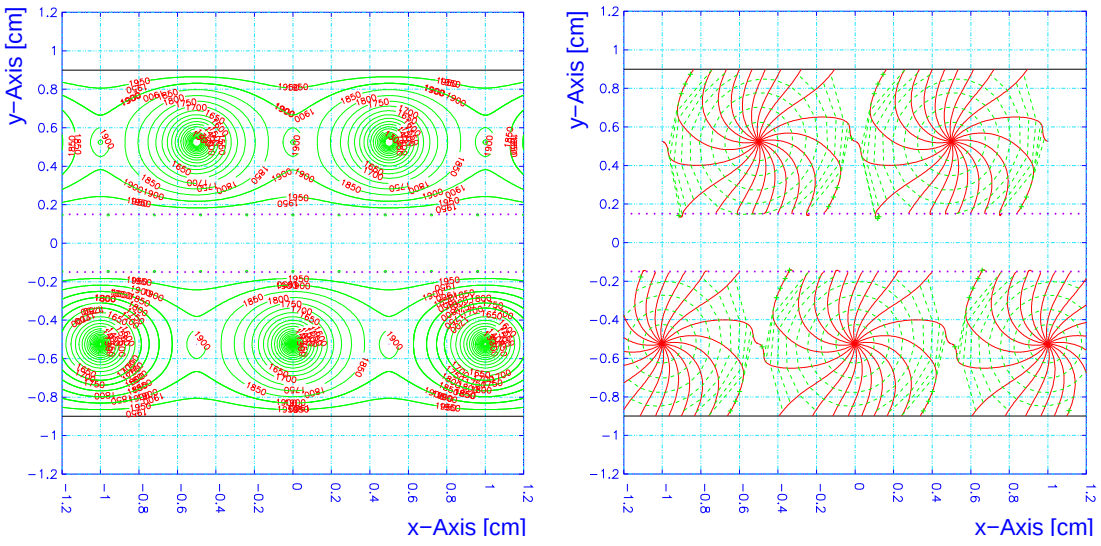

(a) Contour plot of the potential

(b) Drift lines with isochron map

Figure 2.16: Field map and drift lines calculated by GARFIELD simulation with the nominal operated condition in MEG.

Table 2.2: Characteristics and Parameters of DCH.

Structure	16 modules aligned with 10.5° intervals in ϕ direction 2 layers staggered by a half of cell, 9 cells per layer
Chamber Dimension	Trapezoidal shape R_{min}=193.38 mm, R_{max}=278.88 mm (fiducial volume) Z_{min}=385.66 mm, Z_{max}=827.31 mm (fiducial volume)
Cell Dimension	Rectangle cells divided by potential wires 9.0 mm×7.0 mm size, 4.5 mm wire spacing
Sense Wire	Materials : Ni/Cr (80:20) Diameter : 25 μm Tension : 50 gf Resistance : 2200 Ω/m
Potential Wire	Materials : Be/Cu (2:98) Diameter : 50 μm Tension : 120 gf
Cathode Foil	12.5 μm-thick polyimide with aluminum deposition of 250 nm
Vernier Pads	4 pads per cell Pattern period : 50.0 mm Resistance : 47.5 Ω/m
Gas	He:C_2H_6 = 50:50 Typical drift velocity : 4 cm/μs Typical electron diffusion : 140 μm/cm at 1 kV/cm
Frame	Open shape, carbon fiber
Voltage	Sense Wire : + 1750–1850 V Potential Wire and Cathode : Ground
Number of Channels	6 channels/cell × 9 cells × 2 layers × 16 modules = 1728 channels

PMTs which are operational in a high magnetic field. Figure 2.17(a) shows assembled longitudinal sector and Fig. 2.17(b) shows the schematic cross views of scintillator bars.

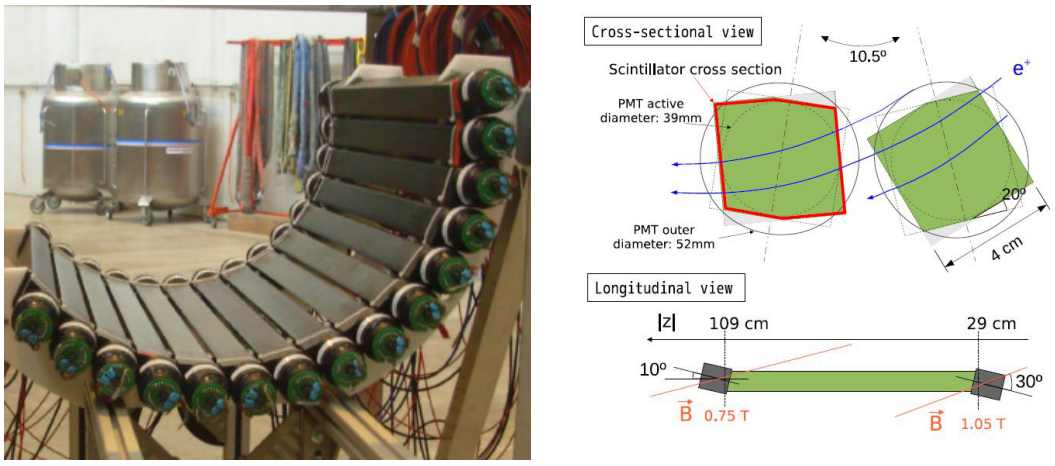

(a) 15 timing counter bars placed in 10° interval.

(b) Cross view of a timing counter bar with PMT on X-Y plane and along the z-axis.

Figure 2.17:

The transversed part consists of 128 curved scintillating fibers to measure the z position of positrons at the surface of the TC as shown in Fig. 2.18. Scintillation photons are detected by 5×5 mm^2 silicon Avalanche Photo-Diodes (APDs) which are attached at both ends.

2.4 Front-end Electronics and Data Acquisition System

In order to get the precise charge estimation, an event-by-event baseline calculation is required to eliminate the influence of the baseline fluctuation due to the low frequency noises. Furthermore, it is needed to separate the pileup events in time down to 10 ns. Therefore we decided to use a fast waveform digitization for the Data AcQuisition system (DAQ) in MEG. All of data from each sub-detector are collected as waveforms by using a fast waveform sampling device called Domino Ring Sampler (DRS) chip which is developed in PSI to satisfy the requirements for the MEG experiment. Events are triggered by using Field Programmable Gate Array (FPGA) system to select the signal-like events efficiently. The programmable trigger system also allows us to build the many kind of triggers for the calibration purpose in a flexible way and it enables to modify the trigger parameters easily.

2.4.1 DRS4

The latest version of DRS which is called DRS4 is the waveform sampler developed in PSI for the fast waveform sampling. The basic idea of DRS is using analog Switched

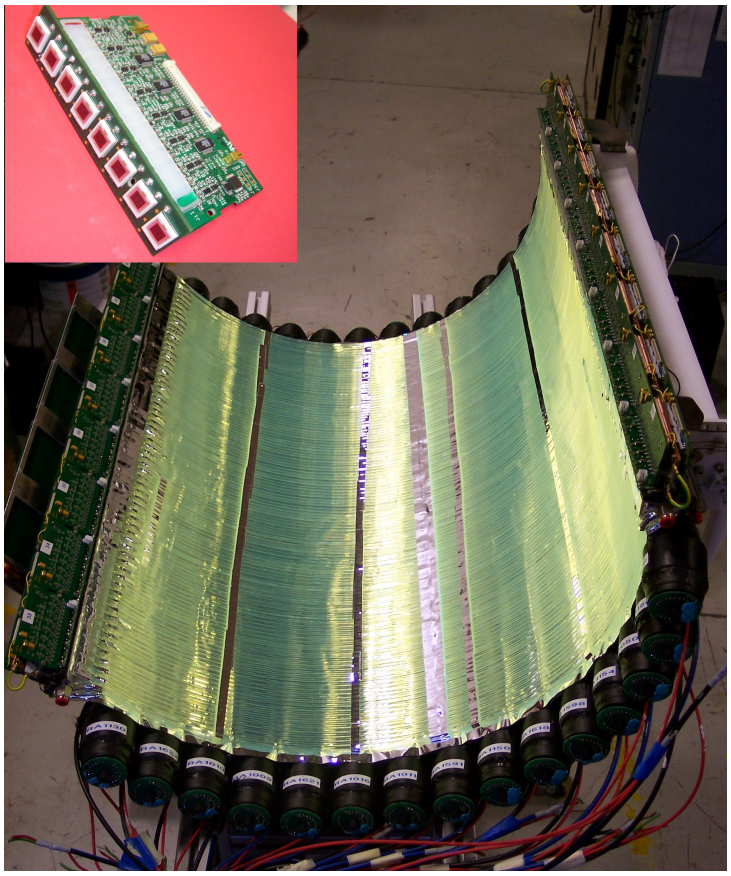

Figure 2.18: Timing counter bars covered with fibers for z position measurement.

Capacitor Arrays (SCA) and writing the data for each capacitor in high sampling speed. There are two chains of capacitors which are connected each other as the analog sampling cells to write waveform data as a differential, which reduces the cross-talk between different channels, in each cell. This structure called domino wave circuit. Figure 2.19 shows the schematic view of the principle of DRS. Each chip has 8 channels and all channels connected to a single external 12-bit ADC (Analog-to-Digital Converter) by using a multiplexer. This design helps to reduce the cost and space on the board. The sampling speed is adjustable up to 5 GHz by modifying a control voltage U_{speed}, which is fixed by using a Phase-Locked Loop (PLL) to an external clock with high precision. Since the LXe and TC detectors require precise time measurements, 1.6 GHz sampling frequency was chosen. In the DCH, 0.8 GHz frequency was chosen because they need less timing requirements than those for other detectors.

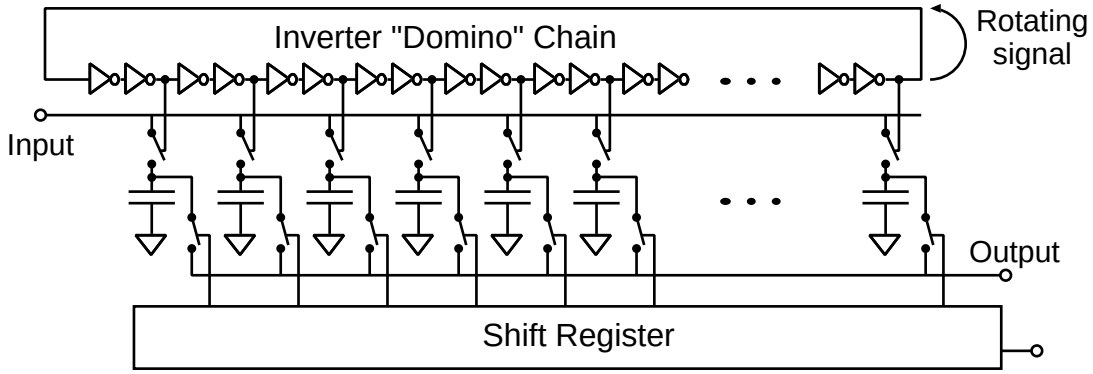

Figure 2.19: Schematic of DRS principle.

2.4.2 Trigger

In order to collect the $\mu^+ \to e^+\gamma$ like events with high efficiency in a high background condition, we combined FADC and FPGA to construct the trigger. For physics data, the following observables are used in the online trigger selection.

- E_γ selection,
- $t_{e\gamma}$ selection,
- direction match selection (DM).

Hereafter, this trigger is called "MEG trigger".

In the E_γ selection, total charge of PMTs in the LXe detector is used with online collection factor for each PMT to select the high energy gamma rays effectively. The $t_{e\gamma}$ selection is done by calculating the time difference between t_{LXe} and t_{TC}. The position of gamma ray is determined by the PMT which detects the largest amount of scintillation photons and convert to the direction of the gamma ray emission assuming the center of the target. Since the signals from DCH are collected in an order of μs time range, they cannot be used for MEG trigger. Instead, the signals from the timing counter have

enough information for MEG trigger, because each sector of TC is segmented in the ϕ direction and there are correlations between ϕ position at TC and the emission angle of positrons with high momenta.

Many types of trigger channels are prepared for the calibration purposes for each sub-detector as well. All of important triggers are summarized in Table 2.3 with their bases of logic.

Table 2.3: Various trigger settings used in the MEG experiment and the prescaling factors in physics run. Approximately $Q_L \sim 30$ MeV,$Q_H \sim 40$ MeV,$T_N \sim 20$ ns and $T_W \sim 40$ ns. DM represents the direction-match algorithm given by the trigger.

Id	Description	Prsc.	Logic
0	$\mu^+ \to e^+\gamma$	1	$(Q_{LXe} > Q_H) \wedge (\lvert\Delta T\rvert < T_N) \wedge$ (narrow DM)
1	$\mu^+ \to e^+\gamma$, low Q	50	$(Q_{LXe} > Q_L) \wedge (\lvert\Delta T\rvert < T_N) \wedge$ (narrow DM)
2	$\mu^+ \to e^+\gamma$, wide angle	500	$(Q_{LXe} > Q_L) \wedge (\lvert\Delta T\rvert < T_N) \wedge$ (wider DM)
3	$\mu^+ \to e^+\gamma$, wide time	200	$(Q_{LXe} > Q_L) \wedge (\lvert\Delta T\rvert < T_W) \wedge$ (narrow DM)
4	$\mu^+ \to e^+\nu_e\overline{\nu}_\mu\gamma$ / Dalitz decay in π^0	1000	$(Q_{LXe} > Q_L) \wedge (\lvert\Delta T\rvert < T_N)$
5	$\mu^+ \to e^+\nu_e\overline{\nu}_\mu\gamma$ wide / CW boron	-	$(Q_{LXe} > Q_L) \wedge (\lvert\Delta T\rvert < T_W)$
6	π^0 with NaI (BGO)	-	$(Q_{LXe} > Q_H) \wedge$ NaI(BGO) time coincidence signal
7	π^0 w/o pre-shower	-	$(Q_{LXe} > Q_H) \wedge$ pre-shower time coincidence signal
8	NaI (BGO) alone		$Q_{NaI} > Q_{threshold}$
9	LXe alone High Q	20000	$Q_{LXe} > Q_H$
10	LXe alone Low Q / CW lithium / α		$Q_{LXe} > Q_L$
12	α selection	22000	$(Q_{LXe} > Q_0) \wedge \alpha$ selection
14	LED	10	100 Hz pulse from LED module
16	Michel DC track + TC hit	-	DCH hits $\wedge$ TIC hits
18	DCH track	10^7	DCH self
19	Cosmic DCH	-	Trigger by Cosmic-ray counters
22	TC alone	10^7	TIC self
31	Pedestal	20000	Clock for pedestal

The trigger id 22 is used to calculate the normalization factor for the analysis by collecting the Michel positrons. From now on, the trigger id 22 is called "Michel trigger". We estimate the efficiency of the positron spectrometer by using "Michel trigger" and the trigger id 18 since the trigger id 18 is independent of the timing counter. The method of the efficiency calculation is described in Sec. 5.2.6 in detail.

Figure 2.20 shows illustration view of the trigger system. The system is mainly divided into 3 sectors. The first one is used to digitize the signals from each sub-detector with the first pre-selection algorithm. The second layer receives data from the first layer and send the data to the third one. The final board, which has an overall view of the event,

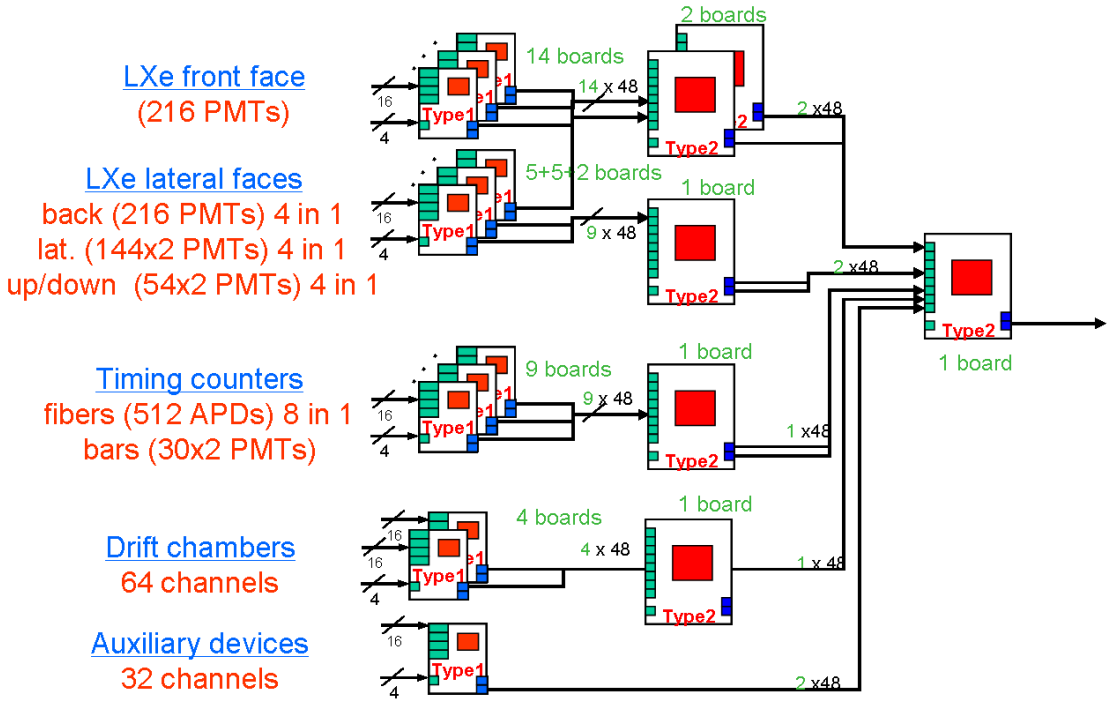

Figure 2.20: Illustration of the trigger system.

generates the trigger signal.

2.4.3 MIDAS

The MIDAS (Maximum Integration Data Acquisition System) which is developed in PSI and TRIUMF [43] is used as a DAQ system in the MEG experiment. The MIDAS is used not only for controlling the DAQ but also for the recording data in special formatted file for MIDAS, the detector monitoring and the alarm system. The MIDAS provides web interfaces in order to enable the real time monitoring as well.

2.5 Simulation and Analysis Framework

Figure 2.21 shows the full chain of the simulation and the analysis framework developed for the MEG experiment. Here we mention both the simulation and the analysis.

2.5.1 Simulation

In order to simulate the any kind of necessary events inside the MEG detectors precisely, the simulation software called `MEGMC` was developed based on `GEANT3` [44] which is Monte Carlo (MC) simulation tool written in FORTRAN 77. The drift lines of electrons inside each cell of the DCH are simulated by `GARFIELD` [45]. In the `MEGMC`, primary events can be generated as shown in Table 2.4. Generated events are written in file with ZEBRA format which was developed in CERN.

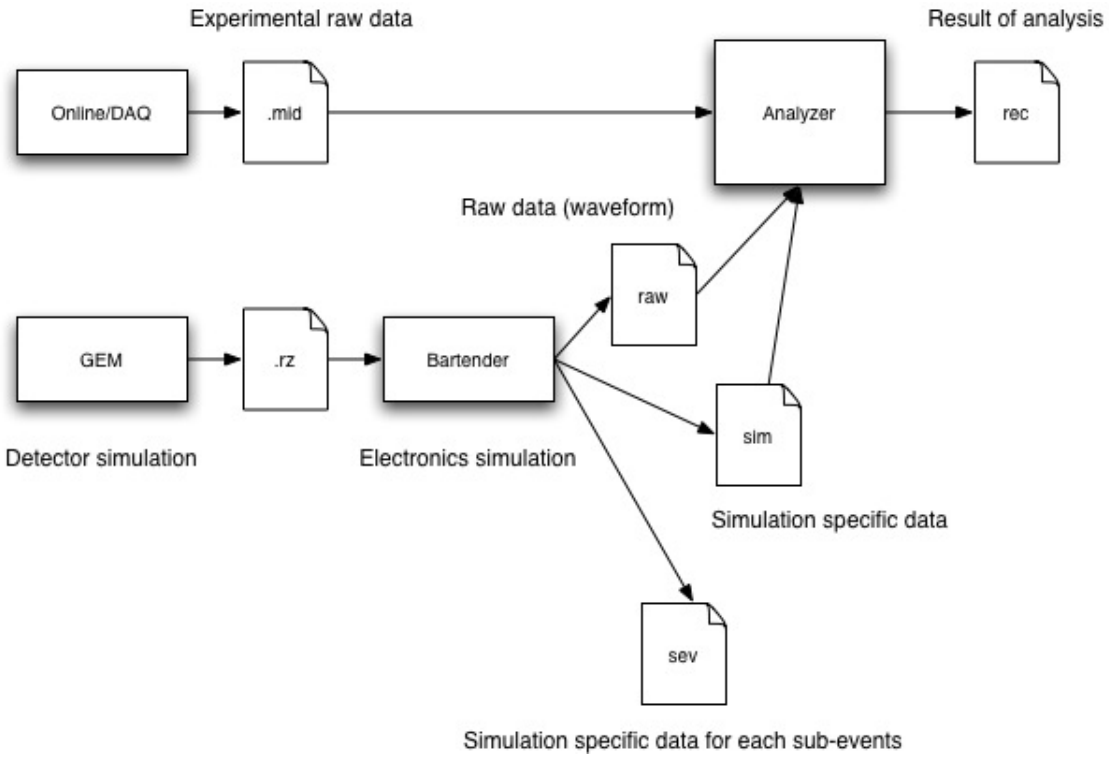

Figure 2.21: Illustration of the full programming chain for the analysis and the MC simulation in MEG.

Table 2.4: List of some important events which are prepared in `MEGMC`.

Event Id	Description
1	$\mu^+ \to e^+\gamma$ signal event
2	Radiative Muon Decay (RMD) event
11	e^+ at 52.8 MeV
12	e^+ from Michel decay
21	γ at 52.8 MeV
22	γ from RMD
23	γ from e^+ annihilation in flight
30	μ^+ beam
50	Cosmic-ray μ
63	α from ^{241}Am source on wire
67	$\pi^0 \to \gamma\gamma$ decay
68	p^+ from CW accelerator + LiF target
69	p^+ from CW accelerator + B target

Since all of data are accumulated as waveforms in the physics run, waveform digitization part should be reproduced for the realistic simulation. Since the analysis framework of the MEG experiment is based on `ROOT` [46], it is required to generate from ZEBRA format file which contains information about the physics interaction inside each sub-detector to `ROOT` format files which contain physics information and data as waveforms. The software called `MEGBartender` was developed based on C++ programming to simulate the waveform digitization. The event mixing by assuming any rate can be also done in the `MEGBartender`.

2.5.2 Analysis

As already mentioned, raw data from each sub-detector are stored as waveforms in the `MIDAS` file. In order to get physical quantities from those raw data files, the analysis software called `MEGAnalyzer` based on the Root based Object oriented Midas Extension (ROME) [47] developed at PSI is used. Details of waveform analysis and the event reconstruction are explained in Chap. 3, and details of the physics analysis are described in Chap. 6.

2.6 Run Status

This section describes the MEG data taking in 2009, 2010 and 2011, because we analyze all the datasets with revised reconstruction and analysis methods. Several drift chamber modules, which had large number of dead channels or completely dead plane due to discharging, were replaced at the beginning of each year's run with new ones tested in a lab. In the lab test, we check the functionality of each new module by using the test apparatus which consists of a vessel which contains helium and air with the same mixture ratio as used in the MEG data taking. Two plastic scintillator bars are mounted at the top and bottom sides of the test apparatus and they are used to trigger the cosmic-ray events which pass through the drift chamber. Due to exchanging the modules, the tracking efficiency was recovered at the beginning of each run.

In the shutdown period between each year, we did an optical survey in order to measure the positions of the target and each drift chamber module.

Muon stopping rates at proton current of 2.2 mA were set to 3×10^7 μ^+/s in all data taking period and eleven different type of triggers were mixed with MEG trigger with prescaling factors written in Table 2.3.

We also took the calibration data in third of twice per week. In each year, we took the charge exchange (CEX) calibration in order to obtain the absolute energy scale of the LXe detector and to measure the energy resolution. Details of calibrations are written in Chap. 4.

2.6.1 Run 2009

In 2009, MEG data taking was done for two months with two different setups of muon momentum degraders of 200 μm and 300 μm, which were used for the first and the second half of the data taking, in order to optimize the muon stopping efficiency at the target.

After the degrader replacement to 300 μm, the stopping efficiency was recovered from 56% to 82%.

In 2009, the APDs of the TICZ fibers were turned-off because the large noise were observed on the waveforms from the drift chambers when they were turned-on.

The amount of collected data corresponds to 6.5×10^{13} stopped muons in the target in 35 DAQ days.

2.6.2 Run 2010

Before the 2010 run, we investigated the noise sources on the DRS boards and the PLL exchanged to ones which have more temperature stability. As these results, the time jitter between different DRS channels were improved to 40–50 ps from those of 110–170 ps.

The APD channels of TICZ detector was turned-on during most MEG data taking in 2010, because they did not make the large noise which was observed in 2009. However, they are not used in the analysis because the large noises were observed in waveforms from APDs themselves.

In 2010 run, physics data taking started in August and ended in November, which was one month earlier than scheduled due to an unexpected quench of the BTS. However the total statistics reached 1.1×10^{14} stopping muons in the target with the data taking of 56 DAQ days.

2.6.3 Run 2011

In 2011 run, 3×3 NaI crystals were replaced with 4×4 BGO crystals in order to better calibrate the energy scale and measure the energy and timing resolutions of the LXe detector in the CEX calibration run. Because of installing the BGO crystals, detection efficiency of CEX events increased and resolution of the opening angle of the CEX events was improved due to the larger stopping power of each crystal compared with that of the NaI crystal (See Table 2.1) used for the CEX calibration taken before 2011. Details of the CEX calibration are described in Chap. 4.

Before starting 2011 run, new method of the optical survey using the laser tracker system was done for more precise alignment for drift chambers. Few more details are described in Sec. 4.3.1.

In 2011, a multiple buffer read-out scheme was implemented in the DAQ system. In this method, data from waveform digitizers are written in the other buffer if the data taken by the last trigger is still stored in the first buffer. Owing to this method, DAQ live time increased from 72% in 2010 to 99%, significantly. This large reduction of the dead time allowed us to use wider direction match criteria. Consequently, the trigger efficiency is also improved from 92% in 2010 to 97% in 2011.

At the beginning of the physics run, huge noises which we cannot ignore were observed in waveforms of drift chambers. After that, we pinned down that there were the following two main noise sources:

- APD channels used for TICZ generate the noise of mainly 40 MHz frequency,
- High voltage modules for DCH cause the noise of manly 14 MHz frequency,

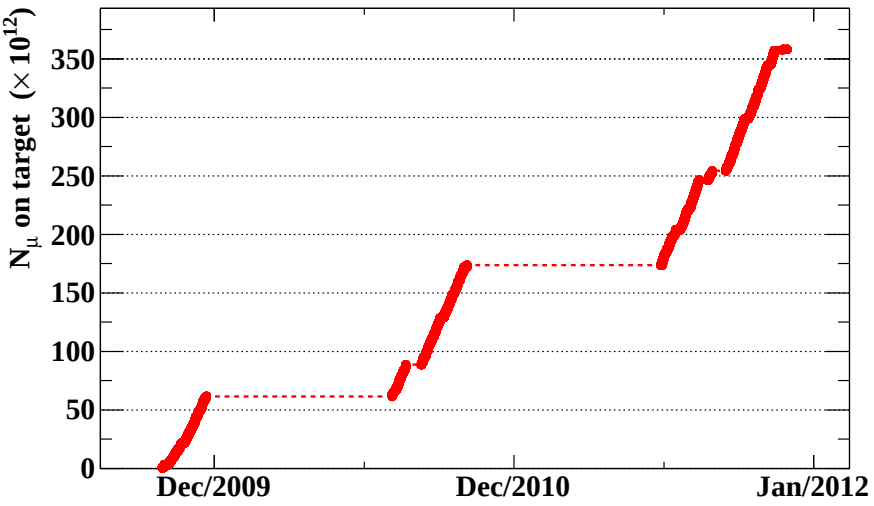

Figure 2.22: Number of stopped muons on the target during physics data taking of 2009–2011.

and we turned off 25% of APD channels which caused the noise component of 40 MHz frequency, and high voltage modules for the drift chambers were replaced with low noise commercial high voltage devices. Because of these efforts, two main noise components almost disappeared. Furthermore, we developed the offline noise reduction in order to recover the efficiency and resolutions during the noisy run period. The details of the offline noise reduction are explained in Sec. 3.2.1.3.

In 2011, there was an unexpected power-cut in the πE5 area and 1.5 weeks DAQ time were lost. Nevertheless, we could collect the physics data corresponding to 1.85×10^{14} muons stopped on the target as shown in Fig. 2.22 in a six month operation including the calibration periods. The total statistics is approximately equivalent to the sum of those obtained in 2009 and 2010.

The total statistics collected in 2009–2011 corresponds to 3.58×10^{14} muons stopped on the target.

Chapter 3

Event Reconstruction

In this chapter, the details of the event reconstruction algorithms are described. Since we newly improve the following three reconstruction algorithms, each of them is explained in detail as well.

- New pileup identification and unfolding method using summed waveform
- Offline noise reduction in the waveform analysis of drift chambers
- Change the code for the track fitting

3.1 Gamma Reconstruction

In order to reconstruct the position, the energy and the timing of gamma rays which enter the LXe detector, the 846 PMTs mounted inside the LXe detector are used as already mentioned in Sec. 2.2. The waveform analysis is performed on the waveform from each PMT to calculate the charge and the timing of photons detected by the PMT in each event. Based on the waveform analysis, position, energy, timing of a gamma ray are reconstructed [48][49][50]. Pileup events are identified and subtracted by using the light yield distribution and the PMT time distribution. A pileup unfolding using the summed waveform analysis is newly implemented in the analysis for 2009–2011 data. The background from cosmic-rays are reduced by applying the topological cut.

3.1.1 Waveform Analysis

The number of detected scintillation photons and the hit time of photons are calculated by analyzing the waveforms from all the PMTs. Figure 3.1(a) shows typical waveform before and after the filtering. The baseline is estimated by averaging the points in the region before the pulse on an event-by-event basis. The pulse time for each PMT is determined by applying the digital constant fraction method with 30% fraction for the given maximum pulse height. In order to maximize the signal-to-noise ratio for the charge determination, a digital high-pass filter, based on a moving-average method, is applied to the raw waveform as shown in Fig. 3.1(b). In this method, the fast component of the waveform is extracted by subtracting the averaged waveform from the original one. The number of moving-average points is 90–100, corresponds to about 10 MHz cutoff

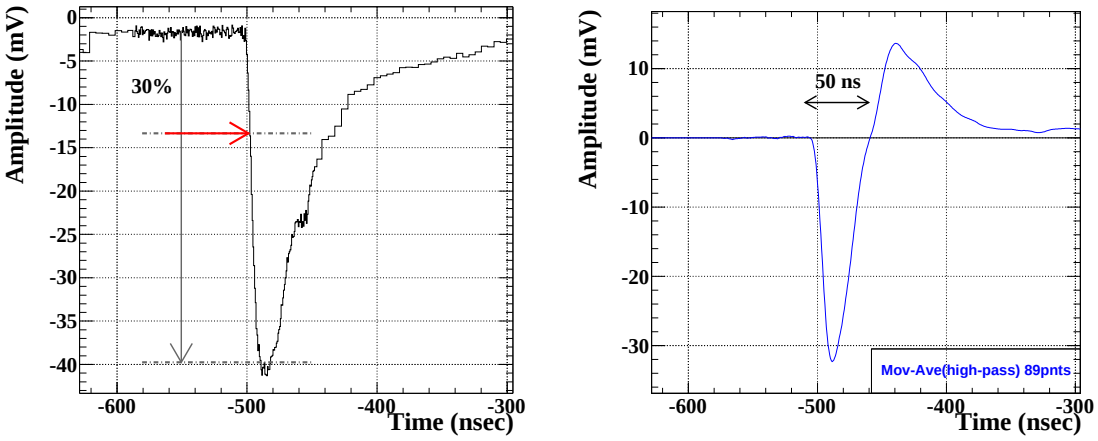

(a) (b)

Figure 3.1: (a) An example of a PMT raw waveform from the waveform digitizer. (b) An example of a waveform with high-pass filter.

frequency. The charge is calculated by integrating the filtered pulse found in each PMT with a 50 ns time window.

The number of photo electrons detected by i-th PMT is calculated by using the equation below.

$$N_{pe,i} = Q_i/(e \cdot G_i), \tag{3.1}$$

where Q_i and G_i are measured charge and the gain of i-th PMT, respectively. The gain of each PMT is determined by using the LED calibration data (See Sec. 4.1.5). Then the total number of scintillation photons detected in i-th PMT is given by

$$N_{npho,i} = N_{pe,i}/(QE_i), \tag{3.2}$$

where QE_i is the quantum efficiency of the i-th PMT. The QE_i is determined by analyzing the calibration data with point-like α sources (See Sec. 4.1.6).

3.1.2 Position Reconstruction

The gamma ray conversion point is reconstructed by using the distribution of the scintillation light detected by the PMTs close to the incident position. The three-dimensional position is determined by fitting the expected light distribution on the PMTs, calculated from the solid angles, to the observed distribution. The interaction position (u, v, w) is determined by minimizing χ^2_{position} defined as

$$\chi^2_{\text{position}} = \sum_{i}^{\text{PMT}} \frac{N_{pho,i} - c \times \Omega_i(u,v,w)}{\sigma_{pho,i}(N_{pho,i})}, \tag{3.3}$$

where c is the free parameter for fitting as well as (u, v, w) and $\Omega_i(u, v, w)$ is the solid angle subtended by the photo-cathode of the i-th PMT. In order to minimize the effect of the shower fluctuation, the fit is done iteratively.

3.1.3 Energy Reconstruction

The reconstruction of the gamma ray energy (E_γ) is based on the sum of the number of photons detected by PMTs. The weight of each PMT is corrected depending on its location, for example, the weight of the outer face PMTs is 2.6 times less than that on the inner face PMTs. Therefore the energy of the gamma ray is calculated as

$$E_\gamma = F(u,v,w) \times S(u,v,w) \times T(t) \times C \times \sum_i (N_{pho,i} \times W_i), \tag{3.4}$$

where $F(u,v,w)$ is a non-uniformity correction factor, $S(u,v,w)$ is a correction factor which depends on the solid angle, $T(t)$ is a correction factor of the light yield changing in time, C is the conversion factor from the number of photons to energy, W_i is the constant weight and $N_{pho,i}$ is the number of photons defined by Eq. (3.2).

3.1.4 Time Reconstruction

We can calculate the time of the first interaction point from each PMT time ($t_{hit,i}$) if the position of gamma ray interaction point is determined. Then the hit time (t_γ) is reconstructed by combining each measurement by using following function,

$$\chi^2_{\text{time}} = \sum_i \frac{t_{hit,i} - t_\gamma}{\sigma_{t,i}(N_{pe})^2}, \tag{3.5}$$

where $\sigma_{t,i}(N_{pe})^2$ is the time resolution of each PMT as a function of the number of photo electrons. The gamma emmision time is reconstructed by minimizing the χ^2_{time} in Eq. (3.5) and subtracting the time-of-flight between the vertex reconstructed by fitting of positron track and the reconstructed conversion point in the LXe detector.

3.1.5 Pileup Identification

At 3×10^7 μ^+/s beam rate, around 15% of MEG trigger events suffer from pileup. Therefore, it is important to recognize and unfold pileup events in such a high rate environment. In order to identify the pileup events, we apply three different methods.

First one is called "pileup elimination", which searches for the peaks by using the light yield distribution in each event. If the second peak is found by this method and the position is far enough from the first peak which has larger reconstructed energy, the expected shape of the light yield distribution of the first peak is calculated except for pileup region, and then the expectation of outputs around pileup region is calculated based on the first reconstructed energy. The output photon distribution of the pileup gamma ray of the second peak is replaced with those expectation and the energy is reconstructed again with replaced outputs of PMTs. Figure 3.2 shows the example of the pileup event which is found by the pileup elimination in an event.

The second one, which is newly implemented in the analysis, is called "pileup unfolding". In this method, the peak search is done in the summed waveform from all PMTs as shown in Fig. 3.3. If multiple peaks are found in sum of waveforms,and the peak which have different time from that of the main pulse is identified as a peak due to the pileup event. Then the pulse, which is identified as a pileup, is subtracted by using template

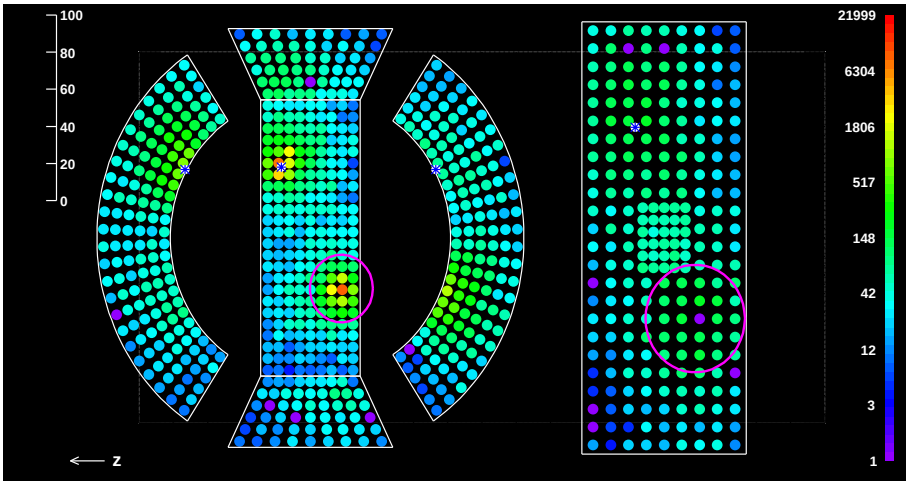

Figure 3.2: An example event with pileup gamma ray which is identified by using the distribution of the light yield. Magenta circles show the pileup cluster.

waveform unless they are close in time (< 5 ns) as shown in Fig. 3.4. By using this method, the pileup events, which are discarded in the previous analysis, are recovered by 7%.

If pileup events cannot be identified by both of two methods, the events, which have worse $\chi^2_{\rm time}$/NDF in the time reconstruction given by Eq. (3.5), are discarded as pileup events. Similarly, if the pileup event is only found in the light distribution but the subtracted energy is negative or larger than 10% of the total energy, the event is discarded.

3.1.6 Cosmic-ray Rejection

There is only a few percent contamination of the cosmic-ray events in the physics data taken by the MEG trigger. The cosmic-ray background events are not so crucial for the analysis, however they are reduced by applying the cosmic-ray rejection algorithm. In order to reject the cosmic-ray background events in the LXe detector, we use a topological cut because most of these events enter the detector from the outer face in contrast to those of gamma rays from the target. Therefore the ratio of the charges collected on the inner and the outer faces of the detector is smaller in cosmic-ray events than in gamma ray events. The reconstructed depth of cosmic ray events are significantly larger than those of signal gamma rays for the same reason. Figure 3.5 shows correlation between the charge ratio and the reconstructed depth. The selection criteria is defined in order to maximize cosmic-ray rejection efficiency while keeping a signal efficiency of 99%. The cut discards 56% of cosmic-ray events. The combined analysis efficiency of the cosmic-ray rejection and the pileup cut is 97%.

3.2 Positron Reconstruction

As we use the spectrometer in order to measure the momentum of positrons, the trajectory of positrons should be reconstructed inside the magnetic field. The equation of motion

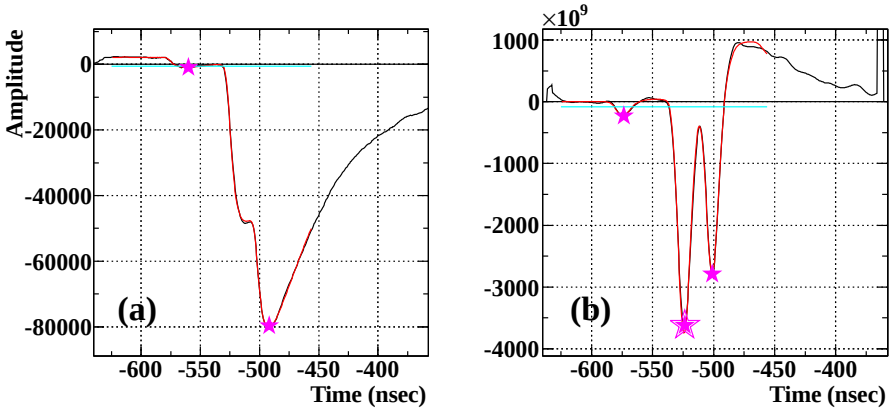

Figure 3.3: An event with pileup which identified by the peak search. Left plot shows the normal waveform after moving-average and right plot shows the differential one. Magenta stars show the found peaks.

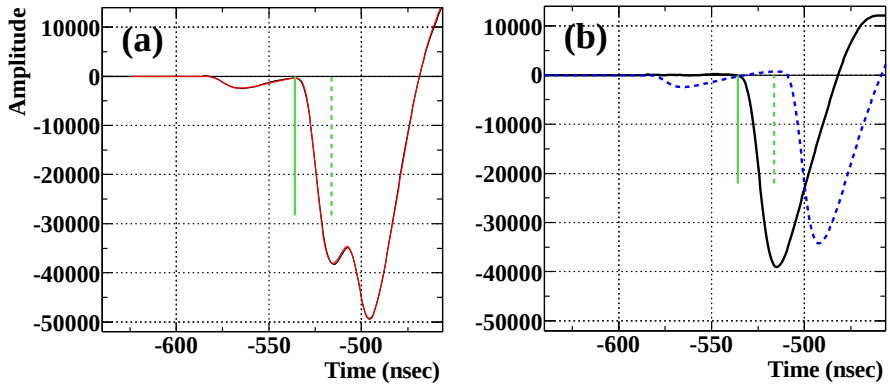

Figure 3.4: An waveform as same event as shown in Fig. 3.3 before (left) and after (right) applying the pileup elimination.

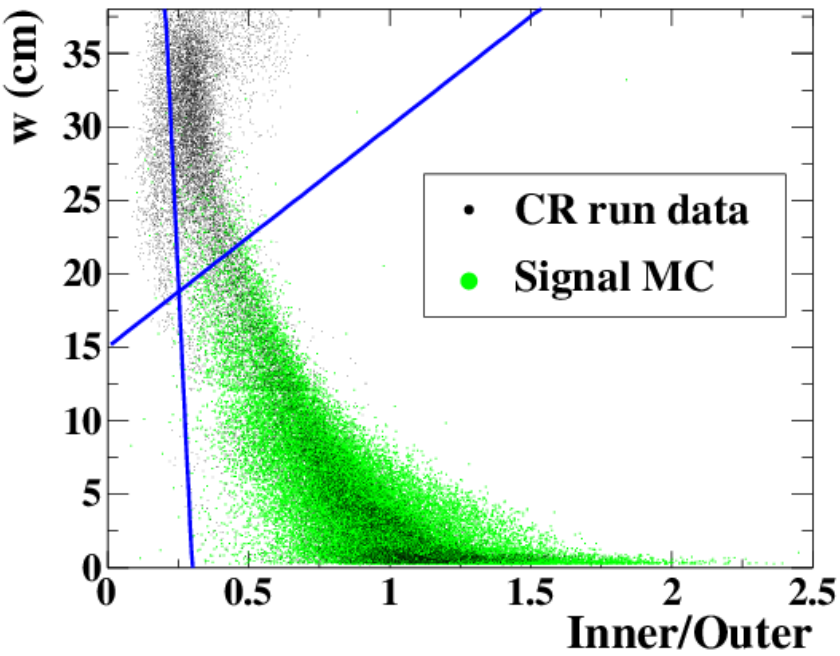

Figure 3.5: Two dimensional scatter plot of the charge ratio on the inner/outer faces vs the gamma ray interaction depth. Black points show the data from cosmic ray runs, and green ones shows the signal Monte Carlo events. The two blue lines show the selection criteria for the cosmic ray rejection.

of charged particles in the magnetic field can be written as

$$\frac{d\boldsymbol{p}}{dt} = q\boldsymbol{v} \times \boldsymbol{B}. \tag{3.6}$$

where $\boldsymbol{p}$ is momentum vector, $\boldsymbol{v}$ is velocity vector and $\boldsymbol{B}$ is vector of the magnetic field. The differential of this equation can be written as

$$\frac{d}{dz}\begin{pmatrix} z \\ x \\ y \\ x' \\ y' \\ \rho \end{pmatrix} = \begin{pmatrix} 1 \\ x' \\ y' \\ \rho\sqrt{1+x'^2+y'^2}[(\boldsymbol{r}' \times \boldsymbol{B})_x - x'(\boldsymbol{r}' \times \boldsymbol{B})_z] \\ \rho\sqrt{1+x'^2+y'^2}[(\boldsymbol{r}' \times \boldsymbol{B})_y - y'(\boldsymbol{r}' \times \boldsymbol{B})_z] \\ \rho' \end{pmatrix}, \tag{3.7}$$

where prime represents the differential of variables on z and $\rho = q/p$. By using this equation, track of charged particles can be reconstructed from discrete points measured by the DCH. The track reconstruction of positrons is generally divided by four steps as follows:

1. Hit reconstruction from waveforms in each cell of drift chambers,
2. Cluster finding to reduce the accidental hits from all hits and make the track finding easier by using clusters.
3. Track finding from clusters.
4. Track fitting from found track candidates.

Details of each step is described below.

3.2.1 Hit Reconstruction

The first important step for the track reconstruction is to measure the position of each hit in the best precision. As we use the drift chamber for the tracking device, the position along the wire (z) and the drift distance between the hit and the wire are the measured variables [51]. In order to do that, we analyze six waveforms from each cell of the drift chamber as shown in Fig. 3.6. In the z measurement, the vernier method is used as already mentioned. In this method, charge from an anode wire and cathode foils are combined to get better resolution than that reconstructed by only using charges from the anode wire. The drift distance is calculated from the drift time of ionized electrons.

3.2.1.1 Z Position

The charge ratio of anode wire ϵ_a is defined by using charge from upstream wire end (Q_U) and one from downstream (Q_D) as:

$$\epsilon_a \equiv \frac{Q_U - Q_D}{Q_U + Q_D}. \tag{3.8}$$

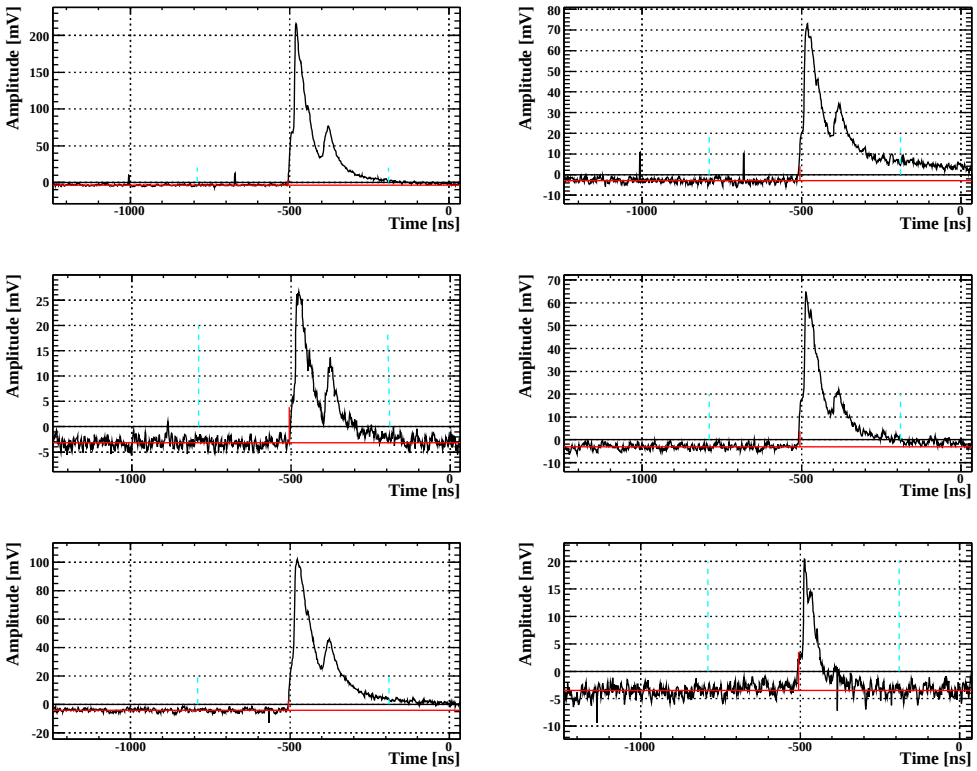

Figure 3.6: Example of waveforms in one cell in an event. Top two waveforms are from both ends of the anode wire, and others are from each side of cathodes. Red horizontal lines show the calculated baseline of each waveform. Red vertical lines at the left edge of each peak show calculated hit timing.

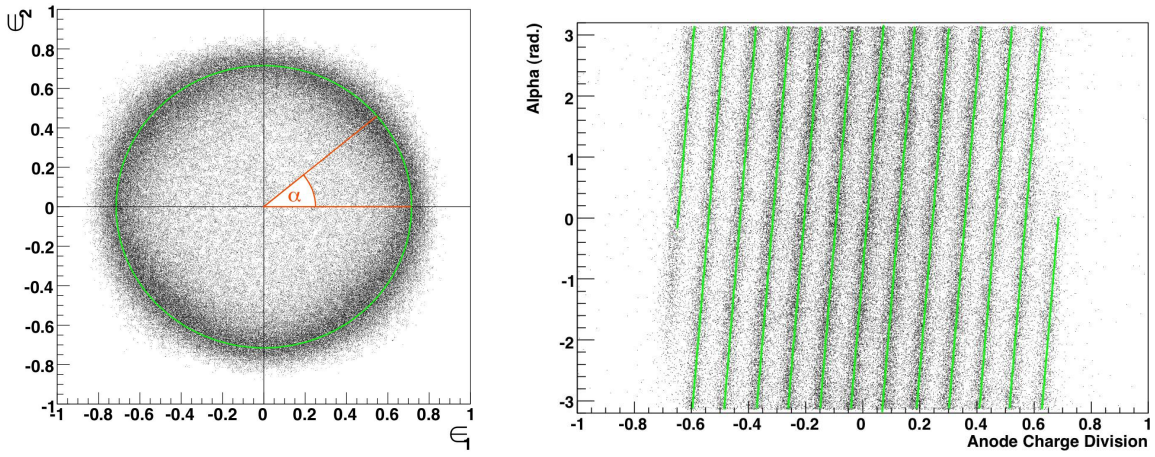

(a) Plot of the vernier circle calculated by charge ratio between each vernier pad.

(b) Calculated α from the vernier circle vs z position, which is normalized with the wire length, reconstructed by the anode.

Figure 3.7: Correlation between the vernier circle and z_a.

Then the reconstructed z position from an anode wire z_a can be written as:

$$z_a = \left(\frac{L}{2} + \frac{Z}{\rho}\right) \cdot \epsilon_a. \tag{3.9}$$

where L is the length of the anode wire, Z is input impedance and ρ represents the resistivity of the wire. Since the resolution of the z measurement by using anode charge is only $\sim$1 cm, the vernier method is essential to get the resolution of single hit z measurement down to $\mathcal{O}(100)$ μm. In the vernier method, the z position is given by

$$z = l \cdot \left(\frac{\alpha}{2\pi} + i - \frac{n}{2}\right), \tag{3.10}$$

where l is the length of one vernier period, which corresponds to 5 cm, n is the number of vernier patterns, and i is the vernier turn from downstream side. Here α is defined as

$$\alpha = \tan^{-1}\left(\frac{\epsilon_2}{\epsilon_1}\right), \tag{3.11}$$

where ϵ_1 and ϵ_2 are charge ratios measured by using inner and outer vernier pads respectively in the same way as Eq. (3.8). As shown in Fig. 3.7(b), i can be determined by comparing α and z_a.

3.2.1.2 Drift Distance

The drift distance of ionized electrons is calculated from the drift time which is determined from the waveform of the anode wire. In the drift chamber waveform analysis, the peak search is done in the waveform from each wire end. Then the time where the peak crosses the threshold which determined by the RMS of pedestal is defined as a hit time as shown in Fig. 3.6. The hit time is translated to the drift time by subtracting the time offset from

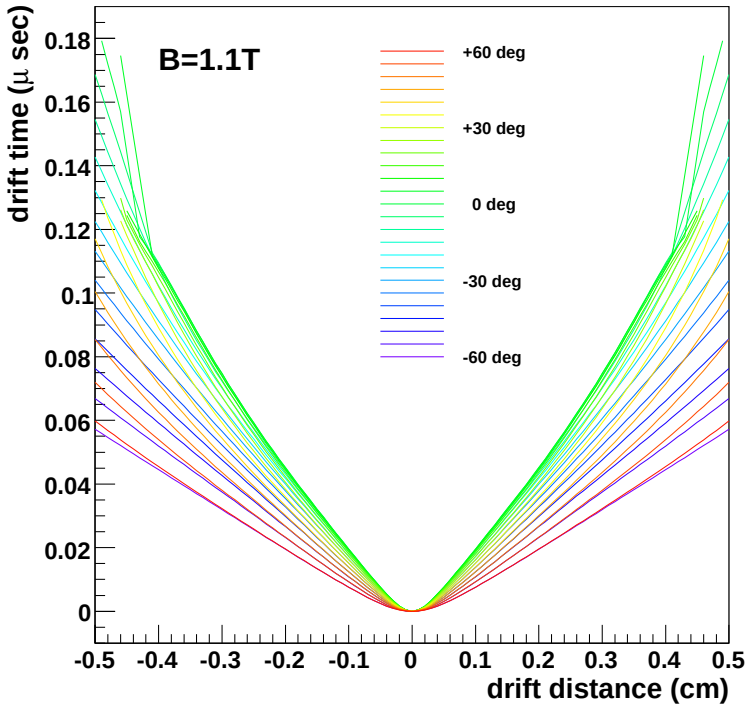

Figure 3.8: Relation between distance from anode wire and hit timing calculated by using the `Garfield` simulation.

cables, electronics and the distance between the hit position and the end of anode wires. Then the drift distance is calculated by using the drift time. Figure 3.8 shows drift time as a function of drift distance for each magnetic field strength. Once the positron track is reconstructed from selected hits with success to propagate to the timing counters, each hit time is refined by using corresponding impact time measured by using the TC. Then the calculation of the drift distance is repeated by using refined drift time.

3.2.1.3 Offline Noise Reduction

Since the z position is reconstructed from the charges calculated by using waveforms of anode wires and cathode pads, the resolution of the z measurement strongly depends on the signal-to-noise ratio of the charge measurement. The performance of the positron measurements can therefore be improved by using the offline noise reduction. At the beginning of 2011 run, strong noise components are observed (see Fig. 3.9). Although almost all periodical and strong noise components disappeared after hardware investigations (see Fig. 3.10), physics data corresponding to approximately a month was affected by the large noise.

We therefore developed the offline noise reduction. It was found that the noise reduction improves the performance in other run periods in 2009–2011 as well and we applied it to all data. Figure 3.11 shows accumulated power spectrum taken in a 2011 noisy run. Large periodical noise components can be seen around 14 MHz and around 40 MHz. Noise components around 40 MHz come from the timing counter APD system and were

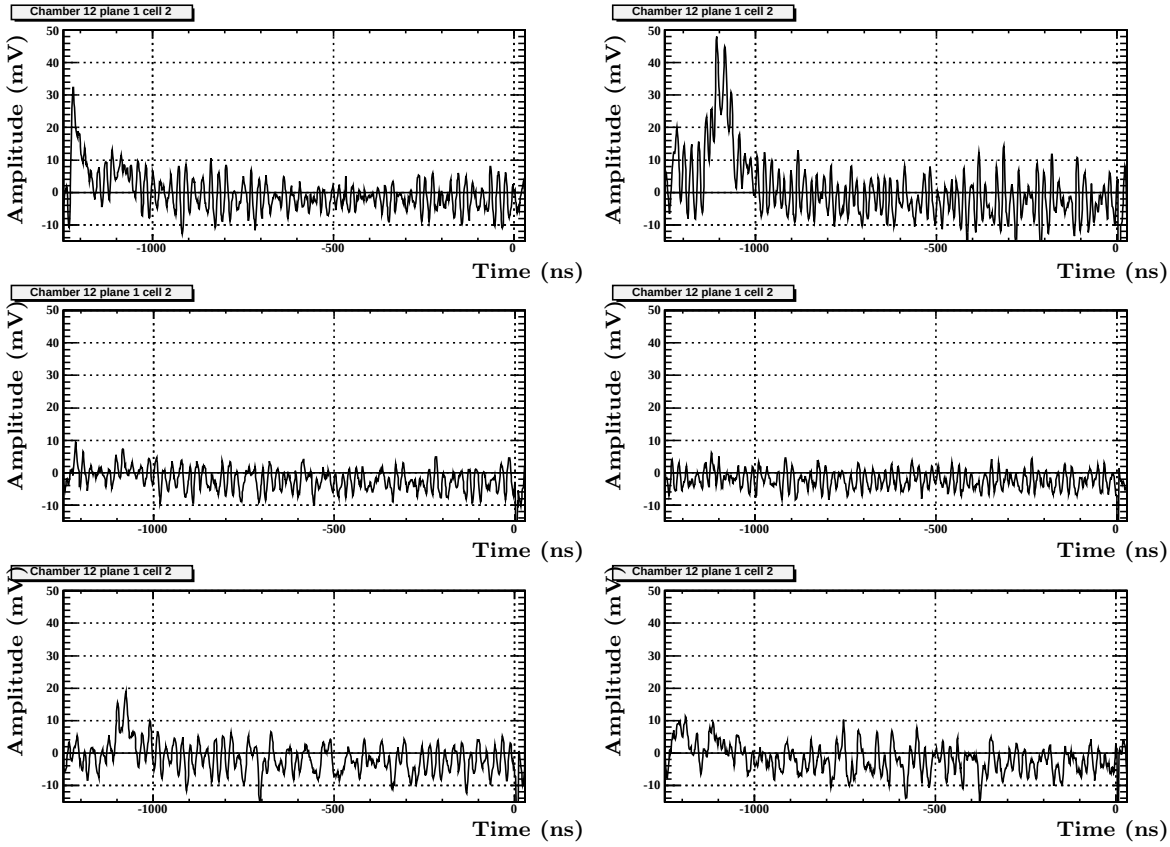

Figure 3.9: Example of DCH waveforms in a cell which taken in the 2011 noisy run period.

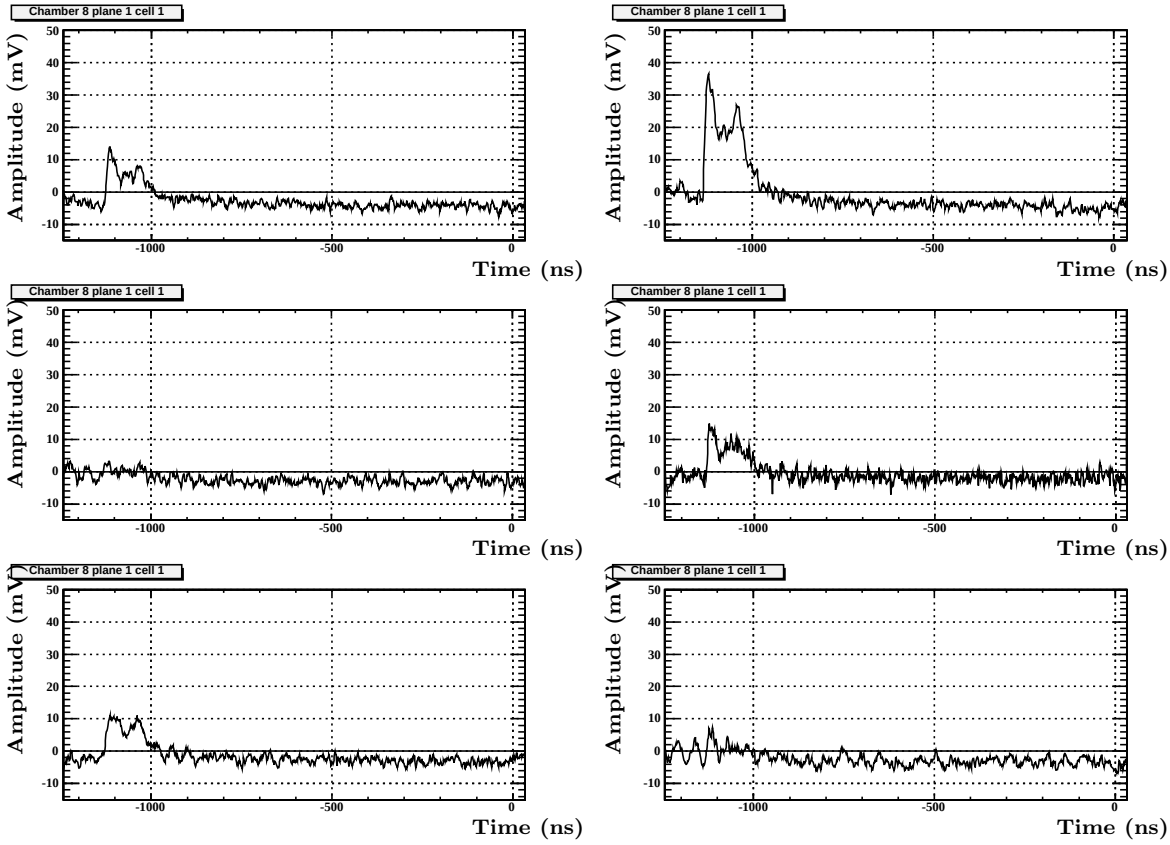

Figure 3.10: Example of DCH waveforms taken after hardware investigations.

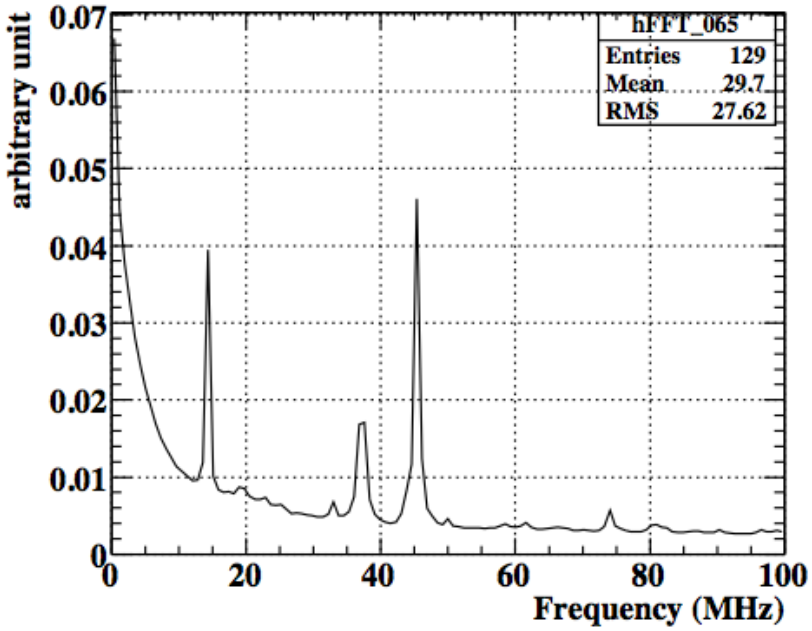

Figure 3.11: Power spectrum of accumulated DCH waveforms taken in the 2011 noisy run period.

suppressed after initializing the system. The 14 MHz component is related to the HV distributors for DCH and was reduced by replacing the HV distributors in 2011.

There are 2-dimensions called imaginary part and real part in the frequency domain (f_j) as:

$$f_j = \Re(f_j) + i \cdot \Im(f_j) \tag{3.12}$$

where i is an imaginary unit and the phase of component j can be calculated by $\Re(f_j)$ and $\Im(f_j)$. The reduction is done for components above 20 MHz and around 14 MHz component. The procedure of the noise reduction is as follows:

1. do the FFT for waveforms in the DCH cells in which hits are found in both wire ends,
2. suppress both $\Re(f_j)$ and $\Im(f_j)$ around a frequency of 14 MHz region by a factor of 10^{10},
3. suppress both $\Re(f_j)$ and $\Im(f_j)$ which have larger amplitude than 0.1 in the power spectrum above 20 MHz region by a factor of 10^{10},
4. do the inverse FFT.

This means that the FFT filtering works as an offline low pass filter. The FFT is done for approximately 120 ns narrower time window than the analysis window to make analysis faster. As shown in Fig. 3.12 (a), waveform after the noise reduction shows less noise and the pulse shape becomes smoother than that before filtering. In 2011 noisy run, the RMS of pedestal is reduced from 2.4 mV to 1.2 mV owing to the noise reduction.

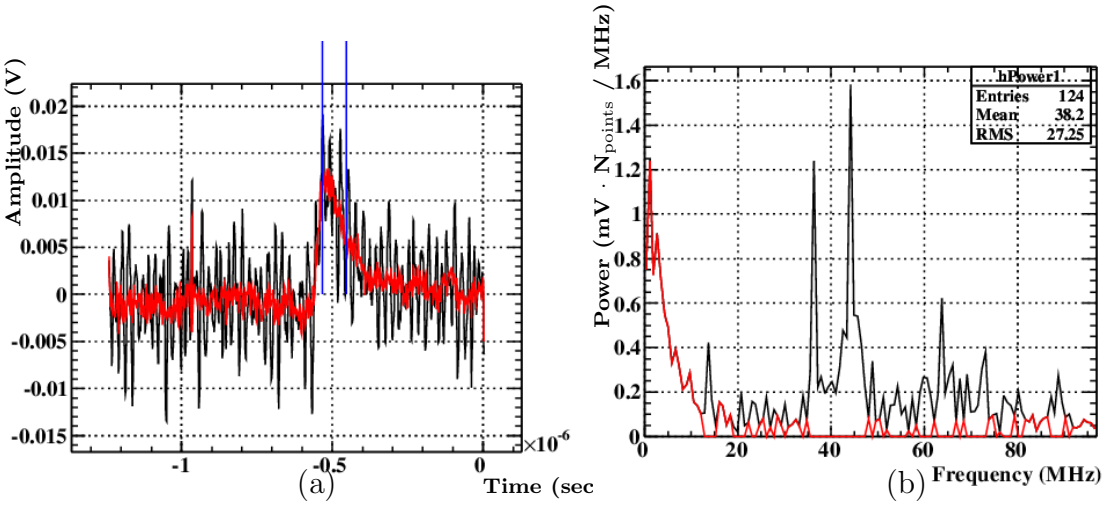

Figure 3.12: Raw DCH waveform (black solid line) and after the filtering (red solid line) in noisy run (a). The charge integration is done for the area between 2 blue solid lines. (b) is the power spectrum of waveform (a) before/after filtering (black/red).

The performance improvements are observed in data taken in 2009 and 2010 as well (See Sec. 5.3.3.1). Therefore the offline noise reduction is applied for all the data taken in 2009, 2010 and 2011. The detailed performance improvements due to the offline noise reduction are written in Sec. 5.3.3.1.

3.2.2 Cluster Finding

Since reconstructed hits include a lot of accidental hits which come from pileup events or are not related to positrons, for example from delta rays or gamma rays, a cluster finding algorithm is applied to choose the hits belonging to the track of positrons effectively. In the cluster finding, neighboring hits in the same chamber module are combined as the single cluster by using following criteria:

- **Hits in same plane** : $\Delta z < 0.2$ cm $+ 0.02 \cdot z_1$ cm, two hits in neighboring cells.
- **Hits in different plane** : $\Delta z < 0.6$ cm $+ 0.04 \cdot z_1$ cm, two hits within one skipped cells.

3.2.3 Track Finding

After the cluster finding, the seeds of the positron tracks are searched for by connecting the neighboring clusters starting from the hit found in the largest R position in order to select the clusters belonging to positron tracks with high enough momentum around 50 MeV. Since the absolute z positions of positrons increase according to the increasing of the DCH module index, track finding algorithm is given by the selection criteria as follows:

$$\begin{aligned} |z_{i+1} - z_i| &< a \cdot |z_i| + b, \\ |r_{i+1} - r_i| &< \Delta r_{\max}, \\ \text{where, } a &= 0.2,\ b = 2 \text{ cm},\ \Delta r_{\max} = 1 \text{ cm}. \end{aligned} \tag{3.13}$$

In the track finding, a circle fitting is done at the same time and the result of the fitting is used as initial information in the track fitting.

3.2.4 Track Fitting

The track fitting is performed for each track candidate found by the track finding. The algorithm of the fitting is based on a Kalman filter technique. It is totally revised in the new analysis and is described in detail in this section.

3.2.4.1 Kalman Filter

In order to reconstruct the trajectories of charged particles precisely, we need to get the best estimate at any measuring points. Here the state vector and the position vector at i-th measuring point are defined as $\boldsymbol{s}_i$ and $\boldsymbol{m}_i$ respectively. If there are no random fluctuation effects such as a Multiple coulomb Scattering (MS), an i-th state vector can be calculated by a function as:

$$\begin{aligned} \boldsymbol{s}_i &= \boldsymbol{f}(\boldsymbol{s}_{i-1}), \\ \boldsymbol{m}_i &= \boldsymbol{h}(\boldsymbol{s}_i), \end{aligned} \tag{3.14}$$

where the $\boldsymbol{f}$ is the function of track modeling and the $\boldsymbol{h}$ is the function to convert from global coordinates to local coordinates of detectors. On the other hand, fluctuation effects should be included in the propagation of particles inside materials. For this reason, the fitting function becomes more complex. Since the Kalman filter was developed as a linear estimator for the state of a dynamic system in presence of noise contributions [52], this technique is suitable to reconstruct the track of particles with random fluctuations, such as the multiple scattering effects, and it is recently used in many particle experiments [53]. Therefore, we adopted this technique for the base of the track fitting of positrons.

From here, a basic procedure of the Kalman filter technique is introduced. In the Kalman filter method, $D \times D$ matrix T (called "transport matrix") and $M \times D$ matrix which are Jacobians of the $\boldsymbol{f}$ and $\boldsymbol{h}$ functions are introduced. Here D is the number of parameters of the state vectors and M is the number of measured parameters at each point. Then Eq. (3.14) can be modified to the linear approximation as

$$\boldsymbol{s}_i = \boldsymbol{s}_{i,0} + T_{i-1}((\boldsymbol{s}_{i-1} - \boldsymbol{s}_{i-1,0}), \tag{3.15}$$

$$\boldsymbol{h}_i = \boldsymbol{h}_{i,0} + H_i(\boldsymbol{s}_i - \boldsymbol{s}_{i,0}). \tag{3.16}$$

where $\boldsymbol{s}_{i-1,0}$ is a reference starting state and $\boldsymbol{s}_{i,0} = f(\boldsymbol{s}_{i-1,0})$. In this scheme, the contribution from the noise in the propagation (MS and energy loss in tracking applications) can be introduced as a covariance matrix C_{i-1}^{i-1}. By using the covariance matrix, the "predicted" i-th state vector $\boldsymbol{s}_i^{i-1}$ and the i-th covariance matrix are given by

$$\begin{aligned} \boldsymbol{s}_i^{i-1} &= \boldsymbol{f}(\boldsymbol{s}_{i-1}^{i-1}), \\ C_i^{i-1} &= T_{i-1} C_{i-1}^{i-1} T_{i-1}^T + Q_i, \end{aligned} \tag{3.17}$$

where Q_i represents the contribution from the noise and $\boldsymbol{s}_{i-1}^{i-1}$ is estimated state vector extracted from the measurements $\boldsymbol{m}_0 ... \boldsymbol{m}_{i-1}$ (this step is called "**Prediction**" in Kalman

filter). Then a parameter written as χ^2 which should be minimized in the fitting is given by

$$\chi^2 = \boldsymbol{s}_i^T C_i^{i-1} \boldsymbol{s}_i + (\boldsymbol{m}_i - \boldsymbol{h}_i(\boldsymbol{s}_i))^T V_i \boldsymbol{h}_i(\boldsymbol{s}_i)), \tag{3.18}$$

where V_i are the $M \times M$ correlation matrices of the single measurements. The minimization is done by the following formulas:

$$\begin{aligned} K_i &= C_i^{i-1} H_i^T (H_i C_i^{i-1} H_i^T + V_i)^{-1}, \\ \boldsymbol{s}_i &= \boldsymbol{s}_i^{i-1} + K_i(\boldsymbol{m}_i - \boldsymbol{h}_{i,0}), \\ C_i^i &= (1 - K_i H_i) C_i^{i-1}, \end{aligned} \tag{3.19}$$

where the $D \times M$ matrix K_i is called "Kalman gain". Once the state vector $\boldsymbol{s}_i$ is updated by Eq. (3.19), $\boldsymbol{s}_i$ and C_i^i are including the information carried by the measurement points up to $\boldsymbol{m}_i$ and this process is called "**Filtering**" in Kalman filter. After repeating "Prediction" and "Filtering" from 0-th measurement point up to N-th one, same procedure can be repeated starting from N-th measurement point and going backward. The best estimate at the i-th measurement point is obtained by averaging the results of the forward and backward filter and this final step is called "**Smoothing**".

In practice, the state vector is defined as $\boldsymbol{s}_i = (x, y, z, p_x, p_y, p_z, t)_i$ where t is time in the track fitting and it can also be translated to the coordinate which is used in the MEG experiment as $(x, y, z, p, \theta, \phi)$ where p is absolute value of the positron momentum. After the fitting for hits belonging to the found track candidate is done, both ends of the positron trajectory are prolongated toward the target and the timing counter. The propagation is stopped when it reaches the middle plane of the target. Figure 3.13 shows the example of the positron trajectory reconstructed by the track fitting.

3.2.4.2 New Track Fitting

In order to improve the precision of the track fitting, the algorithm of the fitting is revised in the new analysis. In the new track fitting, which we call "*new Kalman*", uncertainties of each single hit measurement are regarded as functions of the characteristics of each hit. The function of the z uncertainty depends on the charge over the noise ratio (Q/N) and the track angle θ with respect to the wire. In contrast, the r uncertainty is defined as a constant double Gaussian, because no obvious dependence is observed in data. The definition of the local coordinate and the measurement points are modified as well. In the previous algorithm (called "old Kalman"), the reconstructed cluster position by combining hits found in both planes in a module is used as a single measurement point. In case of the new Kalman, each single hit is regarded as an independent measurement point in new Kalman. Accordingly, a local coordinate is defined at each state vector inside each cell of the drift chamber as (d, z). Here d represents the distance between an anode wire to the hit position of the positron track with a point of closest approach, namely, d corresponds to the drift distance of each hit, and z represents the position along the anode wire, as the same in the global coordinate. In the old Kalman, the position of each cluster, which is reconstructed in each module, is used with the global coordinate. Figure 3.14 shows difference of the single state of a fitted positron-track defined in new/old Kalman.

The calculation method of energy depositions inside the detector is also modified. In the new Kalman, the fitting algorithm based on `GEANE` [54] is used to calculate the interactions of particles inside the detectors, which is already defined in `MEGMC` (See Sec. 2.5.1).

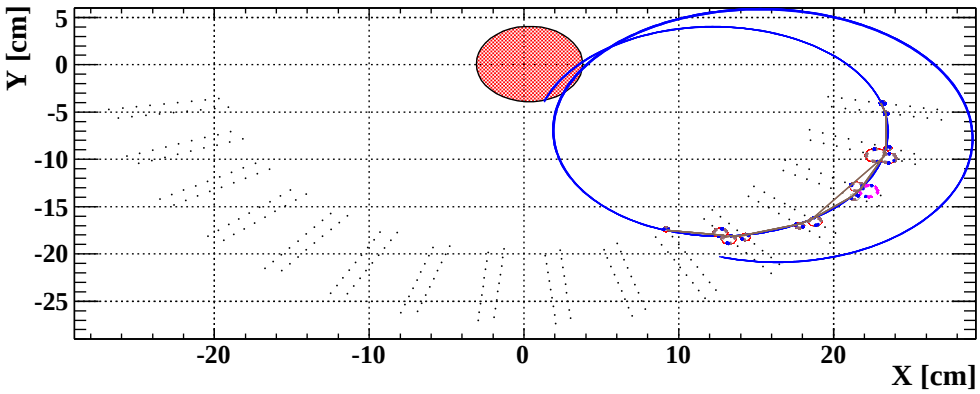

(a) A sample of fitted track shown as blue line in X-Y view.

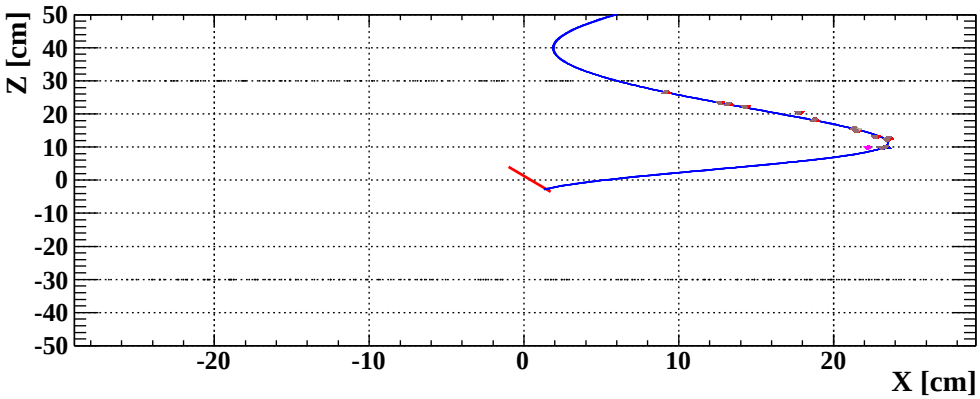

(b) A sample of fitted track shown as blue line in X-Z view.

Figure 3.13: A positron trajectory fitted by using the previous track fitting in an event.

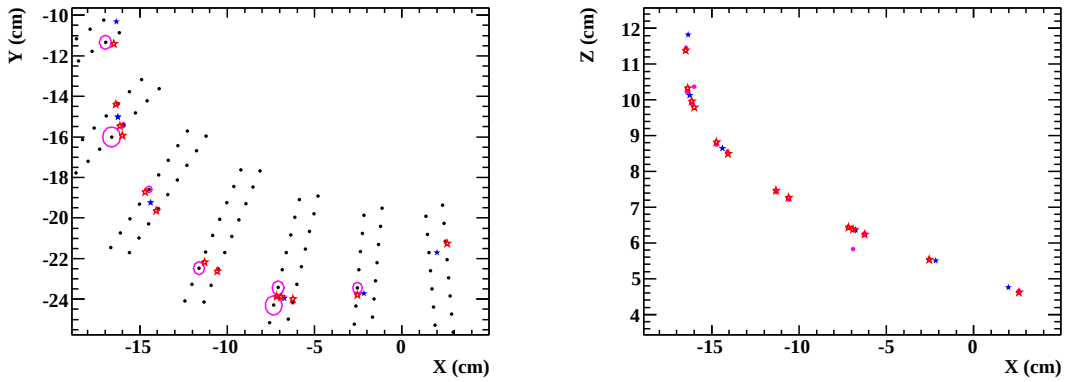

Figure 3.14: Differences of reconstructed hits by using new/old Kalman in X-Y view (left) and X-Z view (right). Red stars show the hits reconstructed by using new Kalman and blue ones show those reconstructed by using old Kalman. Magenta circles in the left plot shows measured hits belonging to the reconstructed track and the radius of each circle shows the measured drift distance. Black points shown in the left plot represent the position of wires.

GEANE also provides the error propagation during the track fitting by using Kalman filter technique.

In the analysis, we also use the previous fitting algorithm (called "old Kalman") for the compatibility check.

3.2.5 Time Reconstruction

The positron time is measured by using 15 scintillating bars as already mentioned in Sec. 2.3.3. If a positron enters a TC bar at time $t_{\rm TC}$, the measured time of the inner and outer PMTs of each bar are read as;

$$\begin{aligned} t_{\rm in} &= t_{\rm TC} + b_{\rm in} + TW_{\rm in} + \frac{L/2 + z}{v_{\rm eff}}, \\ t_{\rm out} &= t_{\rm TC} + b_{\rm out} + TW_{\rm out} + \frac{L/2 - z}{v_{\rm eff}} \end{aligned} \tag{3.20}$$

where $b_{\rm in,out}$ are time offsets, $TW_{\rm in,out}$ are contributions from Time Walk effect, $v_{\rm eff}$ is the effective velocity of light in the bar, L is the bar length and $z_{\rm bar}$ is the impact point along the main axis of the bar and its starting point is in the middle of the bar. From Eq (3.20), the impact time of positrons at TC ($t_{\rm TC}$) is calculated as;

$$t_{\rm TC} = \frac{t_{\rm in} + t_{\rm out}}{2} - \frac{b_{\rm in} + b_{\rm out}}{2} - \frac{TW_{\rm in} + TW_{\rm out}}{2} - \frac{L}{2v_{\rm eff}}, \tag{3.21}$$

which is independent on the positron impact point ($z_{\rm bar}$). Then the emission time of positrons ($t_{\rm e}$) at the target is given by

$$t_{\rm e} = t_{\rm TC} - t_{\rm TOF}, \tag{3.22}$$

where t_{TOF} represents the time of flight of the positron track from the target to the TC determined by using the reconstructed track length (L_{track}) as

$$t_{\mathrm{TOF}} = L_{\mathrm{track}}/c, \tag{3.23}$$

where c is the speed of light.

3.2.6 Impact Point in Timing Counter

The positron impact point can be calculated from two different ways. First one called charge ratio method is using the charge ratio of the charges at the inner and outer PMTs;

$$\begin{aligned} Q_{\mathrm{in}} &= EG_{\mathrm{in}}e^{-\frac{L/2+z}{\Lambda_{\mathrm{eff}}}}, \\ Q_{\mathrm{out}} &= EG_{\mathrm{out}}e^{-\frac{L/2-z}{\Lambda_{\mathrm{eff}}}}, \end{aligned} \tag{3.24}$$

where E is the energy deposit inside the bar, $G_{\mathrm{in,out}}$ takes into account the contributions from the scintillator yield, Q.E. of the PMT and the gain, and Λ_{eff} is the effective attenuation length of the bar. From Eq. (3.24), z_{bar} is given by

$$z_{\mathrm{bar}} = \frac{\Lambda_{\mathrm{eff}}}{2}\left(\ln\frac{Q_{\mathrm{out}}}{Q_{\mathrm{in}}} - \ln\frac{G_{\mathrm{out}}}{G_{\mathrm{in}}}\right). \tag{3.25}$$

The impact point also can be calculated by using $t_{\mathrm{in,out}}$ from Eq. (3.20) as:

$$z_{\mathrm{bar}} = \frac{v_{\mathrm{eff}}}{2} \times (t_{\mathrm{in}} - t_{\mathrm{out}} - (b_{\mathrm{in}} - b_{\mathrm{out}}) - (TW_{\mathrm{in}} - TW_{\mathrm{out}})). \tag{3.26}$$

The former is used for the direction match algorithm in the trigger since it can be calculated fast, while the latter is used for the offline analysis since the resolution is better than that by using the former algorithm.

3.2.6.1 DC-TC Matching

The new tracking code enables to estimate the matching quality between the reconstructed track by the drift chambers and the hit position in the timing counter bars during the fitting. In the new Kalman, the reconstructed track is propagated to the timing counter volume. Then the DC-TC matching quality is classified into the following four categories:

- If the track is successfully propagated inside the volume where the timing counter bar is defined in GEANT and the difference between z position of reconstructed track and z_{TC} (ΔZ_{TC}) is less than 12 cm, zero is assigned to a $TCMatchingQuality$,
- If the matching above fails, a larger bar volume which also includes PMTs is used with same threshold for Δz_{TC}. If this matching succeeds, one is assigned to a $TCMatchingQuality$,
- If both methods above fail, the track is propagated to the point approaching closest to the bar axis. If the radial distance between the track and the hit in TC satisfies $|\Delta R_{TC} - R_{\mathrm{offset}}| < 5$ cm, two is assigned to a $TCMatchingQuality$.

- If all aboves are not succeeded, the larger value (999) is assigned to a $TCMatchingQuality$ as it is the track without the matched TC,

If positrons reconstructed by DCH satisfy at least one of the above three conditions, the drift time of positrons at each hit point is refined by using t_{TOF} at that point.

3.2.6.2 Event-by-Event Uncertainties

Since the new Kalman enables more precise calculation of the error propagation inside the materials of each detector, the fitting error on each variable can be considered as event-by-event uncertainty, which are called "per-error", of the track fitting. Measured variables at the positron side are as follows:

- E_{e} : momentum on the target.
- ϕ_{e} : ϕ emission angle on the target.
- θ_{e} : θ emission angle on the target.
- y_{e} : y position on the target plane.
- z_{e} : z position on the target plane.
- t_{e} : timing at the timing counter.

Except for t_{e}, per-errors of all variables associated to the positron-tracks are determined by the diagonal components of the calculated error matrix at the target. We define the per-errors as:

$$\boldsymbol{\sigma'} = (\sigma'_{E_{\mathrm{e}}}, \sigma'_{\phi_{\mathrm{e}}}, \sigma'_{\theta_{\mathrm{e}}}, \sigma'_{y_{\mathrm{e}}}, \sigma'_{z_{\mathrm{e}}}), \tag{3.27}$$

where 'σ'_x' represents the uncertainty of parameter 'x'. Even though same parameters can be extracted in the previous fitting as well, there were inconsistency between fitted uncertainties and measured resolutions. In the new Kalman, we observed more reliable uncertainties extracted from the error matrix. We therefore decide to use the per-errors in the analysis as an additional parameters which can provide the precise tracking quality on an event-by-event basis.

Chapter 4

Calibrations

In order to improve the performance of each sub-detector, many calibration methods are developed in MEG. The detail of each method is described in this chapter.

4.1 LXe Monitoring and Calibration Methods

It is important to monitor and calibrate the LXe detector to check the stability for the long term data taking. For these purposes, several methods are performed as shown in Table 4.1.

4.1.1 Charge Exchange Calibration

To define the energy scale of the LXe detector, the data using pion Charge EXchange (CEX:$\pi^- p \to \pi^0 n$) interaction are taken by using a Liquid-Hydrogen (LH_2) target instead of the target which is used for the MEG data taking. The neutral pion after the CEX interaction has 28 MeV/c momentum and immediately decays into two gamma rays. These two gamma rays are emitted back-to-back in the π^0 rest frame with an energy of

$$E^*_\gamma = \frac{m_{\pi^0}}{2} \simeq 67.5 \text{ MeV}.$$

In the laboratory frame, the gamma-ray energies are determined by

$$E_{\gamma_{1,2}} = \gamma \frac{m_{\pi^0}}{2} (1 \pm \beta \cos\theta^*) \tag{4.1}$$

Table 4.1: Several calibration and monitoring methods prepared for the LXe detector.

Name	Purpose	Period
Charge Exchange	Energy Scale Calibration	1/year
Cockcroft-Walton	Light Yield Monitoring	1/week
Neutron generator	Light Yield Monitoring	1/week
Cosmic Ray	Light Yield Monitoring	1/week
LED	Gain Monitoring	2/week
Alpha Source	Q.E. Monitoring	2/week

where β is the π^0 velocity and θ^* is the center-of-mass angle between the gamma ray and the π^0 direction. Therefore monochromatic 55 MeV and 83 MeV gamma rays are detectable by selecting back-to-back gamma rays with the BGO (NaI for 2009 and 2010 run) detector placed opposite to the LXe detector as shown in Fig 4.1(a). Figure 4.1(b) shows the correlations of gamma ray energies measured by using the BGO (NaI) detector and the LXe detector. Therefore the absolute energy scale factor of the LXe detector to convert the N_{pho} to the absolute energy is able to be extracted by using those 55 MeV and 83 MeV gamma ray events. The position-dependent energy resolution is also measured by the CEX calibration to construct the signal E_γ PDF. In the CEX runs, the time resolution of the LXe detector is also calculated by using the gamma ray which converted inside the lead converter placed in front of the plastic scintillator bars. Moreover, the

(a)

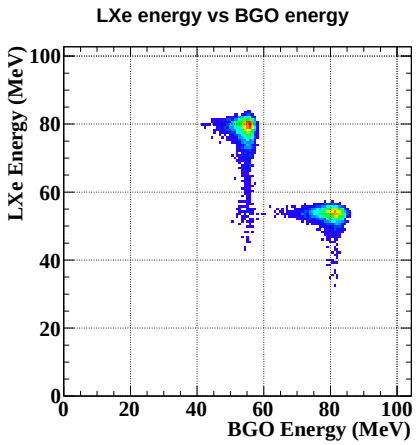

(b)

Figure 4.1: BGO (NaI) mover(a) and two dimensional plot of gamma ray energies measured by the LXe detector and the BGO detector(b).

CEX run is also used to evaluate the position resolution of the detector (See Sec. 5.1.2). It is the most important calibration run for the LXe detector since the absolute energy scale is determined by the CEX run. However, this calibration requires a replacement of the normal muon target with the dedicated LH_2 target and the beam setting must be changed. For this reason, the CEX calibrations are done only once per year. In order to monitor the detector stability and the variation of the energy scale to be corrected, other calibration methods which are written below, are performed more frequently.

4.1.2 Cockcroft-Walton

For monitoring the light yield stability and extracting the position dependent correction factor, calibration runs using a dedicated Cockcroft-Walton (CW) proton accelerator are performed once or twice per week during the MEG data taking. The CW accelerator

was installed in the downstream of the detector and the protons are delivered by a CW beamline. At the CW beamline, protons can be accelerated up to 1 MeV and they are transported to a lithium tetraborate ($Li_2B_4O_7$) nuclear target which is inserted into the COBRA center by an insertion system. In the target, 17.6 MeV gamma rays are produced from the reaction ${}^{11}_{5}\mathrm{Li(p,}\gamma){}^{8}_{4}\mathrm{Be}$. By using the 17.6 MeV gamma rays, we can monitor the light yield stability, correct the non-uniform detector response together with the CEX patch scan, and refine the Q.E. estimation by comparing the peak of α source events (See Sec. 4.1.6).

4.1.3 Neutron Generator

In this calibration, a 9.0-MeV gamma ray line which is generated from nickel ${}^{5}8\mathrm{Ni}(n, \gamma_{9.0}){}^{5}9\mathrm{Ni}$ by using a Neutron Generator. The CEX calibration and CW calibration cannot be done in the muon beam-on condition. In contrast with above two calibration methods, the neutron generator can be done in various beam conditions because it is unnecessary to modify the beamline setups. Therefore this calibration method is suitable for frequent light yield monitoring and was started to be used from 2010 MEG data taking.

4.1.4 Cosmic Ray

In order to check the light yield stability, cosmic-ray data are taken as a high energy source. Although the energies of cosmic-rays are not monochromatic, the landau peaks of cosmic-rays are used to monitor the light yield stability. The energy of the landau peak is around 150 MeV.

4.1.5 LED

The blue light LEDs are attached inside the LXe detector to calibrate the PMT gain (G) as stable light sources. Since the intensity of photons from LEDs is stable enough, G is given by

$$G = \frac{\overline{q}}{e \cdot \overline{N_{pe}}}, \tag{4.2}$$

where $\overline{q}$ is the average of charge, e represents the elementary charge and $\overline{N_{pe}}$ is the average number of photo-electrons in each PMT. Then the square deviation of observed charge (σ_q^2) is given by an equation,

$$\sigma_q^2 = (G^2 + \sigma_G^2) \cdot e^2 \cdot (\sigma_{pe}^2 + \sigma_{\mathrm{LED}}^2) + \sigma_0^2. \tag{4.3}$$

The deviation of the photoelectrons is given by $\sigma_{pe}^2 = \overline{N_{pe}}$ when the number of photoelectrons obeys Poisson distribution. Then the equation above becomes

$$\sigma_q^2 = (G^2 + \sigma_G^2) \times e^2 \times \overline{N_p e} + \sigma_0'^2 \tag{4.4}$$

$$= \frac{(G^2 + \sigma_G^2) \times e}{G} \times \overline{q} + \sigma_0'^2, \tag{4.5}$$

where σ_0' is a constant term and differs from a σ_0 because it contains σ_{LED} and the gain. Because σ_G^2 is small enough compared with G, the relation between σ_q^2 and $\overline{q}$ can be

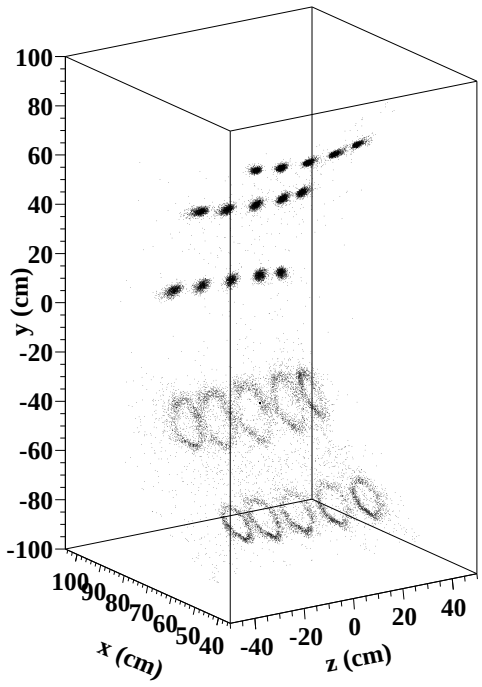

Figure 4.2: Reconstructed positions of 25 α sources inside the LXe detector. In this particular run, the half of the detector was filled with liquid xenon and the other part was filled with gaseous xenon.

regarded as linear. The light intensity can be changed in nine steps and it enables us to calculate the gain of each PMT.

The LED trigger is also included in the MEG physics run with the scaling factor in order to monitor the stability of the PMTs in the muon beam condition.

4.1.6 Alpha Source

The light source with a known intensity is required to evaluated the Q.E. of each PMT by using the following relation; $N_{pho} = N_{pe}/QE$. Therefore 25 ^{241}Am sources are attached and used to calculate the Q.E. of each PMT inside the LXe detector. Each ^{241}Am source emits the 5.5 MeV α particle with $\sim$ 1 kBq decay rate. Five α sources are mounted on a 100 μm gold-plated tungsten wire as point-like sources of scintillation light and five wires are positioned in a staggered pattern to optimize the range of angles and distances so that they are visible from the PMTs Figure 4.2 shows reconstructed positions of the α sources with the detector filled with liquid xenon and gaseous xenon. Since the mean free path of the α particle in liquid xenon is short, the reconstructed positions of α source events form the ring images due to the shadow of the wire from PMTs opposite to the emission direction of the α particle as shown in this figure. By applying a topological cut on the rings, the position of the corresponding α source can be identified. Q.E. of

each PMT is evaluated from the measured charge of α source events compared with those from simulation. In order to reduce the systematic uncertainties related to the α source positions and angles between sources and PMTs, the gamma ray from CW-Li peak events are used for the correction (See Sec. 4.1.2).

The peak of α source events is used for the light yield monitoring as well.

4.1.7 Light Yield History

By combining the results from calibration methods above and the time-dependence of the energy scale obtained by fitting the theoretical spectrum folded with the detector response function to the measured background spectrum (See Sec. 6.3.3.2), time-dependence of the light yield, which is mainly caused by the impurity of the liquid xenon, is determined and then it is corrected. Figure 4.3 show the light yield history of 2009–2011 data before and after the correction. The uncertainty of this correction is less than 0.2% for all the datasets.

4.2 Drift Chamber Calibrations

Since the drift chamber is a position sensitive detector, it is important to measure the positions of each module and wire to improve the position resolutions. In order to measure the position of the DCH, a laser tracker measurement, a Michel positron alignment, and a cosmic-ray alignment are performed. Relative gains and time offsets of all channels are also calibrated by using tracks of Michel positrons and cosmic-rays. An accuracy of the position measurement for positrons is achieved down to 1 mm for z measurement and down to a few hundred μm for r position reconstruction by those calibration methods. Here each calibration is described in detail.

4.2.1 Hit Z Calibration

The z reconstruction of the DCH is determined by charges from two anode ends and four cathode pads. Therefore the reconstructed results depend on the relative gain difference between both sides of pre-amplifiers. This is calibrated by reconstructed tracks of Michel positrons and cosmic-rays. The relative gain of anode signals is corrected by comparing z_a given by Eq. (3.9) and the charge ratios of the cathodes ends (ϵ_1 and ϵ_2 used in Eq. 3.11). Figure 4.4 shows the correlation between z_a and ϵ_1 with a fitting result using a sinusoidal function.

Gain corrections for cathode pads are done in the similar way by using the z positions of reconstructed tracks (z_{track}) instead of z_a. In this case, a vertical offset of the sinusoidal function indicates a relative gain difference between upstream and downstream cathode pads and the gain correction is done so that the offset becomes zero.

4.2.2 Hit Time Calibration

The time offset of each channel is calibrated by using the Michel positrons and cosmic-rays. In this calibration, we calculate the position of the leading edge of the pulse from tracks of positrons or those of cosmic-rays. After subtracting the time difference due to

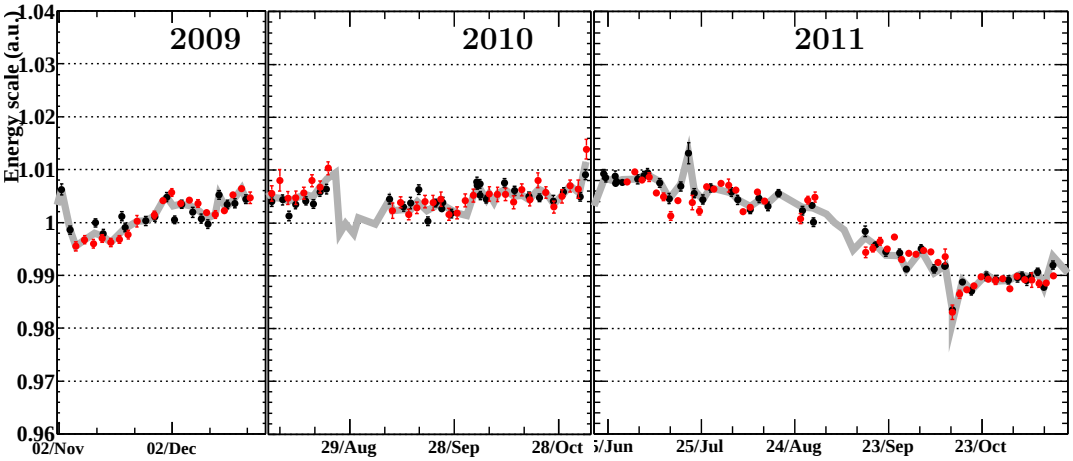

(a)

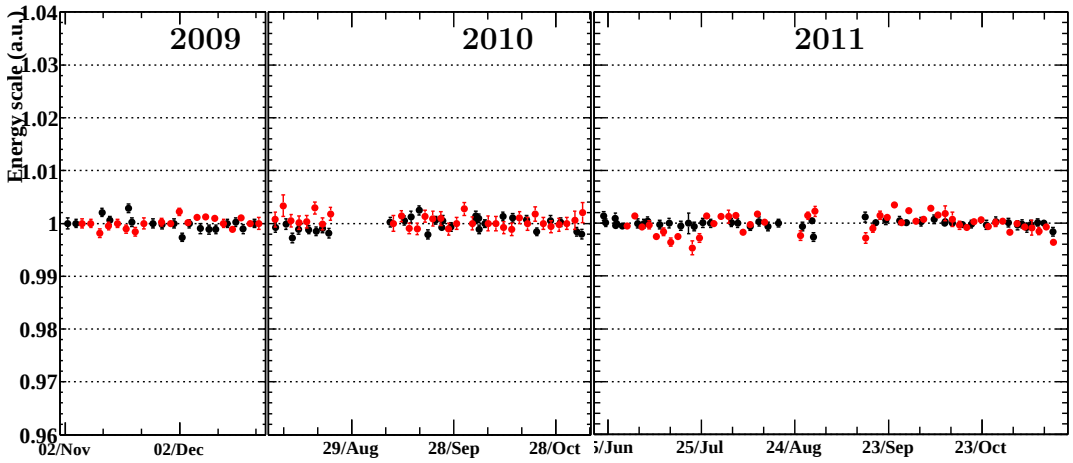

(b)

Figure 4.3: Upper plot shows the light yield history measured by using CW-Li peak (black) and background scale (red). To calibrate the light yield history, other possible sources (CEX 55 and 83 MeV gamma, 9 MeV gamma with neutron generator, cosmic-ray, and alpha source peak) are used. Combined history curve is also shown in this plot with a gray curve. Bottom plot shows same history after the correction by using the combined curve so that it becomes flat.

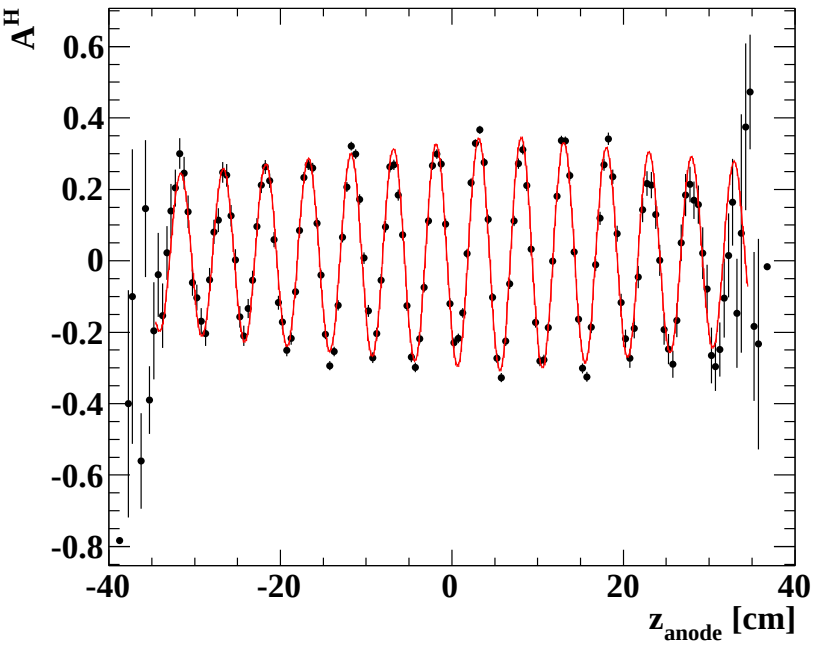

Figure 4.4: Correlation between z_a and the cathode vernier pad asymmetry (black markers), fitted by a sinusoidal function (red line).

the z position of each end, time offsets of both ends are corrected by using average time difference. Time offsets between different channels are also corrected by comparing the average time difference with same tracks which go through the different cells in an event.

4.3 Alignment

As already mentioned, the alignment for the position of each wire is essential to achieve the excellent precision of the track reconstruction. For the drift chamber alignment, we use three different methods. First one is an optical survey measurement and it is used as an initial input for other two software alignments. The alignment by using Michel positrons and cosmic-rays is performed based on the positions of drift chambers measured by the optical survey measurement.

4.3.1 Optical Survey

As an initial alignment for each DCH module, the optical survey is done before starting the MEG run in each year [55]. In 2009 and 2010, the survey measurements using cross-hairs and the theodolite were performed. The cross-hair markers are mounted on the all drift chamber modules both upstream and downstream side and the position of each marker is measured by the theodolite which is placed three different positions in order to measure the three dimensional position (x, y, z). At the same time, the position measurements for the target and the support structure are performed by using cross prints

Figure 4.5: Corner cubes mounted on the downstream side of the drift chambers.

as shown in Fig. 2.5(a) and the small pins, respectively. The accuracy of the position measurement using the theodolite is calculated to be 0.3 mm for x and y, and 0.5–2 mm for z. In 2011, a laser tracker system was newly introduced by using corner cube reflectors mounted at both ends of the top-side of each DCH module as shown in Fig. 4.5. Since the corner cubes are attached to both sides of each module, we can measure not only the position of the module, but also the angular displacement based on the shape of the drift chamber which is measured in the lab. The measurement uncertainty of the laser tracker itself can reach a several tens of μm and the total accuracy including the corner cube displacement is calculated to be 200 μm.

4.3.2 Cosmic Ray Alignment

The cosmic-ray tracks without the magnetic field can be regarding as the simple alignment tool because of their almost straight trajectories while the Michel positrons are bended by the magnetic field. Therefore the cosmic-ray data are taken for the purpose of the drift chamber alignment. In order to trigger the cosmic-ray events, which pass through the drift chambers, dedicated 10 cosmic-ray counters (CRC) are mounted on the outer wall of the COBRA magnet at the opposite side of the LXe detector as shown in Fig. 4.6. These counters are used for the time offset correction and the relative alignment as well (See Sec. 4.2.2 and Sec. 4.3.4.1, respectively).

The alignment procedure is to minimize the residuals of hit position of DCH modules with respect to straight muon tracks, according to the Millipede algorithm [56]. The result is checked by using a sample of Michel positrons which enter twice in the drift chamber volume so-called "two-turn event" in the magnetic field and the edge of Michel spectrum. After the cosmic-ray alignment, the accuracy for each coordinate becomes better than 150 μm.

4.3.3 Michel Alignment

The alignment result can be cross-checked by using the track of Michel positrons, which is called Michel alignment. In the Michel alignment, the measured position of each hit

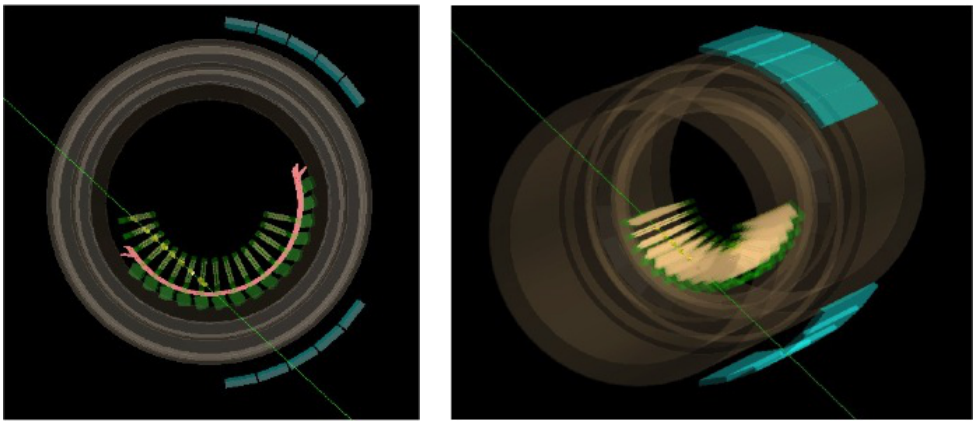

(a) X-Y view (b) Arbitrary view

Figure 4.6: 3D view of 10 cosmic-ray counter bars (shown in cyan). Green line shows a simulated cosmic-ray, which pass through both drift chambers and the cosmic-ray counter.

and the position reconstructed by the track fitting are compared. If the offsets between the hit positions and the fitted positions are found , then they are corrected.

The Michel alignment is also used to check the alignment of the muon target since the track of positrons are projected to the target plane as shown in Fig. 4.7. If there is a misalignment for example, the horizontal displacement, the reconstructed position of target holes should be affected as shown in Fig. 4.8. Therefore if the reconstructed hole position found to be depend on the emission angle of positrons, we can collected this displacement. By using all holes, either vertical displacement or rotations can be corrected with a few hundred μm accuracy.

4.3.4 Relative Alignment

If there is a relative misalignment between the LXe detector and the positron spectrometer, it causes the systematic shift of the opening angle between a gamma ray and a positron. In order to correct that kind of possible misalignment, we use three different methods, a cosmic-ray relative alignment, a CW alignment and an AmBe source alignment. In order to reduce the possible measurement errors, we combined the results from the three approaches above and the result is incorporated into the analysis.

4.3.4.1 Cosmic Ray Relative Alignment

In order to evaluate the relative position difference between the positron spectrometer and the LXe detector, cosmic rays, which pass through both the LXe detector and the drift chambers, are used. The difference of the position is defined as

$$\Delta z = z_{\mathrm{track}} - z_{\mathrm{rec}}, \tag{4.6}$$

$$\Delta v = v_{\mathrm{track}} - v_{\mathrm{rec}}, \tag{4.7}$$

where x_{track} ($x = z$ or v) is the measured position of the cosmic ray on the inner surface of the LXe detector by extrapolating the cosmic ray track reconstructed by the drift cham-

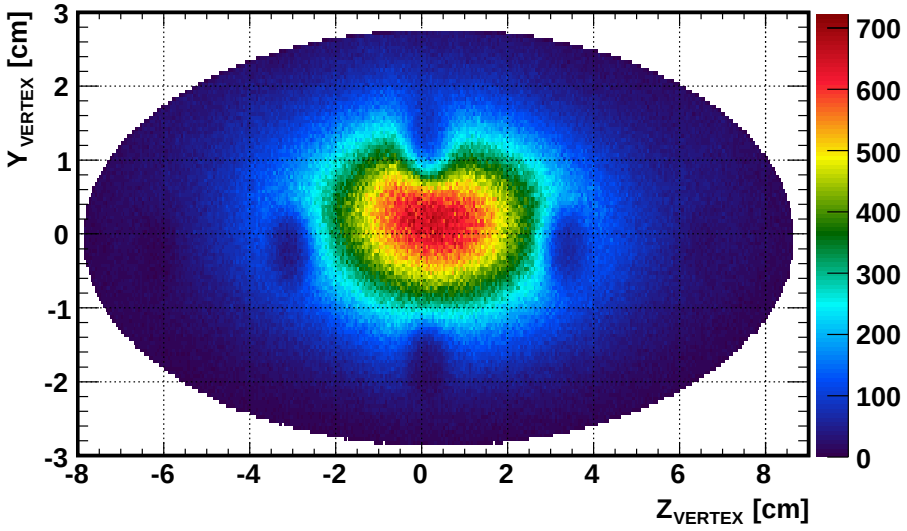

Figure 4.7: Reconstructed positron vertex distribution in Z-Y plane in 2011.

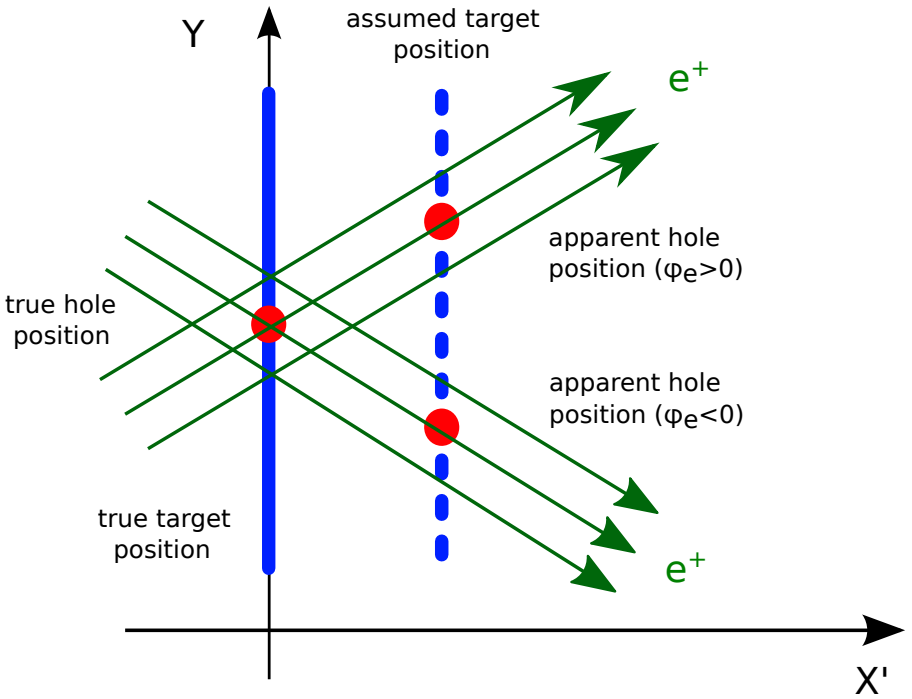

Figure 4.8: An illustration of the software target alignment with Michel positrons in case of the displacement of the target in horizontal axis.

bers, and $x_{\rm rec}$ ($x = z$ or v) represents the position of the same cosmic ray reconstructed by using the LXe detector. Since the drift chambers are aligned with respect to the MEG global coordinate system, the position difference between the DCH and LXe indicates the misalignment of the calorimeter. As a result, the position difference is measured to be $\Delta z = -6.1 \pm 0.7$ mm, here the position accuracy of the drift chambers ~ 0.5 mm is included in the uncertainty, e.g. in 2010 data. We also measure the position displacement in v direction as $\Delta v = -1.9 \pm 0.7$ mm, however we observe that cosmic rays pass through both LXe and DCH in only limited area in v direction. Therefore the measurement along v axis is not sensitive to the displacement of other v region.

4.3.4.2 CW Alignment

A dedicated CW data were taken in 2010 to directly measure the positions of the PMTs mounted inside the LXe detector. In the CW alignment run, lead cubes are put in front of the entrance window of the LXe detector. Then the positions reconstructed by using the LXe detector are compared with the theoretical positions which lead cubes are placed. The results are as follows:

- $\Delta z = -7.3 \pm 1.4$ mm. The uncertainty includes that from the the LiB target position (1 mm), lead cube position (1 mm), statistical uncertainty (0.2 mm).
- $\Delta\phi = 0.3 \pm 1.1$ mrad. Th uncertainty consists of lead positions (1 mm) and statistics (0.5 mm) and translated to the angular uncertainty.

4.3.4.3 AmBe Alignment

A position measurement was performed by using an AmBe source as well in 2009. In this alignment, an AmBe source was placed in front of the LXe detector and the reconstructed position of 4.4 MeV gamma ray events is compared with the source position which was measured by using a laser tracker system. The gamma ray from the source is collimated with 20 mm-thick lead-collimator with a 10 mm-ϕ hole. The measurements were performed in front of two PMTs at $z = 0$ and different v positions, -9.3 and -49.6 cm. Since the alignment of the collimator along the v-axis is not easy due to its rounded shape, only z positions are measured in the AmBe alignment. The difference between the reconstructed and the source z position is calculated to be -5.5 ± 1.8 mm, where error is a quadrature sum of the error of the source position (1.7 mm) and statistical error (0.4 mm). Here the data taken at different positions are averaged. The result is considered to be displacement of the calorimeter with respect to the center of the MEG coordinate system.

4.3.4.4 Combined Result

The relative alignment performed by the three measurements above are combined by taking a weighted mean. Since we need to know the relative alignment between the calorimeter and the spectrometer, the uncertainty of the drift chamber position is added to that of CW and AmBe result. A combined result is obtained as $\Delta z = -6.2 \pm 0.6$ mm. In order to take into account that the measurement is different from the position expected from the design value, the difference divided by $1/\sqrt{12}$ is added to the uncertainty. The

final number to be used in the physics analysis is $\Delta z = -6.2 \pm 2.3$ mm, which corresponds to $\sim 9.1 \pm 3.4$ mrad. Although there were no significant shift observed in ϕ, the same amount of uncertainty is assigned to ϕ conservatively. By adding the uncertainty of the positron analysis (0.75 mrad), $\Delta\phi$ is 0 ± 3.4 mrad.

4.4 Timing Counter Calibrations

4.4.1 Gain Equalization

Since the signal from TC is used to trigger positrons in the MEG trigger, the gain of each PMT needs be equalized to avoid the possible trigger biases. Therefore calibration data from cosmic rays is taken because the distribution of cosmic rays is almost uniform on the longitudinal axis of each bar to equalize the gain of inner and outer PMT.

4.4.2 Time Offsets Correction

Inter-bar time offsets between inner and outer PMTs on each scintillator bar are evaluated by using cosmic rays. Since the distribution of cosmic rays is uniform and isotropic, the time difference between inner and outer PMTs should be flat and centered at zero. The time offsets between different scintillator bars can be calibrated by using two or three hits events in consecutive scintillator bars from both cosmic rays and the positron from Michel decays.

4.4.3 CW-Boron

In the CW calibration runs, a LXe-TC time coincidence trigger to collect events of a pair of two gamma rays from $^{11}\mathrm{B}(p, \gamma_{4.4}, \gamma_{11.6})^{12}\mathrm{C}$ nuclear reaction (E_γ=4.4 MeV and 11.6 MeV). By using this data, possible drifts in the relative timing between the TC and LXe detector can be monitored.

4.5 Relative Time Offset

RMD events make a peak in the distribution of the relative timing between gamma ray and positron since both a positron and a gamma are coincident in this decay. Therefore the alignment of the relative timing can be done by using the timing peak observed in the RMD events. The resolutions of the relative time can be measured by the RMD events as well.

Chapter 5

Performance

We evaluate the performance of each sub-detector by using the data taken in 2009–2011. The performance improvements due to changing the reconstruction algorithm, which are explained in Chapter 3, are presented here as well.

5.1 Performance of the LXe Detector

In this section, the performance of the LXe detector is described in detail.

5.1.1 Gamma Selection

In order to select the gamma ray events coming from muon decays in the target, the selection criteria called `GammaSelection` are defined as follows:

- Without pileup or pileup unfolded with success,
- χ^2_{time}/NDF of the time fitting less than three,
- Gamma ray converted inside the fiducial volume,
- Cosmic-ray rejection cut.

The fiducial volume of the LXe detector is defined as,

- $|u| < 25.0$ cm, $|v| < 71.0$ cm, $0 < w < 38.5$ cm.

5.1.2 Gamma Position Resolution

The position resolution of the LXe detector is evaluated by a Monte Carlo simulation and is validated in dedicated CEX runs by placing a 1.8 cm thick lead collimator at several positions in front of the LXe detector. Figure 5.1 shows the result of position reconstruction projected onto the v coordinate in CEX runs with the collimator. The lead collimator has two slits with 1 cm width along the u coordinate at $v = 0$ and 6 cm. The average position resolutions are estimated to be $\sigma_{u,v} \approx 5$ mm and $\sigma_w \approx 6$ mm, respectively, and they are in good agreement with the values estimated by using the MC simulation.

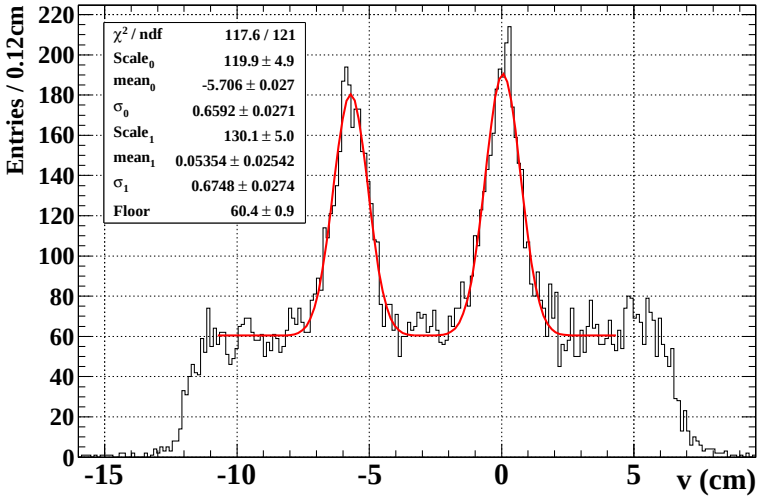

Figure 5.1: Reconstructed position distribution projected on the v-axis with a lead collimator in CEX runs.

5.1.3 Gamma Energy Response

The E_γ resolution is evaluated by using 55 MeV peak in π^0 run at each scanning position of the LXe detector. The fitting function is given as

$$f(x) = f_0(x) \otimes h_{\pi^0}(x), \tag{5.1}$$

and $f_0(x)$ is the response function of the LXe detector parameterized as

$$f_0(x) = \begin{cases} A \cdot \exp\left(\frac{t}{\sigma_{\rm up}^2}\left[\frac{t}{2} - (x - x_0)\right]\right) & x \leq x_0 + t, \\ A \cdot \exp\left(\frac{(x-x_0)^2}{-2\sigma_{\rm up}^2}\right) & x > x_0 + t \end{cases} \tag{5.2}$$

where A is a scale parameter, x_0 is a peak-position parameter, t is a transition parameter, and $\sigma_{\rm up}$ is a resolution parameter that indicates the spread of the distribution in higher energy side. Here h_{π^0} is extracted from the pedestal to take the pileup effect into account. The lower tail is due to interactions with materials in front of the fiducial volume and shower escapes mainly from the inner face. Since there is a position dependence of the energy response, for example the energy resolutions become worse in the narrow region or edge part of the fiducial volume of the detector, the fitting is performed with each subdivided position. Figure 5.2(a) shows fitted result using 2011 CEX data at one subdivided position and Figure 5.2(b) shows resolution map in sigma in u-v plane for $w > 2$ cm. The systematic uncertainties of $\sigma_{\rm up}$ is less than 10% and those of x_0 is less than 0.3% for all positions. For the physics analysis, h_{π^0} is deconvoluted and the pedestal function which is extracted from MEG trigger is convoluted to take into account the difference of the beam settings.

5.1.4 Gamma Timing Resolution

In order to calculate the t_γ resolution, the data taken at the CEX calibration is used. In this calculation, time difference between two gamma rays detected by the LXe detector

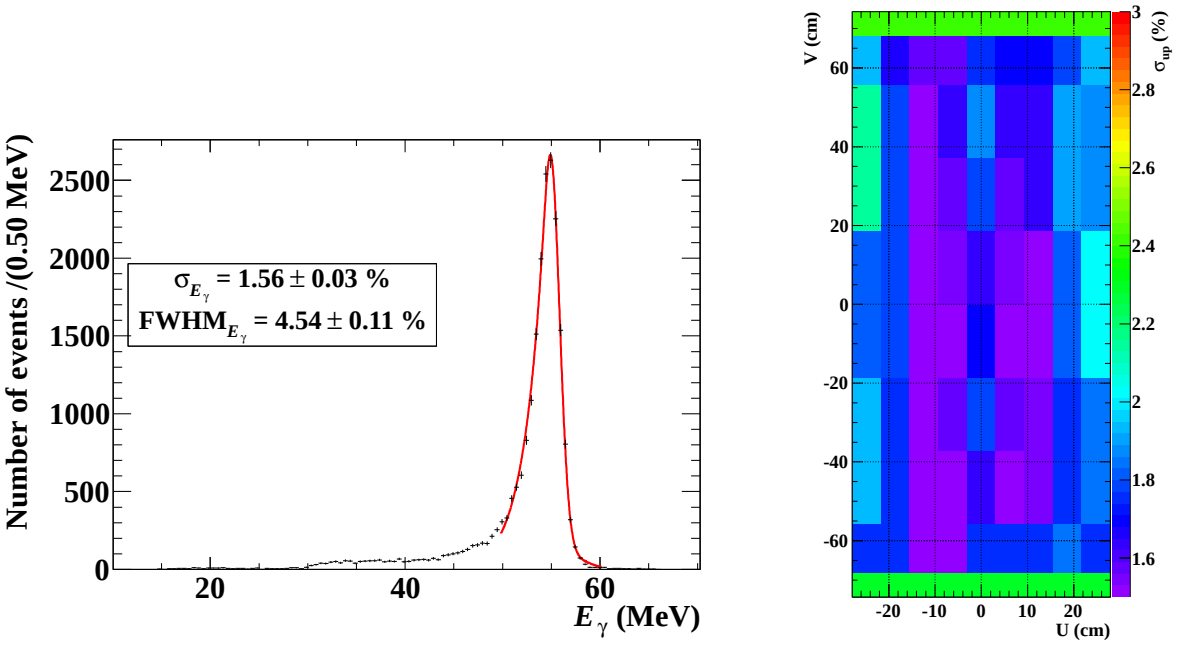

(a) (b)

Figure 5.2: Fitted energy response of the LXe detector for 55 MeV gamma-ray using CEX data taken in 2011 for $w_\gamma > 2$ cm(a). (b) shows measured resolution map in sigma for $w_\gamma > 2$ cm.

and a plastic scintillation counter with the lead converter mounted in front of the BGO (NaI in 2009 and 2010) detector is investigated. After subtracting the contribution from the resolution of plastic scintillation counter and the contribution from the spread of the pion CEX interaction point inside the LH_2 target, the timing resolution is evaluated to be $\sigma_{t_\gamma} = 67$ ps for the 52.8 MeV gamma ray events.

5.1.5 Gamma Efficiency

Due to a high stopping power of the LXe for the gamma ray with the energy around 50 MeV, the LXe detector has good detection efficiency. However, gamma rays also be converted before entering the inner surface of the detector and that kind of events make the inefficiency because of the energy leakage. The efficiency of the LXe detector is found to be $\epsilon_\gamma = 65\%$ in the Monte Carlo simulation for the 48 MeV energy threshold. The difference between the simulation and data is checked by using the π^0 calibration data and the detection efficiency for 55 MeV gamma rays is found to be ϵ_γ =64–67%, consistent with the MC. Taking into account the analysis efficiency of 97% (See Sec. 3.1.6), the combined analysis and detection efficiency for the gamma rays is $63 \pm 3\%$. This detection efficiency is used to calculate the normalization factor (See Sec. 6.5.2).

5.2 Performance of the Positron Spectrometer

The performance of the positron spectrometer are described here in detail.

5.2.1 Positron Selection

Since there are sometimes several reconstructed positrons in an event due to pileup events and duplicates of a positron, we apply the selection in order to select the positron which has large enough momentum and good tracking quality from all of positron-tracks by using measured parameters. The selection criteria called `PositronSelection` are defined as follows;

- $N_{\rm turn} \leq 2$,
- reconstructed tracks which have sufficient matching quality with the timing counter by using following criteria;
  1. $|z_{\rm TC} - z_{\rm track}| < 15$ cm,
  2. $|r_{\rm TC} - r_{\rm track}| < 15$ cm,
  3. $|t_{\rm TC} - t_{\rm track}| < 85$ nsec,
- good fitting quality as follows;
  1. $N_{\rm hits} \geq 7$,
  2. $\chi^2 < 12$,
  3. $\sigma'_{E_{\rm e}} < 1.1$ MeV,
  4. $\sigma'_{\theta_{\rm e}} < 15$ mrad,

Table 5.1: Single hit resolutions of core/tail in each year.

Year	ΔZ (μm)	ΔR (μm)
2009	664(core,68%) / 1683(tail)	159(core,67%) / 423(tail)
2010	730(core,64%) / 1869(tail)	138(core,64%) / 374(tail)
2011	795(core,61%) / 2022(tail)	132(core,68%) / 361(tail)

5. $\sigma'_{\phi_e} < 55$ mrad,

- Target constraint,
- Best ranked track.

In the track finder, sometimes same cluster is shared with different track candidates because of the accidental hits. Therefore the track fitting frequently reconstructs more than one candidate associated to a single real track and this causes the replicated tracks, which we call *ghosts*. Here the parameter to select the best ranked track, called *Ghost Rank* ($G_{\rm Rank}$) is defined as

$$G_{\rm Rank} = 50.716\sigma'_{\phi_e} + 184.934\sigma'_{\theta_e} + 4192.5\sigma'_{E_e} + 0.0327215\chi^2_{\rm track} - 0.224026N_{\rm hits}, \quad (5.3)$$

to identify the fitting quality of each positron. The positron, which has the smallest $G_{\rm Rank}$ value, is selected as the best ranked positron.

5.2.2 Single Hit Resolution

Since the true hit position cannot be known for the reconstructed positron-track, the single hit resolutions of DCH are calculated from the residuals of the reconstructed tracks. Residuals are defined as follows:

$$\Delta Z = Z_{\rm hit} - Z_{\rm track}, \quad (5.4)$$
$$\Delta R = R_{\rm hit} - R_{\rm track}. \quad (5.5)$$

Figure 5.3 shows residual distributions of data taken in 2011. The single hit resolutions are evaluated by fitting double-Gaussian functions to the residual distributions. In Table 5.1, numerical results are summarized for 2009–2011 data. The difference of resolutions is mainly due to the different noise situation, but it is also affected by the gain of anode, misalignment or deformation.

5.2.3 Positron Energy Response

Although the per-error of momentum is used as the resolution for the analysis, average momentum resolution is required to check the reliability of the value of $\sigma'_{\rm E_e}$. In order to evaluate the momentum resolution, Michel spectrum in the time sideband data (the detail of the sideband data is written in Sec. 6.1.4) is fitted by the theoretical Michel

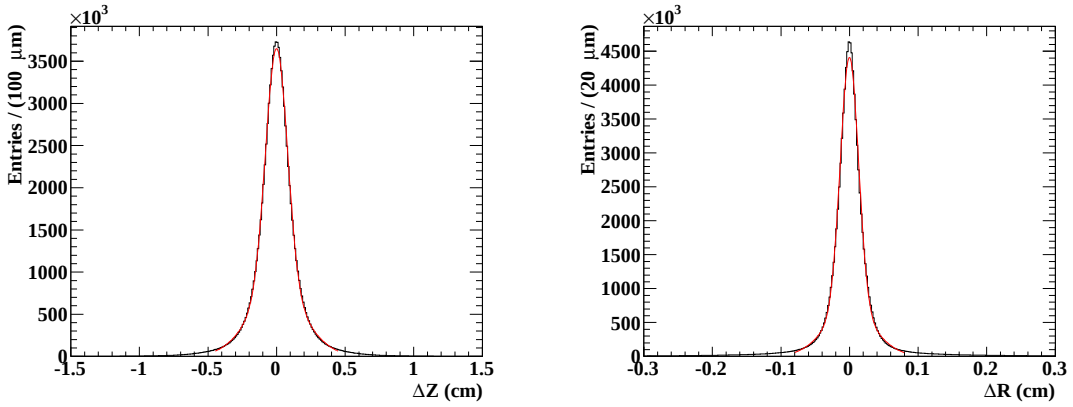

(a) (b)

Figure 5.3: Residual distributions of Z and R in 2011. Red lines are double Gaussian which are used for the fitting.

spectrum multiplied by an acceptance function convolved with a double Gaussian as the resolution of the energy measurement:

$$P({E_\mathrm{e}}^{\mathrm{measured}}) = (((\mathrm{Michel}) * (\mathrm{Acceptance}))({E_\mathrm{e}}^{\mathrm{true}}) \otimes (\mathrm{Resolution}), \tag{5.6}$$

where the acceptance function is defined as:

$$\mathrm{Acceptance}({E_\mathrm{e}}^{\mathrm{true}}) = \frac{1 + \mathrm{erf}(\frac{{E_\mathrm{e}}^{\mathrm{true}} - \mu_{\mathrm{Acc}}}{\sqrt{2}\sigma_{\mathrm{Acc}}})}{2}, \tag{5.7}$$

Figure 5.4 shows the fit result on 2011 data. As a fit result, the resolutions of $\sigma_{E_\mathrm{e}} = 313 \pm 2$ keV in core (84%) and 1.13 ± 0.12 MeV in tail are obtained. Results from the fitting with 2009 and 2010 data are similar to that for 2011 data and shown in Table 5.7 in Sec. 5.4. For the analysis, only the acceptance function is used for and the fit results are shown in Table 6.1 in Sec. 6.3.2.1.

5.2.4 Angular and Vertex Resolutions

The per-errors are used for angular and vertex resolutions in the physics analysis as same for the momentum resolution. The average resolutions are calculated from the analysis using two-turn events. In the two-turn method, a virtual target plane is assumed between the first turn and the second turn. Then we compare the differences between reconstructed variables from the first turn at the plane and reconstructed variables from the second turn at the same plane.

Figure 5.5 shows differences of ϕ_e, θ_e, y_e and z_e between the two turns. The resolutions are extracted from the fitted sigmas of those plots divided by $\sqrt{2}$ by assuming an equal weight for each turn. We correct the difference between two-turn method and the true resolution by using the scaling factor $s = \sigma^{\mathrm{MC,\ true}}/\sigma^{\mathrm{MC,\ two\ turn}}$ which is calculated from the signal monte carlo simulation. The correlations, the details of which are described in Sec. 6.3.2.3, are also taken into account.

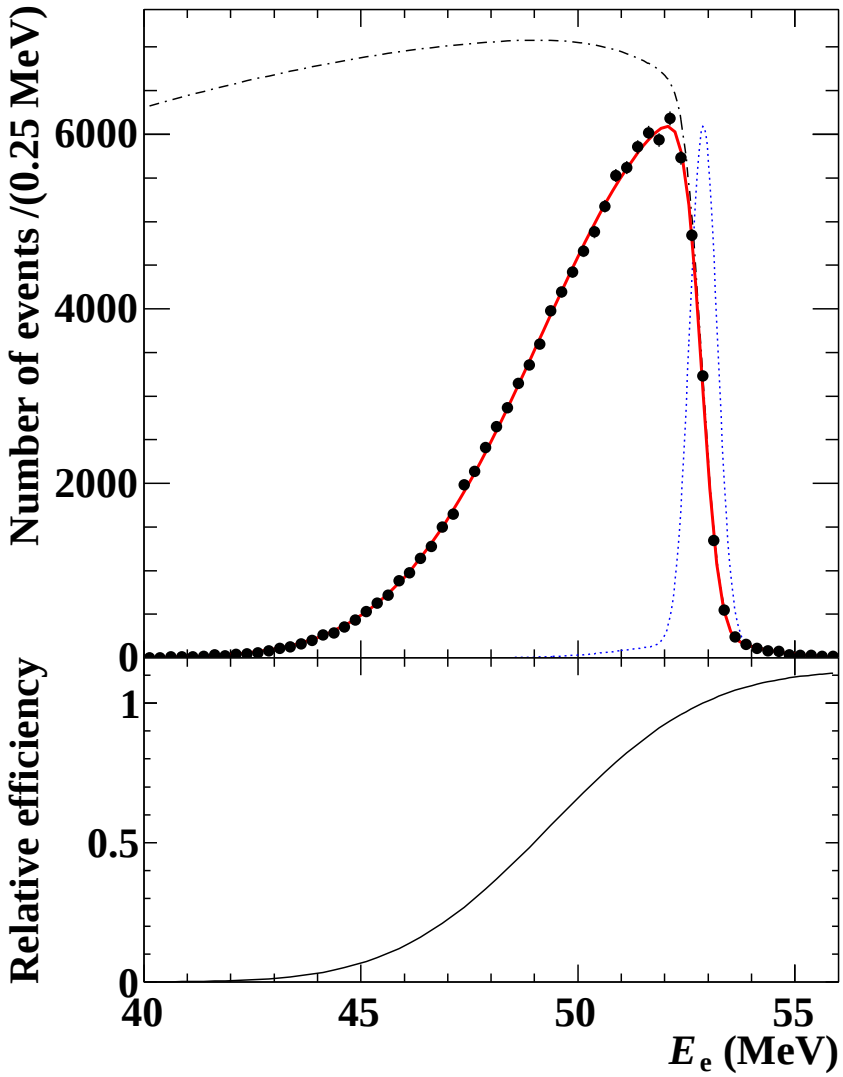

Figure 5.4: A E_e distribution from the data taken in 2011 with a fitting result by using Eq. (5.6). Dashed blue line shows a resolution function centered at 52.8 MeV. Dashed black line is the theoretical Michel spectrum. In the bottom plot, the acceptance function is shown.

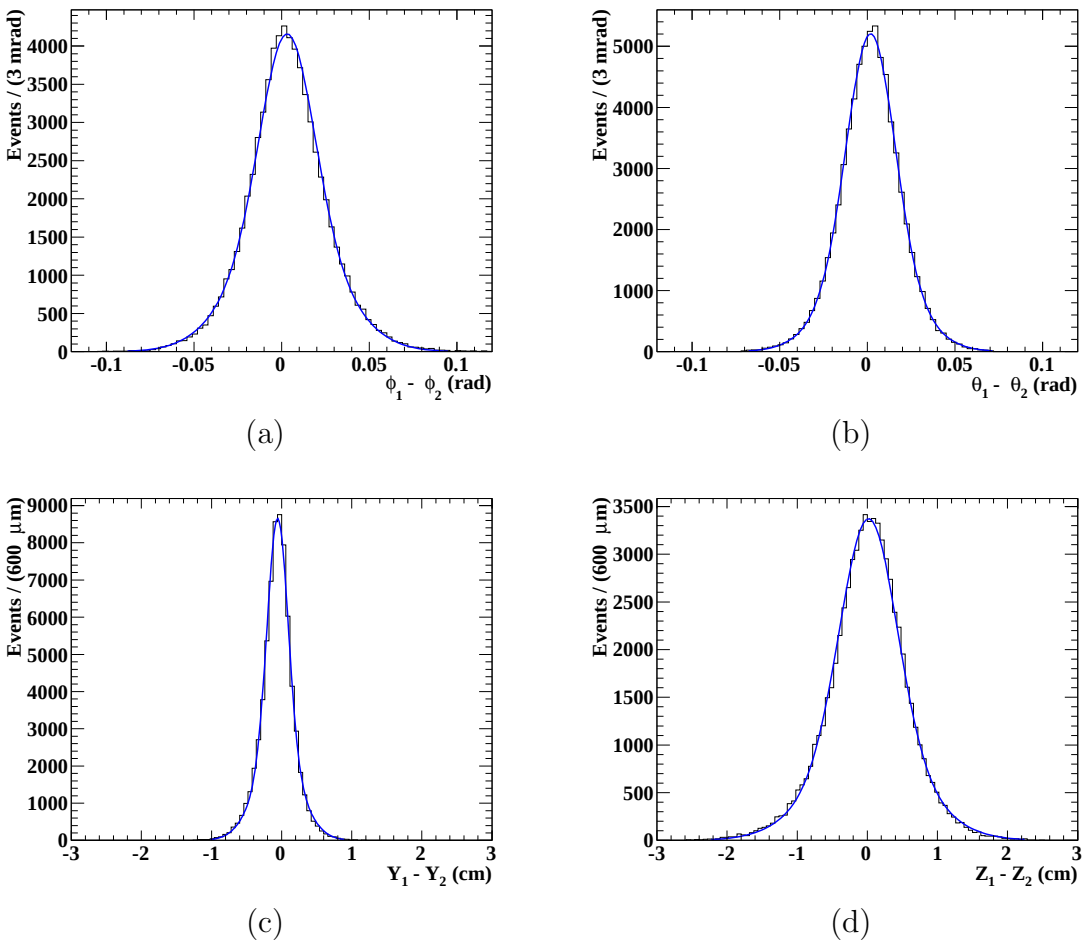

Figure 5.5: Differences of ϕ_e(a), θ_e(b), y_e(c) and z_e(d) between two turns from 2011 data fitted by the double Gaussian function.

5.2.5 Positron Timing Resolution

The time resolution of the positron spectrometer is calculated by combining the contribution from the fluctuation of the fitted track length and that from the resolution of the time measurement of the timing counter. It is calculated to be 107 ps after subtracting the effect from front-end electronics.

5.2.6 Positron Efficiency

The spectrometer efficiency for the signal positron is determined by using the data taken by the Michel trigger which is included in the MEG physics run. The efficiency is determined by

$$\epsilon_{\rm e} = p(\mathrm{DCH}|\mathrm{acc}) \times p(\mathrm{TC}|\mathrm{DCH},\mathrm{acc}) \times p(e\ \mathrm{trg.}|\mathrm{DCH},\mathrm{TC},\mathrm{acc}), \tag{5.8}$$

where $p(\mathrm{DCH}|\mathrm{acc})$ is the probability to detect the positrons if they are inside the acceptance, $p(\mathrm{TC}|\mathrm{DCH},\mathrm{acc})$ is the fraction of positrons detected by the timing counter in all positrons detected by DCH. $p(e\ \mathrm{trg.}|\mathrm{DCH},\mathrm{TC},\mathrm{acc})$ represents the trigger efficiency for Michel trigger and it is calculated to be $\sim 99\%$. By using the data taken with trigger #18 defined in Table 2.3, $p(\mathrm{TC}|\mathrm{DCH},\mathrm{acc})$ is given by

$$p(\mathrm{TC}|\mathrm{DCH},\mathrm{acc}) = \frac{N_{\rm matched}}{N_{\rm good}}, \tag{5.9}$$

where $N_{\rm good}$ is the number of reconstructed positrons and $N_{\rm matched}$ is the number of reconstructed positrons with success to find the related hit in TC.

The numerical value of $p(\mathrm{DCH}|\mathrm{acc})$ is evaluated from the data taken with the Michel trigger. Here the number of selected positrons can be calculated by using the total number of stopped muons at the target ($N_\mu^{\rm stop}$), which is estimated from the proton current and numeric values are written in Sec. 2.6.1, 2.6.2 and 2.6.3, as,

$$\begin{aligned} N_{\rm Michel}^{\rm Obs} \times \mathrm{Prescaling} \times P_{\rm corr} \quad = \quad & N_\mu^{\rm stop} \times \\ & f_{\rm Michel} \times \\ & p(\mathrm{DCH}|\mathrm{acc}) \times \\ & p(\mathrm{TC}|\mathrm{DCH},\mathrm{acc}) \times \\ & p(e\ \mathrm{trg.}|\mathrm{DCH},\mathrm{TC},\mathrm{acc}), \end{aligned} \tag{5.10}$$

where $N_{\rm Michel}^{\rm Obs}$, Prescaling, $P_{\rm corr}$ and $f_{\rm Michel}$ are defined as follows:

- $N_{\rm Michel}^{\rm Obs}$:
  The number of observed positrons passing through the official `PositronSelection`.
- $f_{\rm Michel}$:
  The fraction of Michel positrons in the momentum range from 50 to 56 MeV. It is extracted from MC.
- Prescaling :
  The pre-scaling factor used for the Michel trigger.

- $P_{\rm corr}$:
  The correction factor for Michel trigger to take into account the probability of multi-pileup events. This factor is calculated from the Eq.(5.11) using the live time and the number of fired trigger ($N_{\rm trigger\sharp 22}$).

$$\begin{aligned} R_{\rm meas} &= N_{\rm trigger\sharp 22}/({\rm LiveTime}) \\ &= R_{\rm true} \times \exp(-R_{\rm true} \cdot \Delta T), \\ P_{\rm corr} &= R_{\rm true}/R_{\rm meas}. \end{aligned} \tag{5.11}$$

They are also used for the normalization calculation (See Sec. 6.5.2). Once we obtain the value of $p({\rm TC}|{\rm DCH}, {\rm acc})$, $p({\rm DCH}|{\rm acc})$ is derived from Eq. (5.10). For example, in 2011, the positron efficiency is calculated to be $\epsilon_{\rm e} = (31 \pm 3)\%$.

5.3 Combined Performance

In the physics analysis, the timing resolutions, angular resolutions, vertex resolutions and gamma position resolutions are merged into three observables; $t_{\rm e\gamma}$, $\phi_{\rm e\gamma}$ and $\theta_{\rm e\gamma}$. Here we present the combined resolutions of these three parameters.

5.3.1 Vertex Resolutions

For the analysis, resolutions of relative angles between a gamma-ray and a positron in ϕ and θ should be given by $\theta_{\rm e}$, $\phi_{\rm e}$, positron vertex resolutions, the position resolutions of a gamma ray position. The relative angles are defined as

$$\phi_{\rm e\gamma} = (\pi + \phi_{\rm e}) - \phi_\gamma, \tag{5.12}$$

$$\theta_{\rm e\gamma} = (\pi - \theta_{\rm e}) - \theta_\gamma, \tag{5.13}$$

where θ_γ and ϕ_γ are defined by assuming that a gamma ray decays at the same position as a positron decay vertex $(x_{\rm e}, y_{\rm e}, z_{\rm e})$ as

$$\theta_\gamma = \cos^{-1}\left(\frac{z_\gamma - z_{\rm e}}{\sqrt{(x_\gamma - x_{\rm e})^2 + (y_\gamma - y_{\rm e})^2 + (z_\gamma - z_{\rm e})^2)}}\right) \tag{5.14}$$

$$\phi_\gamma = \tan^{-1}\left(\frac{y_\gamma - y_{\rm e}}{x_\gamma - x_{\rm e}}\right). \tag{5.15}$$

Although the resolution of each variable is defined on an event-by-event basis, average values can be evaluated by using sum of the PDF which is defined later in Sec. 6.3.2.2. They are calculated to be $\sim$9 mrad and $\sim$15 mrad for $\phi_{\rm e\gamma}$ and $\theta_{\rm e\gamma}$, respectively.

5.3.2 Timing Resolution

Overall timing resolution is evaluated from the RMD timing peak observed in the data collected by the MEG trigger. In order to extract the $t_{\rm e\gamma}$ response from the data, a double Gaussian for RMD peak and a flat distribution for accidental background are used. The fitting result from 2011 data is shown in Fig. 5.6. The uncertainty on the mean is calculated to be 15 ps.

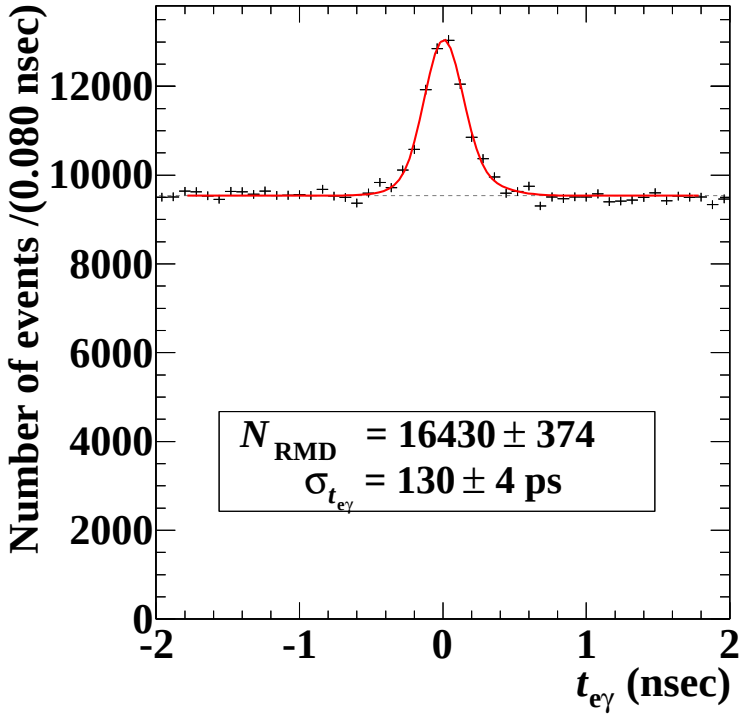

Figure 5.6: Relative time distribution from 2011 data.

5.3.3 Contributions of Reconstruction Improvements

We discuss the performance improvements due to the newly implemented algorithms in the following.

5.3.3.1 Offline Noise Reduction

As already described in Sec. 3.2.1.3, the offline noise reduction is newly implemented in the reconstruction of the positron track. In order to check the performance improvement due to the noise reduction, portions of 2009–2011 data were produced with the official configurations except for one condition that the noise reduction is turned off.

Single Hit z Resolution

The single hit z resolution is evaluated by comparing the z hit positions with the z positions estimated by tracks reconstructed by old Kalman. As shown in Fig. 5.7, the single hit z resolution is improved by applying the offline noise reduction. The total number of hits increased as well.

Single Hit r Resolution

Since the r is determined by reading the edge of the rise time, the r-resolution also can depend on the noise. The noise reduction before reading the edge is therefore tested. In the test, it is found that the r resolution doesn't change so much and it is decided to apply the noise reduction only to measure the z position.

Performance Comparisons

In order to evaluate the efficiency improvement, Michel positrons in sideband data

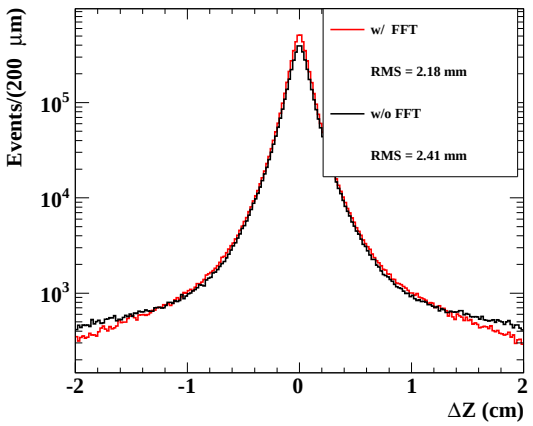

(a) 2009 data

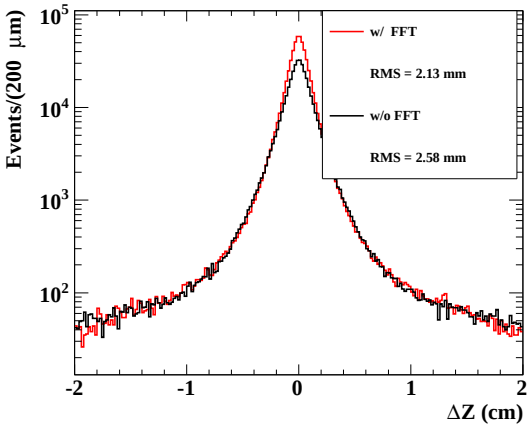

(c) 2011 noisy data

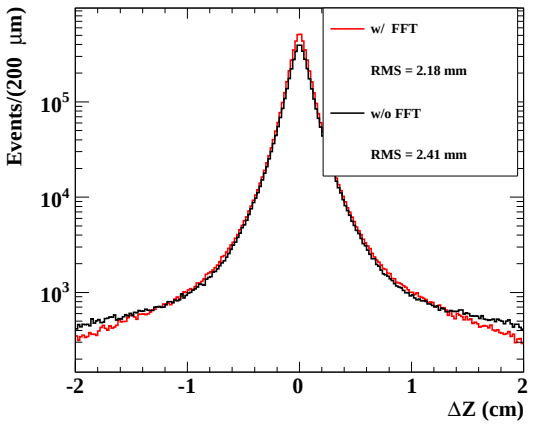

(b) 2010 data

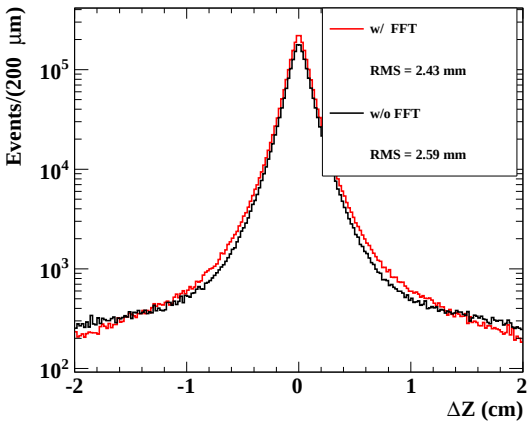

(d) 2011 normal data

Figure 5.7: Residuals of the single hit z-position with/without the noise reduction.

are used. Almost all selection criteria are the same as the selection used as the selection used for the physics analysis, but some parameters are loose as written below. For the resolution checks, only tracks which have two turns are selected.

- $-5 < t_{e\gamma} < 5$ ns and $|t_{e\gamma}| > 1$ ns,
- $-300 < \phi_{e\gamma} < 300$ mrad,
- $-300 < \theta_{e\gamma} < 300$ mrad,
- E_γ : no thresholds.

The relative improvements of the resolutions are calculated by comparing two-turn tracks reconstructed by new Kalman with/without the noise reduction. For the efficiency, the numbers of Michel positrons reconstructed with/without the noise reduction are compared. The average number of hits per track is also calculated from Michel positrons because it is related to the performance.

2009 Data

The improvements are summarized in Table 5.2.

Table 5.2: Performance comparison in 2009.

Parameters	w/o FFT	w/ FFT	Relative improvement (%)
Number of Michel e^+	253707	268403	6
Average number of hits	13.0	13.2	2
RMS of E_e	756 keV	751 keV	<1
RMS of ϕ_e	27.5 mrad	27.1 mrad	2
RMS of θ_e	16.9 mrad	16.6 mrad	2
RMS of y_e	4.65 mm	4.57 mm	2
RMS of z_e	4.72 mm	4.52 mm	4

2010 Data

Table 5.3 shows the improvements due to the noise reduction in 2010 data.

Table 5.3: Performance comparison in 2010.

Parameters	w/o FFT	w/ FFT	Relative improvement (%)
Number of Michel e^+	268778	290548	8
Average number of hits	12.7	12.9	2
RMS of E_e	800 keV	795 keV	<1
RMS of ϕ_e	30.7 mrad	28.7 mrad	7
RMS of θ_e	19.6 mrad	17.8 mrad	9
RMS of y_e	4.85 mm	4.75 mm	2
RMS of z_e	6.16 mm	5.48 mm	11

2011 Noisy Data

In 2011 noisy data, both efficiency and resolutions are significantly improved as shown in Table 5.4. The efficiency improvement is shown in Fig. 5.8. Figure 5.9 shows the difference of Δx ($x = E_e, \phi_e, \theta_e, y_e, z_e$) from two-turn method with/without the noise reduction. The θ_e and the z_e resolutions are directly improved by the noise reduction and the ϕ_e and the y_e resolutions improved as well because more hits are used for the fitting.

Table 5.4: Performance comparison in 2011 noisy run period.

Parameters	w/o FFT	w/ FFT	Relative improvement (%)
Number of Michel e^+	100850	110153	9
Average number of hits	12.8	13.7	7
RMS of E_e	813 keV	784 keV	4
RMS of ϕ_e	31.6 mrad	28.3 mrad	11
RMS of θ_e	19.6 mrad	17.5 mrad	11
RMS of y_e	5.01 mm	4.77 mm	5
RMS of z_e	6.15 mm	5.31 mm	14

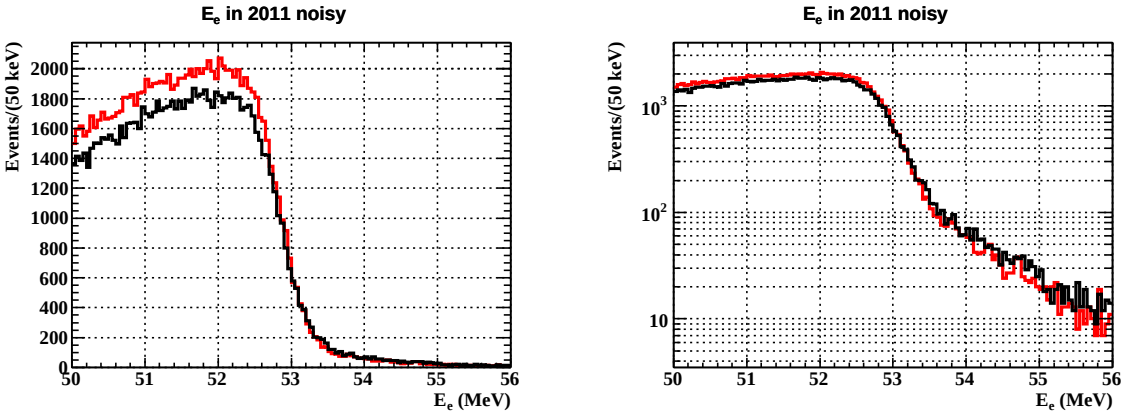

Figure 5.8: E_e spectrum in 2011 noisy run period. Red/black lines are with/without the noise reduction. Right figure shows the log scale of the left figure.

2011 Data

After several hardware investigations, most of strong noise components were suppressed in 2011 run. Even in the lower noise condition, the noise reduction slightly improves performance and is applied also to the data. The performance comparison between with/without the noise reduction is shown in Table 5.5.

2009–2011 All Combined Data

The effect for the 2009-2011 all combined data is also evaluated. The improvements are summarized in Table 5.6 and shown in Fig. 5.10 and Fig. 5.11. As shown in Fig. 5.10, total reconstructed positrons increase while the tail component does not.

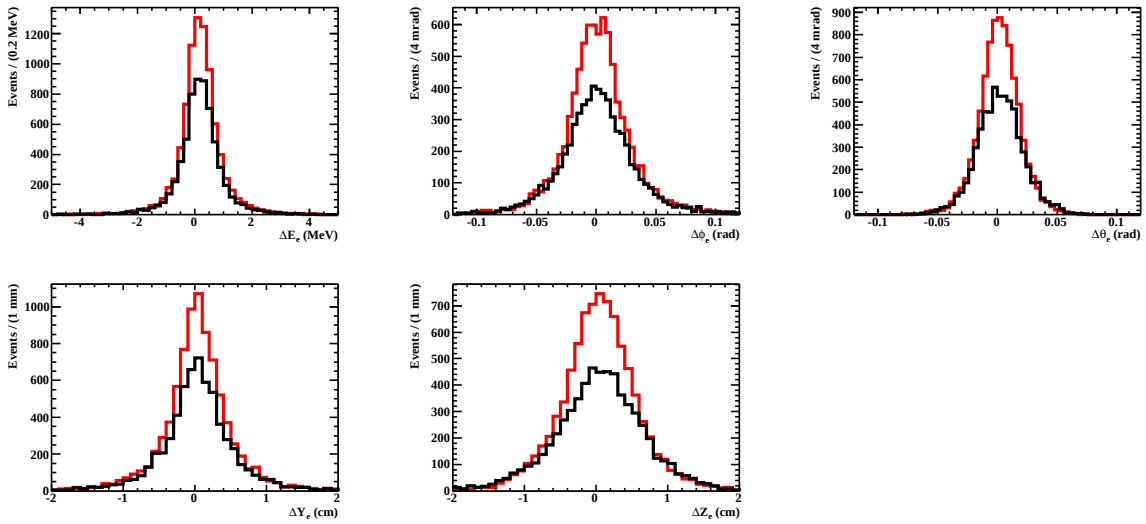

Figure 5.9: Distributions of $\Delta x(x = E_{\rm e}, \phi_{\rm e}, \theta_{\rm e}, y_{\rm e}, z_{\rm e})$ from two-turn events in 2011 noisy run period. Red/black lines are with/without the noise reduction.

Table 5.5: Performance comparison in 2011 run after hardware investigations.

Parameters	w/o FFT	w/ FFT	Relative improvement (%)
Number of Michel e^+	107112	110272	3
Average number of hits	12.0	12.2	2
RMS of $E_{\rm e}$	796 keV	764 keV	4
RMS of $\phi_{\rm e}$	29.6 mrad	29.5 mrad	<1
RMS of $\theta_{\rm e}$	18.5 mrad	18.5 mrad	<1
RMS of $y_{\rm e}$	4.82 mm	4.75 mm	1
RMS of $z_{\rm e}$	5.86 mm	5.86 mm	<1

Table 5.6: Performance comparison for 2009-2011 all combined data.

Parameters	w/o FFT	w/ FFT	Relative improvement (%)
Number of Michel e^+	521788	552922	6
Average number of hits	12.5	12.8	2
RMS of $E_{\rm e}$	796 keV	773 keV	3
RMS of $\phi_{\rm e}$	29.8 mrad	29.0 mrad	3
RMS of $\theta_{\rm e}$	18.8 mrad	18.1 mrad	4
RMS of $y_{\rm e}$	4.84 mm	4.75 mm	2
RMS of $z_{\rm e}$	5.84 mm	5.60 mm	4

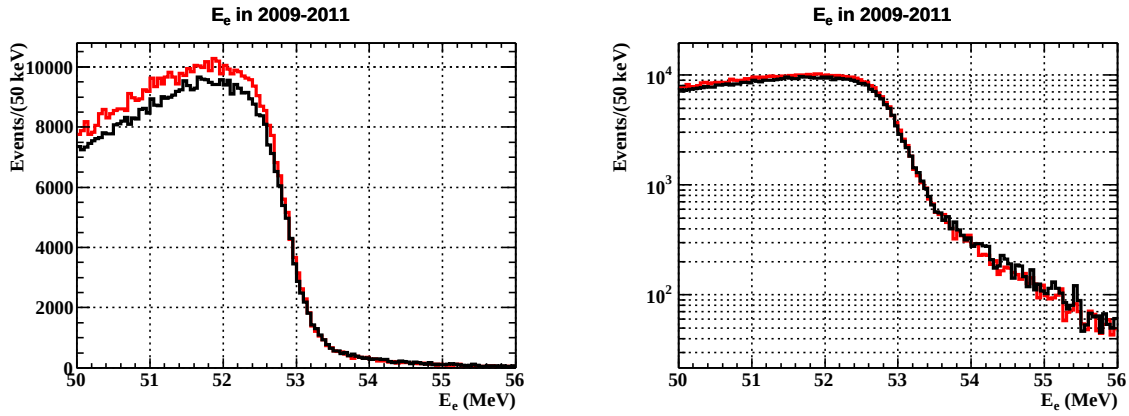

Figure 5.10: E_{e} spectrum in 2009–2011 combined data. Red/black lines are with/without the noise reduction. Right figure shows the log scale of the left figure.

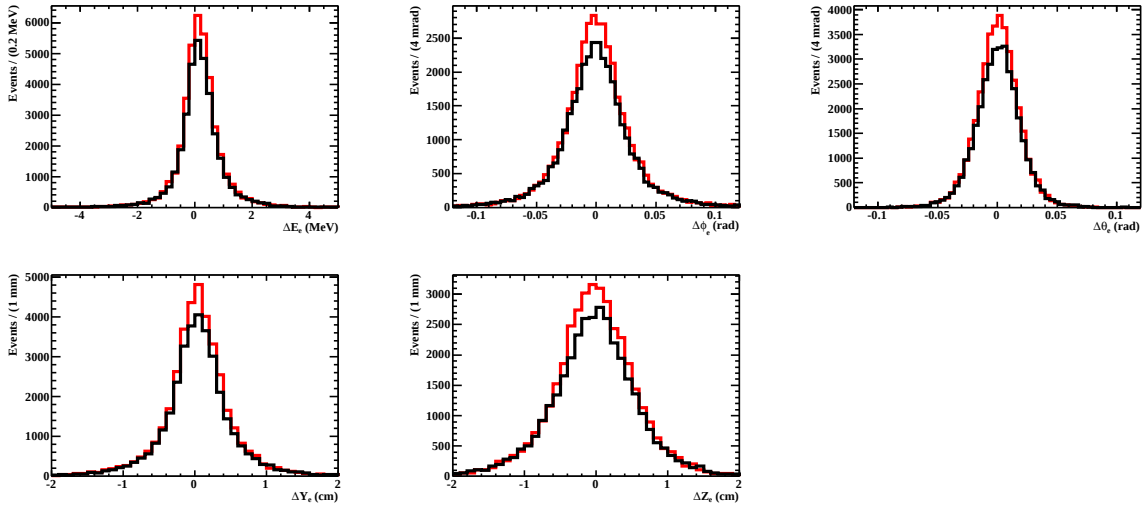

Figure 5.11: Distributions of $\Delta x (x = E_{\mathrm{e}}, \phi_{\mathrm{e}}, \theta_{\mathrm{e}}, y_{\mathrm{e}}, z_{\mathrm{e}})$ from two-turn events in 2009–2011 combined data. Red/black lines are with/without the noise reduction.

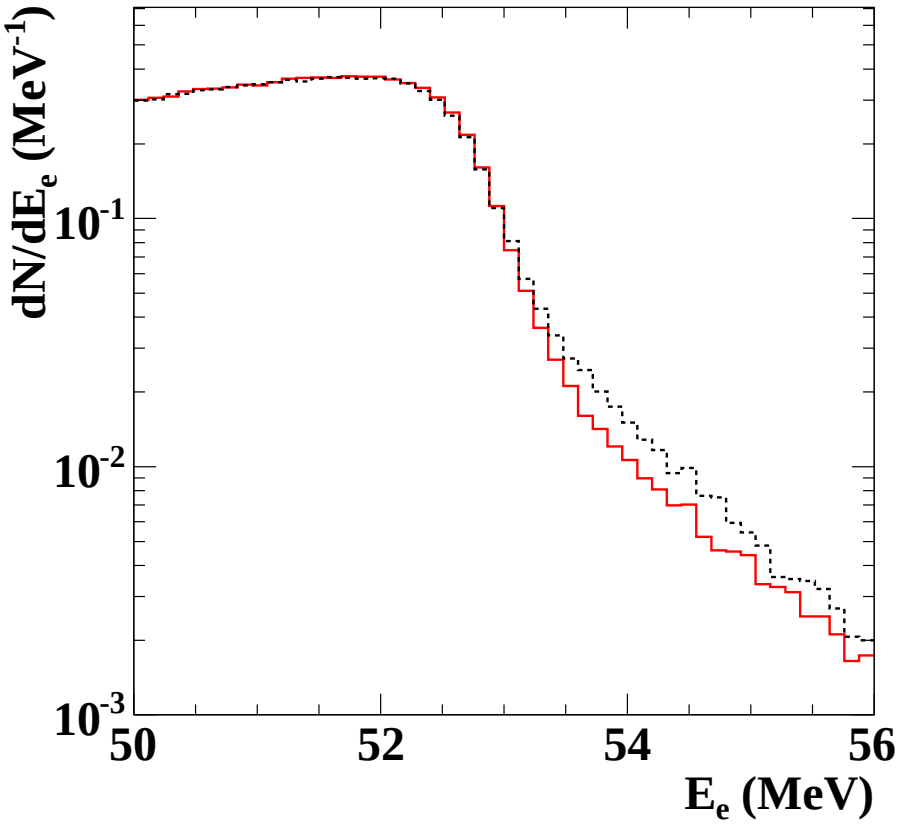

Figure 5.12: Reconstructed energy spectrum of positrons with new track fitting (red) in comparison with that with the previous one (dashed black line). Both spectra are normalized by using the area of each histogram.

5.3.3.2 New Track Fitting

Figure 5.12 shows the positron energy spectrum with new track fitting including the offline noise reduction. Owing to the better precision of the new track fitting, the tail component of the positron energy is reduced. We also obtained a 6% efficiency improvement by using new Kalman in comparison with that by using old Kalman by looking the number of reconstructed positrons in the time sideband and it is confirmed by comparing the calculated normalization factors with new/old Kalman (See Sec. 6.5.2, Table 6.7).

5.3.3.3 Sum Waveform Analysis

As described in Sec. 3.1.5, a new algorithm to reduce the pileup events is applied in the new analysis. Due to the newly implemented pileup unfolding technique, the events in higher energy part of E_γ spectrum are reduced as shown in Fig. 5.13, while the gamma ray detection efficiency is increased by 7%.

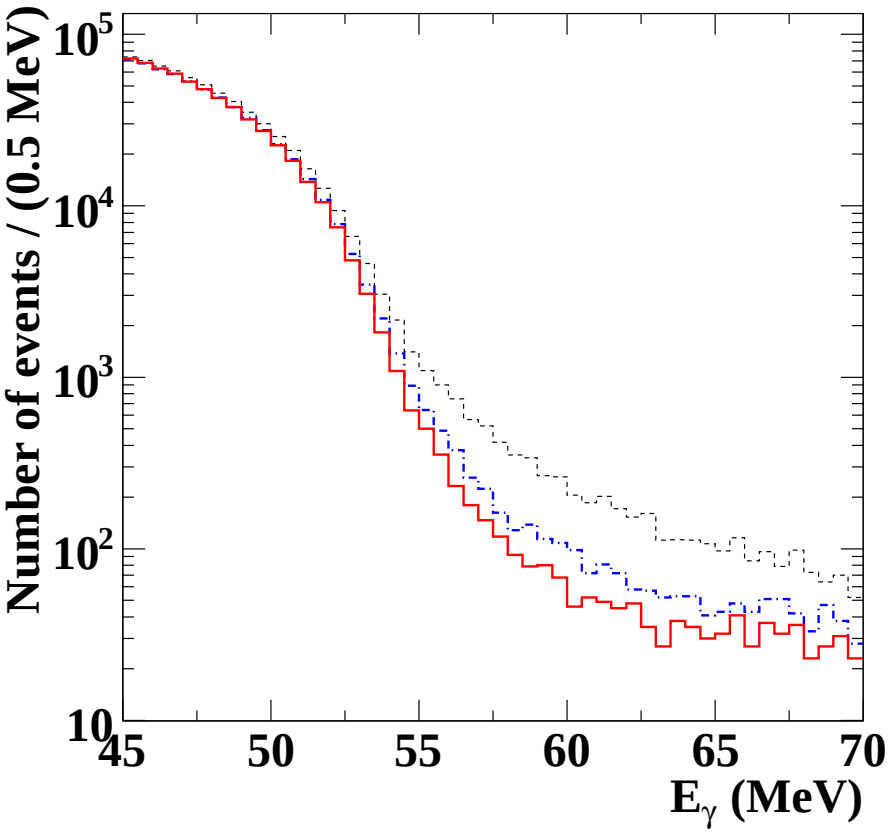

Figure 5.13: Energy spectra of gamma rays in comparison between that by applying new pileup elimination algorithm (red), previous algorithm (blue-dot-dashed) and without the pileup elimination (black-dotted).

Table 5.7: Performance summary.

Variable	2009	2010	2011
Gamma Resolutions			
E_γ (%)	1.9 ($w > 2$ cm), 2.4 ($w < 2$ cm)	1.9 ($w > 2$ cm), 2.4 ($w < 2$ cm)	1.7 ($w > 2$ cm), 2.4 ($w < 2$ cm)
u_γ,v_γ (mm)	5	5	5
w_γ (mm)	6	6	6
t_γ (ps)	96	67	67
Positron Resolutions			
E_e (MeV)	0.31	0.32	0.31
ϕ_e (mrad)	6.6	7.2	7.5
θ_e (mrad)	9.4	11.0	10.6
y_e (mm)	1.1 (core)	1.1 (core)	1.2 (core)
z_e (mm)	1.1	1.7	1.9
t_e (ps)	107	107	107
Combined Resolutions			
$\phi_{\mathrm{e}\gamma}$ (mrad)	8.9	9.0	8.9
$\theta_{\mathrm{e}\gamma}$ (mrad)	15.0	16.1	16.2
$t_{\mathrm{e}\gamma}$ (ps)	156	123	127
Efficiency			
ϵ_γ (%)	63	63	63
ϵ_e (%)	28	35	31
ϵ_trg (%)	91	92	97

5.4 Performance Summary

The performance of the MEG detector in 2009, 2010 and 2011 data is summarized in Table 5.7.

Chapter 6

Physics Analysis

This chapter shows the details of the analysis used for the estimation of the branching ratio of $\mu^+ \to e^+\gamma$ decay from data.

A maximum likelihood analysis is performed to estimate the number of signal events ($N_{\rm sig}$) since only the small number of events are expected to be observed in the signal region. A maximum likelihood function is defined with probability density functions (PDFs). In order to avoid possible human biases, we use a blind analysis procedure. The events close to the $\mu^+ \to e^+\gamma$ signal region were hidden until calibrations and analysis have been fixed for 2011 data. The datasets of 2009 and 2010 are re-analyzed in the same analysis procedure which is used for the 2011 dataset. Although the signal region is closed, all necessary parameters for the analysis can be extracted from events outside of the blind box, the data from the calibration runs, the data taken by the different trigger and Monte Carlo simulation.

The sensitivity is calculated in the same way as our data analysis by using many pseudo experiments assuming null-signal-hypothesis.

In order to translate the number of events to the branching ratio, the normalization factor is calculated by combining results from two different ways, which are called Michel normalization and RMD normalization. The normalization factors for 2009 and 2010 datasets are also calculated again, because of the efficiency improvements due to the offline noise filtering, new Kalman and the pileup unfolding.

In order to improve the sensitivity, the per-errors of observables associated to the positron measurement, which is introduced in Sec. 3.2.6.2, are incorporated into the PDFs. The detailed analysis using the per-errors is described in Sec. 6.3.

6.1 Datasets

We analyzed combined dataset taken in 2009–2011 with the MEG trigger. The datasets taken in 2009 and 2010 are re-analyzed with the new reconstruction methods in order to gain the performance and the experimental sensitivity as already mentioned. The analysis using several sidebands are also performed.

6.1.1 Pre-Selection

We took 10,343, 12,168 and 30,852 physics runs in 2009, 2010 and 2011, respectively. One run contains $\sim$ 5,000 MEG trigger events. To make analysis faster, we apply the pre-selection by using preliminary calibration factors. The selection criteria for the pre-selection are as follows:

- $-6.875 < t_\gamma - t_{\rm TC} < 4.375$ ns,
- $|t_{\rm TrackCandidate} - t_{\rm TC}| < 50$ ns,

where $t_{\rm TrackCandidate}$ is the best estimated time of the hit calculated by the track candidate. Since the time difference between $t_{\rm TrackCandidate}$ is set to wide enough, this cut corresponds to the requirement of which at least one track candidate is reconstructed in an event. The events which are not selected by the pre-selection are used only for the calibrations.

6.1.2 Blind Box

The blind box is defined by using the gamma ray energy and the time difference between a gamma ray and a positron as

- $48 \leq E_\gamma \leq 58$ MeV,
- $|t_{\rm e\gamma}| \leq 1$ ns,

Before opening the blind box, we fix the calibrations and the analysis. The analysis on the datasets in time sidebands, angle sidebands and the reliability check for the newly implemented PDFs by using full Monte Carlo simulation (full-MC) are also done before the un-blinding.

6.1.3 Analysis Region

In order to perform the maximum likelihood fitting, the analysis region, which includes the $\mu^+ \to {\rm e}^+\gamma$ like gamma-positron pair event, is defined as follows;

- $48 \leq E_\gamma \leq 58$ MeV,
- $50 \leq E_{\rm e} \leq 56$ MeV,
- $|\phi_{\rm e\gamma}| \leq 50$ mrad and $|\theta_{\rm e\gamma}| \leq 50$ mrad,
- $|t_{\rm e\gamma}| \leq 0.7$ ns,
- a pair of a positron and a gamma is selected by using the `PositronSelection` and the `GammaSelection`.

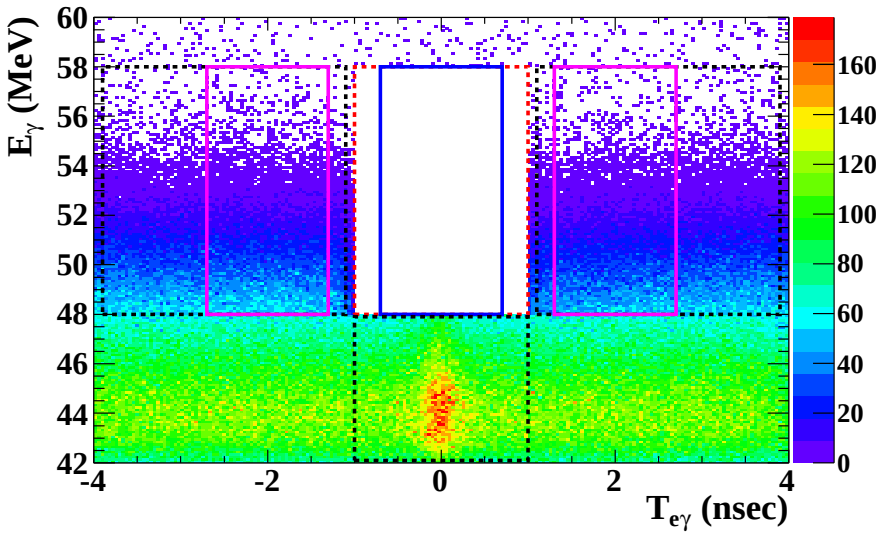

Figure 6.1: Two dimensional event distribution in $t_{e\gamma}$ vs E_γ taken in 2009–2011. The blank box at the center shows the blind box and the inner box with blue lines shows the analysis region. Left and Right boxes with dashed black lines show the sideband data and two boxes with solid magenta lines show the time sidebands which are used for the maximum likelihood fit. A bottom center box shows the energy sideband used to evaluate the expected number of RMD events and the $t_{e\gamma}$ resolution. For the illustration purpose, following loose cuts are applied;$40 \leq E_e \leq 60$ MeV;$40 \leq E_\gamma \leq 60$ MeV;$|\theta_{e\gamma}| \leq 200$ mrad; $|\phi_{e\gamma}| \leq 200$ mrad;$|t_{e\gamma}| \leq 4$ ns.

6.1.4 Sideband Data

We define several sideband datasets in order to perform the calibration, evaluate the parameters required to construct the PDFs and perform the maximum likelihood analysis in the same way as used for the analysis region. Figure 6.1 shows distribution of the data taken with MEG trigger in 2009–2011. As shown in this figure, accidental background is distributed flat in the relative time. Therefore the parameters which are required to construct the accidental background PDFs can be extracted from the data in off-time region called time sidebands. In the same plot, there is the event concentration at the center of the relative time below the blind box (called energy sideband). These events should be the radiative muon decay (RMD) and we can use these events to extract the normalization factor and to calculate the number of RMD events in the analysis region by using the energy sideband. Figure 6.2 shows the two dimensional distribution of the events in relative angles in time sidebands. The asymmetric shape is caused by the trigger direction match algorithm with lower momentum positrons than that of the signal positron.

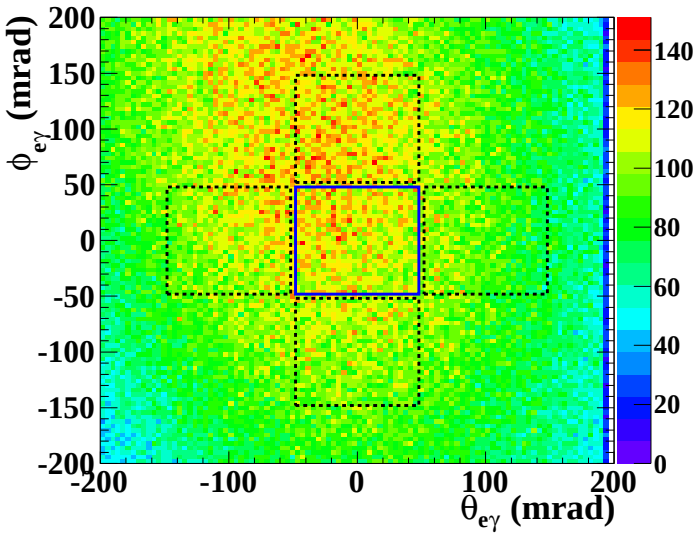

Figure 6.2: Two dimensional event distribution in $\theta_{e\gamma}$ vs $\phi_{e\gamma}$ taken in 2009–2011 in time sidebands. The center box with blue lines shows the analysis region in relative angles. Neighboring four boxes with dashed lines show the angle sidebands which we perform the maximum likelihood fitting. For the illustration purpose, following loose cuts are applied;$40 \leq E_e \leq 60$ MeV;$43 \leq E_\gamma \leq 60$ MeV;$|\theta_{e\gamma}| \leq 200$ mrad; $|\phi_{e\gamma}| \leq 200$ mrad;$|t_{e\gamma}| \leq 4$ ns and $|t_{e\gamma}| > 1$ ns.

6.1.5 Time Sidebands

The regions of the time sidebands are defined as similar to that of signal, but with a negative or a positive side of the time difference between a gamma ray and a positron. In order to perform the maximum likelihood fitting in the time sidebands, two regions are defined as follows:

Negative time:	48	$\leq$	E_γ	$\leq$	58	MeV,
	50	$\leq$	E_e	$\leq$	56	MeV,
	$\mathbf{-2.7}$	$\leq$	$t_{e\gamma}$	$\leq$	$\mathbf{-1.3}$	nsec,
	-50	$\leq$	$\theta_{e\gamma}$	$\leq$	50	mrad,
	-50	$\leq$	$\phi_{e\gamma}$	$\leq$	50	mrad
Positive time:	48	$\leq$	E_γ	$\leq$	58	MeV,
	50	$\leq$	E_e	$\leq$	56	MeV,
	$\mathbf{1.3}$	$\leq$	$t_{e\gamma}$	$\leq$	$\mathbf{2.7}$	nsec,
	-50	$\leq$	$\theta_{e\gamma}$	$\leq$	50	mrad,
	-50	$\leq$	$\phi_{e\gamma}$	$\leq$	50	mrad

A pair of a positron and a gamma is selected by `PositronSelection` and `GammaSelection`.

Time sidebands are used to extract the parameters for the accidental background as well since the accidental background events distribute uniformly in the relative time distribution. For this purpose, loose selection criteria are applied according to the observable, for example, for the background E_e PDF, criteria associated to the gamma ray measurement can be loosen.

6.1.6 Angle Sidebands

Since the RMD events are not included in the time sidebands, the datasets of angle sidebands are helpful to check the maximum likelihood fitting with non-zero RMD conditions. Before opening the blind-box, only four time coincident parts without back-to-back region, which are shown in Fig. 6.2, are partially opened and analyzed. The maximum likelihood fitting is performed in four angle sidebands as follows:

Negative ϕ:	48	$\leq$	E_γ	$\leq$	58	MeV,
	50	$\leq$	E_e	$\leq$	56	MeV,
	-0.7	$\leq$	$t_{\mathrm{e}\gamma}$	$\leq$	0.7	nsec,
	-50	$\leq$	$\theta_{\mathrm{e}\gamma}$	$\leq$	50	mrad,
	$\mathbf{-150}$	$\leq$	$\phi_{\mathrm{e}\gamma}$	$\leq$	$\mathbf{-50}$	mrad
Positive ϕ:	48	$\leq$	E_γ	$\leq$	58	MeV,
	50	$\leq$	E_e	$\leq$	56	MeV,
	-0.7	$\leq$	$t_{\mathrm{e}\gamma}$	$\leq$	0.7	nsec,
	-50	$\leq$	$\theta_{\mathrm{e}\gamma}$	$\leq$	50	mrad,
	$\mathbf{50}$	$\leq$	$\phi_{\mathrm{e}\gamma}$	$\leq$	$\mathbf{150}$	mrad
Negative θ:	48	$\leq$	E_γ	$\leq$	58	MeV,
	50	$\leq$	E_e	$\leq$	56	MeV,
	-0.7	$\leq$	$t_{\mathrm{e}\gamma}$	$\leq$	0.7	nsec,
	$\mathbf{-150}$	$\leq$	$\theta_{\mathrm{e}\gamma}$	$\leq$	$\mathbf{-50}$	mrad,
	-50	$\leq$	$\phi_{\mathrm{e}\gamma}$	$\leq$	50	mrad
Positive θ:	48	$\leq$	E_γ	$\leq$	58	MeV,
	50	$\leq$	E_e	$\leq$	56	MeV,
	-0.7	$\leq$	$t_{\mathrm{e}\gamma}$	$\leq$	0.7	nsec,
	$\mathbf{50}$	$\leq$	$\theta_{\mathrm{e}\gamma}$	$\leq$	$\mathbf{150}$	mrad,
	-50	$\leq$	$\phi_{\mathrm{e}\gamma}$	$\leq$	50	mrad

A pair of a positron and a gamma is selected by `PositronSelection` and `GammaSelection`.

6.2 Likelihood Analysis

In order to take into account the event-by-event difference of the detector responses due to the time-dependence, position-dependence and the per-errors, the likelihood function is defined as

$$\mathcal{L}(N_\mathrm{sig}, N_\mathrm{RMD}, N_\mathrm{BG}) = \frac{e^{-N_\mathrm{obs}}}{N_\mathrm{obs}!} e^{-\frac{(N_\mathrm{RMD}-\langle N_\mathrm{RMD}\rangle)^2}{2\sigma^2_\mathrm{RMD}}} e^{-\frac{(N_\mathrm{BG}-\langle N_\mathrm{BG}\rangle)^2}{2\sigma^2_\mathrm{BG}}} \times \prod_{i=1}^{N_\mathrm{obs}} (N_\mathrm{sig} S(\overrightarrow{x_i}) + N_\mathrm{RMD} R(\overrightarrow{x_i}) + N_\mathrm{BG} B(\overrightarrow{x_i})) \tag{6.1}$$

where N_sig, N_RMD and N_BG are best fit values, which maximize the likelihood, of the number of signal events, radiative muon decay events and the accidental background events respectively, and $\langle N_\mathrm{RMD}\rangle$ and $\langle N_\mathrm{BG}\rangle$ are expected number of RMD and that of accidental background calculated from E_γ and time sideband data respectively. Here $\langle N_\mathrm{RMD}\rangle$ and $\langle N_\mathrm{BG}\rangle$ are evaluated from the time and the angle sidebands data and constrained by σ_RMD and σ_BG, which are also evaluated from the sidebands. $S(\overrightarrow{x_i})$, $R(\overrightarrow{x_i})$ and $B(\overrightarrow{x_i})$

represent PDFs, which depend on the vector of the event-by-event observables($\overrightarrow{x_i}$), for signal events, RMD events and accidental backgrounds, respectively. Here we define the observable as $\overrightarrow{x_i} = (E_\gamma, E_\mathrm{e}, t_{\mathrm{e}\gamma}, \phi_{\mathrm{e}\gamma}, \theta_{\mathrm{e}\gamma})_i$.

6.3 PDF

Since the detector responses depend on the gamma ray positions inside the LXe detector, the fitting quality of the positron track, the correlated measurement values and so on, the event-by-event PDFs of the observables are defined for signal and backgrounds. The background PDFs are determined for the radiative muon decay background (RMD) and the accidental background (BG) separately. Most of parameters of PDFs are extracted from the data outside of the blind box and some of them are calculated from the MC simulation. In the new analysis, per-errors are introduced as already mentioned in Sec. 3.2.6.2. Since we adopt the blind analysis procedure, all PDF parameters are determined and fixed before opening the blind-box. In this section, the details of each PDF, the methods to extract the all parameters, and the systematic uncertainty on each variable are described.

6.3.1 Category PDF

In the previous analysis, two categories called *PositronCategory* of E_e PDFs were defined depending on the quality of the positron track reconstruction (high or low quality tracks), instead of using the per-errors. The positrons are categorized as high quality tracks if they satisfy the following conditions:

- the number of hits is larger than nine,
- less fitting uncertainties of the momentum, the angle and the chi squared of fit,
- differences between the positions reconstructed by the track fitting and the positions which are measured by the timing counter are less than 4 cm.

Then the high quality E_e PDF and the low quality E_e were constructed separately. In each PDF, the energy resolution is defined as a constant parameter. In order to distinguish the PDFs used in previous/present analysis easily, they are called a category/per-event PDF, respectively, hereafter. For the new datasets, we also tested the maximum likelihood fitting by using the category PDF. The *PositronCategory* is also used in the per-event PDF as a parameter to separate the precision of the positron time measurement.

6.3.2 Signal PDF

In the signal E_e, $\phi_{\mathrm{e}\gamma}$ and $\theta_{\mathrm{e}\gamma}$ PDFs, per-errors from the positron-track fitting are newly introduced, while with the previous analysis the averaged PDFs are used with two categories divided by the quality of the position-track fitting. It means that a resolution (σ) is replaced by a product of a sigma of pull (s) and a per-event error (σ') which is calculated by the new Kalman. The correlations between pulls (p') are used instead of

those between raw observables (p) because (p') is found to be constant in the MC while p depends on the per-errors.

The notations used in this section are following.

δ	An error; a difference between the estimated and the true value
μ	A center of the PDF
σ	A resolution of the variable
σ'	An uncertainty of the estimated value
s	A σ of the pull
f	A fraction of the component when a PDF consists of several components
p	A slope parameter between two variables
p'	A slope parameter between pulls of two variables
ρ	A correlation parameter between two variables
ρ'	A correlation parameter between pulls of two variables

The signal PDF is written as:

$$\begin{aligned} S(E_\gamma, E_\mathrm{e}, t_{\mathrm{e}\gamma}, \phi_{\mathrm{e}\gamma}, \theta_{\mathrm{e}\gamma} | u_\gamma, v_\gamma, w_\gamma, x_\mathrm{e}, y_\mathrm{e}, z_\mathrm{e}, \phi_\mathrm{e}) \quad = \quad & S(t_{\mathrm{e}\gamma} | E_\gamma, E_\mathrm{e}) \times \\ & S(E_\gamma | u_\gamma, v_\gamma, w_\gamma) \times \\ & S(E_\mathrm{e} | \phi_\mathrm{e}) \times \\ & S(\phi_{\mathrm{e}\gamma} | u_\gamma, v_\gamma, w_\gamma, x_\mathrm{e}, y_\mathrm{e}, z_\mathrm{e}, \theta_{\mathrm{e}\gamma}, E_\mathrm{e}, \phi_\mathrm{e}) \times \\ & S(\theta_{\mathrm{e}\gamma} | u_\gamma, v_\gamma, w_\gamma, x_\mathrm{e}, y_\mathrm{e}, z_\mathrm{e}, E_\mathrm{e}). \end{aligned} \tag{6.2}$$

6.3.2.1 E_e PDF

The positron-energy response is evaluated by fitting the kinematic edge of the Michel spectrum in the time sideband. By using the same data, parameters for the accidental E_e PDF are measured as well as for the signal E_e PDF. In order to extract the PDF parameters, the theoretical Michel spectrum multiplied by an energy-dependent detector acceptance approximated by an error function is convolved with a response function modeled by a sum of two Gaussian functions with σ'_{E_e} scaled by sigmas of pulls (s_core, s_tail). The fit results are shown in Table 6.1. The energy scale is also calibrated with the fitting. The fitting function is similar to Eq. (5.6), but it is modified to adapt the per-event scheme as

$$\sum_i^{N_\mathrm{data}} (\mathrm{(Michel)} * \mathrm{(Acceptance)}({E_\mathrm{e}}^\mathrm{true}) \otimes \mathrm{(Resolution)}_i), \tag{6.3}$$

where $\mathrm{(Resolution)}_i$ is defined as

$$\mathrm{(Resolution)}_i = f_\mathrm{core} \cdot \mathcal{G}(\mu_\mathrm{core}, s_\mathrm{core} \cdot \sigma'_{E_\mathrm{e}}) + (1 - f_\mathrm{core}) \cdot \mathcal{G}(\mu_\mathrm{tail}, s_\mathrm{tail} \cdot \sigma'_{E_\mathrm{e}}), \tag{6.4}$$

where $\mathcal{G}$ is a Gaussian function and f_core represents the fraction of core Gaussian. We measure the dependence of energy-bias on ϕ_e and θ_e and correct them by shifting data to make the Michel edge independent of the angles. We do not correct the remaining global biases after correcting the angle dependence, but the mean parameters of the PDFs are modified to fit to the biases. In order to extract the $s_\mathrm{core,tail}$ and $\mu_\mathrm{core,tail}$, we fit the function defined by Eq. (6.3) to the data, which is outside of the $t_{\mathrm{e}\gamma}$ center to avoid the contamination of the positrons from RMD, while fixing the parameters of the acceptance

function. Acceptance parameters are extracted from the result of the fitting to the same data with Eq. (5.6).

The systematic uncertainties of PDF parameters are given as covariance matrices from the fitting since there are correlations between different parameters as shown in Fig. 6.3. For the signal PDF, μ_{core}, s_{core} and acceptance parameters (μ_{Acc} and σ_{Acc}, the mean and the width parameters of the error function for representing the acceptance) are fixed. For the accidental background PDF, the correlations in the acceptance parameters and resolution parameters are taken into account.

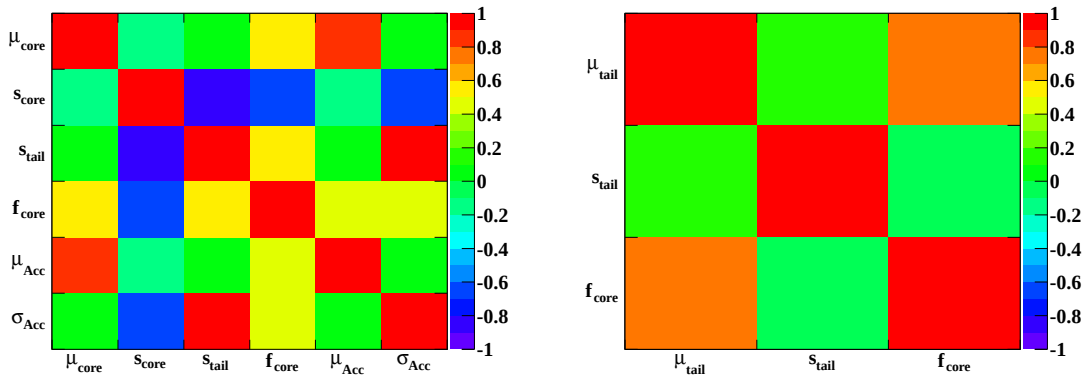

(a) (b)

Figure 6.3: Calculated covariance matrices, (a) for the accidental background PDF, and (b) the signal PDF for 2009 data set.

The global energy scale uncertainty is estimated to be 25 keV by the study with MC; the accuracy of the determination of the energy scale with the Michel fit on the MC samples.

Table 6.1: Parameters for positron energy response. Since errors on all variables are implemented as a covariance matrix in the PDF, they are not shown in this table.

Parameter	2009	2010	2011
f_{core}	0.85	0.85	0.855
μ_{core} (keV)	-5	-12	14
s_{core}	0.98	0.925	0.85
μ_{tail} (keV)	-5	-12	14
s_{tail} (keV)	5.1	4.5	4.12
μ_{Acc} (MeV)	48.64	49.49	49.2
σ_{Acc} (MeV)	2.74	2.73	2.62

6.3.2.2 Angular PDF

The positron angular and vertex resolutions are formed from σ' and s and then the correlations are taken into account; they are therefore event-by-event. Correlations are also implemented as per-event. The general definitions of the per-event slope and the correlation parameter (p'_{xy} and ρ'_{xy}) between two observables (x and y) are:

$$\frac{d\mu_{y/\sigma'_y}}{dx/\sigma'_x} = p'_{xy} \tag{6.5}$$

$$= \rho'_{xy}\frac{s_y}{s_x}. \tag{6.6}$$

In the likelihood analysis, we can identify:

$$\sigma_x = s_x\sigma'_x \tag{6.7}$$

$$p_{xy} = p'_{xy}\frac{\sigma'_y}{\sigma'_x}. \tag{6.8}$$

When a correlation is corrected in the PDF, a resolution is reduced by using s_{inner} defined as:

$$s_{xy,\mathrm{inner}} = s_{xy}\sqrt{1-\rho'^2_{xy}}. \tag{6.9}$$

The angle and the positron-energy PDF for signal is written as:

$$P(\phi_{e\gamma},\theta_{e\gamma},E_e) = P(\phi_{e\gamma} \mid \theta_{e\gamma},E_e) \times P(\theta_{e\gamma} \mid E_e) \times P(E_e), \tag{6.10}$$

where $P(E_e)$ is defined in Sec. 6.3.2.1. In Sec. 6.3.2.3, we describe each correlation. The constant parameters used in the PDFs as well as the systematic uncertainties are summarized in Table 6.2 for sigmas of pulls and in Table 6.3 for correlations. In Sec. 6.3.2.4, the incorporation of the per-event errors and the correlations to the PDF is described.

Table 6.2: Sigmas of pulls for positron angular and vertex responses.

Parameter	2009	2010	2011
$s_{\phi_e,\mathrm{min}}$	0.73 ± 0.07	0.74 ± 0.07	0.74 ± 0.07
s_{θ_e}	1.17 ± 0.05	1.22 ± 0.05	1.25 ± 0.05
$s_{y_e,\mathrm{inner}}$	0.74 ± 0.03	0.73 ± 0.03	0.72 ± 0.03
s_{z_e}	1.16 ± 0.06	1.28 ± 0.06	1.31 ± 0.07

6.3.2.3 Correlations

There are several correlations among the positron observables which are known to be due to the constraint from the fixed target plane, for example, if a positron momentum (E_e) is mis-reconstructed, the ϕ angle of the positron (ϕ_e) and y position of the positron at the target (y_e) are moved from their true values according to the $\delta E_e = E_e^{\mathrm{reconstructed}} -$

Table 6.3: Parameters for the correlations and their uncertainties.

Parameter	2009	2010	2011
$\sigma_{\phi_e}(0)$ [mrad]	8.7 ± 1.4	9.5 ± 1.6	9.8 ± 1.6
k_ϕ [mrad]	7.6 ± 1.1	9.2 ± 1.3	8.4 ± 1.2
c_ϕ [mrad]	-1.7 ± 0.4	-1.7 ± 0.4	-1.7 ± 0.4
$p_{E_e y_e}$ [mm/GeV]	537 ± 5	513 ± 5	516 ± 5
$p'_{\theta_e z_e}$	0.9 ± 0.2	0.9 ± 0.2	0.9 ± 0.2

E_e^{true}. In the previous analysis, the correlation was already included based on the simple geometrical model (See Appendix A). The source of the correlations is almost same as it was included in the category PDF, however, the treatment of them in the new analysis differs from those in the previous analysis. In the category PDF, correlation parameters p_x and ρ_x are implemented as constant parameters while they are no longer constants in the per-event PDF, since these parameters depend on the energy, angular and vertex resolutions and values of resolutions are different in the per-event PDF. We therefore define new correlation parameters p'_x and ρ'_x instead of using p_x and ρ_x as already mentioned and they are independent on the values of the per-event resolutions.

Most of correlation parameters are extracted by analyzing two-turn events and others are calculated from the monte carlo simulation.

σ_{ϕ_e} depending on ϕ_e The ϕ_e resolution $\sigma_{\phi_e}(\phi_e)$ is a function of ϕ_e. This effect is embedded in σ'_{ϕ_e}. In the PDF, $s_{\phi_e,\text{inner}}$, where the $\delta\phi_e$-δE_e correlation is corrected for, is used. Because the correlation depends on ϕ_e, $s_{\phi_e,\text{inner}}$ also depends on ϕ_e as:

$$s_{\phi_e,\text{inner}} = s_{\phi_e,\text{min}} \sqrt{\frac{1 - ({c_\phi}^2 - 2c_\phi k_\phi \tan\phi_e)/\sigma^2_{\phi_e}(0)}{1 + \left(\frac{k_\phi}{\sigma_{\phi_e}(0)} \tan\phi_e\right)^2}}, \tag{6.11}$$

where $s_{\phi_e,\text{min}}$ is $s_{\phi_e,\text{inner}}(\phi_e)$ at ϕ_e where it is minimized. An offset parameter c_ϕ is added. The parameters $\sigma_{\phi_e}(0)$ and k_ϕ are extracted from data by using the two-turn method, and c_ϕ is extracted from the signal MC with a 25% uncertainty conservatively.

$\delta\phi_e$ v.s. δE_e correlation The center of $\phi_{e\gamma}$ PDF is shifted event-by-event by using $p'_{E_e\phi_e}$, which is ϕ_e dependent as:

$$p'_{E_e\phi_e} = \frac{c_\phi - k_\phi \tan\phi_e}{\sqrt{\sigma^2_{\phi_e}(0) + (k_\phi \tan\phi_e)^2}}. \tag{6.12}$$

The effect on the resolution is included in $s_{\phi_e,\text{inner}}$. The constant term in the $\delta\phi_e$-δE_e correlation was used for a systematic uncertainty in the previous analysis, but not included in this time because this uncertainty is included in the systematic uncertainties of μ_{ϕ_e} and μ_{θ_e}; the numbers are written in Sec. 7.4.

$\delta y_{\rm e}$ v.s. $\delta E_{\rm e}$ correlation The same correlation used in the previous analysis is used for the per-event PDF since $p_{E_{\rm e}y_{\rm e}} = p'_{E_{\rm e}y_{\rm e}} \cdot (\sigma'_{y_{\rm e}}/\sigma'_{E_{\rm e}})$ is found to be almost constant. The value of $p_{E_{\rm e}y_{\rm e}}$ is the same as in the average PDF. It is used to calculate the center of $\phi_{\rm e\gamma}$ and $\theta_{\rm e\gamma}$ PDFs.

$$\mu_{\delta y_{\rm e}} = p_{E_{\rm e}y_{\rm e}} \delta E_{\rm e} \tag{6.13}$$

The value of $p_{E_{\rm e}y_{\rm e}}$ is extracted from the data by using the two-turn method. The effect on the resolution is included in $s_{y_{\rm e},\rm inner}$.

$\delta z_{\rm e}$ v.s. $\delta\theta_{\rm e}$ correlation Unlike the $\delta y_{\rm e}$-$\delta E_{\rm e}$ correlation, the $\delta z_{\rm e}$-$\delta\theta_{\rm e}$ correlation can not be used for shifting the center of the PDF because the true value of $\theta_{\rm e}$ of the signal event can not be known. Due to the correlation, $\delta\theta_{\rm e}$ and $\delta\theta_\gamma$ are not independent; therefore $\sigma_{\theta_{\rm e\gamma}}$ is not a quadratic sum of $\sigma_{\theta_{\rm e}}$ and σ_{θ_γ}. The correlation is taken into account when $\sigma_{\theta_{\rm e\gamma}}$ is calculated by adding a correlation term using $\rho_{\theta_{\rm e}\theta_\gamma}$ defined as,

$$\begin{aligned}
\rho_{\theta_{\rm e}\theta_\gamma} &= p_{\theta_{\rm e}\theta_\gamma} \frac{\sigma_{\theta_{\rm e}}}{\sigma_{\theta_\gamma}} && (6.14)\\
&= C_z p_{\theta_{\rm e}z_{\rm e}} \frac{s_{\theta_{\rm e}}\sigma'_{\theta_{\rm e}}}{\sqrt{C_z^2 s_{z_{\rm e}}^2 \sigma'^2_{z_{\rm e}} + \sigma^2_{\theta_{\rm XEC}}}} && (6.15)\\
&= C_z p'_{\theta_{\rm e}z_{\rm e}} \frac{s_{\theta_{\rm e}}\sigma'_{z_{\rm e}}}{\sqrt{C_z^2 s_{z_{\rm e}}^2 \sigma'^2_{z_{\rm e}} + \sigma^2_{\theta_{\rm XEC}}}}, && (6.16)
\end{aligned}$$

where $\sigma_{\theta_{\rm XEC}}$ is a component from the gamma position resolutions in $\sigma_{\theta_{\rm e\gamma}}$. It is assumed that $\delta z_{\rm e}$ can be linearly scaled to $\delta\phi_\gamma$ by using a conversion factor C_z.

The correlation term of the $\theta_{\rm e\gamma}$ resolution is

$$\begin{aligned}
2\rho_{\theta_{\rm e}\theta_\gamma}\sigma_{\theta_{\rm e}}\sigma_{\theta_\gamma} &= 2\rho_{\theta_{\rm e}\theta_\gamma} s_{\theta_{\rm e}}\sigma'_{\theta_{\rm e}} \sqrt{C_z^2 s_{z_{\rm e}}^2 \sigma'^2_{z_{\rm e}} + \sigma^2_{\theta_{\rm XEC}}} && (6.17)\\
&= 2 s_{\theta_{\rm e}}\sigma'_{\theta_{\rm e}} C_z p'_{\theta_{\rm e}z_{\rm e}} s_{\theta_{\rm e}}\sigma'_{z_{\rm e}}. && (6.18)
\end{aligned}$$

In the PDF, $C_z p'_{\theta_{\rm e}z_{\rm e}} s_{\theta_{\rm e}}\sigma'_{z_{\rm e}}$ is replaced by a general function to translate $\sigma_{y_{\rm e}}$ and $\sigma_{z_{\rm e}}$ to the resolution of $\theta_{\rm e\gamma}$ as in Eq. (6.23). The value of $p'_{\theta_{\rm e}z_{\rm e}}$ is extracted from the signal MC and the 25% uncertainty is conservatively assigned.

$\delta\phi_{\rm e\gamma}$ v.s. $\delta\theta_{\rm e\gamma}$ correlation A slope parameter $p'_{\phi_{\rm e\gamma}\theta_{\rm e\gamma}}$ is used to shift the center of the $\phi_{\rm e\gamma}$ PDF. To modify the event-by-event $\phi_{\rm e\gamma}$ resolution, $\rho'_{\theta_{\rm e}\phi_{\rm e}}$ and $\rho'_{z_{\rm e}\phi_{\rm e}}$ are used as the two correlations are independent. Since these correlations are evaluated from MC, 25% uncertainties are conservatively assigned.

$$\begin{aligned}
p'_{\theta_{\rm e\gamma}\phi_{\rm e\gamma}} &= -0.17 + 0.114\,\phi_{\rm e} - 0.294\,{\phi_{\rm e}}^2 - 0.195\,{\phi_{\rm e}}^3 && (6.19)\\
p'_{\theta_{\rm e}\phi_{\rm e}} &= 0.60 - 0.13\,\phi_{\rm e} - 0.21\,{\phi_{\rm e}}^2 && (6.20)\\
p'_{z_{\rm e}\phi_{\rm e}} &= 0.24 - 0.036\,\phi_{\rm e} + 0.14\,{\phi_{\rm e}}^2. && (6.21)
\end{aligned}$$

6.3.2.4 Incorporation of correlations in signal PDF

The center of $P(\theta_{e\gamma} \mid E_e)$ is shifted for the correlation by:

$$\mu_{\theta_{e\gamma}} = \mathcal{F}_\theta(p_{E_e y_e} \delta E_e), \tag{6.22}$$

where $\mathcal{F}_\theta(\delta y_e)$ is a function to translate δy_e to $\delta\theta_\gamma$ with taking into account the position of the muon vertex, the gamma-ray conversion position and the target geometry. The $\theta_{e\gamma}$ resolution is modified to take into account the correlations as:

$$\sigma_{\theta_{e\gamma}} = \sqrt{s^2_{\theta_e}\sigma'^2_{\theta_e} + \mathcal{G}^2_\theta(s_{y_e,\mathrm{inner}}\sigma'_{y_e}, s_{z_e}\sigma'_{z_e}) + 2\mathcal{G}_\theta(0, p'_{\theta_e z_e} s_{\theta_e}\sigma'_{z_e}) s_{\theta_e}\sigma'_{\theta_e} + \sigma^2_{\theta_{\mathrm{XEC}}}}, \tag{6.23}$$

where $\mathcal{G}_\theta(\sigma_{y_e}, \sigma_{z_e})$ is a function to translate σ_{y_e} and σ_{z_e} to the resolution of $\theta_{e\gamma}$ with taking into account the position of the muon vertex, the gamma-ray conversion position and the target geometry.

Similarly, the center of the $\phi_{e\gamma}$ PDF is shifted by:

$$\mu_{\phi_{e\gamma}} = p'_{E_e\phi_e}\frac{\sigma'_{\phi_e}}{\sigma'_{E_e}}\delta E_e + p'_{\theta_{e\gamma}\phi_{e\gamma}}\frac{\sigma'_{\phi_{e\gamma}}}{\sigma'_{\theta_{e\gamma}}}\theta_{e\gamma} + \mathcal{F}_\phi(p_{E_e y_e}\delta E_e), \tag{6.24}$$

where $\mathcal{F}_\phi(\delta y_e)$ translates δy_e to $\delta\phi_\gamma$ similarly to $\mathcal{F}_\theta(\delta y_e)$. The $\phi_{e\gamma}$ resolution is modified as:

$$\sigma_{\phi_{e\gamma}} = \sqrt{s^2_{\phi_e,\mathrm{inner}}\sigma'^2_{\phi_e}\left(1-\rho'^2_{\theta_e\phi_e}\right)\left(1-\rho'^2_{z_e\phi_e}\right) + \mathcal{G}^2_\phi(s_{y_e,\mathrm{inner}}\sigma'_{y_e}, s_{z_e}\sigma'_{z_e}) + \sigma^2_{\phi_{\mathrm{XEC}}}}, \tag{6.25}$$

where $\mathcal{G}_\phi(\sigma_{y_e}, \sigma_{z_e})$ is a function to translate σ_{y_e} and σ_{z_e} to the resolution of $\phi_{e\gamma}$ similarly to $\mathcal{G}_\theta(\sigma_{y_e}, \sigma_{z_e})$, and $\sigma_{\phi_{\mathrm{XEC}}}$ is σ_ϕ from the gamma-ray position resolutions.

6.3.2.5 E_γ PDF

Since we measure the energy responses at different regions of the LXe detector from the CEX data as already described in Sec. 5.1.3, the position dependent E_γ PDF is used on an event-by-event basis according to the reconstructed first conversion point of the gamma ray. In the muon beam condition, the pileup effect differs from that in the pion beam condition. Therefore the convoluted pedestal function (h_{π^0}) in Eq. (5.1) is disentangled and the pedestal function in the muon beam (h_μ) is convoluted and the peak position of the PDF is shifted from 55 MeV to 52.8 MeV.

6.3.2.6 $t_{e\gamma}$ PDF

The new tracking algorithm provides new information about the TC-DC matching, $TCMatchingQuality$. The definition of the variable is given in Sec. 3.2.6.1. The events are classified by this parameter as well as the positron category ($PositronCategory$) representing the quality of positron time measurements. Figure 6.4(a) shows the measured $t_{e\gamma}$ PDFs for the different categories. It is found that the variable $TCMatchingQuality$ well separates the events having different time centers while $PositronCategory$ separates events with different precision. Therefore, in this analysis we separately implement $t_{e\gamma}$ PDFs of signal and RMD for categories defined by the combination of the two variables (in total six categories). The event fractions of the six categories are shown in Fig. 6.4(b). In each category, the PDF is defined as a double Gaussian and parameters are determined by fitting the RMD peak.

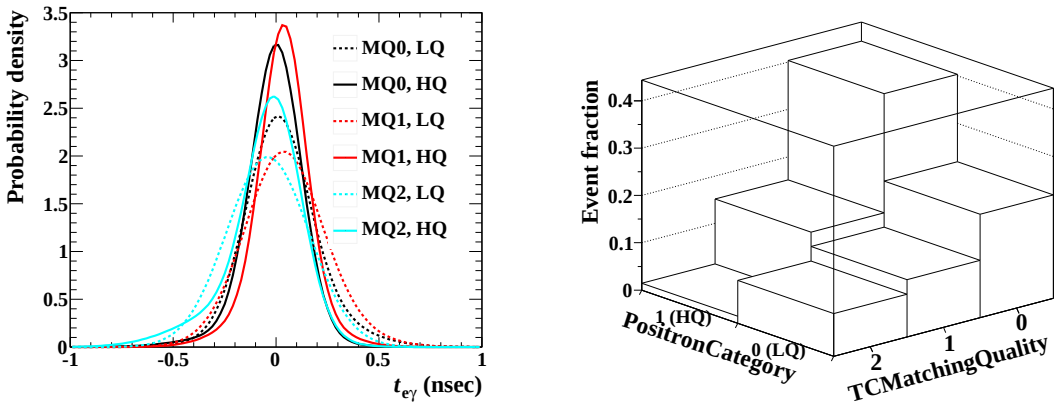

(a) (b)

Figure 6.4: (a) $t_{e\gamma}$ PDFs for different categories (2011). (b) Event fractions of the categories.

$\delta t_{e\gamma}$ v.s. δE_e correlation The correlation between $t_{e\gamma}$ and δE_e, which is observed in the signal MC, is considered in the analysis. The correlation between $t_{e\gamma}$ and δE_e is given by

$$\mu_{\delta_{t_{e\gamma}}} = p_{E_e t_{e\gamma}} \delta E_e, \tag{6.26}$$

where the slope ($p_{E_e t_{e\gamma}}$) is extracted to be 52.81±1.6 psec/MeV from the signal MC.

6.3.3 Accidental Background PDF

The accidental background (BG) PDF is evaluated from the sideband data except for the $t_{e\gamma}$, which is assumed to be a constant function.

$$\begin{aligned} B(E_\gamma, E_e, t_{e\gamma}, \phi_{e\gamma}, \theta_{e\gamma} | u_\gamma, v_\gamma, w_\gamma, \phi_e) &= B(E_\gamma | u_\gamma, v_\gamma, w_\gamma) \times \\ & B(E_e | \phi_e) \times \\ & B(t_{e\gamma}) \times \\ & B(\phi_{e\gamma} | v_\gamma) \times \\ & B(\theta_{e\gamma} | u_\gamma). \end{aligned} \tag{6.27}$$

6.3.3.1 Background E_e PDF

As already mentioned in Sec 6.3.2.1, background E_e PDF is extracted from the data in the time sidebands. These data are fitted by the combined function of the theoretical Michel spectrum and the acceptance error function convolved with the double Gaussian response function according to the event-by-event positron momentum resolution calculated by the per-errors and the correlations.

6.3.3.2 Background E_γ PDF

The background E_γ PDF is determined position-dependently in the same way as the signal E_γ PDF because the fractions of RMD, AIF and cosmic ray (CR) events, which

are all components considered as accidental backgrounds, depend on the position inside the LXe detector. The E_γ spectrum obtained in each position is used as the position-dependent PDF. In order to measure the energy scale stability as mentioned in Sec. 4.1.7, following background modeling is applied. The accidental background E_γ PDF consists of

1. spectrum of gamma ray from RMD in MC,
2. spectrum of gamma ray from AIF in MC,
3. pileup effect from pedestal,
4. detector response,
5. cosmic-ray spectrum in real data,
6. efficiency curves due to the lower and higher trigger threshold.

In order to make the background E_γ PDF including effects above, we use the following methods with the data in both time sidebands. First, the MC distribution of energy deposition in LXe by a single event with gamma ray from RMD or AIF is smeared by using the measured pedestal distribution to take into account the pileup effect. Here the pedestal distribution is shrunk by taking into account the effect of the pileup identification algorithm The shrink factor is determined before fitting and is fixed in the fitting. Then the distribution is convolved with the position-dependent detector response function which is given as a Gaussian; sigma corresponds to the detector resolution and the mean to the energy scale. After adding the CR spectrum measured in the CR runs, the efficiency curves due to the trigger threshold are applied. Here, the trigger efficiency curve is fixed in the fitting. Therefore the fraction of RMD, the fraction of AIF, the resolution, the energy scale, the fraction of CR background and the vertical scaling factor are free parameters when we fit the data with this function. Figure 6.5 shows the background E_γ PDF.

6.3.3.3 Background Angular PDFs

We extracted relative angle ($\phi_{e\gamma}$ and $\theta_{e\gamma}$) PDFs from the time sideband data by using the selection which used for the analysis region apart from looser angular cuts as $|\phi_{e\gamma}| <$ 200 mrad, $|\theta_{e\gamma}| <$ 200 mrad and $E_\gamma >$ 46 MeV in order to gain the statistics. The background $\phi_{e\gamma}$ ($\theta_{e\gamma}$) distribution is divided in five slices of v_γ (u_γ) region and each of them is fitted with a 5th degree polynomial function. The uncertainties on the background angular PDFs are taken into account in the likelihood analysis using the error covariance matrices of the fitting.

6.3.4 RMD PDF

In the RMD events, E_γ, E_e, $\phi_{e\gamma}$ and $\theta_{e\gamma}$ are kinematically correlated. In order to construct the RMD PDFs, the correlations between different observables are taken into account by

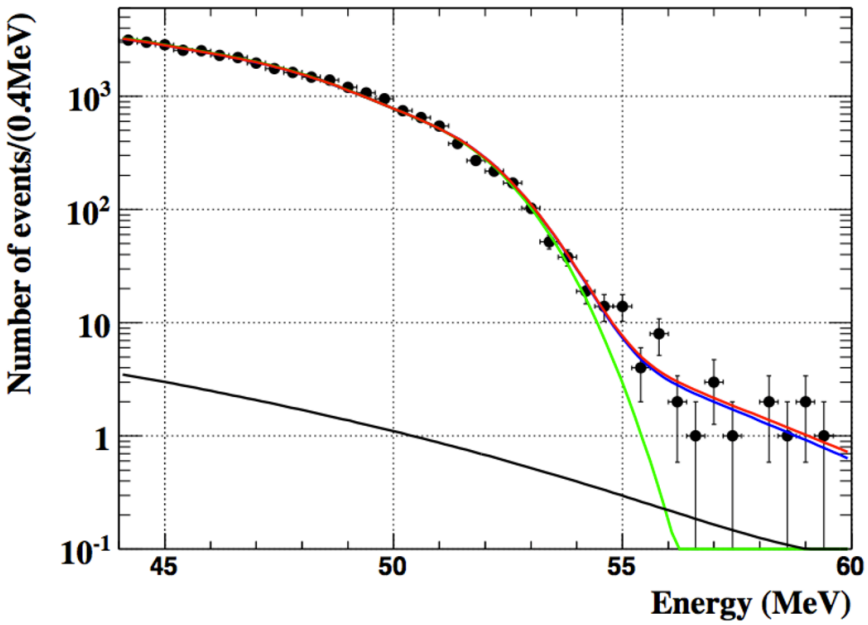

Figure 6.5: An example of the spectrum of the accidental background gamma rays used for the PDF in depth is larger than 2 cm in time sideband. Green line is extracted from the MC distribution of RMD and AIF, Blue line show that convolved with resolution and pedestal, namely acceptance. Solid black line is contribution from cosmic-ray background and Red one shows sum of the blue one and black one.

using the theoretical formula of the RMD given as [14]

$$dB(\mu^+ \to e^+\nu_e\overline{\nu}_\mu\gamma) = \frac{\alpha}{64\pi^3}\beta dx\frac{dy}{y}d\Omega_e d\Omega_\gamma \times \left[F(x,y,d) - \beta\vec{P}_\mu\cdot\hat{p}_e G(x,y,d) - \vec{P}_\mu\cdot\hat{p}_\gamma H(x,y,d)\right]. \quad (6.28)$$

Here $\vec{P}_\mu$ is the muon polarization vector;$\vec{p}_e$ and $\vec{p}_\gamma$ are momenta of the positron and the gamma in the muon rest frame, respectively;$\hat{p}_e$ and $\hat{p}_\gamma$ are their unit vectors defined as $\hat{p}_x \equiv \vec{p}_x/|\vec{p}_x|$ (x = e or γ);β is defined as $\beta \equiv |\vec{p}_e|/E_e$;$d$ is given by $d \equiv 1 - \beta\cdot\hat{p}_\gamma$; and x and y are normalized positron and gamma energies. The allowed ranges of x and y are constrained by the four-body kinematics, electron mass and muon mass. $F(x,y,d)$, $G(x,y,d)$ and $H(x,y,d)$ in the SM are given in Appendix B. As already mentioned in Sec. 2.1.3, we measure the muon polarization at the stopping target. Therefore the muon polarization is set to be $\vec{P}_\mu = 0.89$ in Eq. (6.28). The RMD PDF is defined as follow:

$$\begin{aligned} R(E_\gamma, E_e, t_{e\gamma}, \phi_{e\gamma}, \theta_{e\gamma}|u_\gamma, v_\gamma, w_\gamma, \phi_e, \theta_e) = {} & R(E_\gamma|u_\gamma, v_\gamma, w_\gamma, \theta_e, E_e, \phi_{e\gamma}, \theta_{e\gamma}) \times \\ & R(E_e|\phi_e, \theta_e, \phi_{e\gamma}, \theta_{e\gamma}) \times \\ & R(t_{e\gamma}|E_\gamma, E_e) \times \\ & R(\phi_{e\gamma}|u_\gamma, v_\gamma, w_\gamma, \phi_e, \theta_e, \theta_{e\gamma}) \times \\ & R(\theta_{e\gamma}|u_\gamma, v_\gamma, w_\gamma, \theta_e), \end{aligned} \quad (6.29)$$

where $R(E_\gamma|u_\gamma, v_\gamma, w_\gamma, \theta_e, E_e, \phi_{e\gamma}, \theta_{e\gamma})$, $R(E_e|\phi_e, \theta_e, \phi_{e\gamma}, \theta_{e\gamma})$, $R(\phi_{e\gamma}|u_\gamma, v_\gamma, w_\gamma, \phi_e, \theta_e, \theta_{e\gamma})$ and $R(\theta_{e\gamma}|u_\gamma, v_\gamma, w_\gamma, \theta_e)$ are determined by using Eq. (6.28) considering the detector performance (e.g. resolutions, acceptance of each sub-detector).

6.3.4.1 RMD $t_{e\gamma}$ PDF

The same $t_{e\gamma}$ PDF, as for the signal, but without correcting the $\delta t_{e\gamma}$ v.s. δE_e correlation, is used as the $t_{e\gamma}$ PDF of RMD event. because the mean value of E_e cannot be defined in the RMD event.

6.3.5 Illustration of PDFs

Figure 6.6 shows the average PDFs for the 2009–2011 combined dataset in the analysis region. They are shown only for illustrative-purposes, and not used in the analysis.

In comparison with the average PDFs, two examples of the event-by-event PDFs are shown in Fig. 6.7. Figure 6.7(a) shows the PDFs in the event, in which the positron-track reconstructed with the good quality, observed in the time sideband. On the other hand, Figure 6.7(b) shows the PDFs with worse tracking quality,

6.4 Confidence Region

In order to estimate the upper limit on the number of signal events, we adopt the statistical approach, which is known as the Feldman-Cousins approach [58], with the profile-likelihood ordering as already done in the past analysis [4] because that approach is

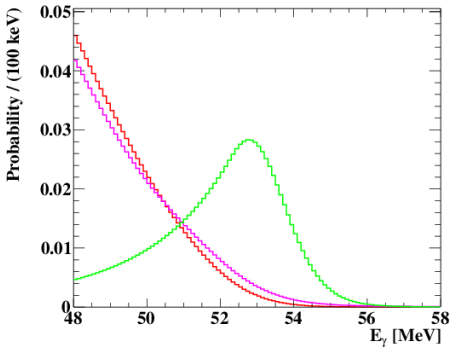

(a) E_γ PDF

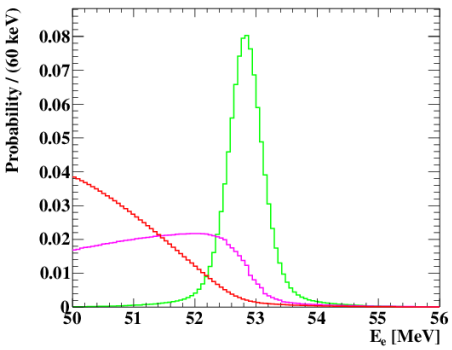

(b) E_e PDF

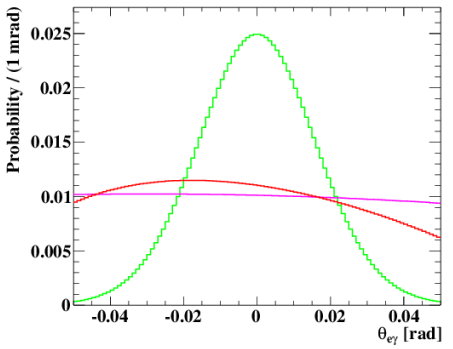

(c) $\theta_{\mathrm{e}\gamma}$ PDF

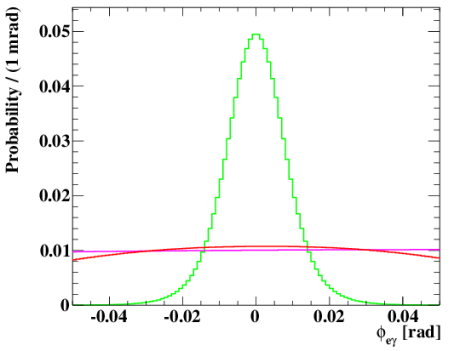

(d) $\phi_{\mathrm{e}\gamma}$ PDF

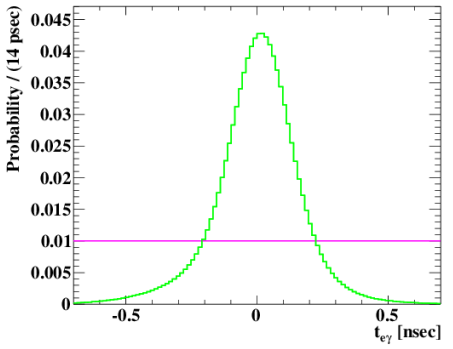

(e) $t_{\mathrm{e}\gamma}$ PDF

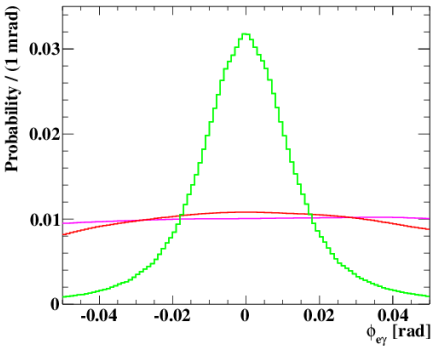

(f) $\phi_{\mathrm{e}\gamma}$ PDF without correcting correlations

Figure 6.6: Average PDFs for the 2009–2011 combined dataset. The green, red and magenta lines show the signal, RMD and BG PDFs, respectively. The correlations between the errors of positron observables are corrected except for (f).

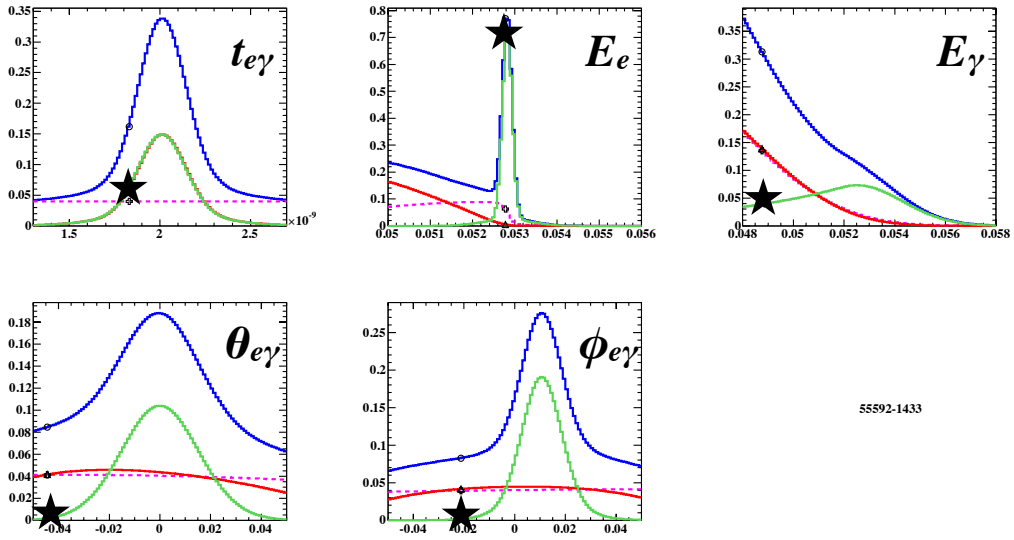

(a) PDFs with better tracking quality

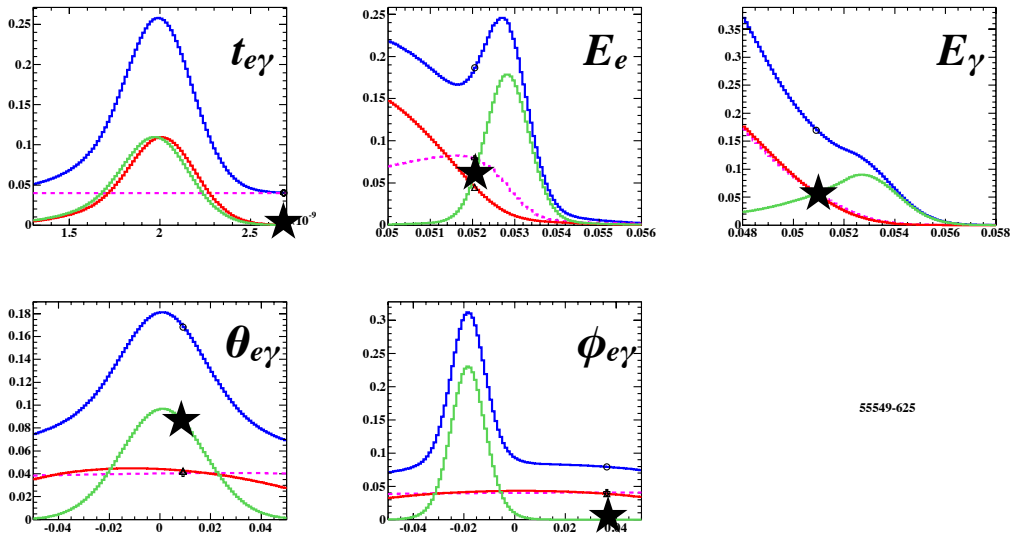

(b) PDFs with worse tracking quality

Figure 6.7: Examples of per-event PDF in typical two events observed in the time sideband. (a) shows PDFs in which the positron-track shows good fitting quality. (b) shows ones in the event with worse fitting quality. Green lines show the signal PDFs, Magenta dashed lines show the accidental background PDFs and red lines show the RMD PDFs. Blue lines are sum of those three PDFs and black stars indicate measured variables.

known to be more accurate method to treat a small number than others. In this method, we generate many toy Monte Carlo experiments (called "toy-MC") by using all PDFs defined in Sec. 6.3 to calculate the confidence level for a given fixed number of signals. The procedure for the calculation of the confidence level is as follows;

1. Calculate the profile-likelihood at j-th toy-MC defined as

$$q^j(N_{\rm sig}) = -2\ln\lambda_{\rm p}^j(N_{\rm sig}), \tag{6.30}$$

$$\lambda_{\rm p}^j(N_{\rm sig}) = \frac{\mathcal{L}(N_{\rm sig}, \hat{\hat{N}}^j_{\rm RMD}(N_{\rm sig}), \hat{\hat{N}}^j_{\rm BG}(N_{\rm sig}))}{\mathcal{L}(\hat{N}^j_{\rm sig}, \hat{N}^j_{\rm RMD}, \hat{N}^j_{\rm BG})}, \tag{6.31}$$

   where $\hat{N}_k$ $(k = {\rm sig}, {\rm RMD}, {\rm BG})$ is the best fit value of the maximum likelihood fit and $\hat{\hat{N}}^j_{\rm RMD}(N_{\rm sig})$ and $\hat{\hat{N}}^j_{\rm BG}(N_{\rm sig})$ are the best fit values for a fixed $N_{\rm sig}$.

2. Calculate $q_i^{\rm Obs}$ on the data in the same way as 1.

3. Find the probability to observe $q(N_{\rm sig})$ which is larger than that observed on the data $(q^{\rm Obs}(N_{\rm sig}))$ as follows;

$$P(N_{\rm sig}) = \sum_j^{N^{\rm MC}} \frac{H(q^j(N_{\rm sig}), q^{\rm Obs}(N_{\rm sig}))}{N^{\rm MC}}, \tag{6.32}$$

$$H(q^j(N_{\rm sig}), q^{\rm Obs}(N_{\rm sig})) = \begin{cases} 1 & (q^j(N_{\rm sig}) > q^{\rm Obs}(N_{\rm sig})), \\ 0 & (otherwise). \end{cases} \tag{6.33}$$

4. Repeat 1–3. and find $N_{\rm sig}$ where the probability become less than 10% to find 90% C.L. intervals.

In the frequentist approach, the probabilities of what $N_{\rm sig}^{\rm obs}$ becomes larger than fixed $N_{\rm sig}$ at each value of $N_{\rm sig}$ are calculated. We therefore set the 90% C.L. lower or upper limit with this method if $P(N_{\rm sig})$ becomes less than 10% at certain lower/upper points of fixed $N_{\rm sig}$ and the bands inside the lower and upper limits are called 90% C.L. intervals. In order to include the effect from the systematic uncertainties, the parameters are randomly fluctuated with their evaluated uncertainties in each toy-MC experiment.

6.4.1 Full-MC study

A reliability check for the newly implemented PDFs is done by a full-MC study. In this study, 100 k signal events are generated using the toy-MC in a wide angular range ($-0.19 \leq \phi_{e\gamma} \leq 0.19$ rad and $-0.19 \leq \theta_{e\gamma} \leq 0.19$ rad) with PDF parameters extracted from the signal full-MC. Then, the agreements of average distributions and correlations between the toy-MC and the full-MC are checked. Figure 6.8(a) shows the comparison of the average true resolutions and those from the toy-MC and they agree well each other. Figure 6.8(b) shows the difference of the correlations observed in the full-MC and those in the toy-MC. $\theta_{e\gamma}$ vs $\phi_{e\gamma}$ correlation shows a small discrepancy between the full-MC and the toy-MC in the large $\theta_{e\gamma}$ region. However, the event fraction of this region is small and the difference is within the level of the systematic uncertainties, namely, the difference is taken into account in the analysis.

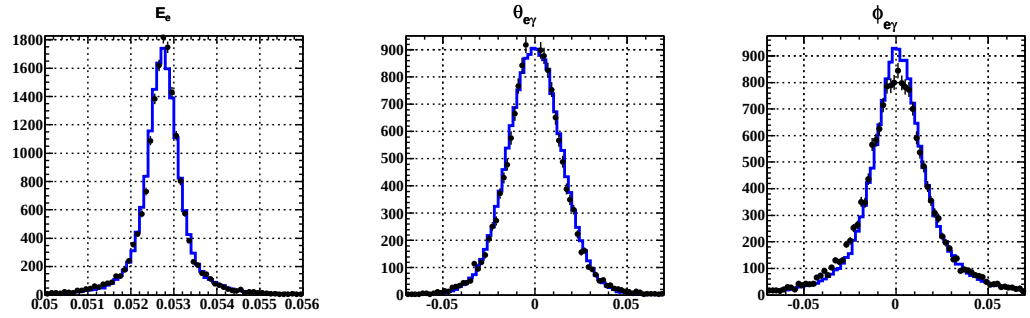

(a)

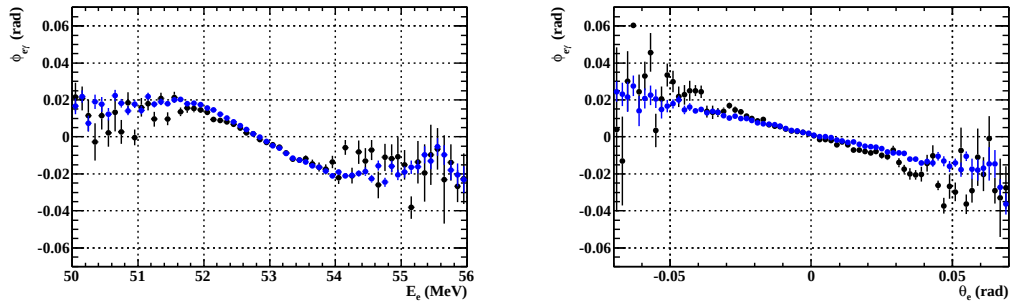

(b)

Figure 6.8: (a) Average distributions of E_{e} (left), $\theta_{\mathrm{e}\gamma}$ (center) and $\phi_{\mathrm{e}\gamma}$ (right) of the full-MC (black markers) and the toy-MC (blue solid line). (b) Average correlations of δE_{e} v.s. $\delta\phi_{\mathrm{e}\gamma}$ (left) and $\delta\theta_{\mathrm{e}\gamma}$ v.s. $\delta\phi_{\mathrm{e}\gamma}$ of the full-MC (black markers) and the toy-MC (blue markers).

6.5 Normalization

The normalization factor (k) is defined by

$$B(\mu^+ \to e^+\gamma) = \frac{N_{\rm sig}}{k} \tag{6.34}$$

to normalize the number of observed events to the branching fraction. In order to calculate the normalization factor, we combine the results from Michel normalization and RMD normalization to reduce the uncertainty. Here we describe the details of the method for each normalization channel and the combined results.

6.5.1 Analysis Efficiency

The analysis inefficiency comes mainly from the tail events outside the analysis window. The escape from angle windows is due to the reconstruction tail, while that from the time window is mainly due to the mis-reconstruction of positron trajectory where one of turns is missed. The inefficiency is evaluated from the MC simulation taking into account the pileup and the detector conditions. The breakdown of the inefficiencies is summarized in Table 6.4. The probability of the missing turn events is also evaluated by comparing the fraction of events showing a characteristic distribution of the reconstructed angle and vertex (Fig. 6.9) between MC and data, and a correction to the MC evaluation is applied from the difference.

Table 6.4: Breakdown of analysis efficiencies

Selection	Michel normalization	RMD normalization
$\lvert t_{e\gamma}\rvert < 0.7$ ns	0.933	1
$\lvert t_{e\gamma}\rvert < 0.7$ ns, $\lvert\theta_{e\gamma}\rvert < 50$ mrad	0.920	0.986
$\lvert t_{e\gamma}\rvert < 0.7$ ns, $\lvert\theta_{e\gamma}\rvert$,$\lvert\phi_{e\gamma}\rvert < 50$ mrad	0.863	0.925

6.5.2 Michel Normalization

The normalization factor from the Michel decay channel ($\mu^+ \to e^+\nu_e\overline{\nu}_\mu$) is written as

$$k_{\rm Michel} = \frac{N^{\rm Obs}_{\rm Michel}}{f_{\rm Michel}} \times ({\rm Prescaling}) \times (P_{\rm corr}) \times p_{\rm DM} \times \frac{\epsilon_{\rm signal}}{\epsilon_{\rm Michel}} \times \epsilon_\gamma \times \epsilon_{\rm analysis}. \tag{6.35}$$

And the definitions of parameters in Eq.(6.35) are written in Sec. 5.2.6 and below.

- $p_{\rm DM}$:
  The efficiency of the trigger direction match for signals since it is not used in the Michel trigger.

- $\epsilon_{\rm signal}/\epsilon_{\rm Michel}$:
  The efficiency ratio of signal/Michel positrons in the analysis region (50–56 MeV). It is calculated by fitting the function, which consists of the theoretical Michel spectrum multiplied with the acceptance function and convolved with the momentum resolution, to data.

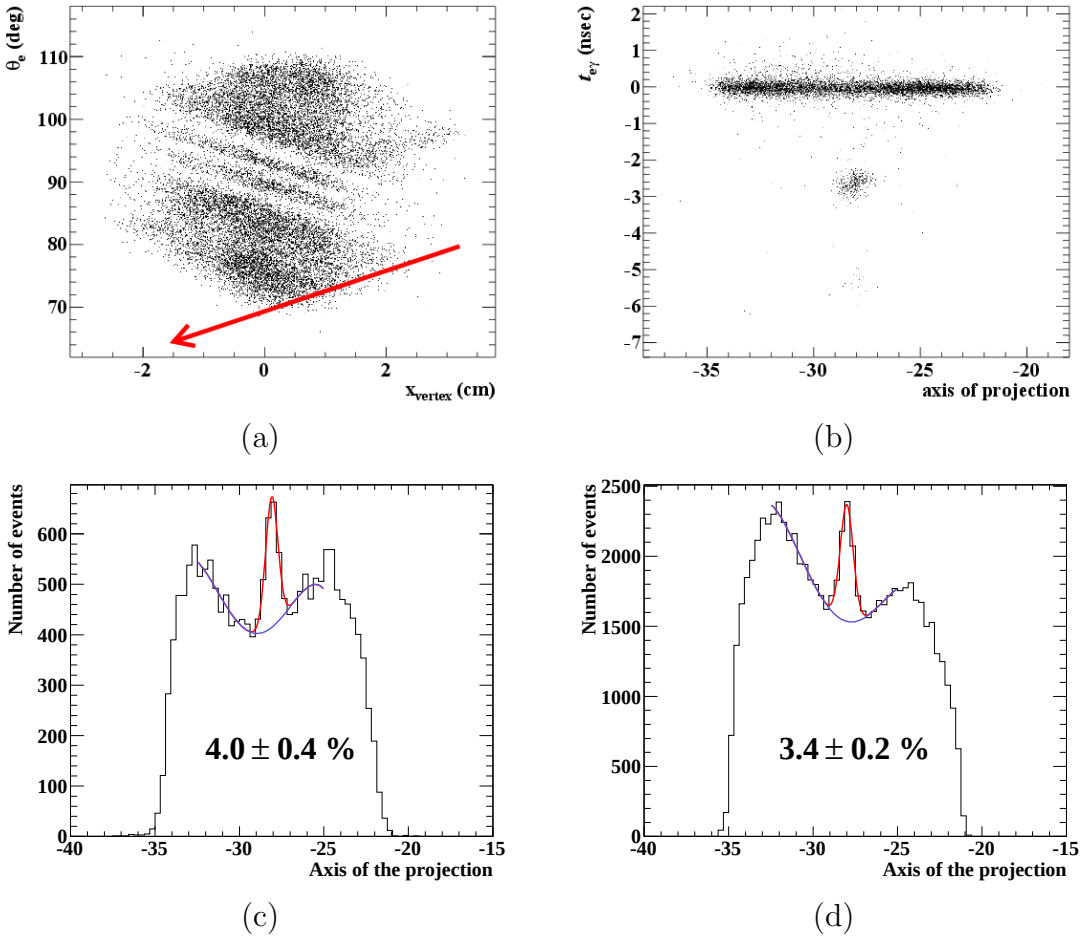

Figure 6.9: (a) Distribution of MC signal events on vertex-angle plane. Missing-turn events make a characteristic pattern on this plane appearing as a band parallel to the red arrow. (b) Scatter plot of the MC events on $t_{e\gamma}$ v.s. a new variable defined by the projection along the red arrow in (a). The missing turn events ranging at the negative $t_{e\gamma}$ are clearly distributed around -28 on the new variable. (c) and (d) show the projected distributions of MC and data (2011), respectively. Fraction of the peak events is estimated by fitting a Gaussian and a quartic function to the distribution and results are shown in (c) and (d).

- ϵ_γ :
  The detection and the analysis efficiency due to the pileup identification and the cosmic-ray rejection for signal γ. See Table 5.7 and Sec. 5.1.5 for more detail.

- $\epsilon_{\text{analysis}}$:
  See Sec.6.5.1.

Because of using the ratio of efficiencies for signal and Michel ($\epsilon_{\text{signal}}/\epsilon_{\text{Michel}}$) to calculate the normalization factor, the large uncertainty due to the instability of the beam intensity and the time-dependence of the efficiency due to the dead channels of DCH are cancelled out. Since the algorithm of the positron-track fitting in the new analysis differs from that in the previous one, the efficiency ratios are different between previous/new estimates.

The results and variables for parameters are shown in Table 6.5 and Table 6.6 for 2009 and 2010, respectively, together with the previous estimates used for the previous publication [4]. In 2011 data, the new waveform analysis for the gamma ray reconstruction has already been included. This means there are only the differences between old Kalman and new Kalman shown in Table 6.7. By comparing the normalization factor of the previous track fitting with that of the new one, the improvement in the efficiency due to the new track fitting is calculated to be 6%. The number of selected positrons is also increased by 6% from the FFT filtering newly applied to the positron track reconstruction. Since a 7% relative efficiency improvement is obtained by new pileup elimination algorithm for gamma rays, we obtained ∼20% total gain of the statistics in comparison with the previous reconstruction algorithms.

Table 6.5: Michel normalization parameters for 2009 data in comparison with the previous estimation

Parameter names	previous estimate	new estimate
$N^{\text{Obs}}_{\text{Michel}}$	15600	19385
Prescaling	1×10^7	1×10^7
P_{corr}	1.14	1.14
p_{DM}	0.915	0.915
$\epsilon_{\text{signal}}/\epsilon_{\text{Michel}}$	1.17	1.09
ϵ_γ	0.99×0.58	0.984×0.645
$\epsilon_{\text{analysis}}$	0.94	0.86
f_{Michel}	0.0991	0.1006
$k^{2009}_{\text{Michel}}(\times 10^{-12})$	1.03±0.09	1.21±0.07

6.5.3 RMD Normalization

The normalization factor from RMD channel is written as

$$k_{\text{RMD}} = \frac{N^{\text{Obs}}_{\text{RMD}}}{\mathcal{B}_{\text{RMD}}} \times \frac{\epsilon_{\text{signal}}}{\epsilon_{\text{RMD}}} \times \epsilon_{\text{analysis}}. \tag{6.36}$$

Since the same data sample as $\mu^+ \to e^+\gamma$ search is used and both positron and gamma-ray are measured, the formula is simpler than Eq. (6.35). Each term is defined as below.

Table 6.6: Michel normalization parameters for 2010 data in comparison with the previous estimation

Parameter names	previous estimate	new estimate
$N^{\rm Obs}_{\rm Michel}$	30670	40597
Prescaling	1×10^7	1×10^7
$P_{\rm corr}$	1.13	1.13
$p_{\rm DM}$	0.922	0.922
$\epsilon_{\rm signal}/\epsilon_{\rm Michel}$	1.23	1.15
ϵ_γ	0.99×0.59	0.631
$\epsilon_{\rm analysis}$	0.94	0.86
$f_{\rm Michel}$	0.0973	0.1006
$k^{2010}_{\rm Michel}(\times 10^{-12})$	2.21±0.20	2.66±0.13

Table 6.7: Michel normalization parameters for 2011 data with old/new Kalman

Parameter names	old Kalman	new Kalman
$N^{\rm Obs}_{\rm Michel}$	51574	59999
Prescaling	1×10^7	1×10^7
$P_{\rm corr}$	1.107	1.107
$p_{\rm DM}$	0.97	0.97
$\epsilon_{\rm signal}/\epsilon_{\rm Michel}$	1.24	1.18
ϵ_γ	0.99×0.628	0.99×0.628
$\epsilon_{\rm analysis}$	0.91	0.86
$f_{\rm Michel}$	0.1006	0.1006
$k^{2011}_{\rm Michel}(\times 10^{-12})$	3.85±0.21	4.10±0.20

- $N^{\rm Obs}_{\rm RMD}$:
  The number of RMD events in a pre-defined window is measured by a binned-likelihood fit to the $t_{e\gamma}$ distribution.

- $\mathcal{B}_{\rm RMD}$:
  The partial branching ratio of RMD in the relevant window is calculated from the theoretical formula (at tree level) convolved with the detector responses.

- $\epsilon_{\rm signal}/\epsilon_{\rm RMD}$:
  The efficiency ratio of signal/RMD can be decomposed into that of positron detection, that of the gamma-ray detection and that of direction match. The positron relative efficiency is evaluated using the acceptance curve extracted from the Michel-spectrum fit. In addition, the momentum-dependent probability of the missing turn is incorporated. The gamma ray relative efficiency is evaluated from the comparison of spectra obtained by the MEG trigger and the trigger♯1 (lower E_γ threshold). The relative efficiency of direction match is evaluated from the distribution of accidental background. The effect of muon polarization, which makes the background distribution non-flat (asymmetric) even in case of a full efficient detector and trigger, is

newly taken into account for this analysis from the distribution of each particle in the self-trigger data.

- $\epsilon_{\text{analysis}}$:
  The same definition as the Michel normalization except for the condition on time window, which is already taken into account in the RMD detection. See Table 6.4.

We evaluate k_{RMD} for 24 statistically independent windows, and the best estimate is computed by a χ^2 fit. The systematic uncertainty on each item correlating among the different windows is inserted in the χ^2 as a pull term.

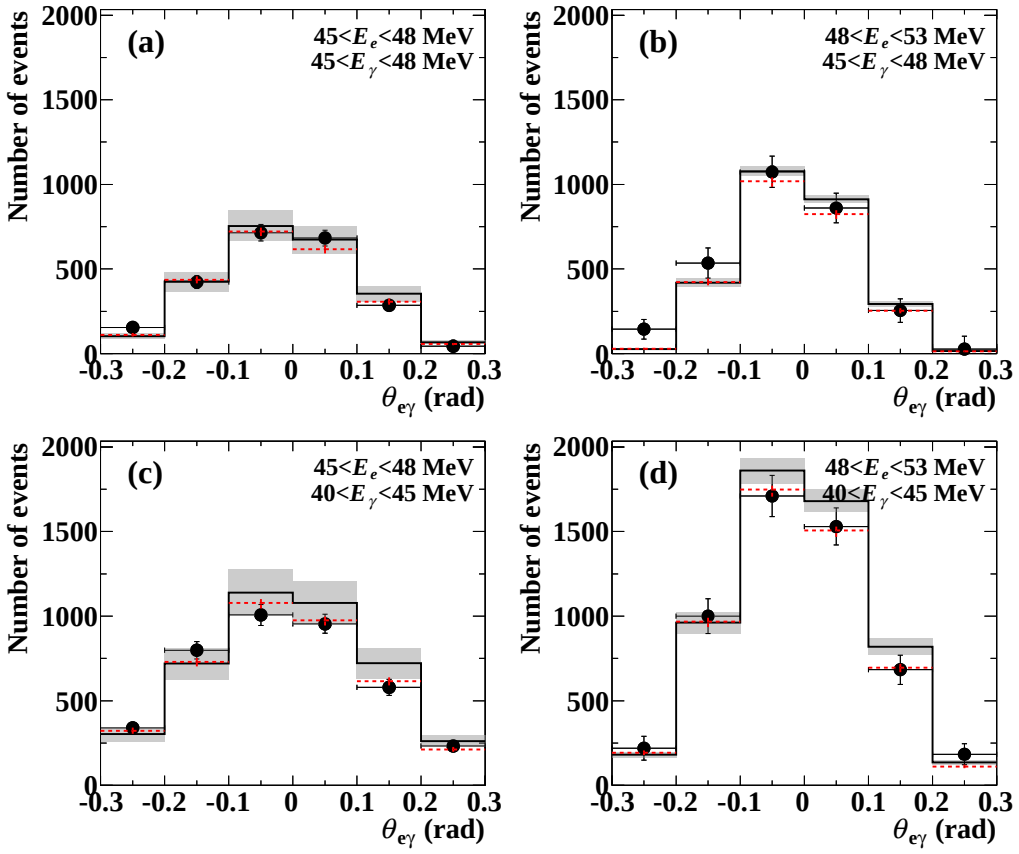

Figure 6.10: Distribution of RMD events in 2009–2010 data. Black dots show the measured distribution. Black solid histograms show the expected distribution calculated from the normalization factor from Michel channel and the best estimate value for each parameter, and the gray bands show the uncertainty. Red dashed ones show the distribution with the best-fit values of normalization and systematic parameters.

The distribution of RMD events is shown in Fig. 6.10 and Fig. 6.11 in 2009–2010 data and 2011 data, respectively.

6.5.4 Combined normalization factors

Since the normalization factors from Michel and RMD are calculated by using different data samples (Michel trigger and MEG trigger), the two methods are almost independent.

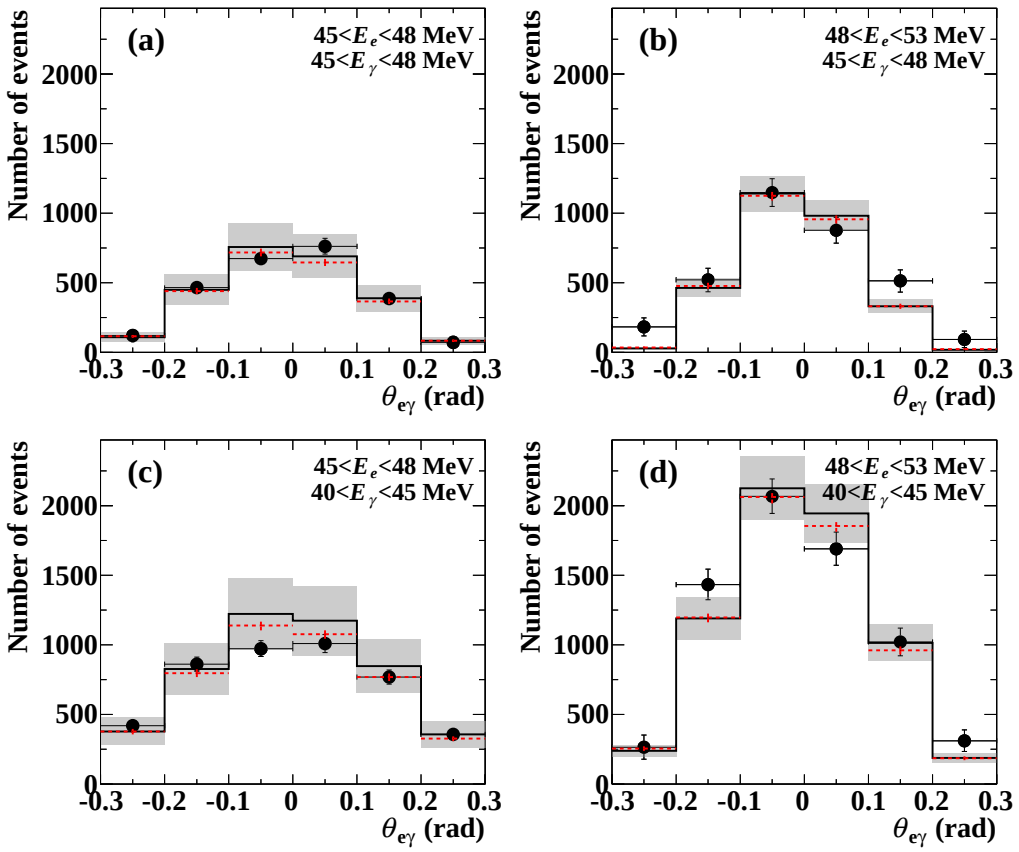

Figure 6.11: Distribution of RMD events in 2011 data. Black dots show the measured distribution. Black solid histograms show the expected distribution calculated from the normalization factor from Michel channel and the best estimate value for each parameter, and the gray bands show the uncertainty. Red dashed ones show the distribution with the best-fit values of normalization and systematic parameters.

Therefore the uncertainties on both factors can be reduced by combining them. The combined normalization factors are shown in Table 6.8. The uncertainty become only 4–5% depending on the dataset.

Table 6.8: Summary of normalization factors calculated for 2009, 2010 and 2011 dataset.

	$k_{\mathrm{Michel}}(\times 10^{12})$	$k_{\mathrm{RMD}}(\times 10^{12})$	$k_{\mathrm{combined}}(\times 10^{12})$
2009	1.21 ± 0.07	1.19 ± 0.06	1.20 ± 0.06
2010	2.66 ± 0.13	2.41 ± 0.13	2.52 ± 0.09
2011	4.10 ± 0.20	3.96 ± 0.24	4.05 ± 0.16

Then the total normalization factor for the combined datasets are calculated to be

$$k_{\mathrm{combined}}^{2009+2010} = (3.72 \pm 0.15) \times 10^{12}, \tag{6.37}$$

$$k_{\mathrm{combined}}^{2009+2010+2011} = (7.77 \pm 0.31) \times 10^{12}. \tag{6.38}$$

Chapter 7

Results and Discussions

In this chapter, we describe the likelihood analysis results on the 2009–2010, 2011 and 2009–2011 datasets. Here the limits are calculated at 90% C.L. if not mentioned explicitly. The results and those of reliability and compatibility between the results from the previous analysis are discussed as well. For the comparison, the results from the previous results are shown in Table 7.1.

7.1 Sensitivity

We define an experiment sensitivity as a median of the upper limits for an ensemble of pseudo experiments with the background-only hypothesis. The 90% C.L. upper limit for each pseudo experiment is calculated by the same way as already described in Sec. 6.4. The median is generally used as an expected outcome of an experiment rather than the mean because it is less affected by anomalous outliers and it is metric independent. Figure 7.1 shows the distribution of the upper limits on the number of signals in 3000 pseudo experiments. The medians of the ensembles are 4.7, 4.6 and 6.0 in number of signals for 2009–2010 combined, 2011 and the 2009–2011 combined datasets, respectively. After the normalization, they correspond to $\mathcal{B}$ of 1.3×10^{-12}, 1.1×10^{-12} and 7.7×10^{-13}, respectively. These results are summarized in Table 7.2. The systematic uncertainties (described later) are included. Since the sensitivity definition is not changed from the previous analysis, they can directly compared and the sensitivity is improved by factor two as shown in Table 7.1 and Table 7.2. Owing to the several reconstruction improvements and the newly implemented per-event PDF, the sensitivity is found to be improved by 20% in the 2009–2010 dataset, which was also analyzed by using the previous analysis method. By adding the 2011 dataset to the 2009–2010 combined dataset, the sensitivity reaches unprecedented region, the order of the 10^{-13}.

Table 7.1: Results from the previous analysis presented in [4].

Data set	Sensitivity	Observed best fit	Lower limit	Observed upper limit
2009–2010 combined	1.6×10^{-12}	-1.5×10^{-12}	–	2.4×10^{-12}

Table 7.2: Calculated sensitivities in each dataset. Systematic uncertainties are included.

Data set	Sensitivity in N_{sig}	Sensitivity in $\mathcal{B}$
2009–2010 combined	4.7	1.3×10^{-12}
2011 only	4.6	1.1×10^{-12}
2009–2011 combined	6.0	7.7×10^{-13}

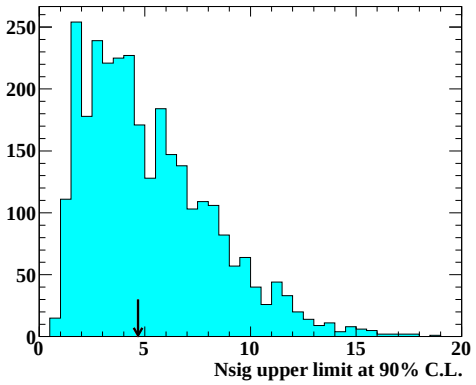

(a)

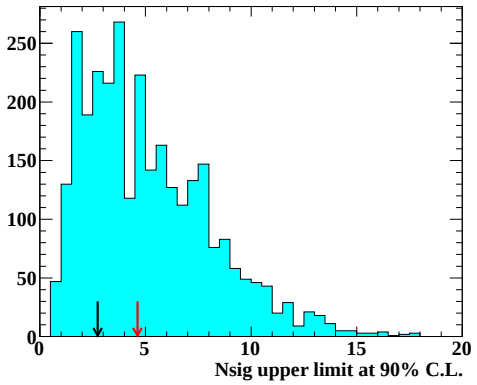

(b)

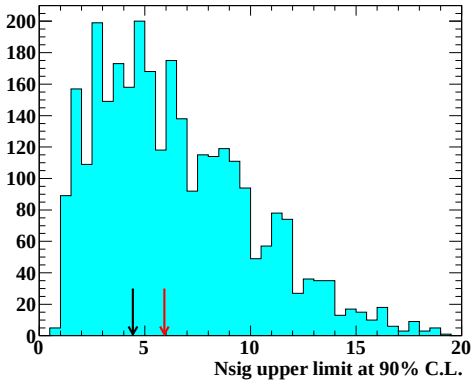

(c)

Figure 7.1: Distributions of the upper limits of the background-only pseudo experiments. (a) 2009-2010, (b) 2011, (c) 2009-2011. The red arrows show the medians of the distributions. The black arrows show the observed limits. In (a), two arrows are overlapped by chance.

Table 7.3: Time sideband results without including systematic uncertainties. The results in the negative $t_{e\gamma}$ sidebands are labeled as 'negative' and those in opposite sides are labeled as 'positive'.

Dataset	$\mathcal{B}$ best fit	$\mathcal{B}$ upper limit
2009-2010 negative	7.7×10^{-13}	3.1×10^{-12}
2009-2010 positive	-2.8×10^{-13}	1.1×10^{-12}
2011 negative	3.7×10^{-15}	1.7×10^{-12}
2011 positive	2.1×10^{-13}	1.4×10^{-12}
2009-2011 negative	3.5×10^{-13}	1.6×10^{-12}
2009-2011 positive	7.8×10^{-14}	8.1×10^{-13}

7.2 Sideband Results

In order to check the reliability of the implemented likelihood function, two kinds of sidebands (time and angle) are analyzed. In time sidebands, the shape of the background events should be consistent with those of implemented accidental background PDFs since signal events and RMD events are not included in the these region. Therefore calculated upper limits should be consistent with those of expected sensitivities calculated in Table 7.2. In angle sidebands, best fit values of N_{RMD} should be consistent with those expected from the RMD analysis. In the sideband analysis, the systematic uncertainties except for those of N_{RMD} and N_{BG} are not incorporated since the effect of the systematic uncertainties are found to be not so large as described in Sec. 7.4.

When the time sidebands are analyzed, the center of the time PDF of signal is shifted so that it is at the center of the sideband time window (± 2 ns). Similarly, when the angle sidebands are analyzed, the center of the $\theta_{e\gamma}$ or $\phi_{e\gamma}$ signal PDF is shifted ± 50 mrad.

7.2.1 Results with Time Sidebands

For both time sidebands, the same expected numbers of accidental background events used for the analysis region are used. The analysis results of $\mathcal{B}$ are summarized in Table 7.3. Figure 7.2 shows the C.L. curves calculated in the Feldman-Cousins method in time sidebands. When positron tracks which have real multi-turns with one or a few missing turns in the reconstruction, the reconstructed emission time on the target must be earlier than the true value. Since single missing turn events of RMD events with 50–56 MeV positron momenta correspond to 2–2.5 nsec in the time-of-flight, only the negative sidebands are affected by the missing turn events of RMD as shown in Fig. 7.2. It is therefore expected that the $\mathcal{B}$ upper limits in the negative sidebands become larger than those in the positive sideband as seen in Table 7.3. On the other hand, the calculated $\mathcal{B}$ upper limits in the positive sidebands look more likely consistent with the evaluated sensitivity in the analysis region.

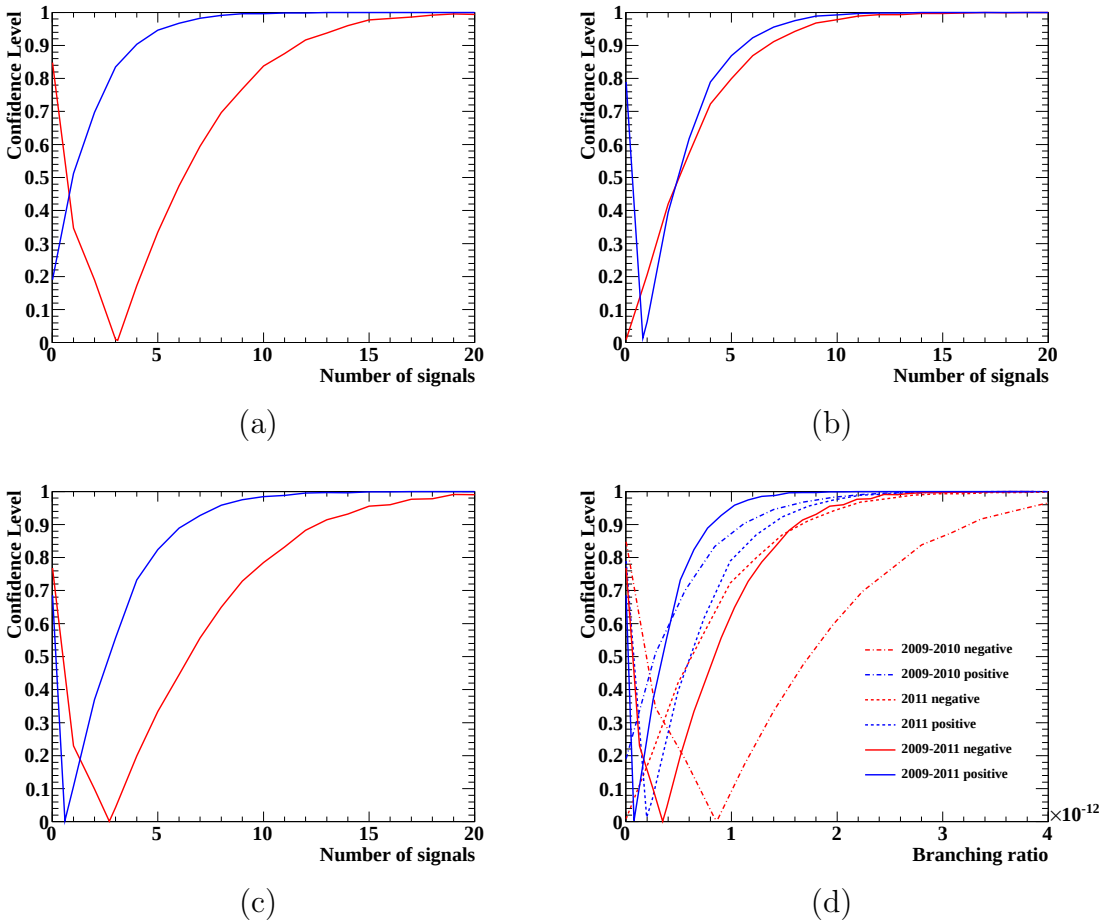

Figure 7.2: Confidence level curves in time sidebands (a)–(c) before normalization and (d) after normalization. (a) 2009-2010, (b) 2011, (c)(d) 2009-2011. Red lines show the results of the negative time sidebands and blue lines show the results of the positive ones.

Table 7.4: Angle sideband results with constraining the number of backgrounds.

Dataset	$\mathcal{B}$ best fit
2009-2010 negative ϕ	7.6×10^{-13}
2009-2010 positive ϕ	-2.9×10^{-12}
2009-2010 negative θ	5.3×10^{-13}
2009-2010 positive θ	-3.5×10^{-13}
2011 negative ϕ	1.2×10^{-12}
2011 positive ϕ	-1.4×10^{-13}
2011 negative θ	-6.1×10^{-13}
2011 positive θ	1.2×10^{-13}
2009-2011 negative ϕ	9.7×10^{-13}
2009-2011 positive ϕ	-1.1×10^{-12}
2009-2011 negative θ	1.9×10^{-14}
2009-2011 positive θ	-1.1×10^{-13}

7.2.2 Results with Angle Sidebands

The accidental background events in $1 \leq |t_{e\gamma}| \leq 3.7$ nsec in the same angles regions are counted and scaled to 1.4 nsec to be used for the constraint. The number of RMD events are calculated from the RMD analysis using the E_γ sideband data. The analysis results in $\mathcal{B}$ are summarized in Table 7.4. Hereafter, $\hat{N}_{\rm sig}$, $\hat{N}_{\rm RMD}$ and $\hat{N}_{\rm BG}$ are used to represen the best fit values of the number of signal, RMD and the accidental background respectively. In the angle sidebands, we can study RMD as well as the accidental backgrounds. To check the RMD PDF implementation and background evaluation, we repeated the fits omitting the constraint terms of $N_{\rm BG}$ and $N_{\rm RMD}$ in the likelihood function. The results are summarized in Table 7.5. The observed numbers are in good agreement with the expectations.

7.3 Result in Analysis Region

The definitions of the analysis region are described in Sec. 6.1.3. The positron is selected by using the selection criteria explained in Sec. 5.2.1 and the gamma selection is done by using the criteria written in Sec. 5.1.1. The blind region of 2011 data is opened after all PDF parameters are determined. From the sideband data, the expected numbers of RMDs and the accidental background events in the analysis region are calculated and constrained. The numeric numbers are summarized in Table 7.6 with the observed number of events in the analysis region. The event distributions around the $\mu^+ \to e^+\gamma$ signal region are shown in Fig. 7.3 and Fig. 7.4. For the illustration purpose, only the events in $\cos\Theta_{e\gamma} < -0.99963$ and $|t_{e\gamma}| < 2.443$ ps regions are shown in plots of E_γ vs. E_e, and $51 < E_\gamma < 55.5$ MeV and $52.385 < E_e < 55$ MeV regions are shown in plots of $t_{e\gamma}$ v.s. $\cos\Theta_{e\gamma}$. Thresholds for E_e, $\cos\Theta_{e\gamma}$ and $t_{e\gamma}$ correspond to 90% signal region and those for E_γ correspond to 75% signal region, which is arbitrary defined.

The best fits of $N_{\rm BG}$, $N_{\rm RMD}$ and $N_{\rm sig}$, maximizing the profile likelihood shown in

Table 7.5: Angle sideband results without constraints on the number of backgrounds (Uncertainties are in 1σ). Parameters in bracket show the expected number of backgrounds and those with a hat show the best fit results.

Dataset	$\langle N_{\mathrm{BG}} \rangle$	$\langle N_{\mathrm{RMD}} \rangle$	N_{obs}	$\hat{N}_{\mathrm{BG}}$	$\hat{N}_{\mathrm{RMD}}$
2009-2010 negative ϕ	1120 ± 17	34 ± 3	1120	1077 ± 35	40 ± 15
2009-2010 positive ϕ	1169 ± 17	36 ± 3	1247	1212 ± 39	46 ± 18
2009-2010 negative θ	1123 ± 17	39 ± 4	1120	1083 ± 36	35 ± 16
2009-2010 positive θ	877 ± 15	24 ± 2	962	963 ± 34	1 ± 12
2011 negative ϕ	1130 ± 18	35 ± 4	1163	1132 ± 37	27 ± 15
2011 positive ϕ	1189 ± 18	37 ± 4	1241	1195 ± 38	47 ± 16
2011 negative θ	1131 ± 18	41 ± 4	1233	1208 ± 38	27 ± 15
2011 positive θ	976 ± 17	25 ± 3	1016	979 ± 34	37 ± 14
2009-2011 negative ϕ	2228 ± 24	69 ± 7	2283	2210 ± 51	66 ± 21
2009-2011 positive ϕ	2365 ± 25	73 ± 7	2488	2404 ± 54	93 ± 24
2009-2011 negative θ	2251 ± 24	80 ± 8	2353	2292 ± 52	61 ± 22
2009-2011 positive θ	1855 ± 22	49 ± 5	1978	1939 ± 48	41 ± 18

Table 7.6: Expected number of background events and the observed number of events in the analysis region defined in Sec. 6.1.3.

Year	$\langle N_{\mathrm{BG}} \rangle$	$\langle N_{\mathrm{RMD}} \rangle$	N_{obs}
2009-2010	1195.7±17.6	83.8±8.4	1291
2011	1219.3±17.8	85.5±8.9	1282
2009-2011	2415.0±25.0	169.3±17.0	2574

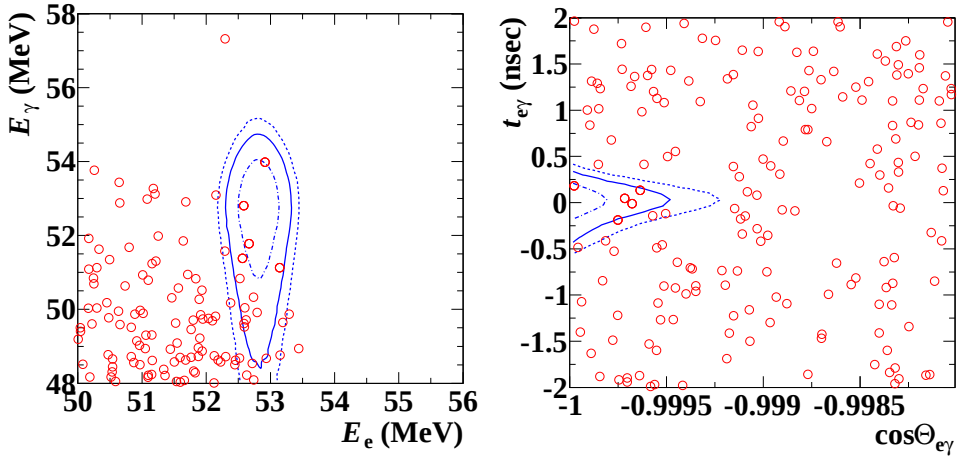

(a)E_γ v.s. E_e, $\cos\Theta_{\mathrm{e}\gamma} < -0.99963$, $|t_{\mathrm{e}\gamma}| < 2.443$ ps

(b)$t_{\mathrm{e}\gamma}$ v.s. $\cos\Theta_{\mathrm{e}\gamma}$, $51 < E_\gamma < 55.5$ MeV, $52.385 < E_\mathrm{e} < 55$ MeV

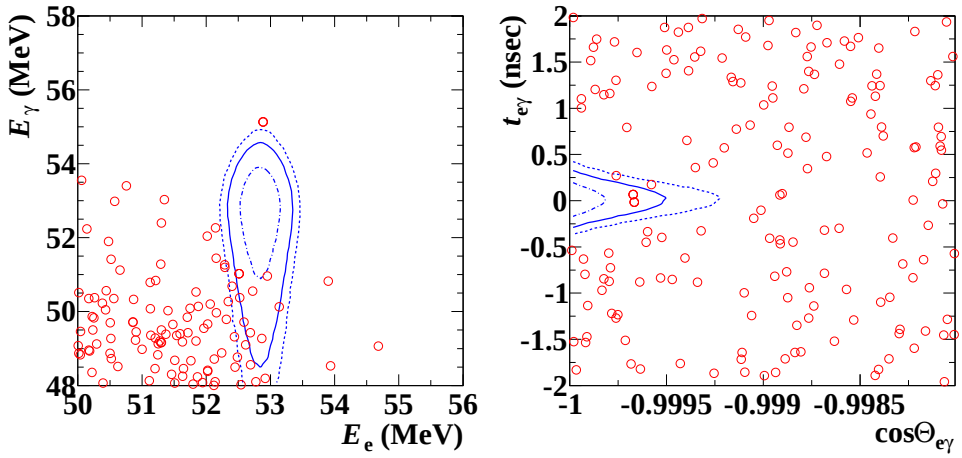

(c)E_γ v.s. E_e, $\cos\Theta_{\mathrm{e}\gamma} < -0.99963$, $|t_{\mathrm{e}\gamma}| < 2.443$ ps

(d)$t_{\mathrm{e}\gamma}$ v.s. $\cos\Theta_{\mathrm{e}\gamma}$, $51 < E_\gamma < 55.5$ MeV, $52.385 < E_\mathrm{e} < 55$ MeV

Figure 7.3: Event distributions in E_γ v.s. E_e and $t_{\mathrm{e}\gamma}$ v.s. $\cos\Theta_{\mathrm{e}\gamma}$. Corresponding datasets are 2009-2010 combined (a)(b) and 2011 only (c)(d), respectively. The signal two-dimensional PDFs are superimposed as contours at 1, 1.645, 2 σ as blue dashed, solid, and dotted lines respectively.

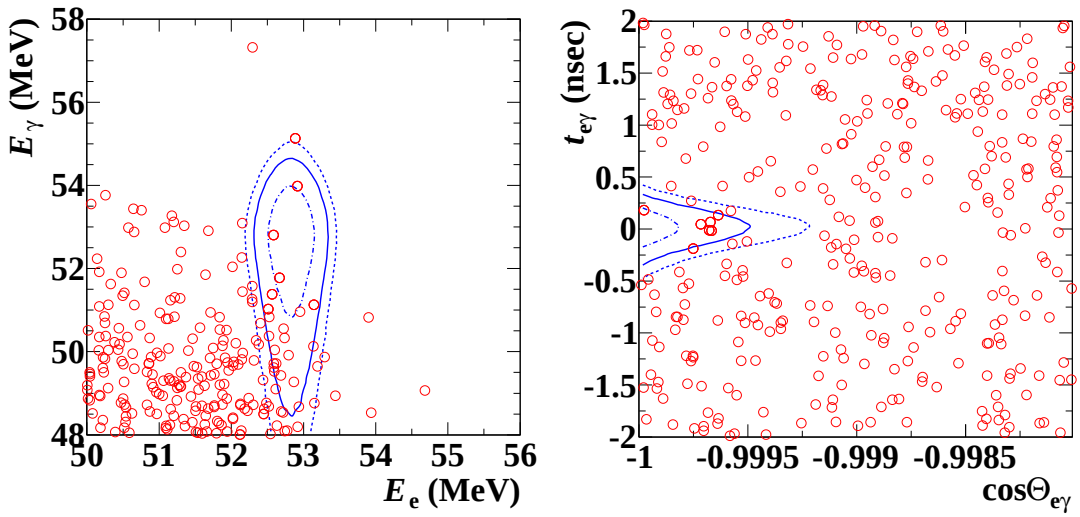

(a)E_γ v.s. E_e,
$\cos\Theta_{e\gamma} < -0.99963$,
$|t_{e\gamma}| < 2.443$ ps

(b)$t_{e\gamma}$ v.s. $\cos\Theta_{e\gamma}$,
$51 < E_\gamma < 55.5$ MeV,
$52.385 < E_e < 55$ MeV

Figure 7.4: Event distributions in the (E_e, E_γ) plane(a) and $(\cos\Theta_{e\gamma}, t_{e\gamma})$ plane(b). Corresponding dataset is 2009-2011 combined. Definition of blue contours are same as those in Fig. 7.3.

Table 7.7: The best fit number of events and the corresponding branching ratios. The uncertainties are MINOS (i.e. profile likelihood ΔNLL method) 1.645σ errors. The numbers with hats show the best fit values.

Year	$\hat{N}_{\rm BG}$	$\hat{N}_{\rm RMD}$	$\hat{N}_{\rm sig}$	$\hat{\mathcal{B}}$
2009-2010	$1198.4^{+26.1}_{-26.0}$	$83.4^{+12.9}_{-12.8}$	$0.3^{+4.1}_{-1.5}$	8.9×10^{-14}
2011	$1215.2^{+26.4}_{-26.3}$	$84.8^{+13.4}_{-13.3}$	$-1.4^{+3.8}_{-1.3}$	-3.5×10^{-13}
2009-2011	$2413.6^{+37.1}_{-37.0}$	$167.5^{+24.2}_{-24.0}$	$-0.4^{+4.8}_{-1.9}$	-5.8×10^{-14}

Fig. 7.8, are summarized in Table 7.7. The corresponding best estimate of $\mathcal{B}_{\mu^+\to e^+\gamma}$ fits are also shown in the table. The corresponding fit results are shown in Fig. 7.5, 7.6 and 7.7.

Figure 7.9 shows the C.L. curves calculated in the Feldman-Cousins method. On the all dataset, only UL are obtained, namely $N_{\rm sig} = 0$ is included in the intervals. Table 7.8 summarizes the confidence intervals. In 2011 dataset, the result shows a smaller $N_{\rm sig}$ upper limit than the sensitivity. The difference between the observed $N_{\rm sig}$ upper limit and the sensitivity is shown by arrows in Fig. 7.1(b); the probability of observing, in 2011 dataset, a $N_{\rm sig}$ upper limit smaller or equal to the observed value is 24%, which is within the statistical fluctuation.

By analyzing the 2009–2011 combined dataset, the upper limit on the branching ratio of the $\mu^+ \to e^+\gamma$ decay is calculated as:

$$B(\mu^+ \to e^+\gamma) < 5.7 \times 10^{-13}, \tag{7.1}$$

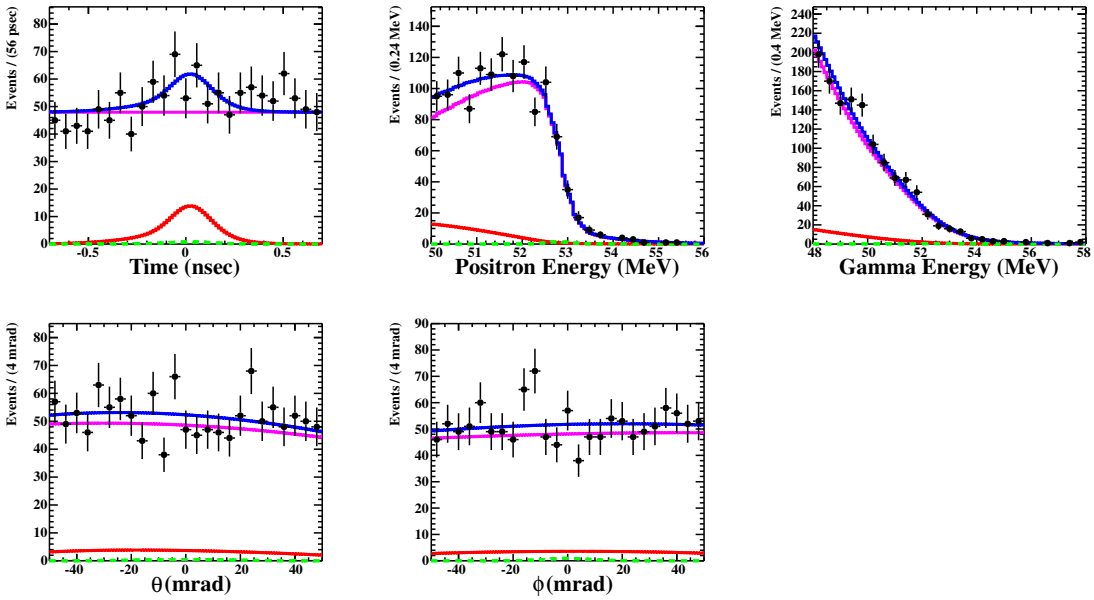

Figure 7.5: Likelihood fit result for 2009–2010 combined dataset in the analysis region. Black markers show the data. Red and pink lines show the best fit for RMD and BG, respectively. Green line shows the best fit for the signal (almost invisible because of the small N_{sig}) and blue one shows total best fit.

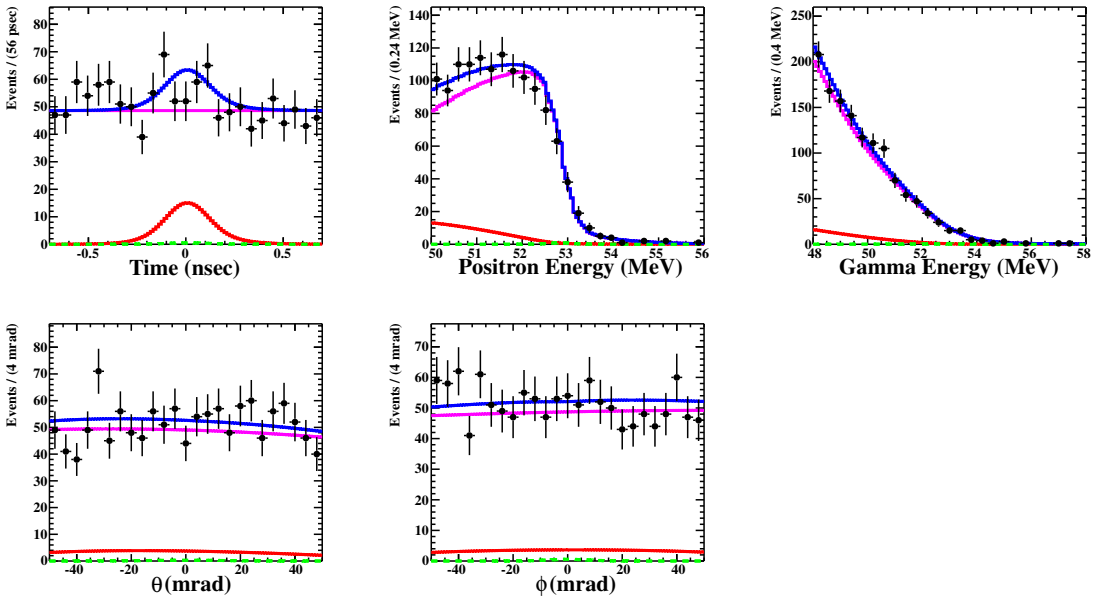

Figure 7.6: Likelihood fit result for 2011 dataset in the analysis region. The definitions of each components are the same as in Fig. 7.5.

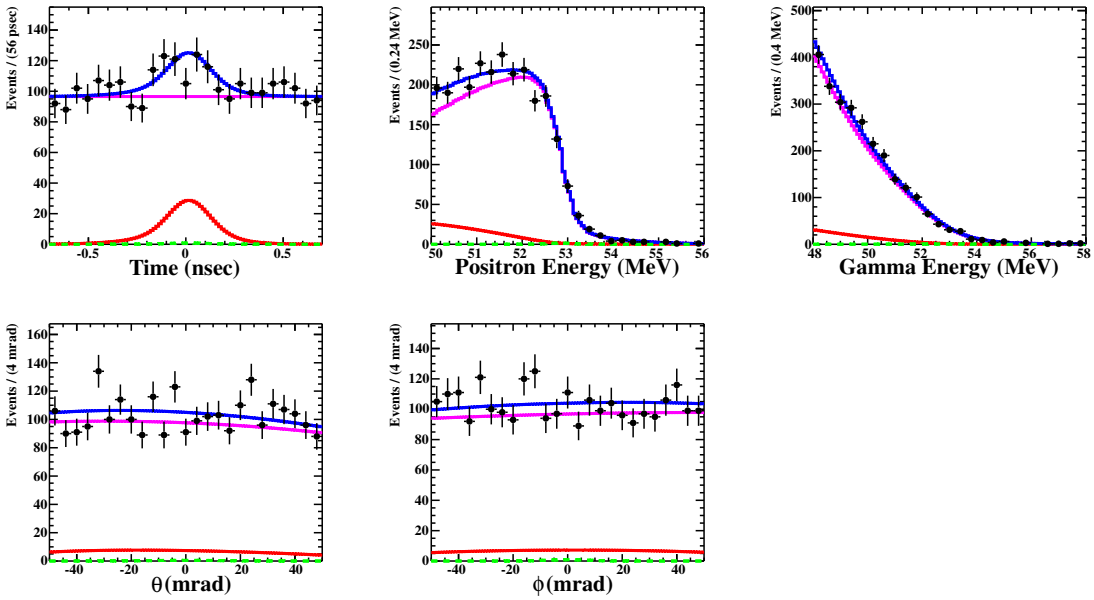

Figure 7.7: Likelihood fit result for 2009–2011 combined dataset in the analysis region. The definitions of each components are the same as in Fig. 7.5.

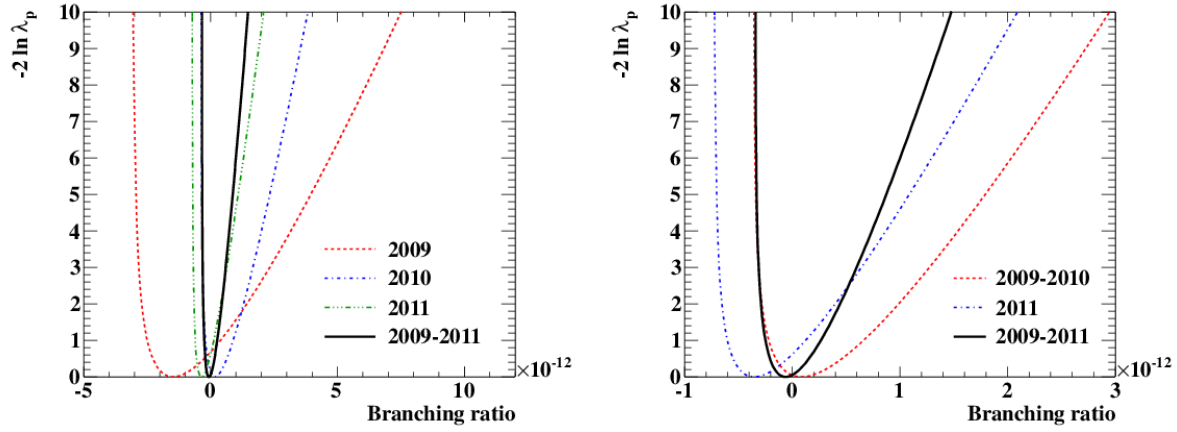

(a) (b)

Figure 7.8: Profile likelihood curves

at 90% C.L. Since no significant excesses of the signal events are observed in all datasets, lower limits (LL) are not given in the results.

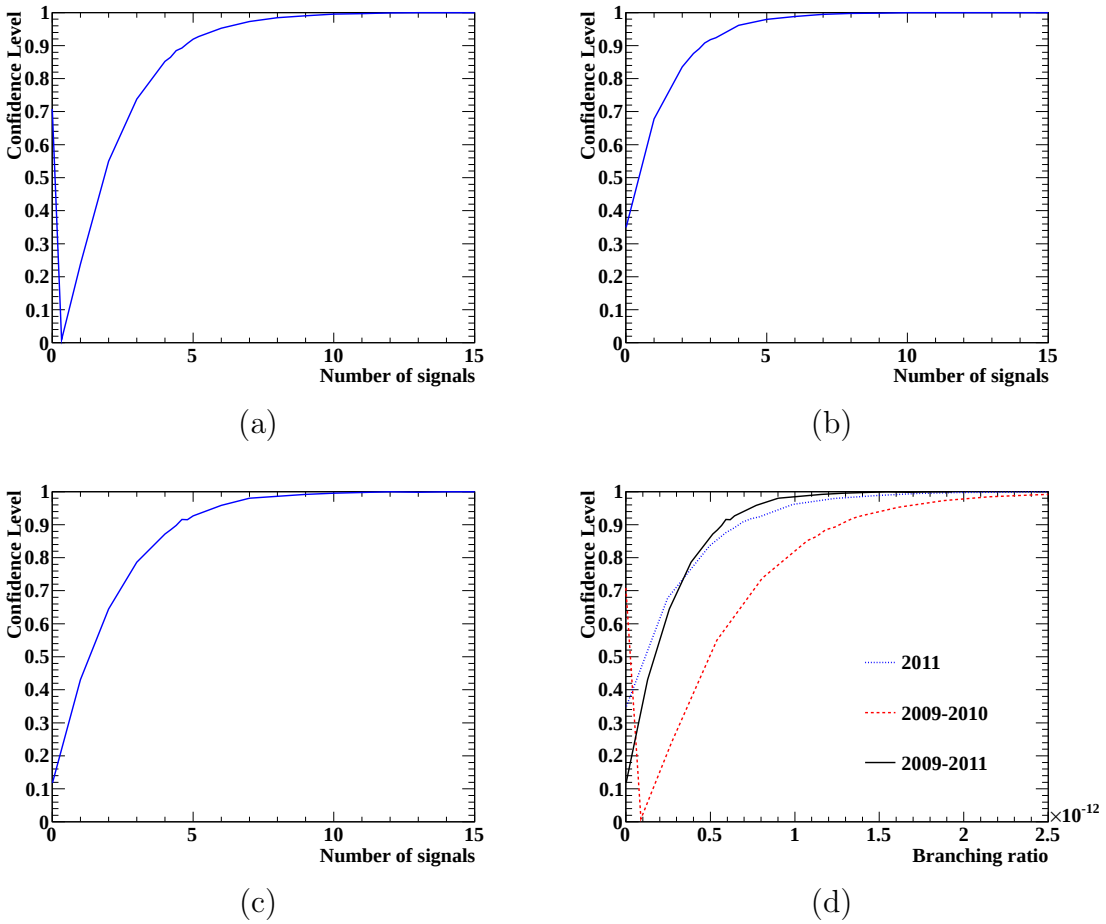

Figure 7.9: Confidence level curves (a)–(c) before normalization and (d) after normalization. (a) 2009-2010, (b) 2011, (c)(d) 2009-2011.

7.4 Effects of Systematic Uncertainties

7.4.1 Uncertainties of Parameters

In this section, systematic uncertainties which were not described in Sec. 6.3 are explained.

The position of the calorimeter was measured from the several kinds of data (See Sec. 4.3.4.1) and the uncertainty is estimated to be 2.4 mrad in θ_γ. We assign the same value to ϕ_γ as described in Sec. 4.3.4.1. The uncertainty became smaller than the previous estimate because the average position including the new measurement using 2011 cosmic-ray data is closer to the hardware-alignment than the previous average.

The effect of correlations due to the global bias of E_e is included by fluctuating the bias in the flat distribution between 0 and the observed global bias. The systematic

Table 7.8: Confidence intervals (upper limits and lower limits if they are set) on the 2009-2010, 2011 and 2009-2011 datasets calculated from confidence level curves shown in Fig. 7.9(d). The numbers in the first table are written in $N_{\rm sig}$ and those in the second are in $\mathcal{B} \times 10^{13}$. A confidence level at 0 is shown only when $\hat{N}_{\rm sig}$ is positive. The results are including the systematic uncertainties.

Year	LL (90% C.L.)	UL (90% C.L.)	UL (95% C.L.)	C.L. at 0
2009-2010	–	4.7	5.8	0.71
2011	–	2.7	3.7	–
2009-2011	–	4.4	5.6	–

Dataset	LL (90% C.L.)	UL (90% C.L.)	UL (95% C.L.)
2009-2010	–	13	16
2011	–	6.7	9.0
2009-2011	–	5.7	7.2

Table 7.9: Uncertainties associated to the drift chamber alignment and the magnetic field.

Variable	Year		
	2009	2010	2011
$\mu_{\theta_{\rm e}}$ [mrad]	1.4	2	1.8
$\mu_{\phi_{\rm e}}$ [mrad]	1.0	2	3
$\mu_{z_{\rm e}}$ [cm]	0.05	0.03	0.10
$\mu_{y_{\rm e}}$ [cm]	0.013	0.008	0.03

uncertainties associated to the drift-chamber alignment and the magnetic field appear as non-zero offsets parameters in the two-turn correlation as:

$$\mu_{\delta y} = c_0 + p_{xy} \cdot \delta x, \tag{7.2}$$

where c_0 is ideally zero while they are measured to be non-zero in the data for parameter x ($x = \theta_{\rm e}, \phi_{\rm e}, z_{\rm e}, y_{\rm e}$). The systematic uncertainties shown in Table 7.9 correspond to the overall biases of the two-turn differences after corrections.

The uncertainties of E_γ scale, which are calculated by combining the effect from light yield correction and the fitting of the 55 MeV gamma ray peak in the CEX run, are 0.33, 0.31 and 0.32% in 2009, 2010 and 2011, respectively. The uncertainties of γ position resolutions are 0.3 mm in (u, v) and 0.7 mm in w. The uncertainty of the center of $t_{{\rm e}\gamma}$ is 15 psec which comes from the fitting uncertainty. The normalization uncertainty is 4% as written in Table 6.8. For all PDF shapes extracted from the sideband or calibration data, namely $t_{{\rm e}\gamma}$ signal, E_γ signal, $E_{\rm e}$ signal, E_γ BG, $E_{\rm e}$ BG and Angle BG, the fitting errors including the correlations between parameters are used.

Figure 7.10 shows the average PDFs for 2011 data with parameters randomized according to their uncertainties. As shown in this figure, the accidental background PDFs

are well controlled and the uncertainties are smaller than those in the signal PDFs.

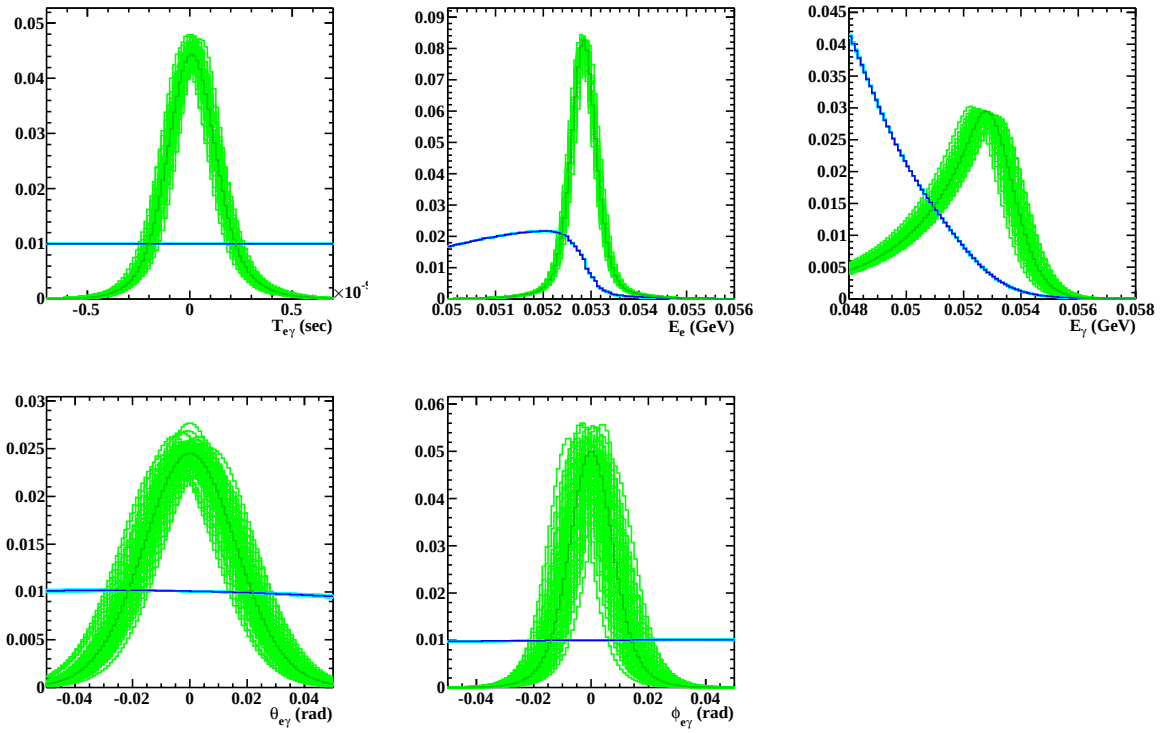

(a)

Figure 7.10: The average signal and background PDFs for the 2011 dataset. The parameters are randomized for each curve according to their uncertainties. Dark green (blue) lines are the signal (BG) PDFs without randomizing parameters and green (cyan) lines are PDFs with randomized parameters.

7.4.2 Comparison of Systematic Uncertainties

The total effect of the systematic uncertainties is a 1% change in the upper limit of the 2009-2011 combined dataset. The effects of uncertainties of N_{RMD} and N_{BG} are confirmed to be much smaller than other uncertainties from the calculation of the upper limit by fixing N_{RMD} and N_{BG} in the fitting. The effects of other uncertainties are compared in this section in the following procedure. This study is done only to disentangle the contribution of each uncertainty. The results are not used for calculating confidence intervals.

1. Generate 100 pseudo experiments with the nominal PDF, $N_{\mathrm{sig}} = \mathrm{Poisson}(4.4)$. The number of signals of 4.4 is the upper limit obtained from the data.

2. Fit the pseudo experiments with the nominal PDF. And calculate the likelihood ratio at the best fit and $N_{\mathrm{sig}} = 4.4$.

Table 7.10: Relative contributions of uncertainties to upper limit of $\mathcal{B}$ in RMS of $\Delta\Delta$NLL.

Center of $\theta_{e\gamma}$ and $\phi_{e\gamma}$	0.18
Positron correlations	0.11
E_γ scale	0.07
E_e bias	0.06
$t_{e\gamma}$ signal shape	0.06
$t_{e\gamma}$ center	0.05
Normalization	0.04
E_γ signal shape	0.03
E_γ BG shape	0.03
Positron angle resolutions (θ_e, ϕ_e, z_e, y_e)	0.03
γ angle resolution (u_γ, v_γ, w_γ)	0.03
E_e BG shape	0.01
E_e signal shape	0.01
Angle BG shape	0.00
Total	0.25

3. Do the same thing on the same 100 pseudo experiments using the alternative PDF. In each experiment, the parameters in the fitting PDF are randomized according to their uncertainties. For the estimation of the effect of the normalization uncertainty, PDF parameters are not changed, but the negative-log-likelihood at randomized N_{sig} according to the normalization uncertainty is used for calculating ΔNLL.

4. Make a distribution of the difference of negative-log-likelihood-ratio at 2. and 3. ($\Delta\Delta$NLL).

The third step is repeated three times. The RMS of the distribution of $\Delta\Delta$NLL is used for comparing the effects. In this procedure, the effects of the uncertainties on the probability density function of the likelihood ratio around the upper limit are measured. Table 7.10 shows the relative contributions (RMS of $\Delta\Delta$NLL) of the uncertainties and Table 7.11 shows those of the correlations in positron observables. The center of $\theta_{e\gamma}$ and $\phi_{e\gamma}$ are determined by the relative alignment (See Sec. 4.3.4.4). From this test, it is found that the largest contribution to the result is the relative displacement between the positron spectrometer and the LXe detector.

7.5 Further Checks

We describe a compatibility check between the present and the previous published results [5][4] due to the difference from the improved analysis method as written in Sec. 6.3, and the change in the observables by the differences of the reconstruction algorithms. An event-by-event check for the highest ranked events are also done.

Table 7.11: Relative contributions of the uncertainties of the correlations in the positron observables to the upper limit of $\mathcal{B}$ in RMS of $\Delta\Delta$NLL.

$\delta\phi_{e\gamma}$:$\delta\theta_{e\gamma}$ correlation	0.09
σ_{ϕ_e} v.s. ϕ_e	0.04
$\delta\phi_e$:δE_e correlation	0.02
Correlation due to E_e bias	0.02
δz_e:$\delta\theta_e$ correlation	0.01
δy_e:δE_e correlation	0.00
δz_e:$\delta\phi_e$ correlation	0.00

Table 7.12: Results from category PDF and comparison without systematic uncertainties.

Dataset	N_{sig} sensitivity	$\mathcal{B}$ sensitivity
2009-2010 category PDF	5.4	1.45×10^{-12}
2009-2010 per-event PDF	4.7	1.3×10^{-12}

Dataset	N_{sig} best fit	$\mathcal{B}$ best fit	N_{sig} UL	$\mathcal{B}$ UL
2009-2010 category PDF	0.4	1.1×10^{-13}	5.7	1.5×10^{-12}
2009-2010 per-event PDF	0.3	8.5×10^{-14}	4.7	1.3×10^{-12}

7.5.1 Result from Category PDF

The likelihood fitting and the full frequentist analysis are performed also with the category PDFs which were used in the previous analysis. The results in the analysis region are shown in Table 7.12. In particular for 2009–2010 combined dataset, it is important to analyze this dataset for a direct comparison. The calculated sensitivity is 5.4 (4.7) in number of signals for the category (per-event) PDF on the 2009-2010 dataset and it corresponds to $\mathcal{B}$ of 1.45×10^{-12} (1.3×10^{-12}) after the normalization. By comparing these two sensitivities, the improvement due to the per-event PDF is directly calculated to be $\sim$10%.

7.5.2 Analysis Compatibility

To evaluate the compatibility, we generate pseudo experiments with taking into account the differences of the reconstruction and the efficiency based on the 2009–2010 combined dataset. A pair of toy-MC experiments, corresponding to the previous and the new analyses, are generated from a common "true" events where the detector responses are not included. The two experiments are generated with taking into account the correlations between the old and the new reconstruction algorithms extracted from data (see Fig. 7.11). The difference of the efficiency are also included in the generation.

Each toy is fitted with the constant PDFs, then the 90% C.L. upper limits are calculated. Figure 7.12 shows the the distribution of the difference in upper limit in N_{sig}

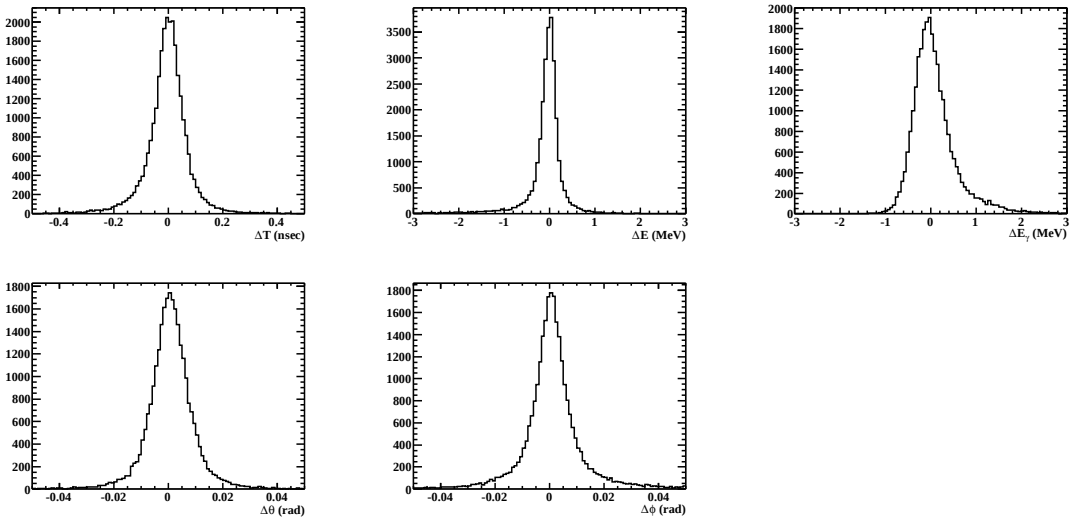

Figure 7.11: Difference of reconstructed $t_{e\gamma}$ (upper left), E_e (upper center), E_γ (upper right), θ_e (bottom left) and ϕ_e (bottom center) in the 2009–2010 data with the old and the new reconstruction algorithms. The definition of Δx is as follows:$\Delta x = x_{\rm new} - x_{\rm old}$.

from the analysis on the pair of pseudo experiments which generated from a common true events. In the previous analysis, the observed $N_{\rm sig}$ upper limit is 7.7 and in the present analysis it is 5.7 with the category PDF. The probability for observing a difference equal to or larger than the observed value is 31%. Therefore the difference of the calculated $N_{\rm sig}$ upper limit between the present and previous analysis can be explained by the difference of the reconstruction methods.

7.5.3 Event-by-Event Check and Comparison

Since we use the unbinned maximum likelihood analysis with event-by-event PDF, events which have high signal-likelihood can be identified and compared. The signal like ordering is determined by using $R_{\rm sig}$, which is defined as

$$R_{\rm sig} = \log_{10} \frac{\mathcal{L}_{\rm sig}}{0.1 \cdot \mathcal{L}_{\rm RD} + 0.9 \cdot \mathcal{L}_{\rm BG}}. \tag{7.3}$$

An event which has the largest $R_{\rm sig}$ value and one has the second largest $R_{\rm sig}$ in 2011 dataset are shown in Fig. 7.13(a) and (b), respectively. In the highest ranked event, one pileup gamma ray is observed, but it is correctly subtracted. Other event are also checked by looking light yield distribution, waveforms of each detector and the shape of PDF in each event and we found no strange behavior.

Figure 7.14 shows five events, which show the highest $R_{\rm sig}$ value in the new/previous analysis. As shown in this figure, observables of the most of these events are changed within the level which we can predicted from Fig. 7.11. The event with third highest $R_{\rm sig}$ disappeared in the new analysis while the different third highest ranked event labeled with red colored number newly appeared in the new analysis. They are found to

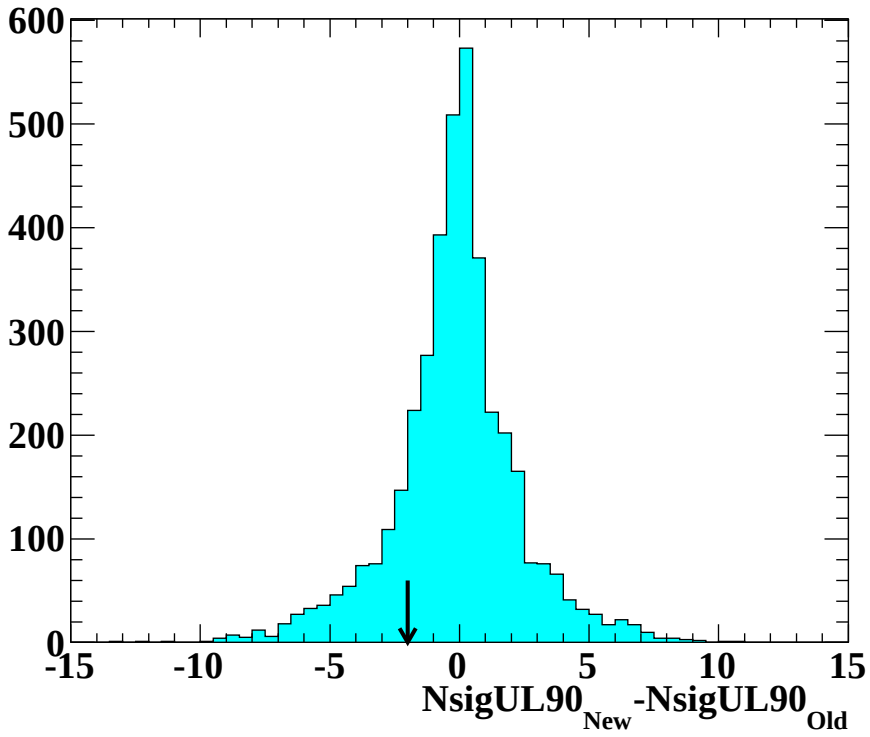

Figure 7.12: Distribution of ΔN_{sig} upper limits. The black arrow shows the observed difference in the 2009–2010 combined dataset.

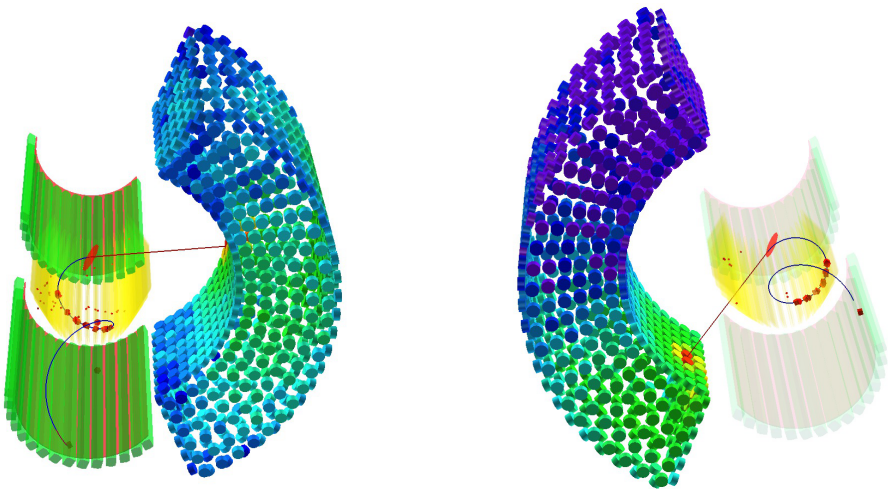

(a) (b)

Figure 7.13: 3D view of reconstructed events which have the first(a) and second(b) largest R_{sig} value.

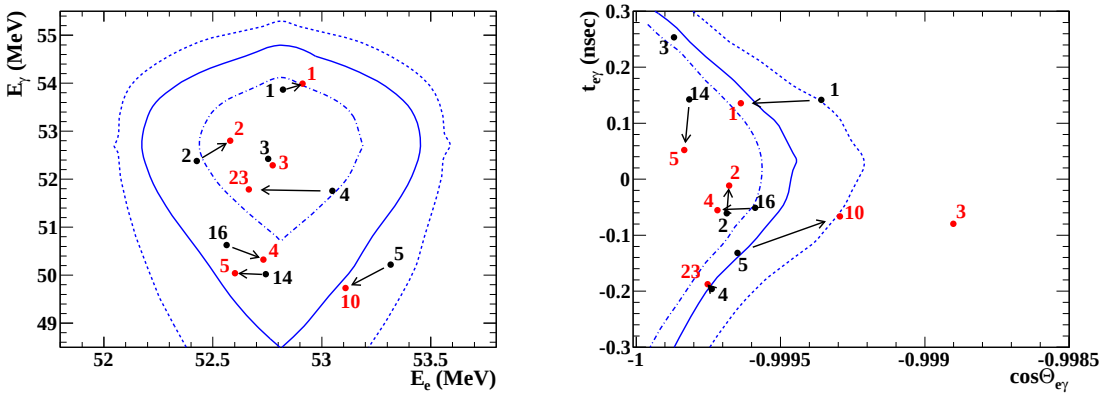

(a) (b)

Figure 7.14: Event-by-event comparison for five high rank events found in new/previous analysis shown by red/black markers. Numbers represent the event of $R_{\rm sig}$ ordering. The signal two-dimensional PDFs are superimposed as contours at 1, 1.645, 2 σ as blue dashed, solid, and dotted lines respectively.

be appeared/disappeared due to the different reconstructed values therefore one cannot satisfy the selection criteria and the other pass the selection criteria.

7.6 Discussions and Prospects

7.6.1 Discussions

From the analysis on 2009–2011 dataset, we set the most stringent upper limit for the $\mu^+ \to e^+\gamma$ decay with increased statistics by adding the 2011 dataset and several analysis improvements. Because of the offline noise reduction, a 6% higher positron efficiency and a few % better angular resolutions are obtained. New track fitting also improves the efficiency by ∼6% and enables us to use the event-by-event positron PDFs. We obtained a 10% sensitivity improvement by adding the event-by-event uncertainties in the analysis instead of using the two category PDFs. The new pileup elimination algorithm gains the efficiency by 7% for gamma rays and reduces the energy tail due to pileup events. For these reasons, we obtained a 20% sensitivity improvement in 2009–2010 dataset with the new analysis than that calculated by the previous analysis. From the compatibility check, the difference in the observed upper limits is consistent with the expectation with a 31% probability.

As a result, we obtain 20 times more stringent upper limit than that of MEGA [2]. Here we summarize the current experimental bounds (90% C.L.) on other muon CLFV processes as already introduced in Sec. 1.3.3 together with a new result which we obtained.

$$B(\mu^+ \to e^+\gamma) < 5.7 \times 10^{-13} \quad [5]$$
$$B(\mu^+ \to e^+e^+e^-) < 1.0 \times 10^{-12} \quad [11]$$
$$B(\mu^- N \to e^- N, \mathrm{Au}) < 7.0 \times 10^{-13} \quad [21]$$

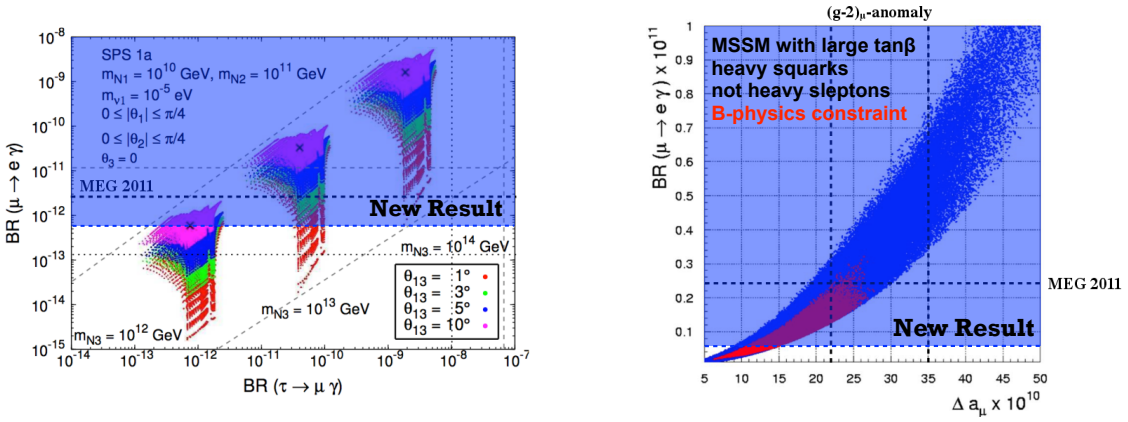

(a) (b)

Figure 7.15: (a) shows $B(\mu \to e\gamma)$ v.s. $B(\tau \to \mu\gamma)$ correlation (Fig. 1.3 in Sec. 1.2.2 [16]) with the new upper limit of $B(\mu^+ \to e^+\gamma)$. (b) shows $B(\mu \to e\gamma)$ v.s. muon g-2 correlation (Fig. 1.5 in Sec. 1.2.3 [20]) with the new upper limit of $B(\mu^+ \to e^+\gamma)$.

Table 7.13: Detector performance which were written in the proposal and those obtained from data taken in 2011.

Parameters	in proposal [3]	in 2011 data
R_μ (Hz)	1×10^8	3×10^7
E_e (%, FWHM)	0.7	1.3
E_γ (%, FWHM)	1.4	$4.0(w > 2$ cm$)/5.6(w < 2$ cm$)$
opening angle (mrad, FWHM)	9	$21(\phi)/38(\theta)$
$t_{e\gamma}$ (ns, FWHM)	0.15	0.3
ϵ_e (%)	95	31
ϵ_γ (%)	70	63

We set the most stringent upper limit in comparison with other CLFV decay searches. If the photonic contributions are dominant in the new physics (See Sec. 1.3.3), the branching ratio of 10^{-13} corresponds to 10^{-15} branching ratio of the $\mu^+ \to e^+e^+e^-$ decay and the $\mu^- N \to e^- N$ conversion. Figure 7.15 shows the same plots shown in Fig. 1.3 and Fig. 1.5 with the 90% C.L. upper limit obtained in the new result. By using this result, we set more stringent constraint on many new physics models than that by using the previous upper limit.

Table 7.13 shows the detector performance which are written in the proposal and those obtained in 2011 data. The muon beam is operated at 3 times lower rate in experiment, it is because the rate capability of the drift chamber is worse than the design value. Besides, worse resolutions cause the smaller signal-to-background ratio and the higher rate does not promise the better sensitivity in this case. Since the scattering effect due to cables and pre-amplifier boards between drift chambers and the timing counter is not considered in the proposal, positron efficiency shows large discrepancy between the design value and the measured one. The single event sensitivities (SES) can be calculated by

using numbers which are shown in Table 7.13 by using an equation given as

$$SES(\mu^+ \to e^+\gamma) = \frac{1}{R_\mu \cdot T \cdot (\Omega_{e\gamma}/4\pi) \cdot \epsilon_e \cdot \epsilon_\gamma \cdot \epsilon_{e\gamma}}, \tag{7.4}$$

where R_μ is the muon stopping rate, T is the total effective run time, $\Omega_{e\gamma}/4\pi$ is ratio of the detector acceptance ratio and is calculated to be $\Omega_{e\gamma}/4\pi \simeq 0.1$. The results are as follows:

$$\begin{aligned} SES_{\text{proposal}}(T = 200 \text{ days } LV) &= 1.1 \times 10^{-14}, \\ SES_{\text{MEG2011}}(T = 200 \text{ days } LV) &= 1.1 \times 10^{-13}. \end{aligned}$$

Here 200 days of DAQ live time is assumed. The effective branching ratio of the accidental background can be calculated from Eq. (1.20) and the results are as follows:

$$B_{\text{acc,proposal}} = 4.1 \times 10^{-15}, \tag{7.5}$$

$$B_{\text{acc,MEG2011}} = 3.6 \times 10^{-13}. \tag{7.6}$$

This means that the SES of the current MEG experiment is already close to the rate of background and thus the evolution of the sensitivity is not proportional to the statistics. Therefore, more background reduction is necessary to search for the $\mu^+ \to e^+\gamma$ decay below 10^{-13}.

7.6.2 Prospects

The MEG experiment finished the physics data taking at the end of the summer in 2013. The final statistics will be doubled by adding the data taken in 2012–2013 to the data which we already analyzed. There are few additional studies which can possibly improve the experimental sensitivity as follows.

- The new measurement of the COBRA magnetic field is under preparation in order to improve the precision down to 0.1%, which is 2–3 times better than that in the last time measurement. This may help to reduce the systematic uncertainties on the positron observables.
- We are now studying the AIF background by searching for the candidate of the AIF gamma ray associated with a positron track which disappears before exiting the drift chamber volume. By using the AIF analysis, the relative alignment can be measured by the similar way as used in the cosmic-ray relative alignment (See Sec. 4.3.4.1). This can help to reduce the uncertainties on the relative angles ($\theta_{e\gamma}$ and $\phi_{e\gamma}$) and they are the most largest uncertainties in the present analysis as shown in Table 7.10. Moreover, it would be a potential tool to identify the background gamma rays from the AIF events and this can help to reduce the background rate in the physics analysis.

Figure 7.16 shows the curve of the sensitivity evolution as a function of the accumulated DAQ time. The sensitivity of 2009–2013 all combined dataset is expected to be reach the left edge of this sensitivity curve, which corresponds to 5×10^{-13} at 90% C.L. The

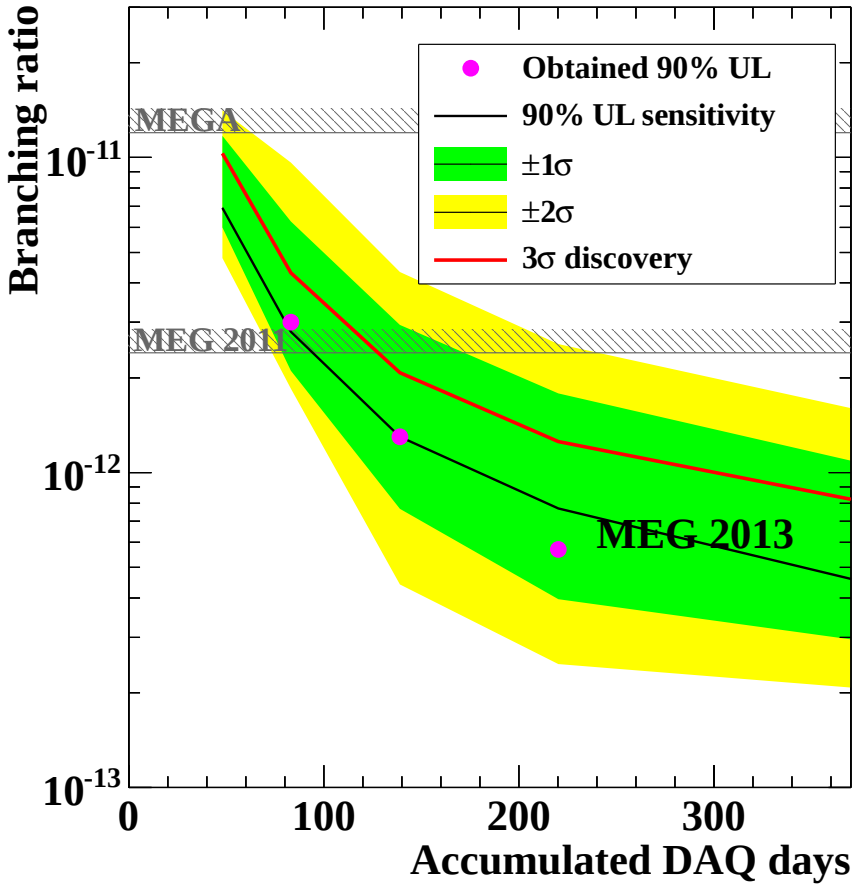

Figure 7.16: Sensitivity curve as a function of the accumulated DAQ time. Black solid curve shows the curve of the expected sensitivity and green and yellow regions express the 1 and 2 σ error bands, respectively. Magenta markers are observed 90% C.L. upper limits. Red solid curve shows a 3 σ discovery potential of the experiment for the $\mu^+ \to e^+\gamma$ decay.

analysis using this dataset will be presented in near future with further improvements as introduced above.

As already mentioned in Sec. 1.3.3, three experiments which will search for the $\mu^+ \to e^+e^+e^-$ and the $\mu^- N \to e^- N$ have been proposed and they are aiming to start physics data taking in the next decade. The proposed physics sensitivity of the $\mu^+ \to e^+e^+e^-$ experiment, the COMET experiment and the Mu2e experiment are expected to be exceed the final expected sensitivity of the current MEG experiment (5×10^{-13}). Therefore, it is very important to search for the $\mu^+ \to e^+\gamma$ decay with a better sensitivity in order to realize the complementary CLFV searches together with those experiments. However, the sensitivity is already close to the background dominated region by using present MEG detector and is not expected to be improved if we continue the experiment with current detectors, according to the Eq. (7.6). Therefore, the significant improvements of resolutions with the higher detection efficiency are required in order to search for the $\mu^+ \to e^+\gamma$ decay with a sensitivity better than the 10^{-13} level.

For this purpose, we already proposed the upgrade experiment of MEG called MEG II [60], in order to search for the $\mu^+ \to e^+\gamma$ decay with a 10 times higher sensitivity than that of MEG. As already discussed, we lose much efficiency between the drift chamber and the timing counter. This will be fixed by replacing 16 moduled drift chambers to the longer size of the stereo-wire drift chamber with a single gas volume. Rate capability should be also a matter for the MEG II experiment and now the test is ongoing. The photo sensors mounted on the inner surface of the LXe detector will be replaced with smaller size silicon-photomultipliers (SiPM). Because of their small size and high granularity, the position and the energy resolutions will be improved, in particular, the events in which gamma rays are converted in narrow region of the detector. Timing counter will be replaced with the subdivided plastic scintillators with small counter with SiPM read-out. Since positrons pass through the several counters, the timing resolution will be improved by using average timing. In MEG II, some optional detectors are also proposed to identify the background, or to improve the resolutions. The upgrade proposal was approved by the science research committee of PSI and many detector R&Ds are ongoing now.

Chapter 8

Conclusion

The $\mu^+ \to e^+\gamma$ decay search is one of the powerful probes of the BSM since many new physics models predict the large branching ratio of the $\mu^+ \to e^+\gamma$ decay although it is forbidden in the SM. In order to search for the $\mu^+ \to e^+\gamma$ decay with a sensitivity which has never been reached before, we developed

1. An innovative gamma ray detector using 900 l LXe and 846 VUV-sensitive PMTs,
2. A positron spectrometer, which is operational in the high rate environment, consists of
   (a) A superconducting magnet with graded field specialized to the 52.8 MeV signal positron,
   (b) Drift chambers, made of ultra low mass materials, which can measure the position in $\mathcal{O}(100)$ μm precision,
   (c) Timing counters which can measure the positron timing less than 100 ps precision,

and the world most intense DC muon beam at PSI allows us to collect the high statistics while suppressing the accidental background rate.

In this thesis, we analyze the data taken during 2009–2011 with several improvements as follows:

- by adding the 2011 data, statistics are doubled in comparison with the previous result of the MEG experiment [4],
- gamma ray pileup unfolding helps to reduce the pileup events and increases the efficiency by 7%,
- apply the offline noise reduction, which gives 6% efficiency improvement and resolutions are also improved by a few %,
- new Kalman filter gains the statistics by 6% and it enables us to use the positron per-event PDFs,
- per-event PDFs give a 10% sensitivity improvement.

As a result, we obtained a sensitivity of 7.7×10^{-13}. This is the first $\mu^+ \to e^+\gamma$ search with a sensitivity below 10^{-12}. No signal excess is observed in the analysis region and the maximum likelihood fitting shows the result consistent with a null-signal hypothesis. Therefore we set 90% C.L. upper limit, which calculated to be

$$B(\mu^+ \to e^+\gamma) < 5.7 \times 10^{-13},$$

on the existence of the $\mu^+ \to e^+\gamma$ decay. This is a four times more stringent upper limit than the previous best limit set by MEG.

Appendix A

Geometrical Model of Correlations

In order to understand the source of the correlation, the simple geometrical model gives good enough solutions. Here we assume the helicoidal approximation of the positron track.

For the extraction of the $\delta\phi_{\rm e}$ vs. $\delta E_{\rm e}$ and $\delta y_{\rm e}$ vs. $\delta E_{\rm e}$ correlations, a circle shape of a positron track is assumed to be projected on the transverese plane as shown in Fig. A.1. When the position of the center of the circle defined as $(X_0, Y_0) = (x_{\rm e} + d_x, y_{\rm e} + d_y)$, they are given as

$$d_x = R\cos\left(\frac{\pi}{2} - \phi_{\rm e}\right) = R\sin\phi_{\rm e}, \tag{A.1}$$

$$d_x = R\sin\left(\frac{\pi}{2} - \phi_{\rm e}\right) = -R\cos\phi_{\rm e}, \tag{A.2}$$

where R is the radius of the circle and $\phi_{\rm e}$ is the emission angle of the positron. Since the transverse momentum of a positron is proportional to the radius of the circle, an error of the positron energy can be approximated to $\delta E_{\rm e}/E_{\rm e} = \delta R/R$. From Eq. (A.1), the $\delta\phi_{\rm e}$ vs. $\delta E_{\rm e}$ correlation is read as

$$\delta\phi_{\rm e} = -2\tan\phi_{\rm e}\frac{\delta E_{\rm e}}{E_{\rm e}}. \tag{A.3}$$

The $\delta y_{\rm e}$ vs. $\delta E_{\rm e}$ correlation can be calculated from the vertical shift of the circle center as

$$\begin{aligned} \delta y_{\rm e} &= \delta Y_0 - \delta d_y, \\ &= \cos\phi_{\rm e}\delta R + \cos\phi_{\rm e}\delta R - R\sin\phi_{\rm e}\delta\phi_{\rm e}, \\ &= \frac{2R}{\cos\phi_{\rm e}}\frac{\delta E_{\rm e}}{E_{\rm e}}. \end{aligned} \tag{A.4}$$

The $z_{\rm e}$ vs. $\theta_{\rm e}$ correlation is extracted by using the same way as two correlations above. Figure A.2 shows the track projected on a plane that is parallel to the Z-axis and tangent to the track helix at the muon vertex. Here d_z is the distance between the vertex V and the position of the track after one turn and the Z_0 is absolute Z position at that point. Therefore the vertex position $z_{\rm e}$ and d_z are given as

$$Z = Z_0 - d_z, \tag{A.5}$$

$$d_z = 2R\cot\theta_{\rm e}. \tag{A.6}$$

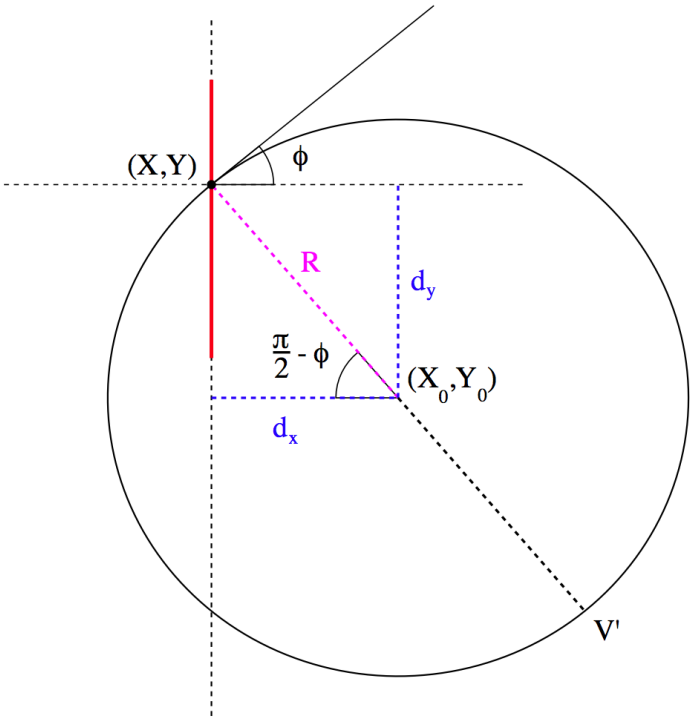

Figure A.1: Extraction of the $\delta\phi_{\rm e}$ v.s. $\delta E_{\rm e}$ and $\delta y_{\rm e}$ v.s. $\delta E_{\rm e}$ correlations. The red vertical line shows the target intersection with the transverse plane passing from the muon decay point $V = (X, Y)$.

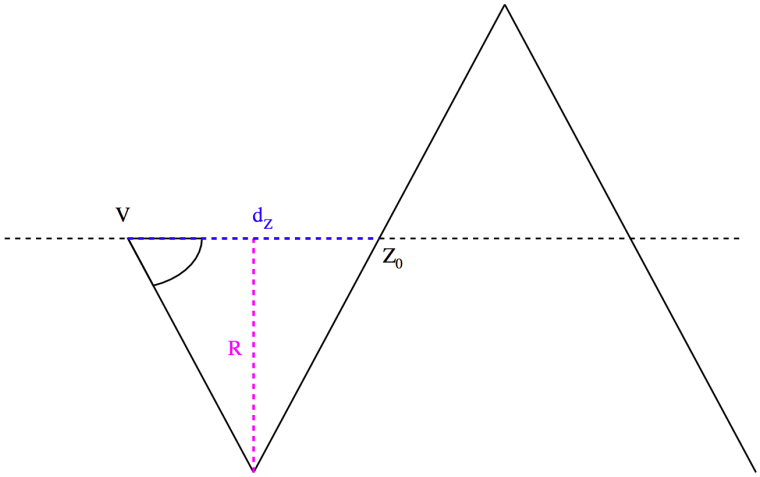

Figure A.2: Extraction of the $\delta\theta_e$ v.s. δz_e correlation.

Assuming that in this case Z_0 does not change, being constrained by the hits, δz_e is given as

$$\delta z_e = -\delta d_z = 2R\left(\frac{1}{\sin^2\theta_e}\delta\theta_e - \cot\theta_e\frac{\delta E_e}{E_e}\right). \tag{A.7}$$

A.1 Implementation of Correlations

In the case of the signal positron, the value of E_e is identical to ${E_e}^{\text{true}} = 52.8$ MeV. Therefore the shifts of the angular and vertex variables due to the geometrical constraint can be corrected by using $\delta E_e = {E_e}^{\text{Measured}} - {E_e}^{\text{true}}$. Besides, the contributions of the correlations to the angular or positrion resolutions can be disentangled since the momentum shift from the true value is identical for the signal case. The practical parameterizations of correlations are described in Sec. 6.3.2.3 in detail.

Appendix B

Radiative Muon Decay

The differential branching ratio of RMD is given in Eq. 6.28. The functions in Eq. 6.28, $F(x,y,d)$, $G(x,y,d)$ and $H(x,y,d)$ in the SM are given as follows:

$$\begin{aligned} F &= F^{(0)} + rF^{(1)} + r^2F^{(1)}, \\ G &= G^{(0)} + rG^{(1)} + r^2G^{(1)}, \\ H &= H^{(0)} + rH^{(1)} + r^2H^{(1)}, \end{aligned} \tag{B.1}$$

where $r = (m_e/m_\mu)^2$.

$$\begin{aligned} F^{(0)} &= \frac{8}{d}\left[y^2(3-2y) + 6xy(1-y) + 2x^2(3-4y) - 4x^3\right] \\ &\quad +8\left[-xy(3-y-y^2) - x^2(3-y-4y^2) + 2x^3(1+2y)\right] \\ &\quad +2d\left[x^2y(6-5y-2y^2) - 2x^3y(4+3y)\right] + 2d^2x^3y^2(2+y), \end{aligned} \tag{B.2}$$

$$\begin{aligned} F^{(1)} &= \frac{32}{d^2}\left[-\frac{y(3-2y)}{x} - (3-4x) + 2x\right] \\ &\quad +\frac{8}{d}\left[y(6-5y) - 2x(4+y) + 6x^2\right] \\ &\quad +8\left[x(4-3y+y^2) - 3x^2(1+y)\right] + 6dx^2y(2+y), \end{aligned} \tag{B.3}$$

$$F^{(2)} = \frac{32}{d^2}\left[\frac{(4-3y)}{x} - 3\right] + \frac{48y}{d} \tag{B.4}$$

$$\tag{B.5}$$

$$\begin{aligned} G^{(0)} &= \frac{8}{d}\left[xy(1-2y) + 2x^2(1-3y) - 4x^3\right] \\ &\quad +4\left[-x^2(2-3y-4y^2) + 2x^3(2+3y)\right] - 4dx^2y(2+y), \end{aligned} \tag{B.6}$$

$$G^{(1)} = \frac{32}{d^2}(-1+2y+2x) + \frac{8}{d}(-xy+6x^2) - 12x^2(2+y), \tag{B.7}$$

$$G^{(2)} = -\frac{96}{d^2}, \tag{B.8}$$

$$\tag{B.9}$$

$$
\begin{aligned}
H^{(0)} &= \frac{8}{d}\left[y^2(1-2y)+xy(1-4y)-2x^2y\right] \\
&\quad +4\left[2xy^2(1+y)-x^2y(1-4y)+2x^3y\right] \\
&\quad +2d\left[x^2y^2(1-2y)-4x^3y^2\right]+2d^2x^3y^3, \qquad \text{(B.10)} \\
H^{(1)} &= \frac{32}{d^2}\left[-\frac{y(1-2y)}{x}+2y\right] \\
&\quad +\frac{8}{d}\left[y(2-5y)-xy\right]+6dx^2y^2, \qquad \text{(B.11)} \\
H^{(2)} &= -\frac{96y}{d^2x}+\frac{48y}{d}. \qquad \text{(B.12)}
\end{aligned}
$$

Acknowledgement

Here I would like to mention many thanks to people who gave me innumerable but many advices and supports up to this day. This thesis must not be able to be finished without their huge amount of contributions.

Prof. Toshinori Mori gave me the chance to study in the MEG experiment and many precious advices during my research period until now and for writing this thesis.

I also express my great appreciation to Prof. Wataru Ootani, Dr. Toshiyuki Iwamoto, Dr. Ryu Sawada, Dr. Yusuke Uchiyama, Prof. Satoshi Mihara, Dr. Hajime Nishiguchi for their technically detailed advices and a large number of supports for me to live in the Switzerland. I thanks to Dr. Hiroaki Natori, Dr. Yasuhiro Nishimura, Dr. Xue Bai and other people in MEG Japanese group for their many advices and helps for my research and life. I have learned plenty of things from above people since I first joined to the MEG-J group.

I greatly thanks to Mr. Daisuke Kaneko and Ms. Miki Nishimura for me to have an exiting research life in Switzerland together with them.

I would like to express my special thanks to my colleagues who are working on PSI, especially for Dr. Stefan Ritt, Dr. Malte Hildebrandt and Dr. Peter-Raymond Kettle for their huge amount of supports and advices.

I am very grateful that I could learn a lot of things about the drift chamber analysis from Dr. Francesco Renga, Dr. Elisabetta Baracchini and Dr. Fedor Ignatov.

There are more people who are working in the MEG collaboration and I express many gratitude to all of them. Contributions from all collaborators are tremendous to complete this thesis.

I also appreciate to many students, staffs and the secretaries of the International Center for Elementary Particle Physics (ICEPP) for their much supports. Especially, I learned many things from students who enter the ICEPP together with me. We studied together about the particle physics and often discussed each other.

I am thankful to my family and friends for their helps to my life. Finally, I would like to express my great appreciation to my wife, Satomi Fujii for her deep love and remarkable supports to me.

December 2013,
Tokyo
Yuki FUJII

Bibliography

[1] ATLAS Collaboration, "Observation of a new particle in the search for the Standard Model Higgs boson with the ATLAS detector at the LHC", Phys. Lett. B **716**, 1–29 (2012); CMS Collaboration, "Observation of a new boson at a mass of 125 GeV with the CMS experiment at the LHC", Phys. Lett. B **716**, 30–61 (2012).

[2] M. Ahmed *et al.*, "Search for the lepton-family-number nonconserving decay $\mu^+ \to e^+\gamma$", Phys. Rev. D **65**, 112002 (2002); M. L. Brooks *et al.*, "New Limit for the Lepton-Family-Number", Phys. Rev. Lett. **83**, 1521–1524 (1999).

[3] T. Mori *et al.*, "Search for $\mu^+ \to e^+\gamma$ down to 10^{-14} branching ratio", Research Proposal to Paul Scherrer Institut, R-99-05 (1999), http://meg.web.psi.ch/docs/prop_psi/index.html.

[4] J. Adam *et al.*, [MEG collaboration], "New Limit on the Lepton-Flavor-Violating Decay $\mu^+ \to e^+\gamma$", Phys. Rev. Lett. **107**, 171801 (2011).

[5] J. Adam *et al.*, [MEG collaboration], "New Constraint on the Existence of the $\mu^+ \to e^+\gamma$ Decay" Phys. Rev. Lett. **110**, 201801 (2013).

[6] S. H. Neddermeyer and C. D. Anderson, "Note on the Nature of Cosmic-Ray Particles", Phys. Rev. **51**, 884–886 (1937).

[7] Particle Data Group, Review of Particle Physics, http://pdg.lbl.gov/.

[8] R. R. Crittenden *et al.*, "Radiative Decay Modes of the Muon", Phys. Rev. **121**, 1823–1832 (1961).

[9] W. Bertl *et al.*, "Search for the decay $\mu^+ \to e^+e^+e^-$", Nucl. Phys. B **260**, 1–31 (1985).

[10] S. Freedman *et al.*, "Limits on neutrino oscillations from $\overline{\nu_e}$ appearance", Phys. Rev. D **47**, 811–829 (1993).

[11] U. Bellgardt *et al.*, "Search for the decay $\mu^+ \to e^+e^+e^-$", Nucl. Phys. B **299**, 1–6 (1988).

[12] R. D. Bolton *et al.*, "Search for rare muon decays with the Crystal Box detector", Phys. Rev. D **38**, 2077–2101 (1988); R. D. Bolton *et al.*, "Search for the Decay $\mu^+ \to e^+\gamma$", Phys. Rev. Lett. **56**, 2461–2464 (1986).

[13] L. Michel, "Interaction between Four Half-Spin Particles and the Decay of the μ-Meson", Proc. Phys. Soc. A **63**, 514–531 (1950).

[14] Y. Kuno and Y. Okada, "Muon decay and physics beyond the standard model", Rev. Mod. Phys. **73**, 151–202 (2001).

[15] W. Fetscher and H.-J. Gerber, "MUON DECAY PARAMETERS", Particle Data Group, http://www-pdg.lbl.gov/1998/muondec_s004259.pdf

[16] S. Antusch *et al.*, "Impact of θ_{13} on lepton flavour violating processes within SUSY seesaw", JHEP **11**, (2006) 090.

[17] K. Abe *et al.*, [T2K Collaboration], "Evidence of electron neutrino appearance in a muon neutrino beam", Phys. Rev. D **88**, 032002 (2013); F. P. An *et al.*, [Daya Bay Collaboration], "Observation of Electron-Antineutrino Disappearance at Daya Bay", Phys. Rev. Lett. *108*, 171803 (2012).

[18] G. W. Benntt *et al.*, "Measurement of the Negative Muon Anomalous Magnetic Moment to 0.7 ppm", Phys. Rev. Lett. **92**, 161802 (2004).

[19] T. Aoyama, M. Hayakawa, T. Kinoshita, and M. Nio, "Complete Tenth-Order QED Contribution to the Muon $g-2$" Phys. Rev. Lett. **109**, 111808 (2012).

[20] G. Isidori *et al.*, "Flavor physics at large tan β with a binolike lightest supersymmetric particle", Phys. Rev. D **75**, 115091 (2007).

[21] W. Bertl *et al.*, [SINDRUM II Collaboration], "A search for $\mu \to e$ conversion in muonic gold", Eur. Phys. J. C **47**, 337–346 (2006).

[22] A. van der Schaaf *et al.*, "A SEARCH FOR THE DECAY $\mu^+ \to e^+\gamma$", Nucl. Phys. **A340**, 249–270 (1980); H. P. Povel *et al.*, "A NEW UPPER LIMIT FOR THE DECAY $\mu^+ \to e^+\gamma$", Phys. Lett. B **72**, 183–186 (1977).

[23] P. Depommier *et al.*, "New Limit on the Decay $\mu^+ \to e^+\gamma$", Phys. Rev. Lett. **39**, 1113–1116 (1977); G. Azuelos *et al.*, "New Upper Limit on the Decay $\mu \to e\gamma\gamma$", Phys. Rev. Lett. **51**, 164–167 (1983).

[24] W. W. Kinnison *et al.*, "Search for $\mu^+ \to e^+\gamma$", Phys. Rev. D **42**, 556–560 (1979).

[25] T. Kinoshita and A. Sirlin, "Radiative Corrections to Fermi Interactions", Phys. Rev. *113*, 1652–1660 (1959).

[26] A. Schöning, St. Ritt *et al.*, "Research Proposal for an Experiment to Search for the Decay $\mu \to eee$", Research Proposal to Paul Scherrer Institut, R-12-03.1 (2013), arXiv:1301.6113v1 [physics.ins-det].

[27] Mu2e Collaboration, "Proposal to Search for $\mu^- N \to e^- N$ with a Single Event Sensitivity Below 10^{-16} (Mu2e Experiment)", a research proposal to Fermilab (2008).

[28] COMET Collaboration, "Experimental Proposal for Phase-I of the COMET Experiment at J-PARC", Proposal for Nuclear and Particle Physics Experiments at J-PARC, KEK/J-PARC-PAC 2012-10, (2012), http://j-parc.jp/researcher/Hadron/en/pac_1207/pdf/E21_2012-10.pdf.

[29] S. Rai Choudhury, A. S. Corneli, A. Deandrea, Naveen Gaur, and A. Goyal, "Lepton flavor violation in the little Higgs model with T parity", Phys. Rev. D **75**, 055011 (2007).

[30] B. Aubert *et al.*, [BABAR Collaboration], "Searches for Lepton Flavor Violation in the Decays $\tau^{\pm} \to e^{\pm}\gamma$ and $\tau^{\pm} \to \mu^{\pm}\gamma$", Phys. Rev. Lett. **104**, 021802 (2010).

[31] K. Hayasaka, K. Inami, Y. Miyazaki, k. Arinstein, V. Aulchenko, T. Aushev, A.M. Bakich, A. Bay *et al.*, "Search for lepton-flavor-violating τ decays into three leptons with 719 million produced $\tau^{+}\tau^{-}$ pairs", Phys. Lett. B **687**, 139–143 (2010).

[32] J. Adam *et al.*, [MEG collaboration], "The MEG detector for $\mu^{+} \to e^{+}\gamma$ decay search", Eur. Phys. J. C **73**, 2365 (2013).

[33] Paul Scherrer Institut (PSI):: High Intensity Proton Accelerators (HIPA), http://www.psi.ch/gfa/accelerators.

[34] Y. Uchiyama *et al.*, [MEG Collaboration], "Measurement of polarized muon radiative decay" arXiv:1312.3217v1 [hep-ex], (2013).

[35] J. Jortner, L. Mever, S. A. Rice, and E. G. Wilson, "Localized Excitations in Condensed Ne, Ar, Kr, and Xe", J. Chem. Phys. **42**, 4250–4253 (1965); N. Schwenter, E.-E. Koch, and J. Jortner, "Electronic Excitations in Condensed Rare Gases", Springer-Verlag, Berlin (1985).

[36] R. Sawada, "A Liquid Xenon Scintillation Detector to Search for the Lepton Flavour Violating Muon Decay with a Sensitivity fo 10^{-13}", Ph. D. Thesis, the University of Tokyo (2005), http://meg.web.psi.ch/docs/theses/sawada_phd.pdf/.

[37] T. Haruyama, K. Kasami, H. Inoue, S. Mihara and Y. Matsubara, "Development of a high-power coaxial pulse tube refrigerator for a liquid xenon calorimeter", AIP Conf. Proc. **710**(1), 1459–1466 (2004).

[38] Hamamatsu Photonics K. K., http://www.hamamatsu.com/.

[39] W. Ootani *et al.*, "Development of a Thin-wall Superconducting Magnet for the Positron Spectrometer in the MEG Experiment", IEEE *Trans.* on Applied Superconductivity **14**, 568–571 (2004).

[40] M. Hildebrandt, "The drift chamber system of the MEG experiment", Nucl. Instrum. Meth. A **623**, 111–113 (2010).

[41] H. Nishiguchi, "An Innovative Positron Spectrometer to Search for the Lepton Flavour Violating Muon Decay with a Sensitivity of 10^{-13}", Ph. D. Thesis, the University of Tokyo (2008), http://meg.web.psi.ch/docs/theses/nishiguchi_phd.pdf/.

[42] D. F. Anderson *et al.*, "A simple vernier method for improving the accuracy of coordinate read-out in large wire chambers", Nucl. Instrum. Meth. A **224**(1–2), 315–317 (1984); D. Green *et al.*, "Accurate 2 dimensional drift tube readout using time division and vernier pads", Nucl. Instrum. Meth. A **256**(2), 305–312 (1987); J. Allison *et al.*, "The diamond shaped cathode pads of the OPAL muon barrel drift chambers", Nucl. Instrum. Meth. A **310**(1–2), 527–534 (1991).

[43] Maximum Integration Data Acquisition System, https://midas.psi.ch/.

[44] "GEANT - Detector Description and Simulation Tool", http://wwwasd.web.cern.ch/wwwasd/geant/.

[45] "Garfield - simulation of gaseous detectors", http://garfield.web.cern.ch/garfield/.

[46] "ROOT, A Data Anaylsis Framework", http://root.cern.ch/drupal/.

[47] ROME. Root based object oriented midas extension. https://midas.psi.ch/rome/.

[48] Y. Uchiyama, "Analysis of the First MEG Physics Data to Search for the Decay $\mu^+ \to e^+\gamma$", Ph. D. Thesis, the University of Tokyo (2009), http://meg.web.psi.ch/docs/theses/uchiyama_phd.pdf.

[49] Y. Nishimura, "A Search for the Decay $\mu^+ \to e^+\gamma$ Using a High-Resolution Liquid Xenon Gamma-Ray Detector" Ph. D. Thesis, the University of Tokyo (2010), http://meg.web.psi.ch/docs/theses/nishimura_phd.pdf.

[50] X. Bai, "Search for the Lepton Flavor Violating Decay $\mu^+ \to e^+\gamma$ with A Sensitivity of 10^{-12}" Ph. D. Thesis, the University of Tokyo (2012), http://meg.web.psi.ch/docs/theses/bai_phd.pdf.

[51] F. Sauli, "PRINCIPLE OF OPERATION OF MULTIWIRE PROPORTIONAL AND DRIFT CHAMBERS", CERN Academic Training Lecture **81**, Experimental techniques in high energy physics, 79–188 (1976).

[52] R. E. Kalman, "A New Approach to Linear Filtering and Prediction Problems", Transaction of the ASME-J. Basic Engineering **D82**, 35–45 (1960).

[53] P. Billoir, "Track fitting with multiple scattering: A new method", Nucl. Instrum. Meth. A **225**, 352–366 (1984); R. Frühwirth, "APPLICATION OF KALMAN FILTERING TO TRACK AND VERTEX FITTING", Nucl. Instrum. Meth. A **262**, 444–450 (1987).

[54] A. Fontanna *et al.*, "Use of GEANE for tracking in virtual Monte Carlo", J. Phys. Conf. Ser. **119**, 032018 (2008).

[55] J. Adam, "New Analysis Method to Confirm the Upper Limit of the Branching Ratio $B(\mu^+ \to e^+ + \gamma)$ from the MEG Experiment" Ph. D. Thesis, ETH ZURICH (2012), http://meg.web.psi.ch/docs/theses/PhDThesis_Adam_2012.pdf

[56] Peter Schlper, G. Steinbrück, and Markus Stoye, "Software alignment of the cms tracker using millepede ii", Comput. Phys. Commun, **182**:1760-1763 (2006).

[57] A. Lenard, "Inner bremsstrahlung in μ-meson decay", Phys. Rev. **90**(5), 968–973, (1953); R.E. Behrends, R.J. Finkelstein, and A. Sirlin, "Radiative corrections to decay processes", Phys. Rev. **101**(2), 866–873 (1956); C. Fronsdal and H. Überall, "μ-meson decay with inner bremsstrahlung", Phys. Rev. **113**(2), 654–657 (1959).

[58] G. J. Feldman and R. D. Counsins, "Unified approach to the classical statistical analysis of small signals", Phys. Rev. D **57**, 3873–3889 (1998).

[59] A. L. Read, "Presentation of search results: the CL s technique", J. Phys. G **28**, 2693 (2002).

[60] MEG Collaboration, "MEG upgrade proposal", Upgrade Proposal to PSI, PSI R99-05.2, arXiv:1301.7225 (2012).